Development and Applications of a Multispectral Microscopic Imager for the In Situ Exploration of Planetary Surfaces

by

Jorge Iván Núñez Sánchez

A Dissertation Presented in Partial Fulfillment
of the Requirements for the Degree
Doctor of Philosophy

Approved April 2012 by the
Graduate Supervisory Committee:

Jack Farmer, Chair
Philip Christensen
Ferran Garcia-Pichel
Mark Robinson
Glenn Sellar
Lynda Williams

ARIZONA STATE UNIVERSITY

May 2012

ABSTRACT

Future robotic and human missions to the Moon and Mars will need *in situ* capabilities to characterize the mineralogy of rocks and soils within a microtextural context. Such spatially-correlated information is considered crucial for correct petrogenetic interpretations and will be key observations for assessing the potential for past habitability on Mars. These data will also enable the selection of the highest value samples for further analysis and potential caching for return to Earth. The Multispectral Microscopic Imager (MMI), similar to a geologist's hand lens, advances the capabilities of current microimagers by providing multispectral, microscale reflectance images of geological samples, where each image pixel is comprised of a 21-band spectrum ranging from 463 to 1735 nm. To better understand the capabilities of the MMI in future surface missions to the Moon and Mars, geological samples comprising a range of Mars-relevant analog environments as well as 18 lunar rocks and four soils, from the Apollo collection were analyzed with the MMI. Results indicate that the MMI images resolve the fine-scale microtextural features of samples, and provide important information to help constrain mineral composition. Spectral end-member mapping revealed the distribution of Fe-bearing minerals (silicates and oxides), along with the presence of hydrated minerals. In the case of the lunar samples, the MMI observations also revealed the presence of opaques, glasses, and in some cases, the effects of space weathering in samples. MMI-based petrogenetic

interpretations compare favorably with laboratory observations (including VNIR spectroscopy, XRD, and thin section petrography) and previously published analyses in the literature (for the lunar samples). The MMI was also deployed as part of the 2010 ILSO-ISRU field test on the slopes of Mauna Kea, Hawaii and inside the GeoLab as part of the 2011 Desert RATS field test at the Black Point Lava Flow in northern Arizona to better assess the performance of the MMI under realistic field conditions (including daylight illumination) and mission constraints to support human exploration. The MMI successfully imaged rocks and soils in outcrops and samples under field conditions and mission operation scenarios, revealing the value of the MMI to support future rover and astronaut exploration of planetary surfaces.

DEDICATION

To my family and friends, whose unconditional love and support have given me strength to excel at every step.

ACKNOWLEDGMENTS

Development of the MMI, testing, and analysis of MMI datasets was carried out at Arizona State University (ASU) and the Jet Propulsion Laboratory (JPL), California Institute of Technology, under contracts with the National Aeronautics and Space Administration (NASA). Laboratory analysis and characterization of test samples was carried out at ASU (petrography, XRD) and the US Geological Survey (USGS) in Denver, CO (VNIR spectroscopy). Analysis of Apollo samples was carried out at NASA's Johnson Space Center (JSC). This research was supported by the NASA Mars Instrument Development Program (MIDP) and the Jet Propulsion Laboratory's Director's Research and Development Fund (DRDF) to JDF and RGS. Support for the deployment of the MMI in the 2010 ILSO-ISRU and 2011 Desert RATS field tests was provided by NASA's Moon, Mars Analog Mission Activity (MMAMA) program to JDF. I would like to acknowledge fellowship support from the NASA Earth and Space Science Fellowship (NESSF) program as well as grant support as a Young Explorers Grant from the National Geographic Society (NGS), a Lewis and Clark Fellowship in Astrobiology from the NASA Astrobiology Institute (NAI) and the American Philosophical Society (AMS), and teaching and research assistantships from the School of Earth and Space Exploration, ASU. Additional travel support to attend professional meetings was provided by travel grants from the NAI, the Lunar and Planetary Institute (LPI), and the ASU Graduate and Professional Student

Association (GPSA). Special thanks to Charles Sarture, Paul Gardner and Andrew Kieta at JPL for their assistance with the design and fabrication of the MMI, Dr. Gregg Swayze (USGS) for providing access to the VNIR spectroscopy laboratory and providing feedback on spectral interpretations, Dr. Carl Allen (JSC) for providing access to the lunar samples from the Apollo collection, Dr. Gerald Sanders (JSC) for his support during the 2010 ILSO-ISRU field test at Mauna Kea, Hawaii, and Dr. Cynthia Evans and Dr. Dean Eppler (both at JSC) for their support during the 2011 Desert RATS field test. Additional thanks to Vicki Mills and Nicole Marin (ASU) for assistance with preparation of test samples and preliminary analysis of XRD results, Dr. Charles Meyer, Andrea Mosie, Carol Schwarz, and Terry Parker at JSC and Scott Nolte at JPL for their technical assistance with setting up the MMI in the lunar glove box and the handling of the Apollo lunar samples, and Dr. Daniel Winterhalter at JPL for the JPL/JSC initiative. I would like to especially thank my faculty advisor/mentor, Dr. Jack Farmer, for his guidance, friendship, and contributions made towards every aspect of this project as well as scientific and financial support. Finally, I would like to acknowledge Dr. Glenn Sellar, Dr. Mark Robinson, Dr. Phil Christensen, Dr. Lynda Williams, Dr. Ferran Garcia-Pichel, and Dr. Ronald Greeley for their invaluable input in this research as members of my graduate committee. Sadly, Dr. Greeley passed away a few months before the completion of this dissertation. He will be greatly missed.

TABLE OF CONTENTS

CHAPTER Page

CHAPTER Page

CHAPTER Page

CHAPTER Page

LIST OF TABLES

LIST OF FIGURES

Figure Page

Figure Page

Figure Page

Figure Page

CHAPTER 1

INTRODUCTION

Imaging at the microscale – in the form of a geologist's hand lens – has long been an essential tool for terrestrial field geology. Microtextural analysis of rocks using a hand lens, when combined with a knowledge of mineralogy, provides a powerful combination for assessing the origin of a rock. Armed with such information, the trained field geologist is often in a position to immediately assign a rock to one of three basic petrogenetic categories (igneous, sedimentary or metamorphic) and to begin to interpret past geological processes based on the interplay of textural and compositional information. In addition, comparisons of weathered and unweathered surfaces can reveal important information about the geologic processes currently active at a site.

The capabilities provided by a hand lens are recognized as essential for the surface exploration of planetary environments in our solar system. For example, a hand lens was included as a brush-scriber-lens tool carried onboard the Apollo 12 and 14 missions to aid the astronauts in observing and marking hand-sized specimens (Allton 1989). However, the tool was not used in the field due to the difficulty of viewing a sample through a helmet (Allton 1989). Never the less, such capability is still considered crucial for the exploration of planetary surfaces. The utility of a hand lens was demonstrated with the addition of the Microscopic Imager (MI) as part of the Athena Payload (Squyres et al. 2003) on the highly

successful Mars Exploration Rover (MER) mission (e.g., Herkenhoff et al. 2003; Herkenhoff et al. 2004). Imagery at the hand lens scale (several cm field of view resolved to several tens of microns) provided *in situ* by the Microscopic Imagers on the MERs (Herkenhoff et al. 2004) and the Robotic Arm Camera (Keller et al. 2008) on the Phoenix lander was vital to the success of these missions and to the Mars Exploration Program (Herkenhoff et al. 2004, 2006, 2008) that a microimager is one of the instruments now recognized as essential for Mars surface missions (e.g., NRC 2007; MEPAG ND-SAG 2008; MEPAG MRR-SAG 2009). In particular, one of the critical capabilities identified for a future caching rover in a Mars Sample Return (MSR) campaign includes an arm-mounted instrument, capable of interrogating the abraded surfaces of rocks to create co-registered 2-D maps of mineralogy and microtexture (MEPAG ND-SAG 2008; MEPAG MRR-SAG 2009). Such spatially-correlated data sets are considered crucial for identifying the best candidate samples for caching through *in situ* petrogenetic interpretations, assessments of past habitability and of the potential for preserving biosignatures. The 2018 caching rover was deemed by the Planetary Decadal Survey for the decade 2013-2022 to be the highest priority Flagship mission at the end of the decade (NRC 2011). The capability to characterize *in situ* the mineralogy of rocks and soils within a microtextural context is also regarded as essential for future rover and human exploration of the Moon (NRC 2007a).

To address the desired capabilities as identified above to create co-registered 2-D maps of mineralogy and microtexture necessary for the *in situ* characterization of geologic samples for future rover and human based exploration of the Moon and Mars, a new Multispectral Microscopic Imager (MMI) has been developed. The MMI advances the capabilities of current microimagers by combining microscopic imaging with visible/near-infrared reflectance spectroscopy, to obtain mineralogical information within a microtextural context. MMI images require minimal surface preparation and provide data sets that are intermediate to what geologists acquire in the field, using a hand lens, and in the lab using thin section petrography.

Chapter 2, “Development and Science Applications of a Multispectral Microscopic Imager (MMI) for the Astrobiological Exploration of Mars” provides an overview of the MMI along with results from imaging experiments of a suite of geological samples comprising a wide range of Mars-relevant analog environments to better understand and document the capabilities of the MMI in future surface missions to Mars. In particular, the MMI imaged a broad range of well-characterized igneous and sedimentary rock samples that record sedimentary processes and environments favorable for the preservation of biosignatures. The samples were characterized using traditional laboratory methods (including visible/near-infrared spectroscopy, X-ray diffraction, and thin section petrography) to provide a comparison to MMI-based petrogenetic

interpretations to evaluate instrument performance and feedback information for future instrument design improvements.

To further develop the MMI and assess the value of the instrument for lunar exploration, 18 lunar rocks and four soils, from a reference suite spanning a broad compositional range found in the Apollo collection, were analyzed with the MMI in a N_2-filled glovebox at NASA's Johnson Space Center. The measurements provided the means to assess the effectiveness of the MMI spatial and spectral capabilities to characterize the texture and mineralogy of lunar rocks and soils. The JSC observations also tested the capabilities of the instrument to operate in a glovebox environment to support future human exploration of the Moon. MMI-based petrogenetic interpretations were compared with results published in the literature. This work is presented in Chapter 3, "Exploring the Moon at the Microscale: Observations of Apollo samples with the Multispectral Microscopic Imager (MMI)".

Chapters 2 and 3 provide an overview of the MMI and demonstrate its capabilities to provide co-registered mineralogical and microtextural information to properly identify the petrogenesis of rocks and soils relevant for the Moon and Mars. While the two investigations mark a significant step in the development of the MMI to analyze "real-world" samples in a controlled laboratory environment, they do not represent "real-world" conditions as would be expected with a field deployment or actual human mission. As such, to better assess the performance of the MMI to operate

under field conditions (including daylight illumination) and simulated mission constraints to support human exploration, a field-portable, tripod-mounted rugged version of the MMI was deployed in the field as part of the 2010 International Lunar Surface Operations - In Situ Resource Utilization (ILSO-ISRU) field test on the slopes of Mauna Kea volcano, Hawaii and inside the GeoLab in the Deep Space Habitat (DSH) as part of the 2011 Desert Research and Technology Studies (RATS) field test at the Black Point Lava Flow in northern Arizona. The 2010 ILSO-ISRU field test provided the first opportunity to deploy the MMI in the field. Because the MMI operates by illuminating a sample surface using low power LEDs, artificial ambient light or daylight illumination is significantly stronger and would thus overwhelm the LED illumination, unless data collection was done after sunset or daylight illumination was reduced such as with a sunshade. Thus, the test provided a unique opportunity to assess the performance of the MMI and its ability to successfully operate using a sunshade in a Moon/Mars analog field site under variable conditions, including full daylight illumination, with unprepared, irregular surfaces. Following the successful demonstration in the 2010 ILSO-ISRU field test, a new opportunity arose to deploy the MMI in a different environment to test the performance of the instrument under mission operations conditions. The deployment of the MMI inside the GeoLab as part of the 2011 Desert RATS field test provided a unique opportunity to test whether the MMI could also be used as a tool by astronauts to support manned

missions to planetary surfaces, in this case a mission to a near-Earth asteroid (NEA). In particular, the test provided the opportunity to assess whether 1) the MMI could be successfully integrated inside the GeoLab and incorporated into the processing workflow of samples; 2) be operated by crew members with little familiarity with the instrument and remote support from mission control; 3) provide rapid characterization of mineralogy and microtexture of samples for further analysis with other instruments in the GeoLab and support real-time planning of science activities; and 4) operate under the simulated mission constraints associated with a mission to a NEA, including 50 second communications and data transfer delay, and limited operation time by crew members. Results from these two field deployments along with recommended improvements to make the instrument a more capable tool for future human exploration are presented in Chapter 4, “Field Analog Studies with the Multispectral Microscopic Imager (MMI): Applications for Moon/Mars Exploration”.

Finally, culminating in Chapter 5, “Concluding Thoughts” is a brief review of the findings contained in the previous chapters and acts as a summary of the accomplishments of the work presented in Chapters 2-4.

CHAPTER 2

DEVELOPMENT AND SCIENCE APPLICATIONS OF A MULTISPECTRAL MICROSCOPIC IMAGER FOR THE ASTROBIOLOGICAL EXPLORATION OF MARS

2.1. Introduction

An immediate objective in the exploration of Mars is the discovery of past or present habitable environments on Mars that could have supported microbial life and provided conditions favorable for the capture and preservation of biosignatures (e.g., NRC 2007; Des Marais 2008; MEPAG 2010; NRC 2011). In the analysis of aqueously-formed sedimentary rocks, spatially integrated microscale texture with mineralogy provides essential data for inferring both primary depositional environments and secondary (post-depositional) diagenetic processes. Such integrated data sets are regarded as essential for accurate *in situ* assessments of paleoenvironments, past habitability, and the potential for a fossil biosignature record. Microtextural analysis of rocks using a hand lens, when combined with a knowledge of mineralogy, provides a powerful combination for assessing the origin of a rock. Armed with such information, the trained field geologist is often in a position to immediately assign a rock to one of three basic petrogenetic categories (igneous, sedimentary or metamorphic) and to begin to interpret past geological processes based on the interplay of textural and compositional information. In addition, comparisons of weathered and unweathered

surfaces can reveal important information about the geologic processes currently active at a site.

Imaging at the microscale—in the form of a geologist's hand lens—has long been an essential tool for terrestrial field geology. Imagery at the hand lens scale (several cm field of view resolved to several tens of microns) provided by the Microscopic Imagers on the MERs (Herkenhoff et al. 2004) and the Robotic Arm Camera (Keller et al. 2008) on the Phoenix lander has proven so vital to the success of these missions and to the Mars Exploration Program (Herkenhoff et al. 2004, 2006, 2008) that a microimager is one of the instruments now recognized as essential for Mars surface missions (e.g., NRC 2007; MEPAG ND-SAG 2008; MEPAG MRR-SAG 2009). The microtextures of rocks and soils, defined as the microspatial interrelationships between constituent mineral grains, pore spaces, and secondary (authigenic) phases (e.g., cements) of minerals, provide essential data for inferring both primary formational processes and secondary (postformational) diagenetic processes. Such observations are fundamental for properly identifying rocks, interpreting the paleoenvironmental conditions they represent, and assessing the potential for past or present habitability. Multispectral, visible-to- near-infrared microimages could provide context information for evaluating the spatial (and implied temporal) relationships between constituent mineral phases characterized by other mineralogical methods that lack context information. Microimaging could also provide highly desirable contextual

information for guiding the subsampling of rocks for potential caching or additional analyses with other in situ instruments.

This paper provides an overview of the Multispectral Microscopic Imager, MMI, which has been designed to create multispectral, microscale reflectance images of geological samples, where each image pixel in the image is a visible/near-infrared spectrum. This enables the discrimination and mapping of a wide variety of rock-forming minerals, within a microtextural framework, fundamental data for inferring petrogenesis. We have used the MMI to image a broad range of well-characterized igneous and sedimentary rock samples that are representative of the types of geologic materials that are expected to occur on Mars. Particularly well-represented in the suite of test samples are lithotypes that record sedimentary processes and environments favorable for the preservation of biosignatures, including pristine igneous rocks, aqueously altered volcanic materials, detrital and chemical sedimentary rocks and hydrothermal sinters. At critical stages in developing the MMI instrument, we have used these data sets to evaluate instrument performance and feedback information to upgrade and improve instrument design. We have been particularly interested in improving the capability to map phases, or phase assemblages at a spatial and spectral resolution useful for determining the paragenesis (relative temporal relationships of different minerals and microtextural elements) in samples. This step allows the investigator to advance beyond simply identifying the type of rock, to an interpretation of

its diagenetic history, which is needed to understand the post-burial events that have affected a rock and how the lithologic system evolved over time. Such analyses are a logical next step in microscale imaging on Mars and bring the geologist much closer to the types of petrologic analyses routinely used by geologists in the field and laboratory. In combination, these data provide an effective basis for selecting and prioritizing the best samples (from a field of possibilities), for analysis using onboard lab instruments, or for caching to return to Earth.

2.2. Instrument Description

2.2.1. Current Version of the MMI

The version of the MMI used to acquire the data sets presented here evolved over a time frame of several years from previous less capable versions (Sellar et al. 2006; Nuñez et al. 2009a, 2009b). The current system consists of a field-portable, tripod-mounted, un-cooled Indium- Gallium-Arsenide (InGaAs) focal plane array (FPA) and a 21-band multi-wavelength light-emitting diode (LED) illumination array that generates multispectral, microscale, reflectance images of geological samples, where each pixel of an image consists of a spectrum ranging from the visible (0.463 μm) to the short-wave infrared (1.735 μm) (Figure 2.1). The characteristics of the major components of the instrument are described in the following subsections.

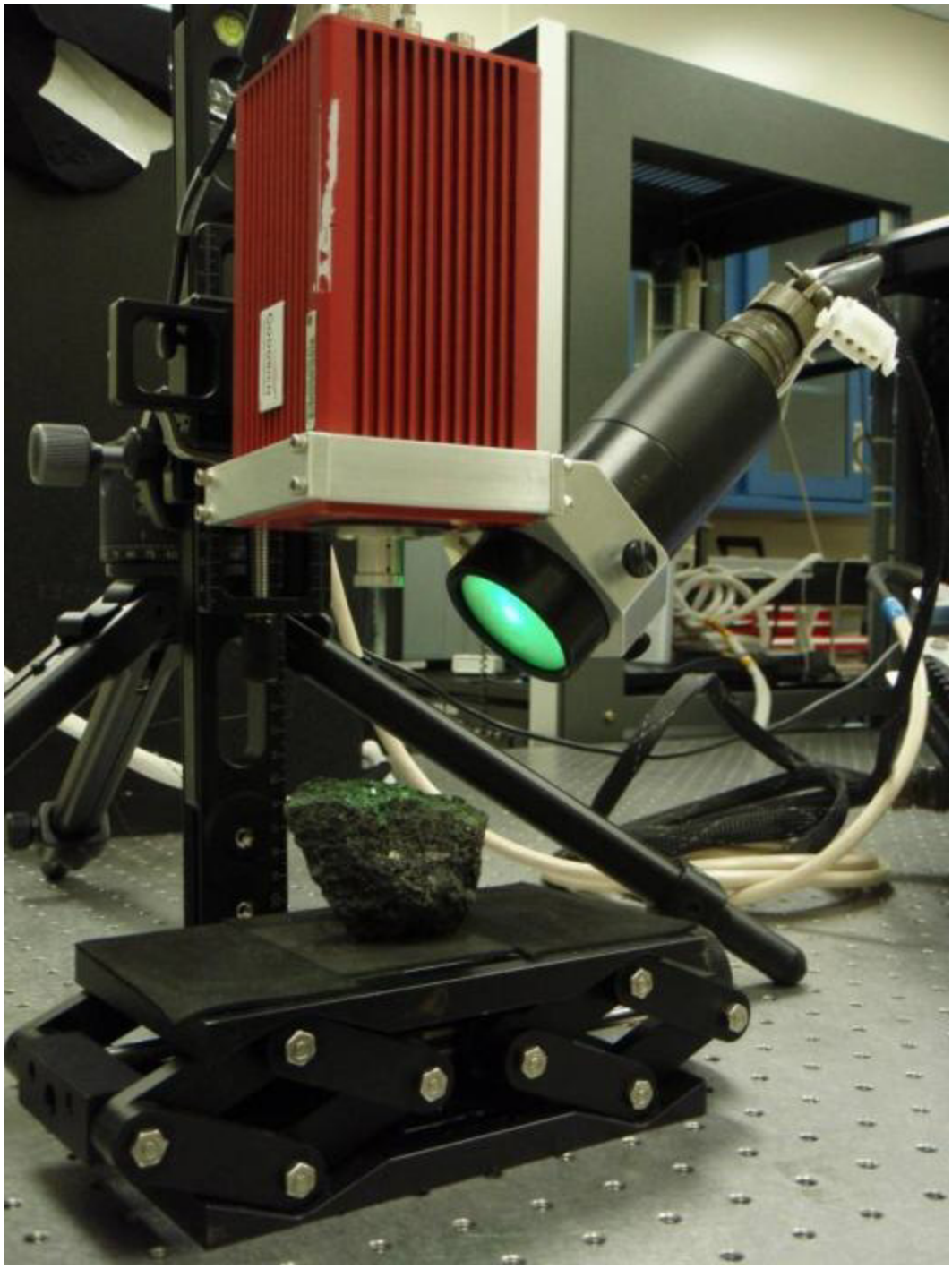

Figure 2.1. Image of the Multispectral Microscopic Imager (MMI). MMI shown with field-portable, tripod-mounted, un-cooled Indium-Gallium-Arsenide (InGaAs) focal plane array (FPA) camera (red) and illumination device (black), i.e. illuminator, containing 21-band multi-wavelength light-emitting diode (LED) illumination array.

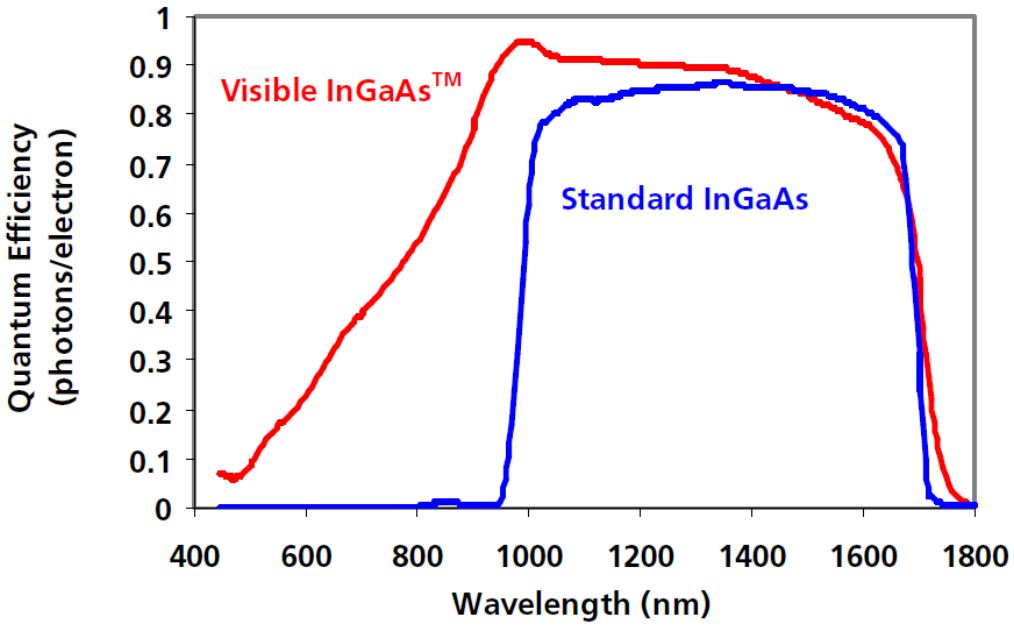

Figure 2.2. Comparison of MMI InGaAs FPA Quantum Efficiency to Standard InGaAs. Manufacturer-provided (from the Goodrich Corporation) spectral quantum efficiency of the InGaAs FPA (red) employed by the MMI compared to standard InGaAs FPAs (blue). The MMI FPA detection range extends to the visible to enable the imaging of surfaces in natural color and thereby eliminate the need for multiple detectors. In contrast to an InGaAs detector, a CCD detector's quantum efficiency drops around 1000 nm.

2.2.2. Camera Head

The current version of the MMI uses a commercial camera made by the Goodrich Corporation that employs an un-cooled, substrate-removed Indium-Gallium-Arsenide (InGaAs) focal plane array (FPA). The detector is sensitive over the spectral range of 0.4 to 1.8 μm with a quantum efficiency > 65% from 1.0 to 1.6 μm. Unlike standard InGaAs detectors, which have a general detection range of 0.9 to 1.7 μm, the MMI FPA detection range extends to 0.4 μm to enable the imaging of materials in natural color (Figure 2.2), thus eliminating the need for multiple detectors.

The MMI FPA consists of 640 x 512 pixels with a square-shaped pixel pitch of 25 μm. Within the operating temperature range of -10 °C to +40 °C, the MMI FPA has a full well depth of 800,000 electrons, a read noise of < 300 electrons, and a gain of ~ 50 e^-/DN. The analog output signal of the focal plane array (FPA) is digitized with a resolution of 14 bits using an analog-to-digital converter. The digitized image undergoes a pixel-by-pixel 2-point correction (offset and response gain) and bad pixel substitution. The offset compensates for the dark current signal (i.e. residual current when there is no incident illumination), and the gain compensates for the photoresponse non-uniformity. The digital image is then stored in a video frame buffer and converted into composite analog video using a 14-bit digital-to-analog converter. The conversion to 14-bit digital images enables the retention of a greater amount of information compared to the 12-bit or 8-bit conversions employed by most cameras.

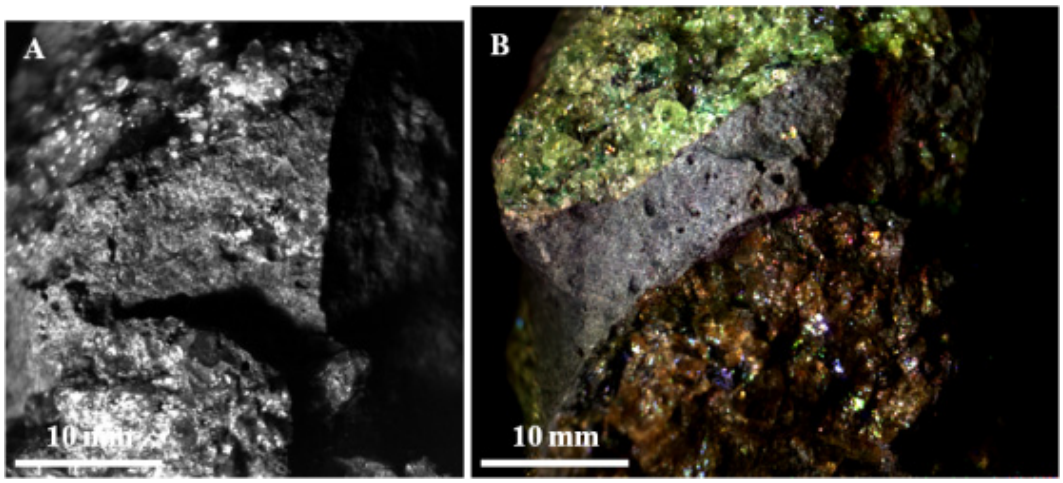

Figure 2.3. Comparison of MER MI Image with MMI Image of San Carlos Basalt. Comparable images obtained with engineering spare of the MER MI camera (left) and MMI (right) of same sample of San Carlos basalt. The MMI RGB image is composed of bands 641, 522, and 463 nm respectively. The MER MI field-of-view is 31 x 31 mm at 30 μm/pixel spatial resolution while MMI field-of-view is 40 x 32 mm at 62.5 μm/pixel spatial resolution. Both images are scaled to their respective sizes relative to one another. Despite half the spatial resolution as the MER MI camera, the MMI still provides significant detail and textural information that enables the identification of small and large textural elements, with the addition of color and spectral information. In both images, the sample is illuminated from the left.

2.2.3. Optics

A custom micro-imaging lens with a range of 0.4 to 1.8 μm was designed and fabricated specifically for the MMI. The lens was designed with a slow focal ratio (F/10) to provide a ~5 mm depth of field suitable for imaging natural surfaces (Sellar et al. 2006; Nuñez et al. 2009a). This ratio results in a working distance of 63 mm from the lens to the working plane and a field of view (FOV) of 40 mm x 32 mm, with a sampling scale of 62.5 μm/pixel. The resulting instantaneous field of view (IFOV) of 62.5 μm/pixel was a tradeoff reflecting the desire to maximize depth of field, while retaining a large enough FOV to be able to accurately place MMI images into larger context images obtained with other instruments, such as the Panoramic Camera (Pancam) onboard the Mars Exploration Rovers (Bell et al. 2003). While the MMI IFOV of 62.5 μm/pixel is approximately half the IFOV of the MER MI of 30 μm/pixel (Herkenhoff et al. 2003), the images reflect a balance between the resolution required to differentiate mineral grains the size of fine sand, with a context large enough to place grains within the recognizable microtextural elements of a rock (Figure 2.3). This last point is important, because of an impressive heritage gained by field geologists over the last century interpreting rocks at the handlens scale. Future developments of the MMI include improving the IFOV of the MMI from the current 62.5 μm/pixel to equal that of the MER MI of 30 μm/pixel (see Future Work section), which reflects an empirically-established optimum obtained by imaging microtextures of a wide range of lithotypes

to obtain adequate information for robust interpretations of petrogenesis.

2.2.4. Illumination System

The Robotic Arm Camera (Keller et al. 2007) and MECA Optical Microscope (Hecht et al. 2008) instruments onboard the Mars Phoenix mission (Smith et al. 2008), as well as the Rosetta Lander Imaging System (Mottola et al. 2007) onboard the Rosetta mission to comet 67P/ Churyumov- Gerasimenko have demonstrated the capabilities of light-emitting diode (LED) illumination systems to provide color images without the need for a filter wheel mechanism, multiple FPAs, or Bayer-pattern filters.

The illumination device, i.e. illuminator, of the MMI (Figure 2.1) employs commercial off-the-shelf, multi-wavelength LEDs to illuminate the sample in 21 different wavelengths ranging from the visible to the short-wave infrared, i.e. 0.463 to 1.735 μm. Effective wavelength band center and bandpass (i.e. Full-width at half maximum, FWHM) information for the LED wavelengths is given in Table 2.1. A plot of normalized MMI LED wavelengths is shown in Figure 2.4. This has advanced the capabilities of the current version of the MMI beyond previous versions (Sellar et al. 2006; Nuñez et al. 2009) by extending the spectral range into the short-wave infrared and increasing the number of spectral bands. This extends beyond the capabilities of current flight microimagers (see Table 2.2), including the Phoenix Robotic Arm Camera (RAC) (Keller et al. 2007) and Mars Science Laboratory's (MSL) Mars Hand Lens Imager (MAHLI)

(Edgett et al. 2009), as well as current flight multi-spectral imagers (see Table 2.3), including the Panoramic Camera (PanCam) on the Mars Exploration Rovers (Bell et al. 2003) and Mast Camera (Mastcam) on MSL (Malin et al. 2010; Bell et al. 2012).

The multi-wavelength LEDs consist of 1-4 wavelength emitters per LED. The LEDs are packed together in the illuminator in a small cylindrical housing and placed behind a matted 30° diffuser cover to achieve uniform illumination over the entire FOV, thereby reducing any variation in illumination geometry. Variations in illumination geometry can produce grossly inaccurate spectral artifacts, especially if a sample target has crevices, shadowed spaces between particles, or specular surfaces (Sellar et al. 2006). The MMI illuminates the target with an angle of ~ 45° to reduce specular reflections and provide topographical information about surface roughness. Acquiring images of the target during successive cycles of illumination with each LED wavelength, provides color information for the targets and allows for generation of color images in the visible range simulating natural color.

Table 2.1. MMI LED Band Centers and FWHM

Wavelength Center (nm)	FWHM (nm)
463	27
522	45
603	19
641	22
667	23
700	25
741	28
756	28
811	32
842	46
884	45
908	63
935	49
970	44
1050	57
1224	63
1290	96
1430	118
1521	145
1660	150
1735	92

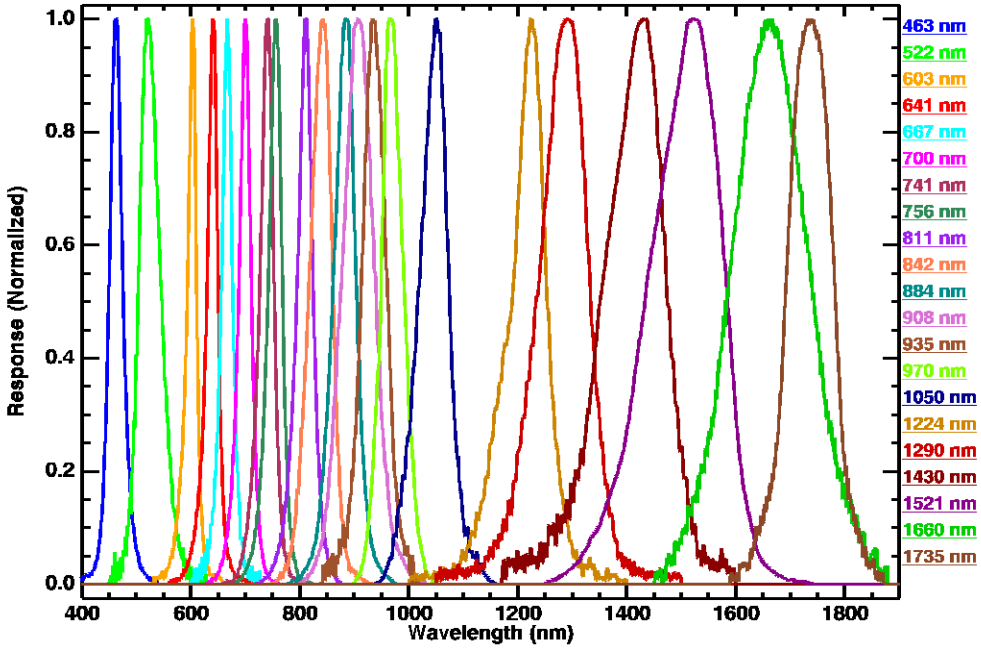

Figure 2.4. Plot of Normalized MMI LED Wavelength Bands. The labels on the right correspond to the effective wavelength band center position. The short-wave infrared LED bands (1050 nm – 1735 nm) have wider bandpasses compared to the visible and near infrared LED bands (463 nm – 970 nm). Band center and bandpass values are provided in Table 2.1.

Table 2.2. Comparison of MMI to Current Micro-Imagers

Item	MER MI[1]	Phoenix RAC[1,2]	MSL MAHLI[1,2]	MMI
Detector Type	CCD	CCD	CCD	InGaAs
Array Size (pixels)	1024 x 1024	512 x 256	1600 x 1200	640 x 512
FOV (mm)	31 x 31	11.2 x 5.6 (15.5 x 7.8)	23.2 x 17.4 (48 x 36)	40 x 32
Depth-of-Field (mm)	3	1.4 (2.3)	0.9 (~4)	5
Spatial Resolution (µm/pixe	30	23 (30)	14.5 (30)	62.5
Detection Range (nm)	400 - 1000	400 - 700	400 - 700	400 - 1800
Number of Bands	2 (Includes Dust Cover)	3	4 (Includes UV LED)	21
Illumination	Ambient	LED (RGB)	LED (White)	LED (Multispectral)
Color Information	Grey Scale	RGB	RGB	Multispectral

[1.] Sources: Herkenhoff et al. 2003; Keller et al. 2008; Edgett et al. 2009.

[2.] Data for highest spatial resolution and same spatial resolution as MER MI in parentheses.

Table 2.3. Comparison of MMI to Current Multispectral Imagers

IMP[1]		MER Pancam[1]		Phoenix SSI[1]		MSL MastCam[1]		MMI	
λ (nm)	FWHM	λ (nm)	FWHM	λ (nm)	FWHM	λ (nm)	FWHM	λ (nm)	FWHM
		432	32						
445	26	436	37	445	23	445	10	463	27
480	27	482	30	485	23	495	37		
530	30	535	20	533	28	527	7	522	45
						554	38		
600	21	601	17	604	16	590	88	603	19
						640	44	641	22
670	20	673	16	672	18	676	10	667	23
								700	25
750	19	753	20	753	19	751	10	741	28
								756	28
800	21	803	20	802	21	805	10	811	32
								842	46
860	34	864	17	860	36	867	10		
		880	20			880	10	884	45
900	41	904	26	900	44	908	11	908	63
930	27	934	25	932	27	937	11	935	49
970	31			966	31			970	44
1005	29	1009	38	1000	27	1012	21	1050	57
								1224	63
								1290	96
								1430	118
								1521	145
								1660	150
								1735	92

[1.] Smith et al. 1997; Smith et al. 2001; Bell et al. 2003; Smith et al. 2008; Malin et al. 2010; Bell et al. 2012.

2.2.5. Mass, Power, Volume, and Data

The mass of the MMI is ~ 1kg, including the illuminator and mounting bracket. The camera assembly is 158 mm high (along the borehole), 76 mm long and 76 mm wide. The illuminator is 110 mm long and has a diameter of 56 mm. The illuminator is positioned at a working distance of ~ 45 mm from the target surface (Figure 2.1).

The camera is powered using a 7-28 V DC power supply and consumes less than 5 W during operation. The LEDs require 1 – 4 V and consume 0.5 – 15 mW, depending on the emitter activated. Individual 14-bit raw images comprise 640 Kbytes of data. When calibrated and combined to form a 21 band datacube, the image cube comprises ~26 Mbytes of data.

2.3. Measurement Protocol and Calibration

2.3.1. Data Acquisition

The MMI camera and illuminator are operated using a custom program developed in the graphical programming environment, LabVIEW (a commercial software package sold by National Instruments). The program operates in two distinct modes: 1) Live mode and 2) Image acquisition mode. The live mode is primarily used to view the target for focusing and adjustment of camera exposure settings for each wavelength for use during image acquisition. During image acquisition mode, the program commands the camera and illuminator to acquire a series of “dark” (with LED turned off) and illuminated images at the corresponding

settings for each wavelength. For each wavelength, the camera first acquires a series of dark images (10 frames for strong bands and 40 frames for weaker bands), which are averaged. It then acquires a series of illuminated images (same number of frames as dark), which are also averaged. The images are averaged to reduce the level of noise associated with the dark current of the detector and to reduce any variability in intensity due to any potential instability of the LEDs. The averaged dark image is then subtracted from the averaged illuminated image to generate a final dark-subtracted image for the corresponding wavelength. This subtraction eliminates any signal contribution from the detector as well as ambient light from the surrounding environment. The procedure is automatically repeated for each wavelength resulting in 21 separate dark-subtracted images that are stored for further processing.

2.3.2. Data Calibration and Generation of Image Datacubes

MMI-generated 21-band dark-subtracted images are obtained of the sample target of interest, as well as a 50 % reflectance Lambertian Spectralon standard (produced by Labsphere). Because the reflectance target is non-uniform at the resolution scale of the MMI (Figure 2.5A), the target is shaken along the x-axis and y-axis at a frequency faster than the shutter speed of the camera to generate a smooth, uniform image (Figure 2.5B). Any potential artifacts contributed to the signal from the shaking are eliminated by averaging over the 10-40 frames.

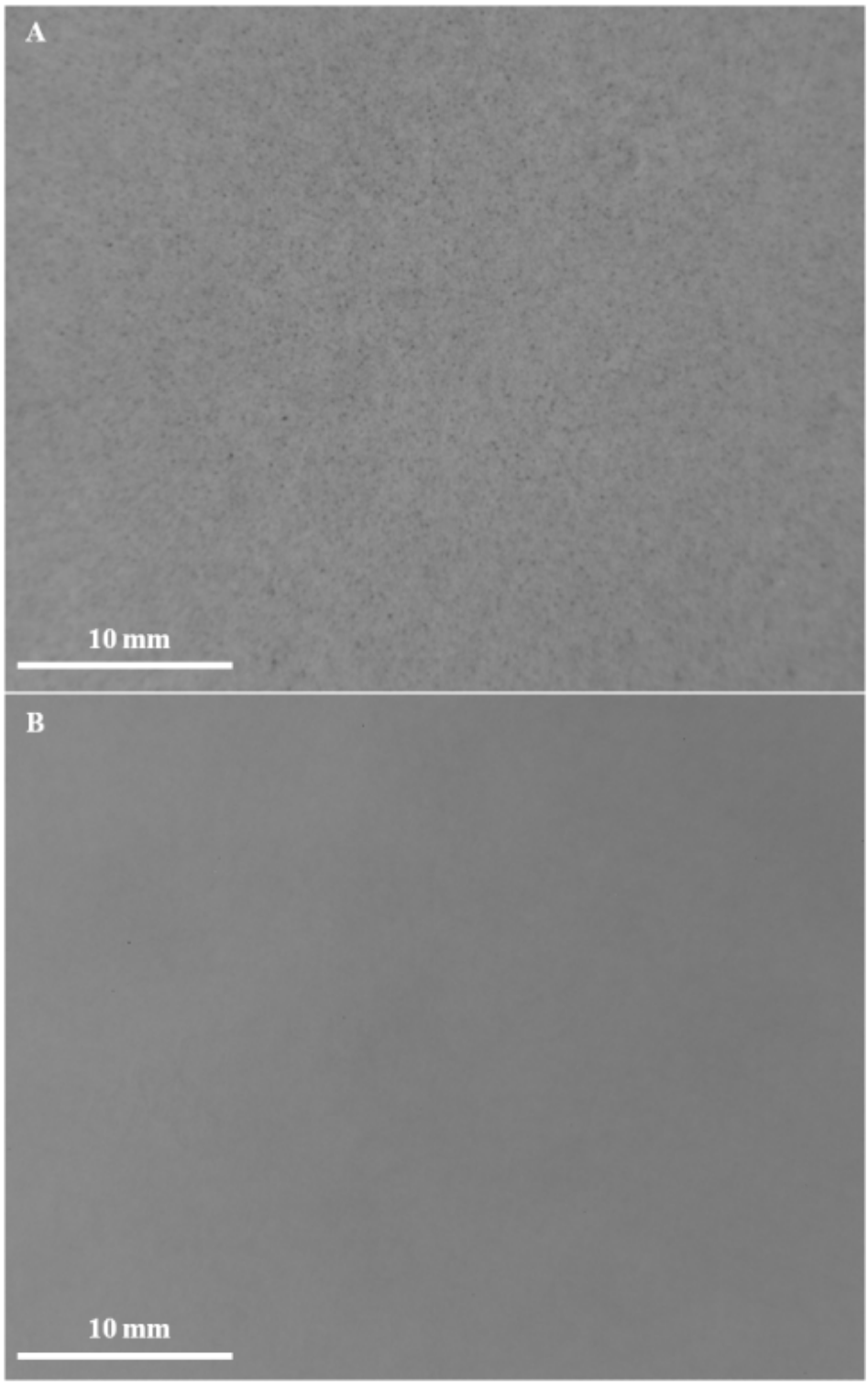

Figure 2.5. Comparison of MMI Images of 50 % Reflectance Spectralon Target. Image above corresponds to target not moved while image below corresponds to target moved to produce a uniform image. Image field-of-view is 40 x 32 mm.

Image processing and calibration is performed using routines written in the Interactive Data Language (IDL) programming environment. Bad pixels are corrected by replacing each bad pixel with a mean of nearby pixels, weighted by the distance of the nearby pixel from the bad pixel. Each wavelength target image is then flat-fielded and converted from raw digital number (DN) values to reflectance using the respective wavelength image of the 50 % reflectance Spectralon standard. The calibrated images are then co-registered and stacked together along the 3rd axis (wavelength dimension) to form an image datacube with spatial coordinates (X, Y) and wavelength in the 3rd dimension (Z). As a result, each pixel has a spectrum of 21 bands ranging from the visible (0.463 μm) to the short-wave infrared (1.735 μm). Generation of higher-level data products such as band ratios and false color maps are described in the section below.

2.4. Methods

2.4.1. Suite of Samples Used for Test

A suite of igneous and sedimentary rock samples was used to test and validate the performance of the MMI. These samples were selected to provide a broad range of microtextural types and grain sizes, with simple to complex mineralogies, including Fe-rich compositions that were perceived to be more easily analyzed over the wavelength range provided by the MMI. Results obtained with these test samples were used to further improve the design and development of the instrument, and most

importantly, to maximize scientific return by improving data reduction methods and the generation of data products. Rock targets consisted predominantly of square “tiles” approximately 15 mm x 15 mm obtained by sawing and grinding naturally occurring natural rock samples (e.g. silicates, oxides, carbonates and evaporites) to a surface roughness comparable to that generated by the Mars Exploration Rover’s Rock Abrasion Tool (RAT) (Gorevan et al. 2003). Many of the geologic samples used showed diagnostic spectral features within the MMI’s detection limits, while others contained fine-scale microtextures and grains sizes that challenged the MMI’s spatial resolution limits. A few unprepared natural samples showing coarse surface relief were also used to test the MMI’s depth of field and focusing capabilities.

MMI test samples were in large part selected to represent geologic materials either known to occur on Mars, or which could be reasonably be expected to occur there. Over half of the samples used are of particular interest for Astrobiology in represented textures and compositions indicative of habitable environments, based on the influence of liquid water. An example mosaic of MMI visible color composite images simulating natural color of the rock targets used is presented in Figure 2.6.

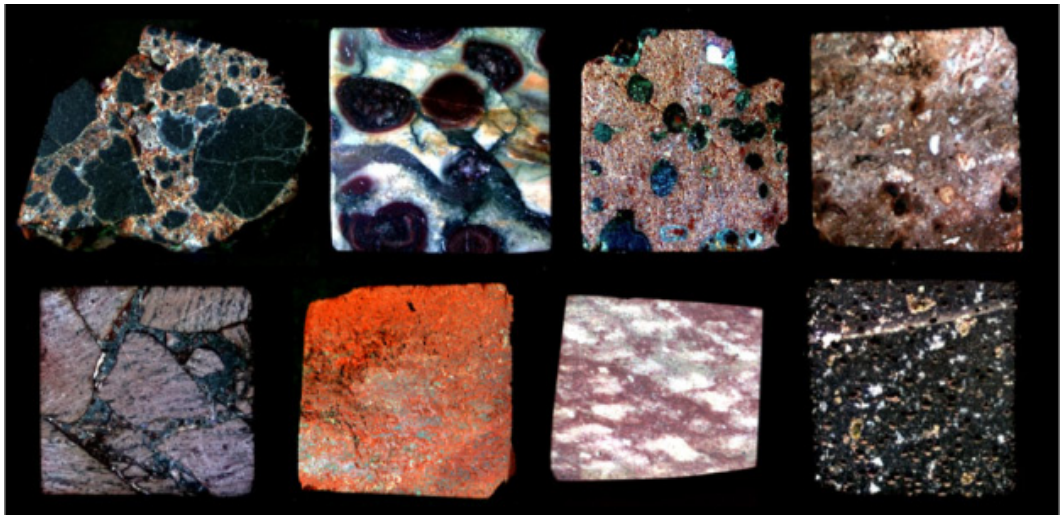

Figure 2.6. Mosaic of MMI Images of Sample Rock Targets Used. Mosaic of MMI color composite RGB images of some of the sample rock targets used to develop and test the performance of the MMI. The RGB images are composed of bands 641, 522, and 463 nm respectively to simulate true color and are linear stretched. The rock targets are approximately 15 x 15 mm in size. A subset of the sample rock targets are described in more detail in this paper.

All the samples were characterized in detail using a variety of compositional and mineralogical laboratory techniques, including high-resolution visible/near-infrared spectroscopy, X-ray powder diffraction, and thin section petrography. These datasets provided “ground truth” observations for assessing the performance of the MMI instrument in detecting minerals and reliably locating them within a microtextural framework. In the sections that follow, a subset or the MMI test samples are described in more detail, to demonstrate the capabilities of the instrument for conducting petrologic investigations.

2.4.2. Visible/Near-Infrared Spectroscopy

To provide a comparison to spectra obtained with the MMI as well as provide an independent assessment of mineralogy, particularly for samples containing amorphous Fe-oxides and hydrated volcanic glass, not easily identified with XRD, visible/near-infrared/shortwave infrared (VNIR/SWIR) laboratory spectra were obtained from each sample. For this study, two to four measurements were taken from the sample, with each measurement representing a slightly different region of interest on the sample surface. The spectra obtained represented integration over a spot size diameter of approximately 6 mm. Samples were analyzed using a full range ASD VNIR/SWIR lab spectrometer over a wavelength range of 0.35 – 2.5 μm, using a halogen lamp for illumination and a Spectralon reference panel for calibration. The ASD spectrometer has a bandpass spectral resolution of 5 nm over the spectral range of 0.35 – 1.0 μm, 12

nm over the spectral range of 1.0 – 1.8 μm, and 11 nm over the spectral range of 1.8 – 2.5 μm. For each measurement, 20 spectra were acquired and averaged. Offsets between internal spectrometers were corrected, and spectra converted to absolute reflectance using a NIST traceable Spectralon reflectance spectrum. Corrected spectra were written as individual ascii files for display and analysis with the remote sensing and image analysis software, ENVI (Environment for Visualizing Images - a commercial software package sold by ITT Visual Information Solutions). Spectral features were compared in ENVI to spectra from the US Geological Survey (USGS) spectral library (Clark et al. 2007). Additional spectra from the Keck/NASA Reflectance Experiment Laboratory (RELAB) spectral library (Pieters and Hiroi 2004) and NASA/JAXA Advanced Spaceborne Thermal Emission and Reflection Radiometer (ASTER) spectral library (Baldridge et al. 2009) were used to supplement the USGS spectral library.

Visible/near-infrared reflectance spectroscopy is well-suited for the detection of a variety of crystalline and amorphous materials. Within the range from 0.35 μm to 2.5 μm, diagnostic absorption features associated with electronic and vibrational processes enable the identification of a wide range of primary igneous and alteration minerals, including silicates, oxides, carbonates, and hydrated minerals. The primary igneous minerals olivine and pyroxene are distinguished by the positions and shapes of their broad absorptions from electronic processes near 1.0 and 2.0 μm

(Clark 1999 and references therein, Figure 2.7A). Among alteration products, ferric minerals are distinguished mainly by the positions and relative strengths of absorptions of electronic processes in the region from 0.4 μm to 1.0 μm (Clark 1999 and references therein, Figure 2.7A), while hydrated silicate minerals, like phyllosilicates, zeolites and opaline silica are distinguished by the positions, shapes, and relative strengths of overtones and combinations of fundamental vibrational absorption features of OH and H_2O over the 1.0 to 2.5 μm region (Clark 1999 and references therein, Figures 2.7C and 2.7D). Sulfates are also detected by absorption features of overtones and combinations of fundamental vibrations related to their bound water in the region from 1.0 to 2.5 μm (Clark 1999 and references therein, Figure 2.7E). Carbonates may be detected by overtones and combinations of fundamental vibrations of CO_3 in the wavelength region from 2.0 to 2.5 μm (Clark 1999 and references therein, Figure 2.7F). For hydrated silicates, the region from 2.1 to 2.5 μm provides diagnostic spectral features, due to the shift in wavelength position of the combination metal-OH bending plus OH stretching vibrational absorption features, where the precise wavelength position depends on the mineral structure and type of octahedral cation (Mg, Al, Fe) (Bishop et al. 2002b). This enables the distinction of Fe/Mg-rich smectite clays, such as the Fe-rich end-member nontronite (band center at 2.29 μm) and the Mg end-member, saponite (band center at 2.31 μm), from Al-rich smectite, such as montmorillonite (band center at 2.21 μm).

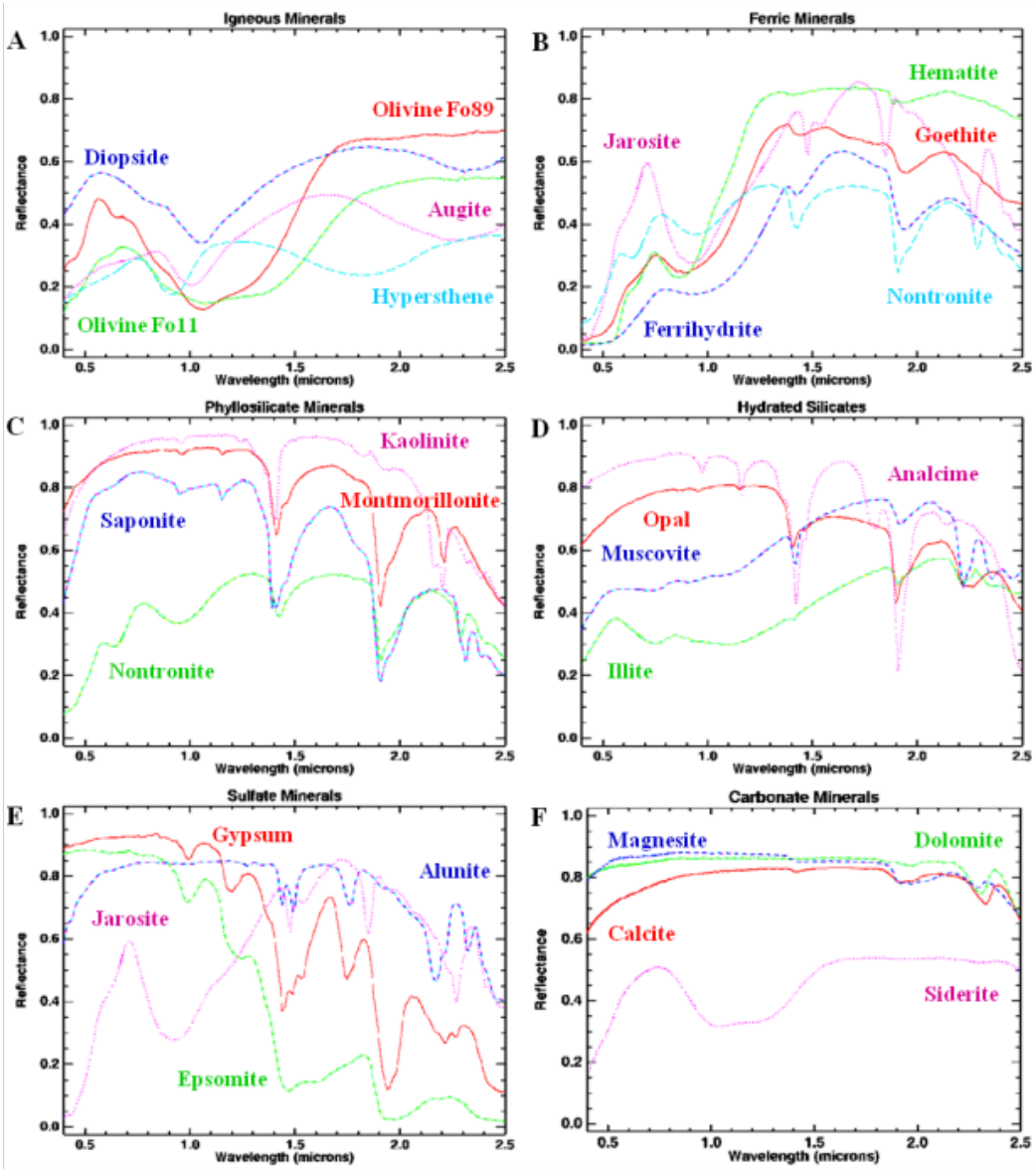

Figure 2.7. Example Library Spectra of Minerals Identified with Visible/Near-Infrared Spectrometer.

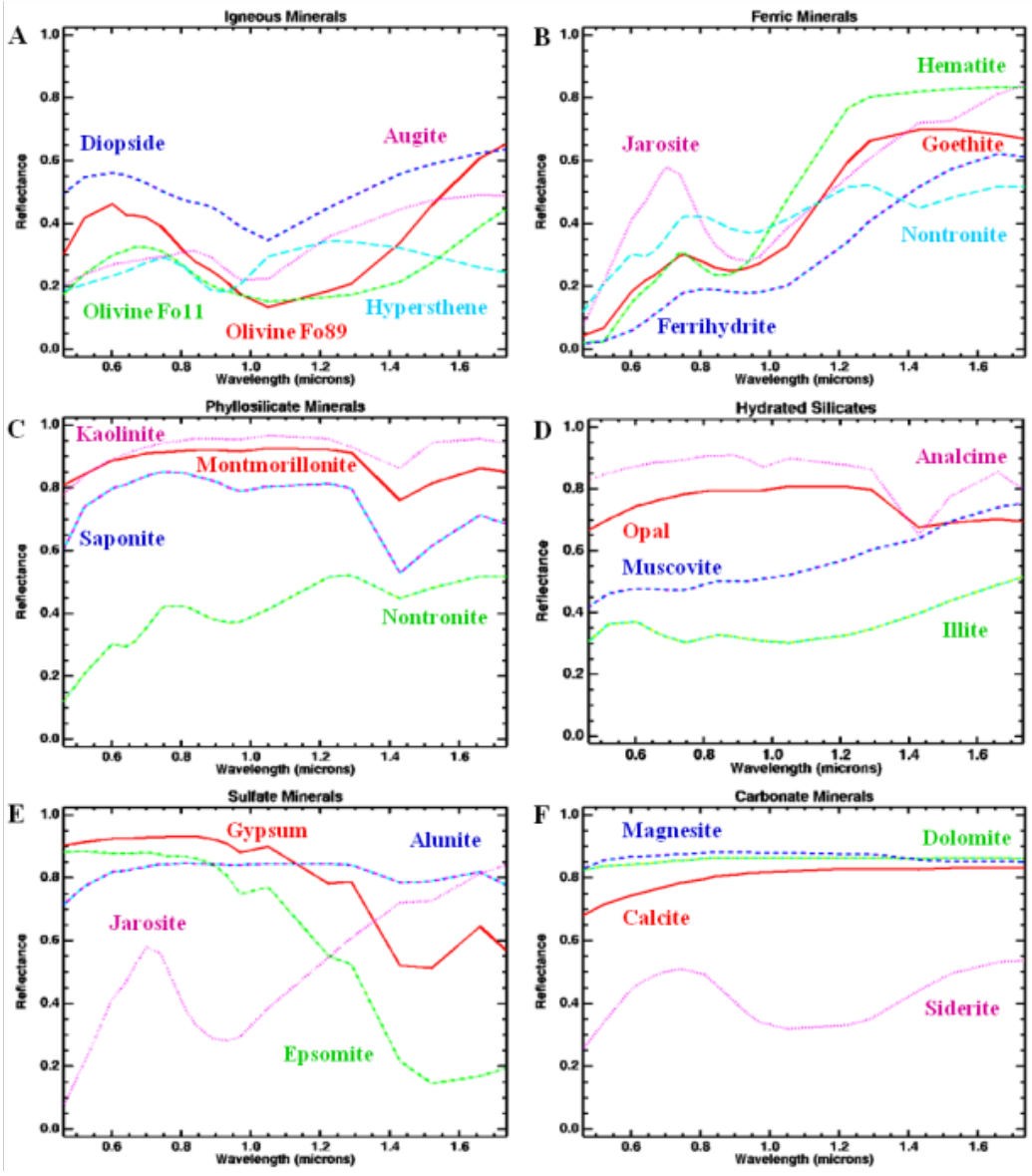

Figure 2.8. Example Library Spectra of Minerals Convolved to MMI Bandpasses. Example laboratory library spectra of minerals presented in figure 2.7 convolved to the MMI wavelength bandpasses listed in table 1.

Sample ASD spectra were convolved to the MMI spectral range and resolution based on the instrument's LED band centers and full-width at half maximum (FWHM) (Table 2.1). For this, ENVI was used to enable a direct comparison between spectra obtained with the MMI and spectra obtained with an ASD. The spectral libraries were also convolved to the MMI bandpasses in ENVI to enable mineral identification of spectral features in MMI spectra and to provide direct comparisons as well as to better assess the performance of the MMI in mineral identification over the current wavelength range and resolution.

2.4.3. X-Ray Diffraction

X-ray powder diffraction was used to determine the bulk mineralogy of each "unknown" sample and assess the accuracy of the spectral analyses. X-ray diffractograms were obtained by a Siemens D-5000 diffractometer with a 7.58° wide position-sensitive detector. The incident beam was Cu-Kα radiation (40 kV, 30mA) with a 1.0 mm antiscatter slit. A nickel foil was used to limit the beta lines for copper. No monochromator was used. Powders for bulk analysis were initially crushed and ground in 100 % ethanol using an agate mortar and pestle. The dried sample was then passed through a 150 μm mesh sieve yielding sample powders for XRD that were < 150 μm. The <150 micron size fraction was loaded onto an aluminum slide mount to produce a random grain distribution for XRD analysis. Samples were run over a 2θ range of 5–65° at 0.02° step intervals, with a step time of 2 seconds. This method was used to increase

SNR and to bring out the diffraction peaks of ordered phases above any background generated by amorphous phases like volcanic glass, or nanophase Fe oxides present in many of the samples. Major mineral phases were identified with the analytical software, Jade (developed by Materials Data, Inc. – MDI), by matching diffractograms to the International Centre for Diffraction Data (ICDD) library database.

2.4.4. Thin Section Petrography

Splits of the rock samples from which the “unknown” rock targets were obtained, were cut and sent out to Spectrum Petrographics, Inc. (Vancouver, WA), for the preparation into standard (30 μm thickness) petrographic thin sections. Section surfaces were ground to standard polish and left unstained and uncovered. The thin sections were studied under an immersion oil mounted cover slip using a Nikon Eclipse E600 polarizing microscope (manufactured by the Nikon Corporation), under reflected and transmitted light illumination, plane and polarized light and using a gypsum plate to enhance some fabric elements in thin section. The system provided a high-precision rotating stage with an attachable mechanical stage, to enable the capability to return to specific spots on the section. Each sample was imaged under plain and cross-polarized light, as well as reflected light, to provide an integrated view of the microtexture, mineralogy and paragenetic history of each sample. Thin section petrography provided a particularly useful context for interpreting the results of X-ray powder diffraction and visible/near-infrared spectra,

which provide integrated information over large areas of the sample. Minor mineral components identified using XRD, or VNIR methods could, in most cases, be located within thin sections, once their presence was known.

2.4.5. Image Processing and Spectral Analysis

Applying remote sensing techniques developed for analysis of multispectral imagery, MMI multispectral images were processed and analyzed using ENVI. Simple three-band RGB color composites simulating natural color and VNIR false- color images were prepared for each sample. Bands 0.641, 0.522, and 0.463 μm were used respectively to generate visible RGB color composite images simulating natural color, while other visible/infrared bands (ex. RGB: 1.43, 0.908, and 0.522 μm) were used to generate the visible/near-infrared RGB color composite images. Each image employed a default linear stretch to enhance color differences. Additional subtle color differences in the color composite images were exaggerated in ENVI by applying a decorrelation stretch (Gillespie et al. 1986) to the bands. The decorrelation stretch enhances subtle color variations in an image by applying a Principal Component (PC) transformation to each band, followed by contrast stretching of each transformed band, and finally re-transforming each band back into the original image. Through this process subtle color differences were dramatically enhanced, allowing better discrimination among different materials within samples. Similar processing methods were also

successfully applied to multispectral Pancam images obtained by the Mars Exploration Rovers Spirit and Opportunity (e.g., Farrand et al. 2006, 2007; Weitz et al. 2010).

For MMI data, a variety of methods were used to identify regions of interest (ROIs) from which representative spectra, i.e. “spectral end-members”, could be extracted. These spectral end-members, or spectra from “image end-members”, are averages of spectra from multiple pixels extracted from the image that represent specific microtextural and compositional domains that have a typical spectral signature present in the image datacube. The spectral end members, which consisted of averages from 100 to 1000 pixels, were in some cases single phases, but more often consisted of mixed phase assemblages (particularly where fine-grained materials too small to resolve at the MMI pixel scale were present). These end-members when mapped to the sample, helped define the paragenesis of the rock. The ROIs were identified through the combined use of decorrelation stretch of false-color composite images in ENVI, band ratios targeting absorption features associated with the presence of Fe^{2+}, Fe^{3+} and OH/H_2O, as well as Minimum Noise Fraction Transformation (MNF) function (Green et al. 1988) and Pixel Purity Index (PPI) algorithm (Kruse et al. 1993; Rowan et al. 2004) provided with the ENVI software.

The MNF function is a Principal Component-based analysis that consists of two transformations intended to reduce the data volume in a

dataset by ordering the resulting MNF bands in order of their increasing noise level. As a result, most of the reflectance variation in a data set can be explained in the first few MNF bands, with the rest of the MNF bands containing variance contributed primarily by noise. This information can be used to assess the level of spectral variability in an image. An image with a higher level of spectral variability (i.e., greater number of possible spectral end-members) will have a greater number of MNF bands with coherent information (Farrand et al. 2006). In contrast, an image with a low level of spectral variability (i.e., low number of spectral end-members) will have most information in the first few bands, with the remaining bands dominated by noise.

In our analysis, an MNF transformation was applied to each MMI image datacube to generate MNF bands. The MNF bands with high signal/noise were selected by visual inspection of the resultant MNF images. Image pixels from the MNF bands were examined using two-dimensional scatter plots (e.g., MNF band 1 vs. MNF band 2), and visualization of the n-dimensional cloud using ENVI's N-D Visualizer tool. The low-noise MNF bands were used to identify spectrally pure pixels with the Pixel Purity Index (PPI) algorithm in ENVI (Kruse et al. 1993; Rowan et al. 2004). The PPI function determines the number of times a given pixel in n-dimensional space can be considered extreme relative to other pixels in the scene. The PPI was processed at 5000 iterations, with a threshold of 15. The output image highlights pixels that are considered extreme.

Extreme pixels were plotted in n-dimensional space by using ENVI's N-D Visualizer to reveal groups of unique end-member pixels. The end-member pixels were mapped and displayed on the images and visually inspected.

The pixels identified through MNF and PPI methods, along with those identified through decorrelation stretch and band ratios, were selected as ROIs from which the representative spectral classes (end-members) were extracted. These spectral end-members were then used to produce maps showing the distribution of spectral signatures in the sample using the Spectral Angle Mapper (SAM) classification method in ENVI.

The SAM algorithm allows for supervised classification of multispectral/hyperspectral reflectance data with user-defined spectral classes (end members) that are used to match the unknown materials in an image (Kruse et al. 1993). With this method, the known and unknown spectra are plotted as vectors in n-dimensional space; the spectral angle between the two classes is then calculated, and a match is made by using a given threshold angle. Because the algorithm only utilizes the vector direction in its calculation, this method is insensitive to surface illumination, which is reflected by vector length.

Using the spectral end-members generated from the ROIs as the input parameters, the SAM algorithm matched the end-members with the unknown spectra in the rest of the image. The Single Value threshold

option was used in ENVI with an angle threshold of 0.1 radians. The classification resulted in a spectral “end-member map” showing the distribution of spectral end- members in the sample.

The spectrum from each spectral end-member was then compared to library spectra from the USGS spectral library (Clark et al. 2007) as well as some spectra from the RELAB (Pieters and Hiroi 2004) and ASTER (Baldridge et al. 2009) spectral libraries, convolved to the MMI wavelength range and resolution, using the Spectral Analyst tool in ENVI to identify best– fit minerals (or rocks) for each spectral end-member. The Spectral Angle Mapper (SAM) and Spectral Feature Fitting (SFF) methods within the Spectral Analyst tool in ENVI were used to rank the match of each end-member spectrum to those in the spectral library. The suggested spectral library matches were ranked in order of best-to-worst match. The Spectral Feature Fitting method is an absorption-feature-based methodology in which the fit of a spectrum of interest, in this case the spectral end-member, is compared to reference spectra, e.g. USGS library spectra, using a least-squares technique. The reference spectra are scaled to match the image spectra after the continuum is removed from both datasets. Methods used for generation of continuum-removed spectra are those described in Clark and Roush (1984) and Clark et al. (2003).

Spectra of the suggested spectral library matches and spectral end-members were visually compared to identify the best-fit spectra, whether

mineral(s), mineral group(s), assemblages or whole rock. Careful consideration was taken to make sure that the suggested mineral matches "made sense" in relationship to the inferred rock origin based on the geologic context, microtexture, and general composition, within the limitations of the wavelength range and resolution of the MMI (see section below).

2.4.6. Mineral Absorptions in MMI Range

The Multispectral Microscopic Imager (MMI) advances the capabilities of current microimagers such as the Phoenix Robotic Arm Camera (RAC) and Mars Science Laboratory Mars Hand Lens Imager (MAHLI), by extending the spectral range from the visible to the short-wave infrared, from 0.463 to 1.735 μm, and increasing the number of spectral bands to 21. Within the MMI's wavelength range and resolution, absorption features associated with electronic and vibrational processes enable the identification and mapping of a wide range of primary igneous and alteration minerals, including iron-bearing basaltic silicates like pyroxene and olivine (e.g., Adams 1974; Cloutis et al. 1986; Morris et al. 2000), iron oxides and iron oxyhydroxides with varying degrees of crystallinity (e.g., Singer 1982; Sherman et al. 1982; Morris et al. 1985, 1993, 2000; Bell et al. 1990, 2000), and other iron-bearing phases such as ferric sulfates, ferric carbonates, or iron-bearing clay minerals (e.g., Sherman et al. 1982; Cornell and Schwertmann 1996; See Figure 2.8).

Although the MMI wavelength range does not extend to longer wavelengths up to 2.5 μm (Figure 2.7) needed for the definitive identification of many hydrated silicates, sulfates and carbonates. However, the MMI is able to detect the presence hydrated minerals, including hydrated silicates and sulfates, based on a characteristic absorption feature at ~1.4 μm associated with the overtones of structural OH stretching vibrations (Figure 2.8). This enhanced capability enables the MMI to detect and map a larger variety of hydrated mineral classes compared to existing microimagers. Detecting and mapping hydrated minerals within a sample greatly enhances the value of the MMI for astrobiological investigations to explore for past habitable conditions based on the presence of water.

2.4.7. Contribution of Instrument Error to MMI Spectra

Efforts to estimate the contribution of instrument error and spatial variability to the MMI-generated spectra were made. These consisted primarily of imaging a standard of a known reflectance over the entire field of view and comparing the MMI-generated reflectance values of different parts of the target (i.e. spectra of different ROIs) with the known reflectance values obtained with a laboratory instrument. In this case, we imaged a 50% reflectance Spectralon standard and extracted the spectra of five different regions of interests throughout the field of view including all corners and center (Figure 2.9). The ROIs consisted of boxes of 50x50 pixels, which spectra were added together (i.e. 2500 spectra for each box

and 12500 spectra for all boxes combined) to generate mean (solid lines) and standard deviation values (dashed lines) for the reflectance of each ROI. These were plotted and compared to the absolute reflectance values of the reflectance standard, obtained with an ASD spectrometer at the USGS Spectroscopy laboratory, convolved to the MMI bandpasses (Figure 2.9).

The pixel to pixel variation throughout the MMI field of view was very low with most bands having standard deviation values of less than ±0.005 for each ROI box with the two longest infrared bands (i.e. bands 1.66 and 1.735 μm) having slightly higher values of less than ±0.007 (Figure 2.9). The standard deviation values for all bands increased when the pixels of all five ROI boxes were combined (i.e. red spectra in Figure 2.9) increasing the standard deviation for all bands to less than ±0.011. This increase is a result of greater variation in the mean values for each ROI, which correspond to different parts on the target in the field of view (Figure 2.9). The mean values for each ROI are spread over a range in which the difference between the highest and lowest values is under 0.03. As a result, when compared to the actual values of the reflectance target (black spectrum), the values for the ROIs (including standard deviation) differ from the actual values by less than ±0.015. Despite the variability in the spectra associated with different parts of the target, the mean for all the ROIs combined (i.e. red spectrum) averages out to be consistent with laboratory values of the calibration target with deviations of less than 0.01.

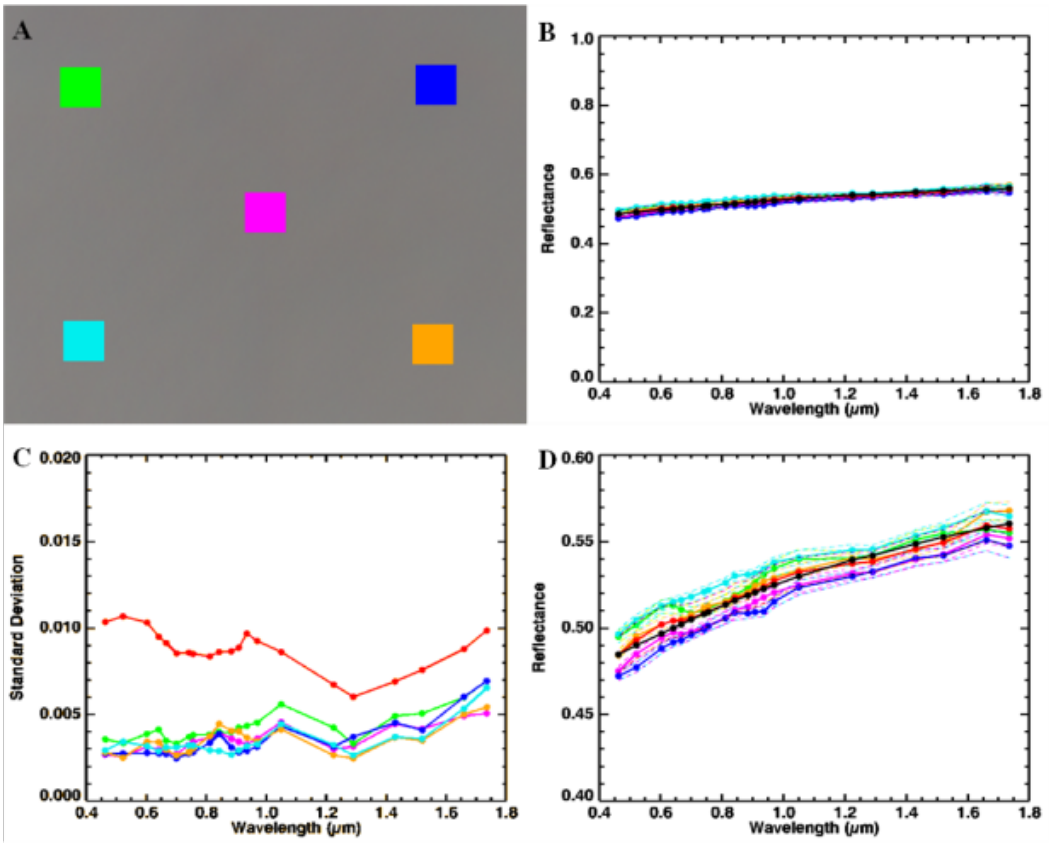

Figure 2.9. MMI Images and Spectra Used to Determine Instrument Error. Upper left image (9A): MMI RGB image (bands R= 641; G=522; B=463 nm) of 50% reflectance target with boxes corresponding to ROIs used to generate spectra mean and standard deviation to determine variability along FOV and estimate contribution of instrument error to spectra variability. The boxes consist of 50x50 pixels and correspond to colored spectra in following figures. Bottom left image (9C): Plot of standard deviation values from mean spectra for corresponding ROIs. The red spectrum corresponds to all the 5 boxes combined. Upper and bottom right images (9B and 9D): Spectra mean (solid lines) and standard deviation (dashed lines) of ROI boxes composed of 50x50 pixels (red spectra consists of all 5 boxes combined). The black spectrum corresponds to the actual values of the 50% reflectance target convolved to the MMI bandpasses and provides a comparison to the MMI-generated spectra. The top image is scaled from 0 to 1 reflectance while the bottom image is scaled from 0.4 to 0.6 to highlight variations between spectra and divergence from the actual values.

2.5. Results

In this section we provide imaging results obtained with the Multispectral Microscopic Imager (MMI) of analog rock types. These results are compared with higher resolution laboratory results of the same samples obtained from visible/near-infrared spectroscopy, X-ray diffraction and thin section petrography. Laboratory results are used as “ground truth” observations for assessing overall performance of the MMI as a tool for providing sample-based interpretations of petrogenesis.

2.5.1. Vesicular Basalt (Sample 17)

Basalts are widespread lithotypes of Mars (e.g., Christensen et al. 2000; McSween et al. 2003; Hamilton and Christensen 2005; Haskin et al. 2005; McSween et al. 2006a, 2006b). The sample basalt described here (sample 17) is a fine-grained vesicular basalt containing phenocrysts of plagioclase and pyroxene, with minor olivine. It was collected from a lava flow located along the southeastern coast of Hawaii, near South Point.

2.5.1.1. MMI Images and Spectra of Sample 17

MMI-generated color composite images of sample 17, along with a corresponding spectral end-member map are shown in Figure 2.10. Included is a visible-color RGB composite image composed of MMI bands 0.641, 0.522, and 0.463 μm (respectively), to simulate natural color and a visible/near-infrared color RGB composite image composed of MMI bands 1.521, 0.884, and 0.641 μm (respectively), to bring out subtle color differences in materials due to spatial variations in mineral composition.

Figure 2.10D shows a spectral end-member map generated in ENVI using a supervised classification, while Figure 2.11 shows spectra plots for the corresponding end-member spectra, along with matching library spectra.

A comparison of MMI images shows that the sample contains white- and olive-green-colored phenocrysts (in visible color image) within a moderately vesicular, dark-colored, aphanitic matrix (i.e. groundmass). The bright line on the left side of the sample is a saw mark. The white phenocrysts range in size from approximately 125 μm to 1250 μm, while the olive- green phenocrysts range from 125 μm to 1875 μm. The vesicles have a mean diameter of 438 μm and range in size from 190 to 780 μm.

Analysis of the MMI images for Sample 17 reveals the presence of five main spectral end-members (as shown in Figures 2.10D and 2.11A). Three of these spectral end-members are associated with the olive-green phenocrysts present in the sample.

The first spectral end-member, mapped in blue, is associated with the dark, fine-grained matrix. The VNIR spectrum has a low reflectance and exhibits a predominantly flat spectrum with a very shallow absorption present at the 1.05 μm band.

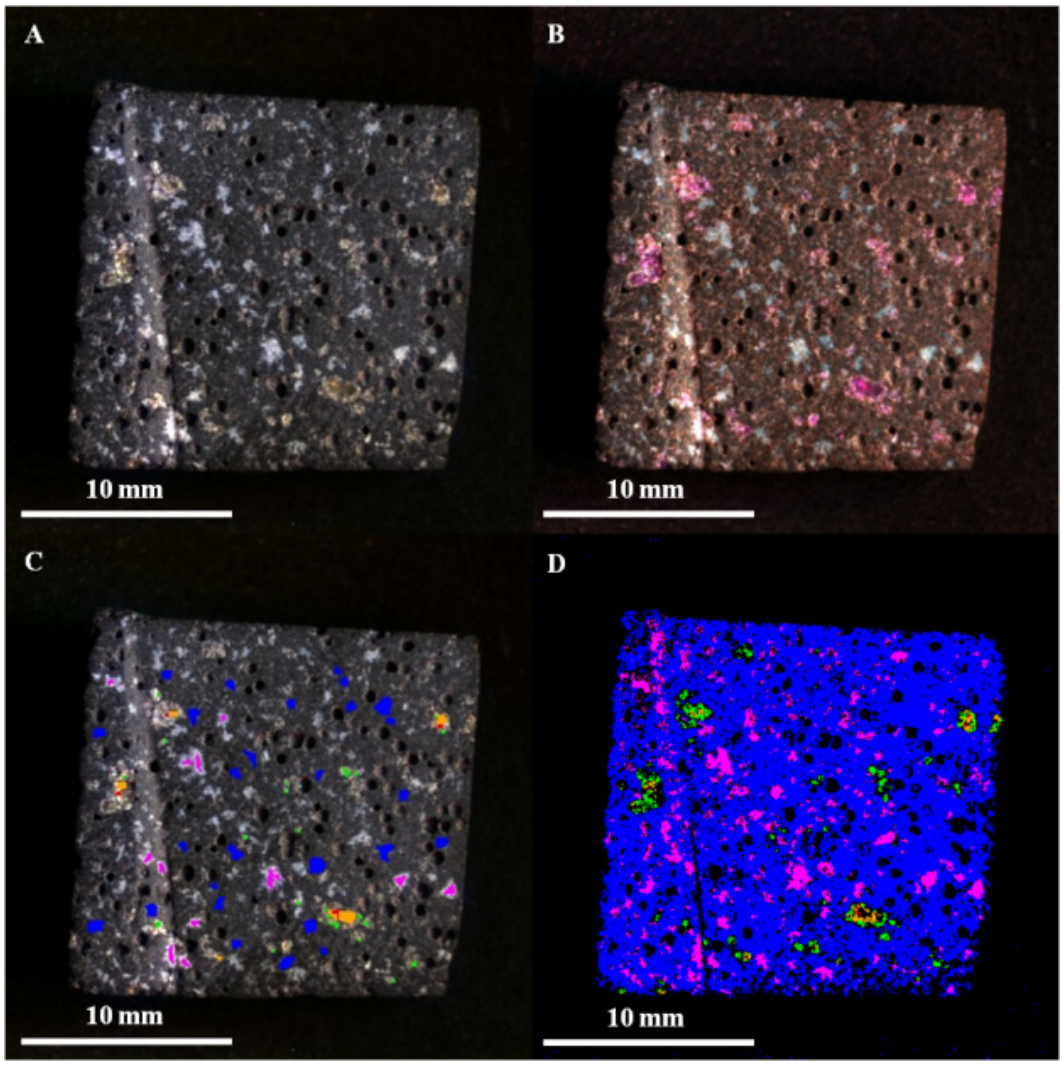

Figure 2.10. MMI-Generated Color Composite Images and End-Member Map of Sample 17. Visible-color (A) and false-color (B) composite images, visible-color composite image with regions of interest (C), and corresponding spectral end-member map based on ROIs of sample Unknown 17 acquired by the Multispectral Microscopic Imager (MMI). Each MMI Sub-frame image size is 25x25 mm at 62.5 µm/ pixel. Figures A-C are linear stretched. Figure 2.10A: Visible-color RGB composite image composed of MMI bands 0.641, 0.522, and 0.463 µm respectively to simulate true-color. Figure 2.10B: False-color RGB composite image composed of MMI bands 1.521, 0.884, and 0.641 µm respectively to bring out subtle color differences in materials due to variations in composition. Figure 2.10C: Visible-color RGB composite similar to figure A with regions of interest (ROIs) used to generate end-member map (Figure 2.10D) and spectral end-members (Figures 2.11A & 2.11B). Figure 2.10D: End-member map generated in ENVI using supervised classification with ROIs as input parameter to map end-members distribution.

The second spectral end-member, mapped as magenta, is associated with the white- colored phenocrysts. The spectrum has a broad, sinusoidal shape with a broad peak centered on the 0.641 μm band, a gradual decreasing slope towards the infrared and a broad, shallow absorption feature centered around the 1.224 μm band.

The third spectral end-member, mapped as green in the spectral end-member map, is associated with most of the smaller olive-green phenocrysts, and also lines the edges of the larger olive-green phenocrysts. The spectrum has a peak centered at 0.667 μm and a broad, V- shaped absorption feature centered around 1.05 μm.

The fourth spectral end-member, mapped in red, is associated with the interior of the large olive-green phenocrysts, most visible in the large phenocryst towards the bottom right side of the sample. The spectrum has a peak centered between 0.641 μm and 0.667 μm, and a broad, bowl-shaped absorption centered at 1.05 μm.

The fifth spectral end-member, mapped in orange, is associated with the interior of the large olive-green phenocrysts, between the red and green spectral end-members (Figure 2.10D). The spectrum has a peak centered at 0.667 μm, and a broad, bowl-shaped absorption centered at 1.05 μm. Reflectance of this end-member is lower than the third (red) and fourth (green) spectral end-members discussed above.

2.5.1.2. Comparison to Library Spectra

The MMI end-member spectra were compared to spectra from USGS spectral library (Clark et al. 2007) convolved to the MMI range and resolution (see Table 2.1) to determine best-fit minerals (Figure 2.11).

The matrix (blue end-member) spectrum is most consistent with the library spectrum for basalt. Generally speaking, basalt has a flat spectrum in the visible/near-infrared (VNIR) due to the intimate mixture of the fine-grained minerals. However, the weak absorption at 1.05 μm may be due to the presence of either high-Ca clinopyroxene (such as diopside), or olivine in the matrix.

The magenta end-member spectrum does not contain diagnostic absorption features that can definitively suggest a particular mineral. However, the broad, shallow absorption at 1.224 μm is similar to the convolved library spectrum for plagioclase. Like quartz, plagioclase does not exhibit diagnostic absorption features within the visible/near-infrared range. To detect fundamental Si-O absorption features associated with quartz or plagioclase, requires spectra from the mid-infrared (Clark 1999 and references therein). However, Fe^{2+} substituting Ca^{2+} in seven coordinated sites in plagioclase produces crystal field electronic transitions resulting in broad, shallow bands in the VNIR range at about 1.2–1.3 μm (Burns 1993). Given the mafic composition of the sample, the white color in the visible color composites and the broad, shallow absorption at 1.224

μm, the magenta spectral end-member is consistent with plagioclase feldspar.

The green end-member spectrum is consistent with the library spectrum for high-Ca clinopyroxene, with a best match to the mineral diopside. Within the MMI spectral range and resolution, diopside exhibits a characteristic V-shaped absorption centered at 1.05 μm. This contrasts with other clinopyroxenes (e.g., augite), which show an absorption feature shifted closer to 1.0 μm with an absorption between the 0.97 μm and 1.05 μm bands. Olivine also exhibits an absorption at 1.05 μm at the MMI wavelength and resolution. However, the absorption feature is wider than that in diopside (see below). On this basis, it is concluded that the best match is with diopside.

The red and orange end-member spectra both match the library spectra for olivine, with best matches to Fe-rich olivine, or possibly olivine of intermediate Fe-Mg composition. The orange spectrum is very similar to that of the red end-member but has a lower reflectance. The difference may be attributed to either grain size effects (e.g., Hapke 1993; Clark 1999), which affect the overall reflectance and depth of absorption features, or may be due to a fine-grained mixture of pyroxene and olivine grains. At the MMI range and resolution, olivine has a characteristic broad, bowl-shaped absorption centered at 1.05 μm. In comparison, high-Ca clinopyroxenes such as diopside also have an absorption at 1.05 μm, but is distinguished by a narrower V-shaped absorption feature (Figure 2.11).

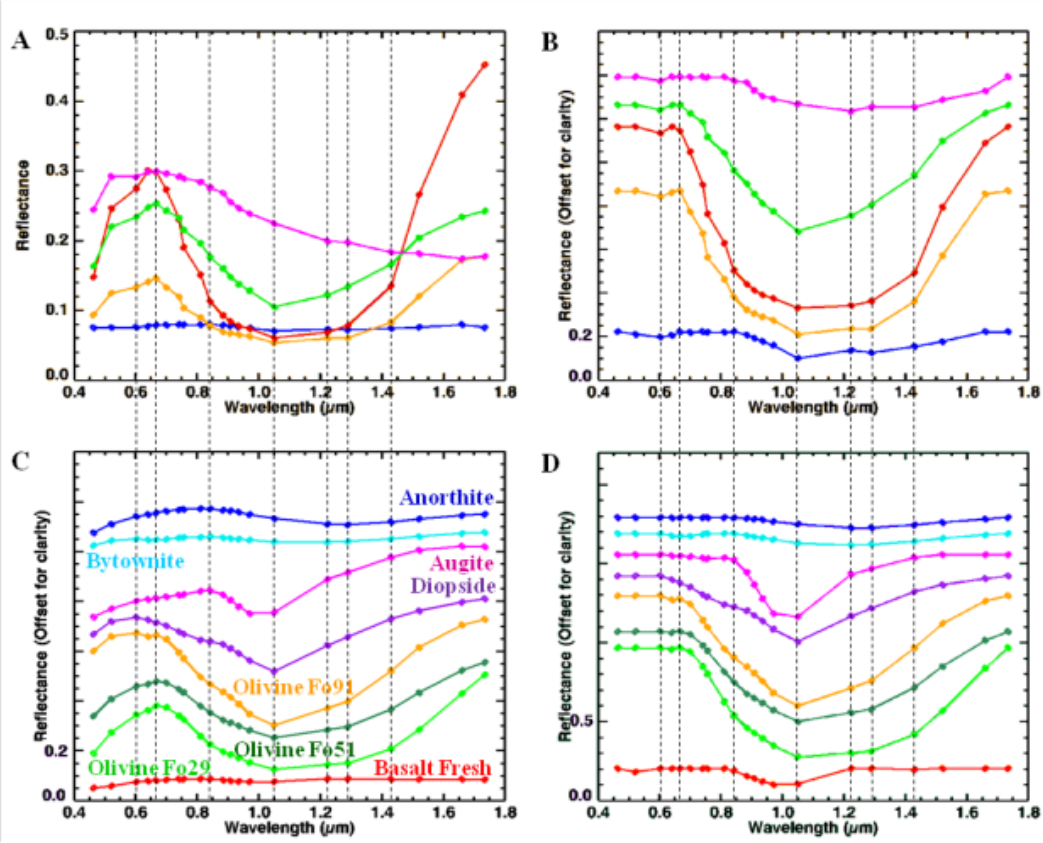

Figure 2.11. MMI-Generated Spectra of End-Members of Sample 17 Compared to Library Spectra. MMI-generated spectra of end-members (A & B) from sample Unknown 17 (Figure 2.10) and representative matching library spectra convolved to MMI bandpasses in table 2.1 (C & D). Vertical lines correspond to MMI bands 0.603, 0.667, 0.842, 1.05, 1.224, 1.29, and 1.43 μm. See text for details on features and discussion. Spectra on the left are normal, while spectra on the right are continuum-removed. Continuum-removed and library spectra are offset for clarity.

Since the exact position of the 1.05 μm olivine absorption depends on the Mg/Fe ratio (Burns 1970; King and Ridley 1987; Sunshine and Pieters 1998; Isaacson and Pieters 2010), the shift can be used to further distinguish between Fe-rich and Mg-rich olivine. Fe-rich olivine (fayalite) exhibits a broader-shaped absorption at 1.05 μm compared to Mg-rich olivine (forsterite). In addition, the position of the associated peak shifts from 0.603 μm for Mg-rich, to 0.667 μm for an intermediate to Fe-rich composition (Figure 2.11). The peak position at 0.667 μm, along with the broad-shaped absorption at 1.05 μm, is consistent with an olivine of intermediate to Fe-rich composition.

2.5.1.3. Interpretation of MMI Results

MMI images and associated spectra of sample 17 suggest that the sample is a vesicular basalt with predominantly plagioclase and clinopyroxene phenocrysts, along with pyroxene-rimmed olivine phenocrysts. The fine-grained groundmass and vesiculated texture is consistent with rapid cooling of a volatile-rich lava. The intermediate to Fe-rich composition of the olivine suggests that the magma originated from a more evolved mantle source (BVSP 1981).

2.5.1.4. Laboratory Observations of Sample 17

2.5.1.4.1. Visible/Near-Infrared Spectroscopy

Visible/near-infrared spectra were collected from three locations (A-C, Figure 2.12) on sample 17, targeting the major mineralogical and microtextural components of the sample.

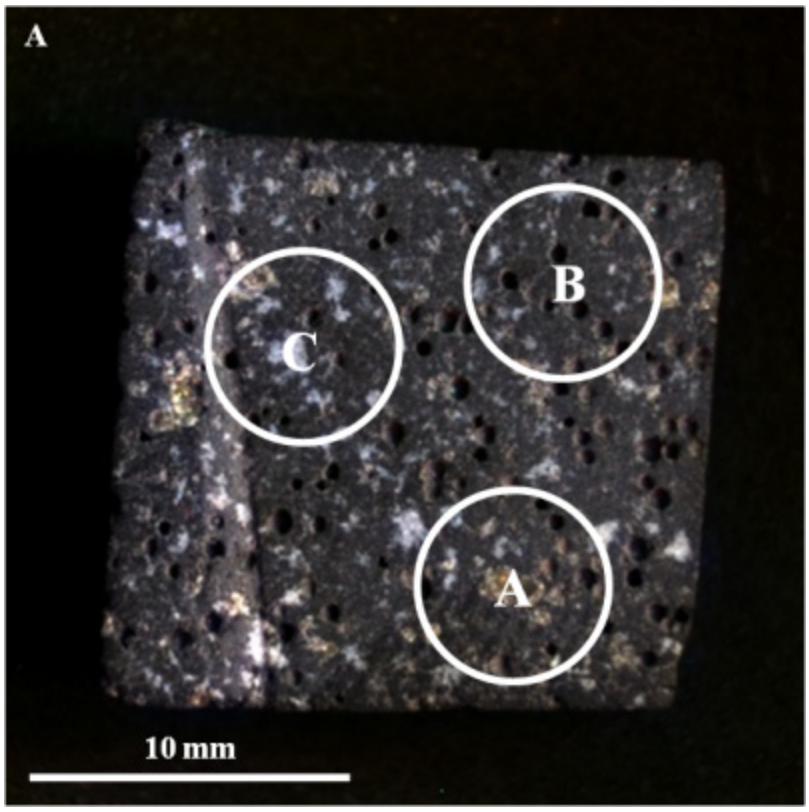

Figure 2.12. Areas on Sample 17 Analyzed with Visible/Near-Infrared Spectrometer. Visible-color, sub-frame image of sample Unknown 17 acquired by the Multispectral Microscopic Imager (MMI) composed of bands RGB = 0.641, 0.522, 0.463 μm respectively to simulate true-color with white circles (A – C) marking areas analyzed by visible/near-infrared laboratory spectrometer (spectra are shown in Figure 2.13A). Image size is 25x25 mm at 62.5 μm/ pixel. Visible/near-infrared laboratory spectrometer spot size diameter is ~6 mm.

Figure 2.13 displays the spectra acquired for the range 0.35 μm to 2.50 μm along with corresponding library spectra. The positions of absorption features are marked with vertical dashed lines. Each ~6 mm spot for the spectrometer was centered on a major component of interest, but included portions from other domains in the spectrum.

Spot A (blue spectrum in Figure 2.13A & B) was centered on a large olive-green phenocryst, but incorporated a small amount of the surrounding matrix and white phenocrysts. The spectrum obtained shows a broad absorption feature centered at 1.07 μm (centered at 1.08 for continuum-removed) as well as minor features at 0.86 and 1.28 μm (centered at 0.87 and 1.29 μm for continuum-removed). Compared to the USGS spectral library (Clark et al. 2007), this spectrum is most consistent with Fe-rich olivine. Mg substitutes with Fe in the olivine structure, forming a solid solution series. The main olivine absorption near 1.05 μm shifts to shorter wavelengths as Mg content increases (Burns 1970; King and Ridley 1987; Sunshine and Pieters 1998; Issacson and Pieters 2010). Consequently, the absorption for Mg end member (i.e., forsterite) shows a major absorption between 1.03 and 1.05 μm, while the Fe-rich end member (i.e. fayalite) exhibits a major absorption between 1.05 and 1.08 μm (Sunshine and Peters 1998; Isaacson 2010).

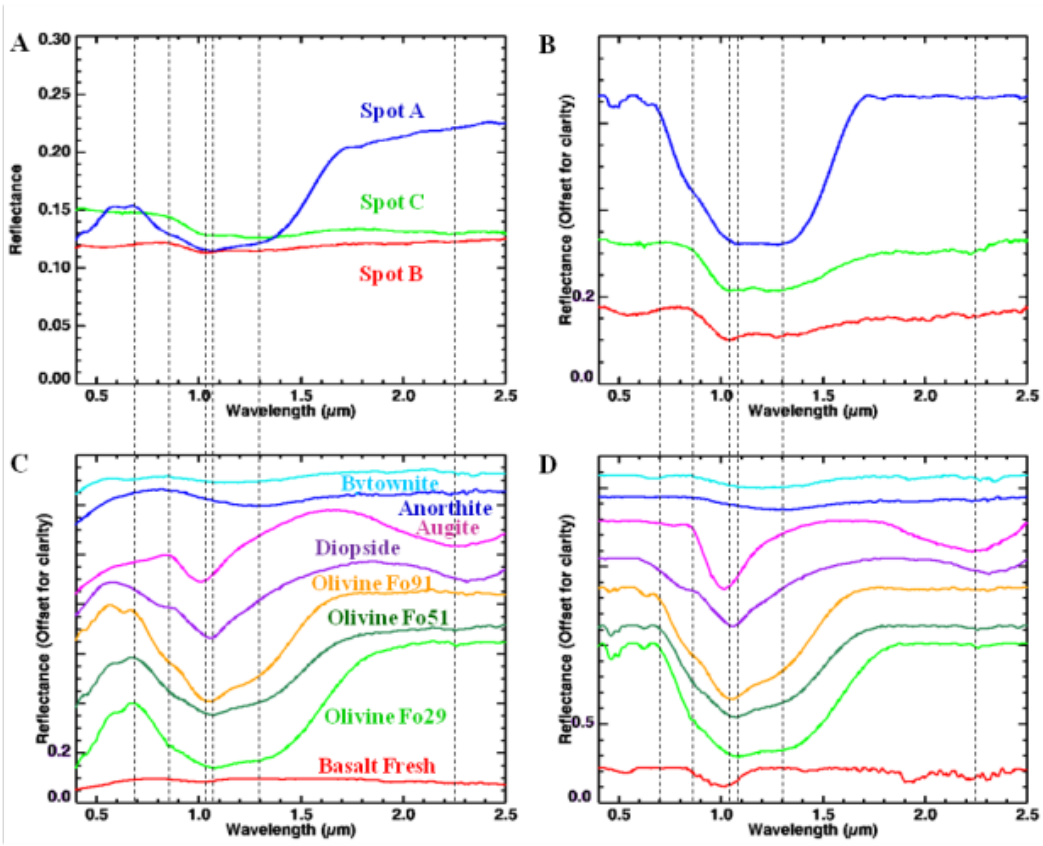

Figure 2.13. Visible/Near-Infrared Spectra of Sample 17 Compared to Library Spectra. Visible/near-infrared spectra (A & B) collected from spots A – C on sample Unknown 17 (Figure 2.12) with laboratory spectrometer and representative matching library spectra (C & D). Vertical lines correspond to features at 0.67, 0.86, 1.03, 1.07, 1.28, and 2.23 μm. See text for details on features and discussion. Spectra on the left are normal, while spectra on the right are continuum-removed. Continuum-removed and library spectra are offset for clarity.

Spot B (red spectrum, Figure 2.13A & B) was centered on the dark-toned matrix material, but incorporates a few white phenocrysts. The spectrum has a relatively flat, low reflectance curve with an absorption centered at 1.03 μm (centered at 1.04 μm for continuum-removed). An additional broad, shallow shoulder is also present at 1.28 μm. Compared to the USGS spectral library (Clark et al. 2007), the spectrum is most consistent with “basalt”. The absorption centered at 1.03 μm is most likely due to the presence of pyroxene, while the 1.28 μm feature is most likely contributed by smaller concentrations of olivine in the matrix. The pyroxene and olivine features are most likely contributed by microlites in the basalt matrix.

Spot C (green spectrum, Figure 2.13A & B) was centered on a large white phenocryst, but also includes some of the surrounding matrix. The spectrum has a relatively flat reflectance curve, with a decreasing slope towards longer wavelengths and two broad absorption features centered at 1.03 and 1.28 μm, respectively (centered at 1.04 and 1.29 μm respectively for continuum-removed). An additional broad absorption is also present at 2.23 μm. Based on comparisons to spectra in the USGS spectral library (Clark et al. 2007), the 1.03 and 2.23 μm absorptions are attributed to high-Ca clinopyroxene (best match to augite) and the 1.28 μm absorption is attributed to olivine present in the surrounding fine matrix. Plagioclase feldspar, which appears white in visible color, does not exhibit diagnostic absorption features within the visible/near-infrared range. To

detect fundamental Si-O absorption features associated with feldspar or quartz, one needs to search in the mid-infrared (Clark 1999 and references therein). However, Fe^{2+} substituting Ca^{2+} in seven coordinated sites in plagioclase feldspar produces crystal field electronic transitions resulting in broad, shallow bands in the VNIR range at about 1.2–1.3 μm (Burns 1993). This absorption feature in feldspars is pretty weak and would likely be swamped by stronger absorptions in similar positions from Fe minerals. The position of the 1.28 μm feature is consistent with the position for plagioclase feldspar, however the 1.28 μm absorption has a narrower full width at half maximum compared to library spectra for plagioclase feldspar, which is therefore more consistent with the shoulder in olivine.

2.5.1.4.2. X-ray Diffraction

X-ray diffraction (XRD) of bulk powdered material was used to determine the bulk mineralogy of sample 17 and provide a “ground truth” for the MMI and visible/near-infrared results. The X-ray diffractogram contains crystalline peaks of plagioclase feldspar, pyroxene and olivine (Figure 2.14). Maximum 2θ peaks are indicative of Ca-rich plagioclase feldspar at 27.87°, pyroxene (best fit with high-Ca clinopyroxene) at 29.8°, and olivine at 36.37°. Significant background intensity in the diffractogram is related to amorphous volcanic glass in the sample matrix. The 2θ peaks are consistent with primary basaltic minerals (e.g. pyroxene, plagioclase feldspar, and olivine) with no evidence for secondary alteration minerals.

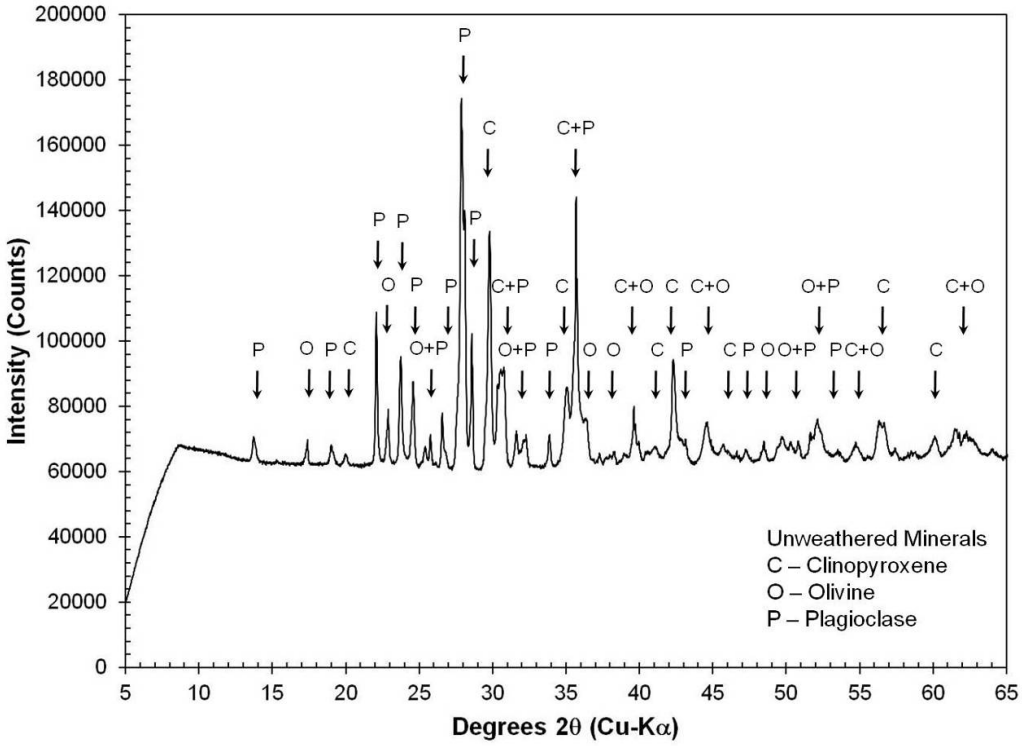

Figure 2.14. X-Ray Diffractogram of Sample 17. X-ray powder diffractogram of bulk powder of sample Unknown 17. Mineral symbols on the peaks are clinopyroxene (C), olivine (O), and plagioclase feldspar (P). Significant background intensity is related to fluorescence of iron in Fe-bearing minerals.

2.5.1.4.3. Thin Section Petrography

Petrographic thin sections were obtained of sample 17 and analyzed to constrain the texture and mineralogy as well as provide a context for the VNIR and XRD results. Observations under plain and cross-polarized light reveal clinopyroxene, olivine, and plagioclase feldspar phenocrysts as well as small orthopyroxene crystals embedded in a vesicular matrix (i.e. groundmass) dominated by fine-grained glass with small pyroxene crystals and plagioclase “microlites” (Figures 2.15 and 2.16).

The olivine grains in the sample are distinguished by an olive-green color in hand sample and colorless appearance under plain light in thin section with high relief (Figures 2.16A). They also exhibit a lack of cleavage with distinctive irregular fracturing as well as upper second-order interference colors (light blue) that distinguish them from surrounding pyroxene grains (Figures 2.16B).

The clinopyroxene grains in the sample are distinguished by a colorless appearance under plain light in thin section with a fairly high relief (Figures 2.16A). They also exhibit good cleavages at near 90° angles and more elongated crystal habit, a large extinction angle as well as middle second-order interference colors (dark blue – purple – yellow) that distinguish them from the olivine and orthopyroxene grains (Figures 2.16B).

The small orthopyroxene grains in the sample are distinguished by a colorless appearance under plain light in thin section with a moderate relief (Figures 2.16A). They also exhibit good cleavage with euhedral crystal habit, parallel extinction, and first-order interference colors (yellow – orange) that distinguish them from the olivine and clinopyroxene grains (Figures 2.16B).

The plagioclase feldspar phenocrysts in hand sample are composed of multiple smaller grains of plagioclase feldspar grouped together when viewed under thin section. They are distinguished by a colorless appearance under plain light in thin section with low relief (Figures 2.16C). The crystals exhibit characteristic polysynthetic twinning and low first-order interference colors (white – light grey) that distinguish them from the olivine and pyroxene grains (Figures 2.16D).

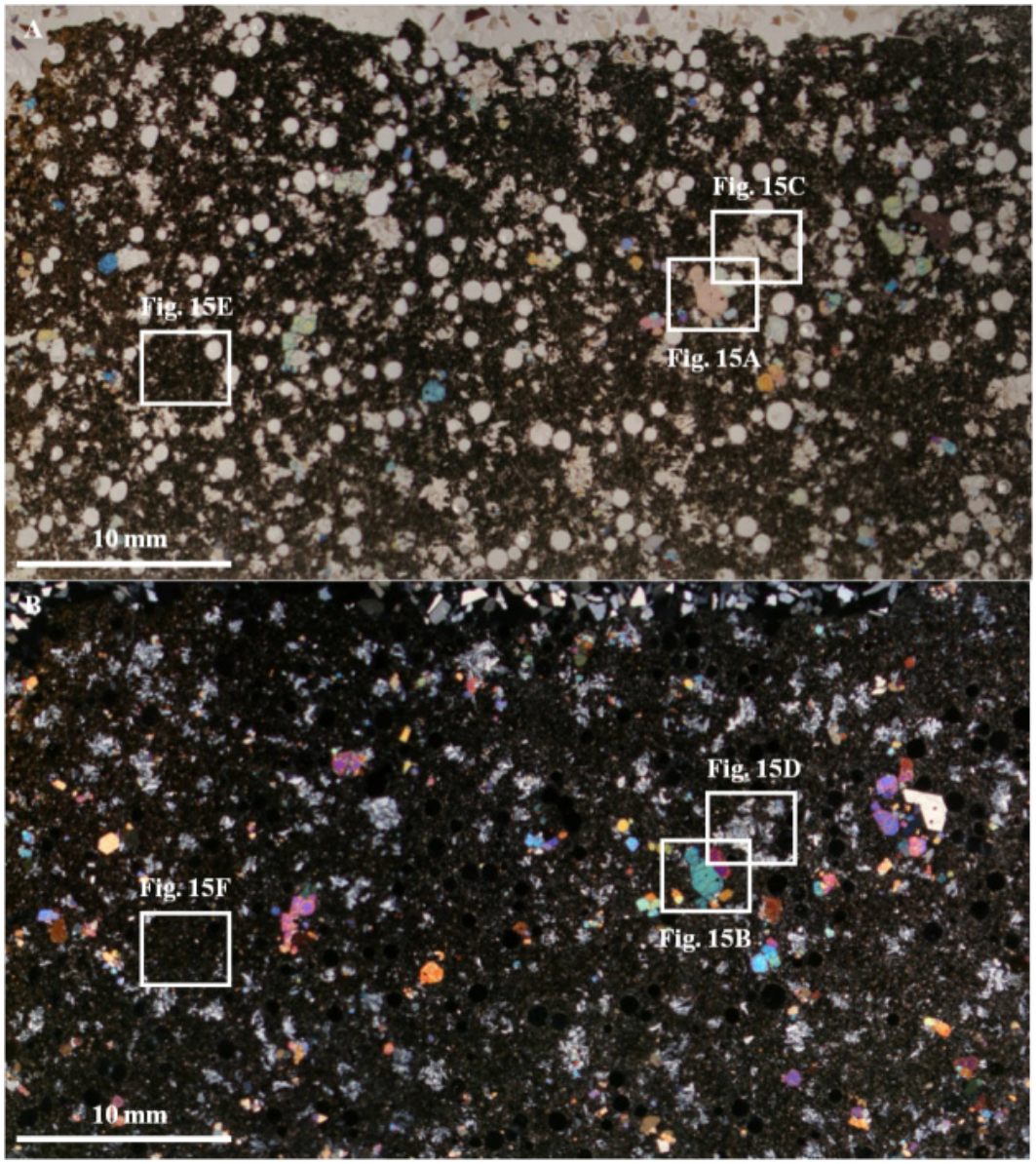

Figure 2.15. Plain- and Crossed-Polarized Light Context Images of Thin Section of Sample 17. Plain-polarized light (A) and crossed-polarized light (B) thin section mosaic images of sample Unknown 17 with outlines of close-up images shown in Figures 2.16 targeting main elements of the sample. These include pyroxene and olivine grains (Figure 2.16 A & B), plagioclase feldspar grains (Figure 2.16 C & D), and basalt matrix with microlites (Figure 2.16 E & F).

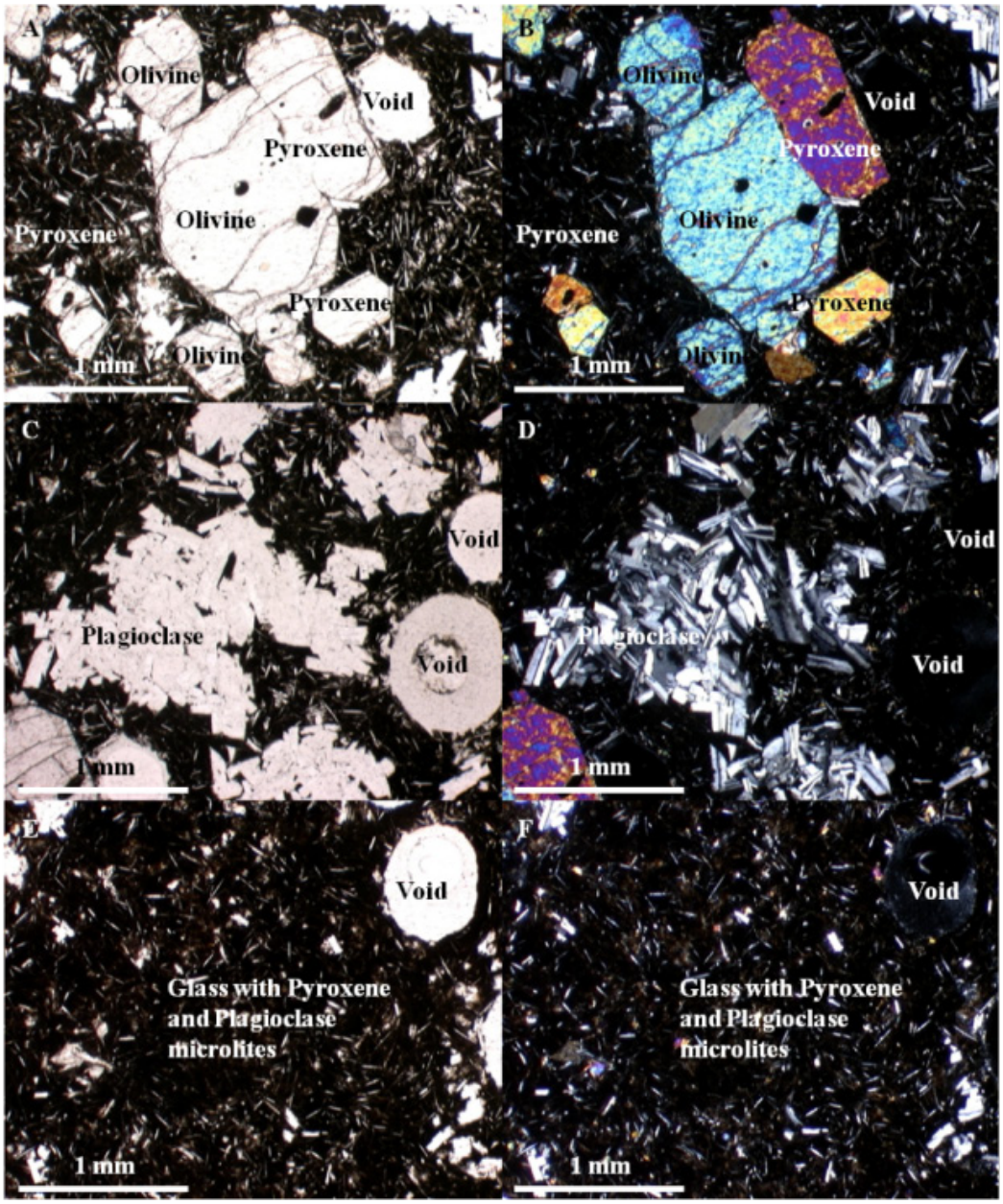

Figures 2.16. Plain- and Crossed-Polarized Light Images of Magnified Areas of Thin Section of Sample 17. Magnified plain light (left) and crossed-polarized light (right) thin section images of Unknown 17 targeting main elements with components labeled. These include pyroxene and olivine grains (Figure 2.16 A & B), plagioclase feldspar grains (Figure 2.16 C & D), and basalt matrix with pyroxene and plagioclase microlites (Figure 2.16 E & F).

2.5.2. Silicic Volcanic Breccia (Sample 14)

Sample 14 is a silicic volcanic breccia composed of angular clasts of a fine-grained, flow banded rhyolite, cemented by calcite and ferric oxide/oxy-hydroxide cements. The sample was collected from the Owen's Gorge area, south of Long Valley caldera southeast of Mammoth Lakes California.

2.5.2.1. MMI Images and Spectra of Sample 14

Figure 2.17 shows MMI-generated color composite images of sample 14 composed of visible and infrared bands, along with a corresponding spectral end-member map. Figure 2.17A is a visible-color RGB composite image comprised of MMI bands 0.641, 0.522, and 0.463 μm, to simulate true-color. Figure 2.17B is a false-color RGB composite image composed of MMI bands 1.43, 1.05, and 0.741 μm, to bring out subtle color differences resulting from variations in composition. Figure 2.17D shows a spectral end- member map generated in ENVI using a supervised classification with ROIs (Figure 2.17C) as input parameters for mapping end-member distributions. Corresponding spectra are shown in Figures 2.18 A and B, along with matching library spectra (Figure 2.18 C-F).

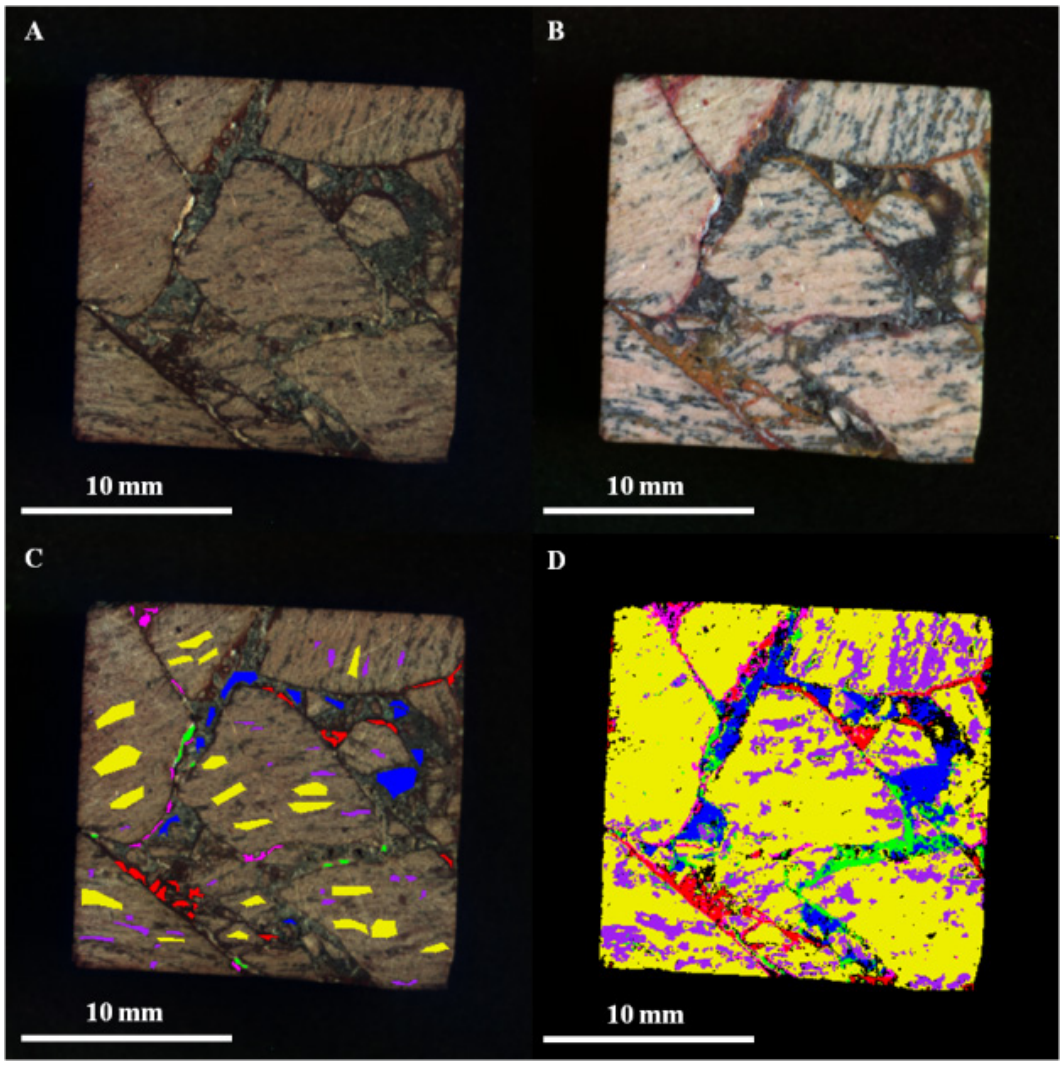

Figure 2.17. MMI-Generated Color Composite Images and End-Member Map of Sample 14. Visible-color (A) and false-color (B) composite images, visible-color composite image with regions of interest (C), and corresponding spectral end-member map based on ROIs of sample Unknown 14 acquired by the Multispectral Microscopic Imager (MMI). Each MMI sub-frame image size is 25x25 mm at 62.5 µm/ pixel. Figures A-C are linear stretched. Figure 2.17A: Visible-color RGB composite image composed of MMI bands 0.641, 0.522, and 0.463 µm respectively to simulate true-color. Figure 2.17B: False-color RGB composite image composed of MMI bands 1.43, 1.05, and 0.741 µm respectively to bring out subtle color differences in materials due to variations in composition. Figure 17C: Visible-color RGB composite similar to figure A with regions of interest (ROIs) used to generate end-member map (Figure 2.17D) and spectral end-members (Figures 2.18A & 2.18B). Figure 2.17D: End-member map generated in ENVI using supervised classification with ROIs as input parameter to map end-members distribution.

MMI images show that the sample consists of very poorly sorted, clast-supported volcaniclastic breccia made up of tan- colored sub-angular to sub-rounded (roundness 0.5-0.7) volcaniclasts, with sphericities ranging from 0.1 to 0.5 (see Powers 1953). The breccia is cemented by dark red and grey-colored cements (seen in visible color image, Figure 2.17A). Clasts are very fine grained and have whispy, dark grey internal laminations. The clasts appear to be of similar composition (i.e. monolithologic) and range from medium sand (0.25 mm), to medium pebble- (10 mm) sized grains, with small to medium pebbles being dominant. The dark red and grey cements are very fine grained (too fine for the MMI spatial resolution) and entirely fill the irregular pore spaces between clasts. In thin section, the dark red cement appears first in paragenesis, lining pore walls. The grey cement appears later in paragenesis, mostly filling the central interiors of pores. In addition to the early dark red cement, there is a second, less abundant pore-lining cement phase that is white in color. This white-colored cement is visible in Figures 2.17 A & B and appears to be contemporaneous, or to slightly post-date, the more abundant red cement. Both the red and white cements are present as small patches within grains and could be in part, alteration products.

Spectral analysis of MMI data for Unknown 14 indicates the presence of at least six spectral end- members. These spectral end members are based on sampling of discrete microtextural ROIs shown in

Figure 2.17C. Comparative spectral analysis of ROIs indicates that the red cement actually consists of two distinct spectral components (see below). The spectral end member map shown in Figure 2.17 shows the spatial distribution of the six spectral end members averaged from the ROIs is Figure 2.17D.

The red and magenta end-members are associated with the dark red cement in Figure 2.17B. The red end member spectrum has a strong spectral inflection at 0.522 μm, a peak at 0.741 μm, a strong absorption centered between bands 0.842 and 0.884 μm (centered at 0.884 μm for continuum-removed), a strong positive slope from 0.908 to 1.224 μm and a high reflectance (relative to other portions of the sample) from 1.224 to 1.735 μm in the short-wave infrared.

The magenta end-member, associated with the dark red cement in Figure 2.17B. Spectrally (Figure 2.18), it differs from the red spectral end member in having a strong spectral inflection at 0.522 μm, a peak at 0.756 μm, a strong absorption centered at 0.935 μm (centered at 0.97 μm for continuum-removed), a strong positive slope from 1.05 μm and a high reflectance (relative to other portions of the sample) from 1.29 to 1.735 μm.

The blue end member is associated with the dark grey, pore-filling cement visible in Figures 2.17A & B. Figure 2.18 shows that spectrally, this end member has a low reflectance (relative to other portions of the sample) and exhibits a predominantly flat spectrum with a very shallow

sinusoidal-shaped curve. No absorption features are present that would be diagnostic for a particular mineral.

The green end member in Figure 2.17D is associated with the patchy, white colored phase that coats the clasts in a few areas of the MMI image. In Figure 2.18, the spectrum has a steep positive slope from 0.463 to 0.667 μm, a high reflectance (relative to other portions of the sample), with a shallow negative slope towards the infrared from 0.7 to 1.735 μm, a broad weak absorption centered between 0.97 and 1.05 μm, and a strong absorption centered at 1.43 μm. Small patches of both the red and white cements occur with the interior of a few clasts, suggesting they may, in part, be alteration phases.

The yellow end-member is associated with the interior matrix (i.e. groundmass) of the clasts (Figure 2.17). The spectrum (Figure 2.18) has a strong positive slope from 0.463 to 0.756 μm, an absorption centered at 0.884 μm (centered at 0.884 μm for continuum-removed), a shallow positive slope from 0.935 to 1.735 μm, and a weak absorption centered at 1.43 μm.

The purple end-member is associated with the dark grey thin whispy laminations within the angular clasts. The spectrum has a positive slope from 0.463 to 0.756 μm, a shallow negative slope from 0.756 to 1.735 μm, and weak absorptions centered at 0.935 and 1.43 μm.

2.5.2.2. Comparison to Library Spectra

To determine best fit minerals, MMI end-member spectra for sample 14 were compared to library spectra from USGS and RELAB spectral libraries, convolved to the MMI range and resolution (see Table 2.1; Figure 2.18). Based on this analysis the blue end-member spectrum, which occurs as a late pore-filling cement, has low reflectance and does not contain any diagnostic absorption features to enable the identification of a particular mineral, or mineral class.

The red end-member spectrum is consistent with the library spectrum for hematite. At MMI range and resolution, hematite has a strong inflection at 0.522 μm and a strong diagnostic absorption centered between 0.842 and 0.884 μm (centered at 0.884 μm for continuum-removed) (Figure 2.18). In contrast, goethite, has a wider absorption (compared to hematite) centered at 0.908 μm (centered between 0.935 and 0.97 μm for continuum-removed). The position of the absorption features, however, can shift slightly depending particle size and crystallinity (e.g., Morris et al. 1985, Clark 1999).

The magenta end-member is consistent with the library spectrum for an iron oxyhydroxide, such as goethite (α-FeO(OH)), lepidocrosite (γ-FeO(OH)), or ferrihydrite (~$5Fe_2O_3 \cdot 9H_2O$). Ferrihydrite has a broad absorption centered at 0.935 μm (For continuum-removed, centered between 0.97 and 1.05 μm) and a peak at 0.811 μm, while lepidocrosite has a narrower, more symmetrical absorption (compared to ferrihydrite)

centered at 0.935 μm (0.97 μm for continuum-removed) and a peak at 0.756 μm (Figure 2.18). The peak at 0.756 μm and absorption centered at 0.97 μm for continuum-removed, suggests the best match is with lepidochrosite. However, it is important to note that goethite can have a similar absorption resulting from particle size effects, and distinguishing between these two phases in the present case is not possible.

The green end-member spectrum is consistent with library spectra for a hydrated clay mineral (e.g. montmorillonite or kaolinite), opaline silica, and some zeolites. At the MMI wavelength range and resolution, these minerals have a strong absorption centered at 1.43 μm (Figures 2.8 and 2.18) due to the OH stretching overtone. In contrast, hydrated sulfate minerals like gypsum, kieserite, epsomite or alunite, or zeolites like natrolite, have a broader absorption that encompasses both the 1.43 and 1.521 μm bands. The green spectral end-member has an absorption centered at 1.43 μm. This absorption feature does not appear to encompass the 1.521 μm band, thereby suggesting that a match with a hydrated sulfate or zeolite like natrolite is less likely. The weak absorption centered between 0.97 and 1.05 μm is most likely due to a small spectral contribution from a thin coating of the magenta end-member; however it could also be due to a contribution from the (2v1 + v3) combination and overtone band of water at 0.97 μm from the hydrated mineral (Figure 2.18; Herzberg 1945; Hunt and Salisbury 1970; Clark et al. 1990).

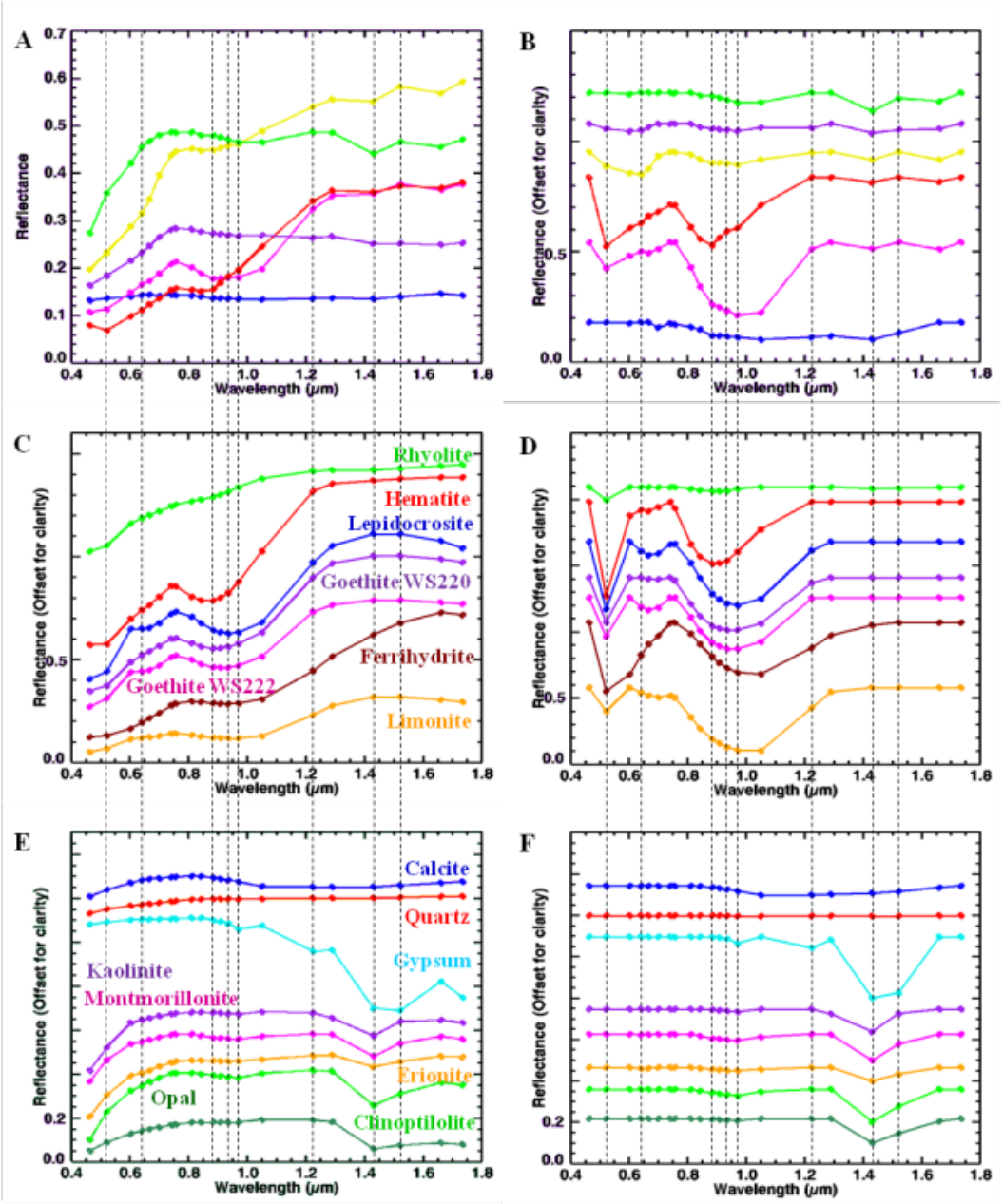

Figure 2.18. MMI-Generated Spectra of End-Members of Sample 14 Compared to Library Spectra. MMI-generated spectra of end-members (A & B) from sample Unknown 14 (Figure 2.17) and representative matching library spectra convolved to MMI bandpasses in table 1 (C – F). Vertical lines correspond to MMI bands 0.522, 0.641, 0.884, 0.935, 0.97, 1.224, 1.43, and 1.521 μm. See text for details on features and discussion. Spectra on the left are normal, while spectra on the right are continuum-removed. Continuum-removed and library spectra are offset for clarity.

The yellow end-member spectrum has absorptions and an overall spectral shape consistent with a mixture of several fine-grained minerals. The absorptions present at 0.884 and 1.43 μm suggest the presence of both hematite and an unidentified hydrated mineral. However, the overall shape of the curve does not appear to be a good match with a mix of just these two minerals alone, but is more consistent with additional phases that lack diagnostic absorptions within the MMI wavelength range and resolution. Comparison of the yellow end-member spectrum to the library spectra of rocks and minerals suggest a whole rock match that is consistent with a felsic volcanic rock like rhyolite (Figure 2.18). The hematite component of the spectrum could be due to oxidation of small microlites of mafic minerals within the groundmass, with the hydration feature being related to the hydration of feldspar microlites (also present in the groundmass based on thin section analysis) to form clay minerals.

The purple and yellow end-member spectra are distinctive spectra that are both associated with the interiors of clasts in sample 14. The yellow end-member exhibits an overall positive slope in the spectrum from 0.756 to 1.735 μm, while the purple end-member exhibits an overall negative slope in the spectrum over the same range. However, with the exception of weak absorptions at 0.935 and 1.43 μm, the yellow spectral end member, (which dominates the clasts in this rock) lacks diagnostic absorption features that would enable the identification of specific minerals. The weak 0.935 μm absorption is consistent with an Fe-

oxyhydroxide, while the absorption at 1.43 μm is consistent with the presence of an unspecified hydrated mineral. Similar to the yellow end-member spectrum, the presence of both iron and hydrated mineral features in the purple spectrum is consistent with alteration of a rhyolite groundmass. The negative slope in the spectrum from 0.756 to 1.735 μm may result from a higher hydrated mineral abundance.

2.5.2.3. Interpretation of MMI Results

The MMI images and associated spectra reveal that sample 14 is a silicic volcanic breccia composed of fine-grained, light-colored angular clasts. Clasts exhibit a linear fabric consistent with flow banding, and are cemented by a dominant, late paragenetic pore-filling mineral that is dark grey in natural and false color images. This late cement is preceded in paragenesis by less abundant, dark red iron oxide and oxyhydroxide cements (as hematite and lepidochrosite/goethite) and a low abundance, patchy hydrated mineral cement (as a hydrated silica) that is white in color. The monolithologic composition of the clasts, their poor-sorting and angular shapes, indicates minimal transport from the source area. These compositional and textural features are consistent with an origin as an auto-brecciated silicic lava flow, or possibly a well-sorted near-vent pyroclastic airfall deposit. The cement compositions indicate that fluids of differing composition percolated through open pore spaces in the rock during its post-burial history, cementing the rock early, before significant compaction. The presence of Fe-oxides/oxyhydroxides and hydrated silica

as early cement phases fluids is consistent with early diagenetic fluids that were oxidizing and of neutral to alkaline pH.

2.5.2.4. Laboratory Observations of Sample 14

2.5.2.4.1. Visible/Near-Infrared Spectroscopy

Visible/near-infrared lab spectra were collected from three locations (A-C) on the surface of sample 14, to target the major compositional and microtextural components of the sample (Figure 2.19). Figure 2.20 displays the spectra acquired over the range 0.35 μm to 2.50 μm along with corresponding library spectra. Figure 2.21 displays a close-up of spectral region 1.8 – 2.5 μm from Figure 2.20, along with corresponding library spectra. The positions of absorption features are marked with vertical dashed lines. Because the ASD spot size is ~6 mm in diameter, care was taken to ensure that each spot was centered on the major component of interest. However, as with sample 17, data obtained were composite spectra that usually included more than one phase, or fabric element.

Spot A on sample 14 (blue spectrum in Figures 2.20A & B, 2.21A & B) was collected from the center of a large volcanic clast and incorporated all of the phases making up the rock. The resulting spectrum indeed appears to be a composite of multiple minerals, with a broad absorption centered at 0.87 μm (0.91 μm for continuum-removed), and strong absorptions at 1.43, 1.91, 2.30 and 2.35 μm, and a weak absorption at 2.26 μm. Compared to spectra in the USGS (Clark et al. 2007) and

RELAB (Pieters and Hiroi 2004) spectral libraries, the broad absorption centered at 0.87 μm (centered at 0.91 μm for continuum-removed) can be attributed to hematite. The absorptions at 2.30 μm and 2.35 μm, along with the weak absorption at 2.26 μm are consistent with the library spectrum for the phyllosilicate celadonite ($K(Mg,Fe^{2+})Fe^{3+}(Si_4O_{10})(OH)_2$). Celadonite is a dioctahedral mica containing Mg, Fe^{2+} and Fe^{3+} that forms a solid solution series with the more common mineral, muscovite ($KAl_2(AlSi_3O_{10})(OH)_2$) (Rieder et al. 1998). Celadonite, which is a common authigenic mineral formed under low temperature hydrothermal alteration (Bowen et al. 1989; Bishop et al. 2008), has characteristic paired absorptions at 2.30 and 2.35 μm, due to Fe_2-OH and Mg_3-OH combination bands, respectively, as well as a weak absorption at 2.26 μm due to the AlFe-OH combination band (Bishop et al. 2008). There is an additional weak band at 2.47 μm for celadonite in library spectra; however, this feature is not observed in the sample spectrum.

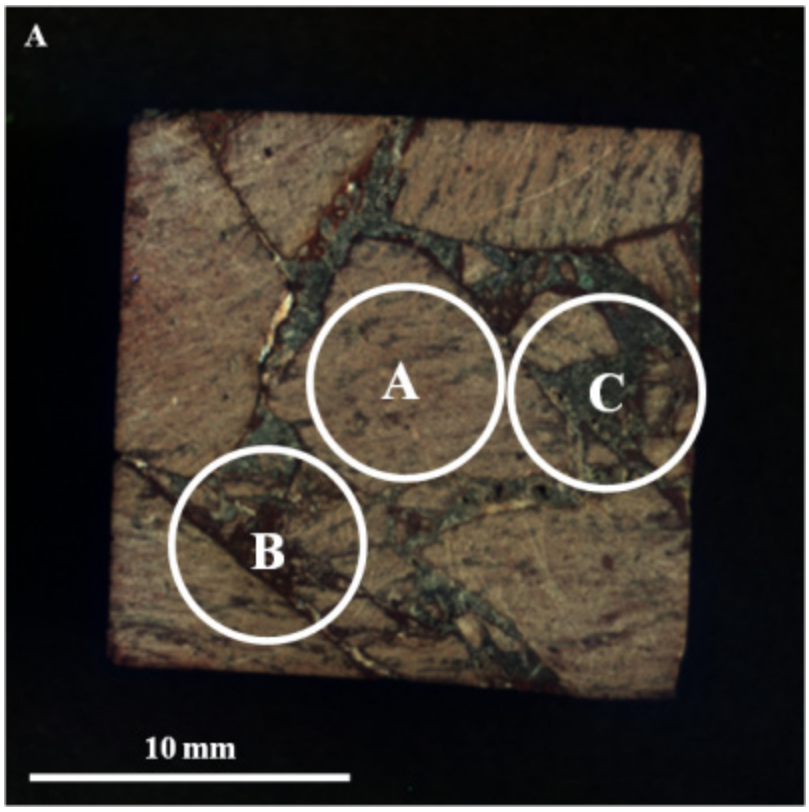

Figures 2.19. Areas on Sample 14 Analyzed with Visible/Near-Infrared Spectrometer. Visible-color, sub-frame image of sample Unknown 14 acquired by the Multispectral Microscopic Imager (MMI) composed of bands RGB = 0.641, 0.522, 0.463 μm respectively to simulate true-color with white circles (A – C) marking areas analyzed by visible/near-infrared laboratory spectrometer (spectra are shown in Figures 2.20A). Image size is 25x25 mm at 62.5 μm/ pixel. Visible/near-infrared laboratory spectrometer spot size diameter is ~6 mm.

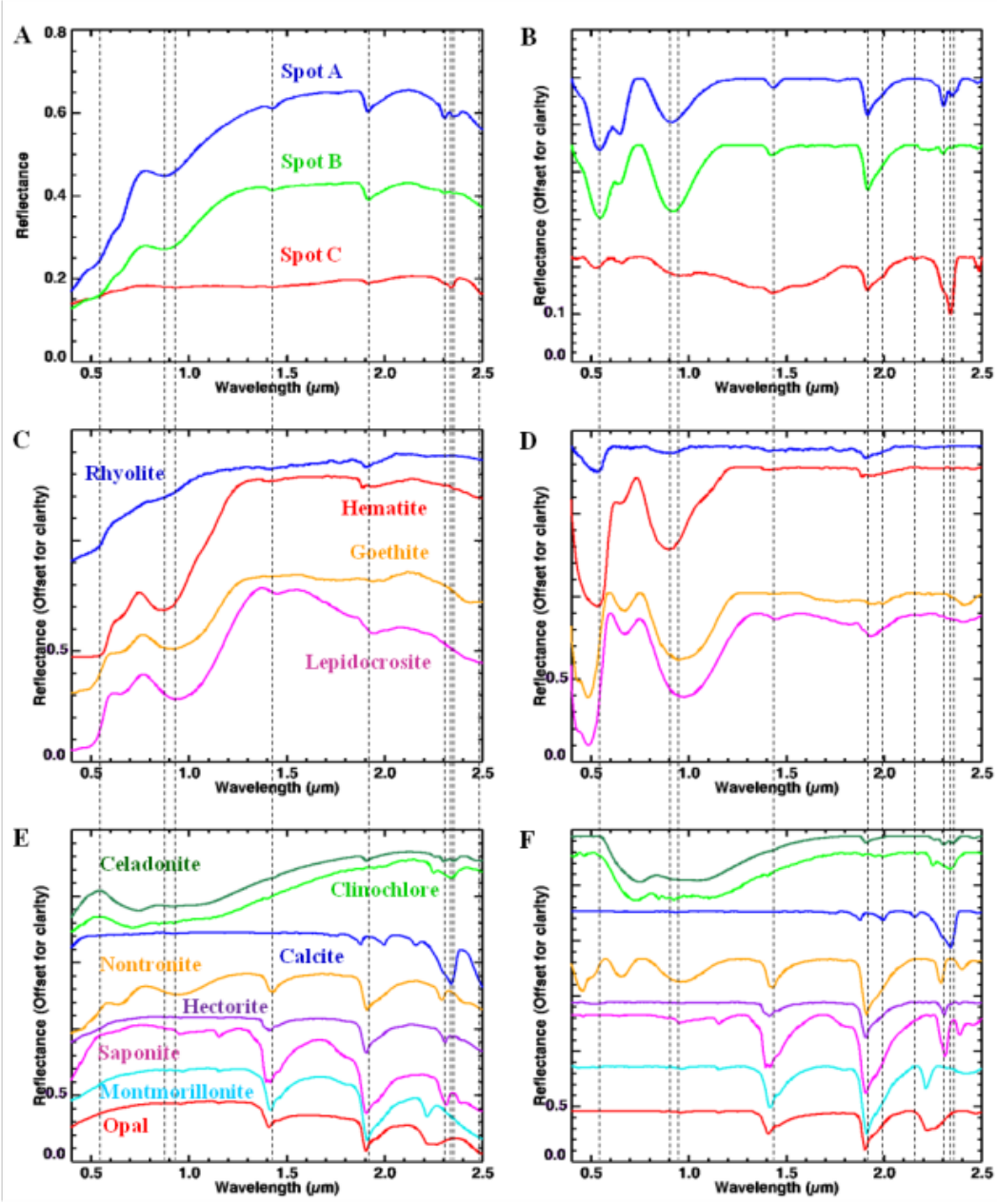

Figures 2.20. Visible/Near-Infrared Spectra of Sample 14 Compared to Library Spectra. Visible/near-infrared spectra (A & B) collected from spots A – C on sample Unknown 14 (Figures 19) with laboratory spectrometer and representative matching library spectra (C – F). Vertical lines correspond to features at 0.53, 0.87, 0.93, 1.42, 1.91, 2.3, 2.34, 2.35, and 2.5 μm. See text for details on features and discussion. Spectra on the left are normal, while spectra on the right are continuum-removed. Continuum-removed and library spectra are offset for clarity.

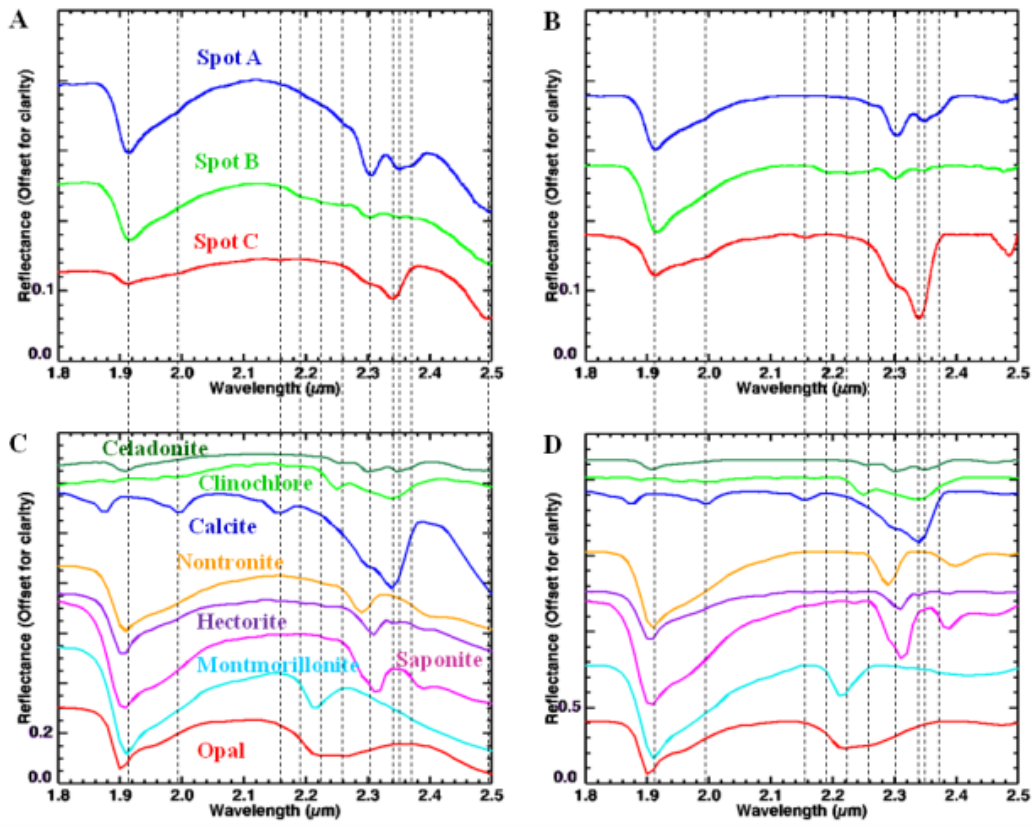

Figure 2.21. Visible/Near-Infrared Spectra of Sample 14 Compared to Library Spectra with 1.8-2.5 μm Region Magnified. Close-up of spectral region 1.8 – 2.5 μm from Figures 20 of visible/near-infrared spectra (A & B) collected from spots A – C on sample Unknown 14 (Figures 2.19) with laboratory spectrometer and representative matching library spectra (C & D). Vertical lines correspond to features at 1.91, 1.99, 2.16, 2.19, 2.22, 2.26, 2.3, 2.34, 2.35, 2.37, and 2.5 μm. See text for details on features and discussion. Spectra on the left are normal, while spectra on the right are continuum-removed. All spectra are offset for clarity.

Spot B on sample 14 (green spectrum in Figures 2.20A & B, 2.21A & B) is centered on the red colored cement, but also incorporates some smaller volcanic clasts. The spectrum is similar in shape to the blue spectrum (Spot A Figure 2.19), but has a lower reflectance and different absorption features in the 2.0 to 2.5 μm range. The composite spectrum exhibits a broad absorption feature at 0.87 μm (0.91 μm with continuum-removed), with narrower absorptions at 1.42 μm, 1.91 μm and 2.30 μm, and additional weak absorptions at 2.19 μm, 2.22 μm, 2.26 μm, 2.35 μm and 2.37 μm. Compared to spectra in the USGS spectral library (Clark et al. 2007), the broad feature centered at 0.87 μm (centered at 0.91 μm for continuum-removed) is most likely due to hematite. The absorption features at 1.42, 1.91, 2.19, 2.22, 2.26, 2.30, 2.35, and 2.37 μm appear to be a mixture of hydrated minerals. Absorptions at 1.42 μm, 1.91 μm and 2.30 μm are consistent with an intermediate Fe/Mg smectite clay, while the weak absorptions at 2.22 and 2.26 μm are consistent with the library spectrum for amorphous hydrated silica (i.e. Opal-A). The weak absorptions at 2.19, 2.35 and 2.37 μm are more difficult to associate with a particular mineral, but may be from kaolinite, or perhaps another phyllosilicate.

Spot C on sample 14 (red spectrum in Figures 2.20A & B, 2.21A & B), was centered on the dark grey cement, but also incorporates smaller amounts of the dark red cement and volcanic clasts. The spectrum has a low reflectance and appears to be a composite of multiple minerals with

absorptions at 1.42, 1.91 μm, along with a pair of strong absorptions at 2.34 and 2.50 μm. Additional weak absorptions are observed at 1.99 μm and 2.16 μm, along with a broad absorption centered at 0.93 μm (0.96 μm with continuum-removed). Compared to library spectra (Clark et al. 2007), the strong absorptions at 2.34 and 2.50 μm and weak absorptions at 1.99 and 2.16 μm are most consistent with calcite. Absorptions at 2.3 μm and 2.5 μm are overtones of fundamental absorptions for carbonate which occur in the 6–15 μm range (Lane and Christensen 1997), the precise wavelength positions varying with the specific cation(s) present (Hunt and Salisbury 1971; Gaffey 1987). The broad absorption at 0.93 μm (0.96 μm with continuum-removed), is consistent with the library spectrum for an iron oxyhydroxide, like goethite, or lepidochrosite (Morris et al. 1985). This is in contrast with the 0.87 μm absorption in the blue and green spectra (Spots A & B respectively), which is consistent with hematite. The broad absorption at 0.93 μm is due to Fe^{3+}, while the 1.4 and 1.9 μm absorptions are due to vibrational overtones of H_2O, most likely due to adsorbed water or a minor hydrated mineral component, with features in the 2.0 to 2.5 μm being masked by the strong carbonate absorptions. In summary, the red spectrum is a composite of the dark grey, calcitic cement (possibly micritic because of the dark color) and small amounts of the surrounding red cement, in this case, an iron oxyhydroxide.

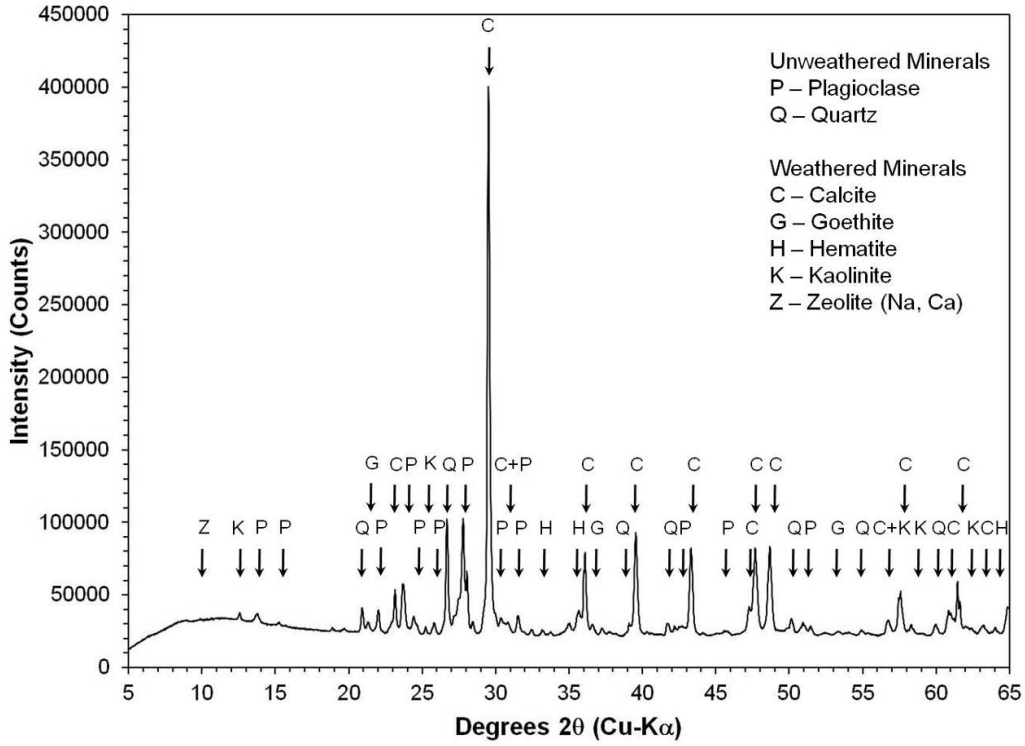

Figure 2.22. X-Ray Diffractogram of Sample 14. X-ray powder diffractogram of bulk powder of sample Unknown 14. Mineral symbols on the peaks are calcite (C), goethite (G), hematite (H), kaolinite (K), plagioclase feldspar (P), quartz (Q), and calcium-sodium zeolite, e.g. heulandite or stilbite (Z).

2.5.2.4.2. X-ray Diffraction

High resolution X-ray diffraction (XRD) was carried out on a bulk powdered sample of sample 14 to determine the mineralogy as a “ground truth” analysis for the MMI and visible/near-infrared lab results. The powder diffractogram of Unknown 14 shows strong maximum 2θ intensity peaks for calcite at 29.53°, quartz at 26.68°, and plagioclase feldspar (best fit to albite) at 27.78°. Additional smaller maximum 2θ intensity peaks are present for hematite at 33.19°, goethite at 21.32°, kaolinite at 12.57°, and calcium-sodium zeolite, such as heulandite or stilbite at 9.89° (Figure 2.22). The 2θ peaks are consistent with both primary volcanic minerals of felsic composition (e.g. quartz and plagioclase feldspar), and secondary alteration minerals and cements (e.g. calcite, Fe-oxides/hydroxides, clay minerals and zeolites).

2.5.2.4.3. Thin Section Petrography

Petrographic thin sections were obtained of sample 14 and analyzed to constrain the texture and mineralogy and provide additional context for interpreting the XRD and VNIR results. Observations under plain and cross-polarized light revealed that the angular volcanic clasts to consist of predominantly of volcanic minerals, containing small quartz and plagioclase feldspar crystals (Figures 2.23 and 2.24). The feldspar microlites within clasts are oriented parallel to each other, confirming the previous suggestion of flow banding. Clasts exhibit thin opaque coatings of dark brown, to black iron oxide (interpreted to be hematite or goethite),

which appear to be alteration rinds. Pore-filling cements show the following paragenetic relationships in thin section (Figure 2.24 C-D): 1) Early introduction of a finely-crystalline, low birefringence mineral of low optical relief (likely a zeolite, such as stilbite or heulandite, which both exhibit shief-like crystal forms, consistent with what is seen in thin section), 2) ~contemporaneous introduction of calcite microspar (identification based on high optical relief and birefringence), 3) lastly, the introduction of a reddish-brown, translucent iron oxide (consistent lepidocrocite).

Locating in thin sections, the iron oxides identified by XRD can be quite challenging. Under plane-polarized light, the opaque iron oxide coatings on volcanic clasts have a dark brown, to black color which consistent with either hematite or goethite identified from XRD. In contrast, the pore-filling iron oxide cement is translucent, with reddish brown, to orange color, most consistent with lepidocrocite (Figure 2.23 C-D). However, the color of all these phases in plane light can overlap, leading to uncertainty.

To summarize, the alteration history of sample 14 begins with dark brown iron oxide forming as coatings, or alteration rinds on volcanic clasts following deposition. This was flowed by an initial wave of cementation, which introduced zeolites (e.g., heulandite) and carbonate (calcite) into pore spaces. This was followed by the introduction of a reddish-brown translucent, iron oxyhydroxide (lepidochrocite) which completely filled the

remaining pore space. During the period of cementation, volcanic clasts were further altered, with volcanic glass undergoing crystallization, and feldspars altering to clays (kaolinite) and other fine-grained phyllosilicates, including celadonite (which is a common replacement mineral for ferromagnesian silicates in volcanic rocks).

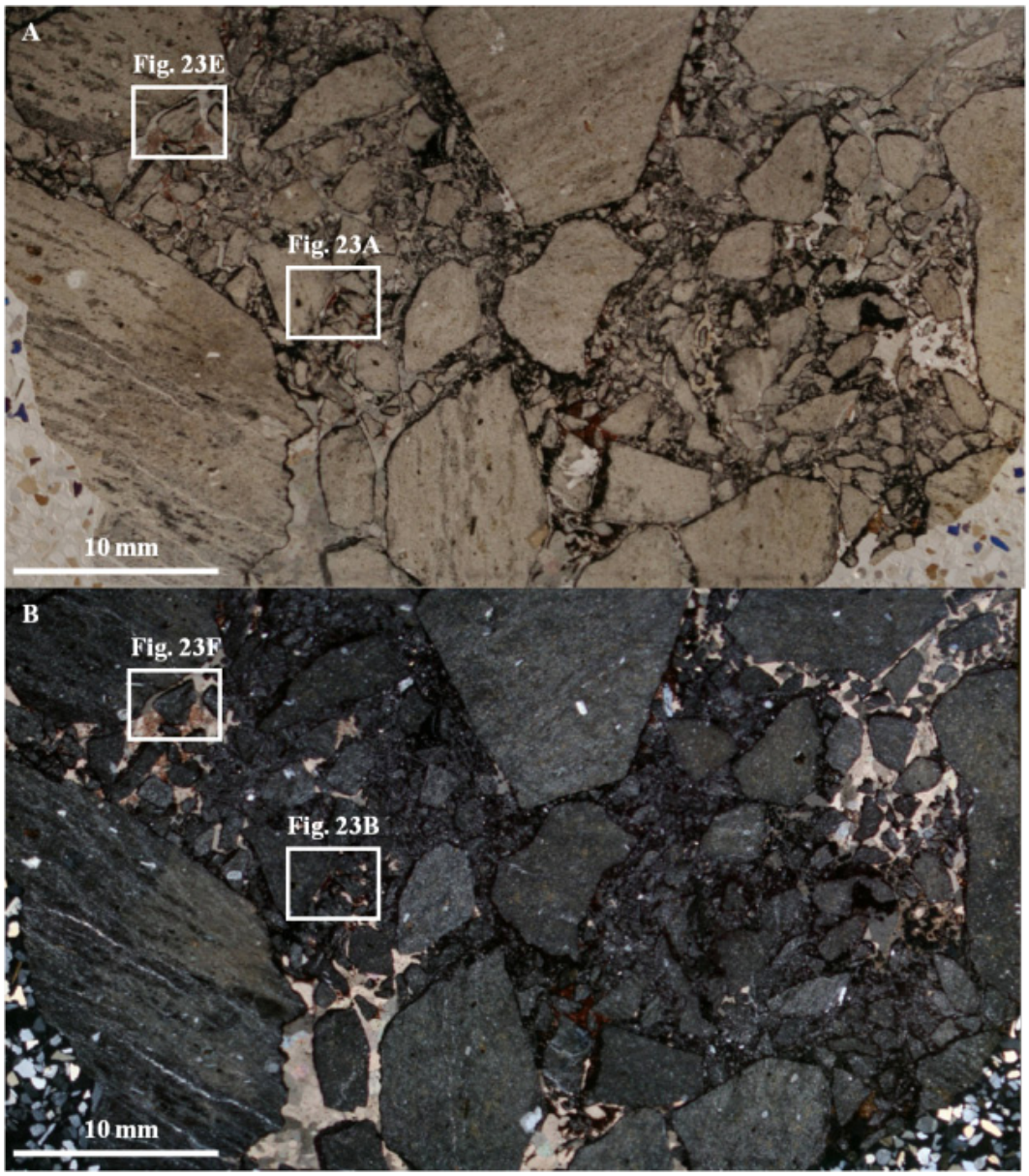

Figure 2.23. Plain- and Crossed-Polarized Light Context Images of Thin Section of Sample 14. Plain-polarized light (A) and crossed-polarized light (B) thin section mosaic images of sample Unknown 14 with outlines of close-up images shown in Figure 2.24 targeting main elements and matrix components of the sample. These include matrix cements (Fig. 2.23 A & B) and clasts (Fig. 2.23 E & F).

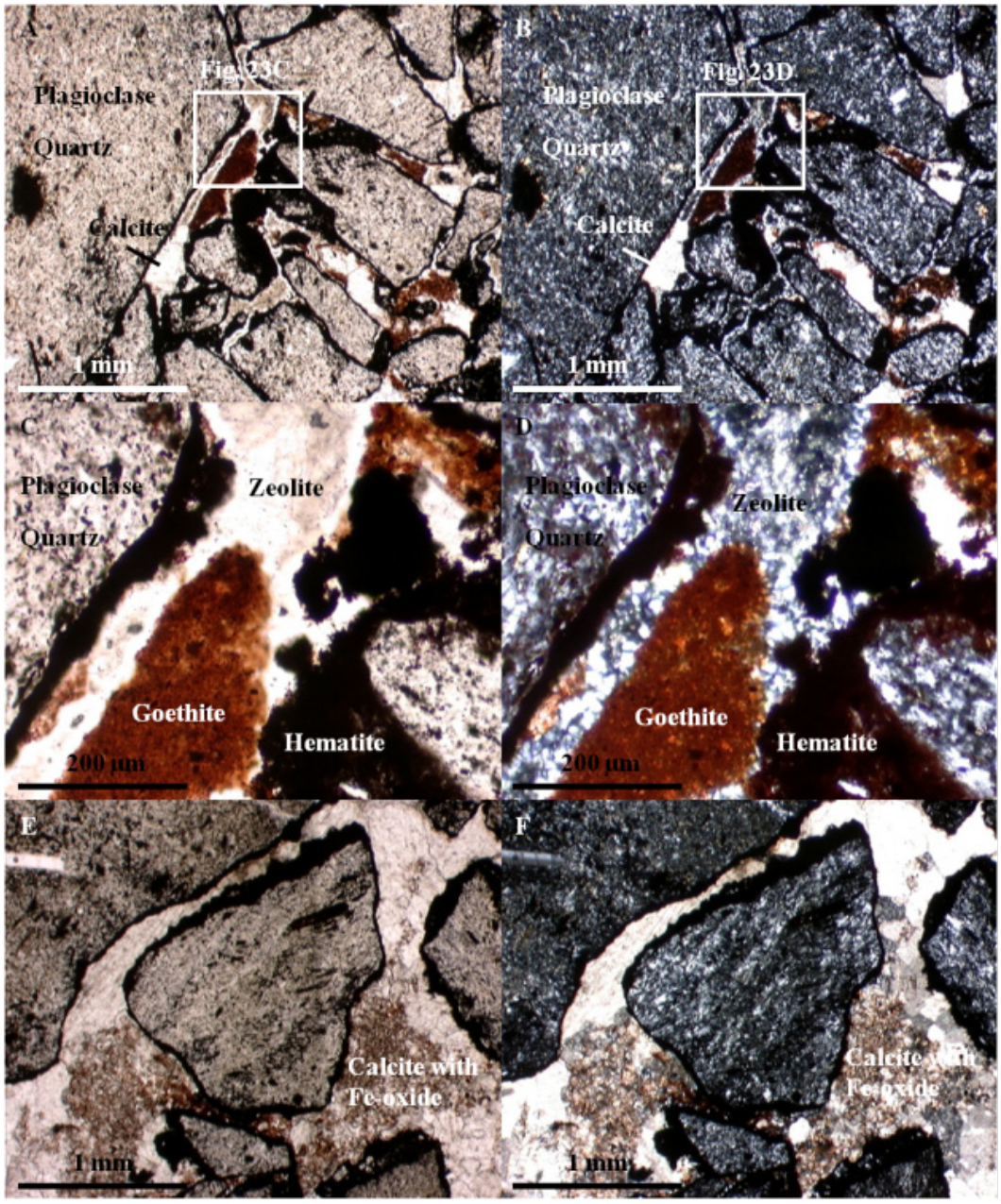

Figure 2.24. Plain- and Crossed-Polarized Light Images of Magnified Areas of Thin Section of Sample 14. Zoomed-in plain light (left) and crossed-polarized light (right) thin section images of Unknown 14 targeting main elements and matrix components labeled. These include matrix cements (Fig. 2.23 A & B) and clasts (Fig. 2.23 E & F). Images C & D are close-ups of A & B to show the cross-cutting relationships of the cements to the clasts. The crossed-polarized images are slightly overexposed to bring out color variations between the Fe-bearing cements.

2.5.3. Basaltic Volcanic Breccia (Sample 10)

Sample 10 is a palagonitized basaltic volcanic breccia composed of sub-angular to sub- rounded basalt clasts cemented by Fe-oxides, zeolites and Fe-smectites. The sample was collected (by JDF) from Hlöðufell, a Pleistocene tuya (subglacial) volcano located about 10 km southwest of Langjökull in central Iceland.

2.5.3.1. MMI Images and Spectra of Sample 10

Figure 2.25 A-D shows MMI color composite images of sample 10, along with a corresponding spectral end-member map. These images include a visible-color RGB composite image, composed of MMI bands 0.641, 0.522, and 0.463 μm (to simulate natural color) and a visible/near-infrared color RGB composite image composed of MMI bands 1.66, 0.97, and 0.756 μm respectively (to bring out subtle color differences in materials due to variations in composition). Figure 2.25D is a spectral end-member map generated in ENVI using a supervised classification with ROIs (shown in Figure 2.25C), as input parameters. Corresponding spectra for these compositional end-members are shown in Figure 2.26, along with matching library spectra from the USGS and RELAB spectral libraries.

The MMI images reveal that the sample consists of poorly sorted mixture of black, fine grained clasts with sub-angular to rounded (roundness 0.5-0.9) shapes and sphericities ranging from 0.7 to 0.9 (see Powers 1953) in a matrix (cement)-supported fabric. Cements include

orange, light-grey and white-colored components (visible color image, Figure 2.25A) that have a patchy, non-uniform distributed. Clasts are very fine grained and do not show internal fabrics, such as vesicularity, bedding or other features. Clasts appear to be of similar composition (i.e. monolithologic), ranging in size from medium sand (0.25 mm) to medium pebbles (10 mm), with small, to medium pebbles dominating the sample. Cements are very fine- grained and pre-compactional, filling large primary pore spaces between clasts. The light-grey cement component appears to line the walls of the clasts while the white and orange-colored cements appear to mostly fill interior pore spaces. The granule-sized dark clast in the middle of the sample exhibits a distinctive, grey-colored rind that is not observed in neighboring clasts. Spectral analysis of the MMI image reveals the presence of eight spectral end-members associated with sample 10 (as seen in Figures 2.24D and 2.25A). Two of these spectral end-members are associated with the clasts and six with the matrix.

The dominant compositional end-member, mapped as blue in the spectral end-member map, is associated with the fine-grained matrix of the clasts. The spectrum associated with this end member exhibits a low reflectance, flat shape, with one weak absorption centered at 1.05 μm.

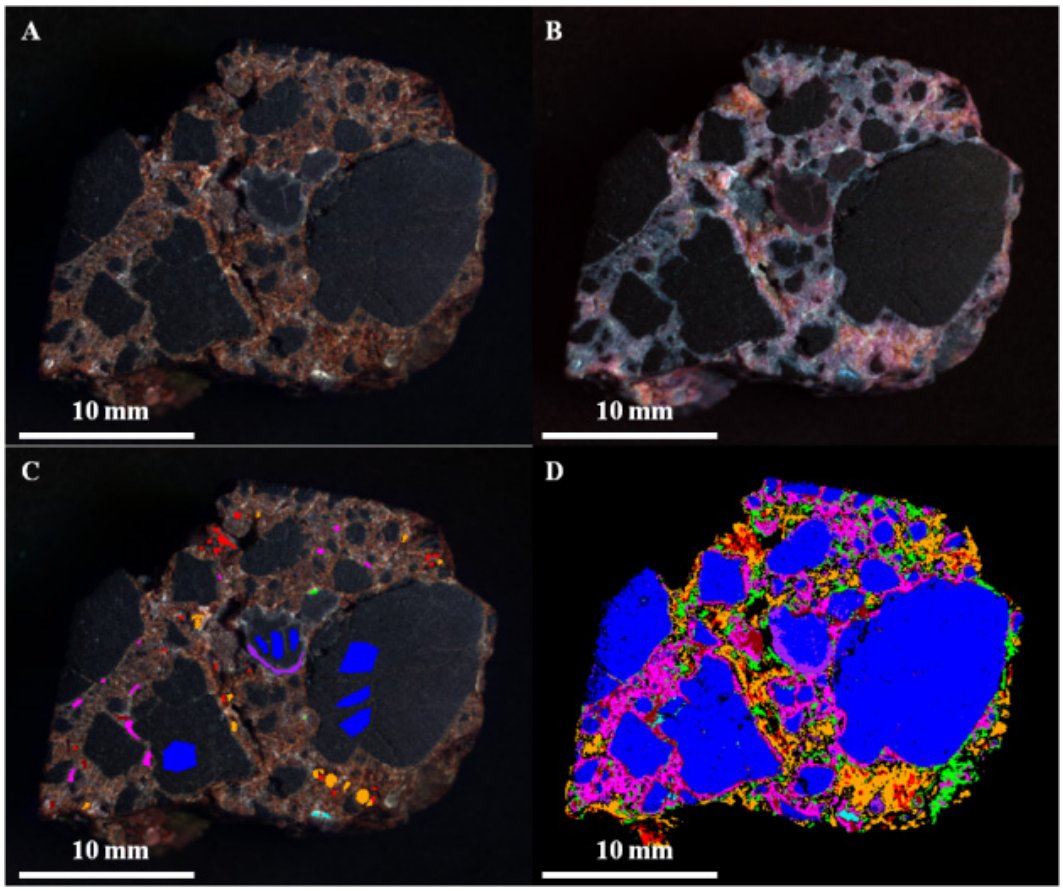

Figure 2.25. MMI-Generated Color Composite Images and End-Member Map of Sample 10. Visible-color (A) and false-color (B) composite images, visible-color composite image with regions of interest (C), and corresponding spectral end-member map based on ROIs of sample Unknown 10 acquired by the Multispectral Microscopic Imager (MMI). Each MMI sub-frame image size is 30x25 mm at 62.5 µm/ pixel. Figures A-C are linear stretched. Figure 2.25A: Visible-color RGB composite image composed of MMI bands 0.641, 0.522, and 0.463 µm respectively to simulate true-color. Figure 2.25B: False-color RGB composite image composed of MMI bands 1.66, 0.97, and 0.756 µm respectively to bring out subtle color differences in materials due to variations in composition. Figure 2.25C: Visible-color RGB composite similar to figure A with regions of interest (ROIs) used to generate end-member map (Figure 2.25D) and spectral end-members (Figures 2.25A & 2.25B). Figure 2.25D: End-member map generated in ENVI using supervised classification with ROIs as input parameter to map end-members distribution.

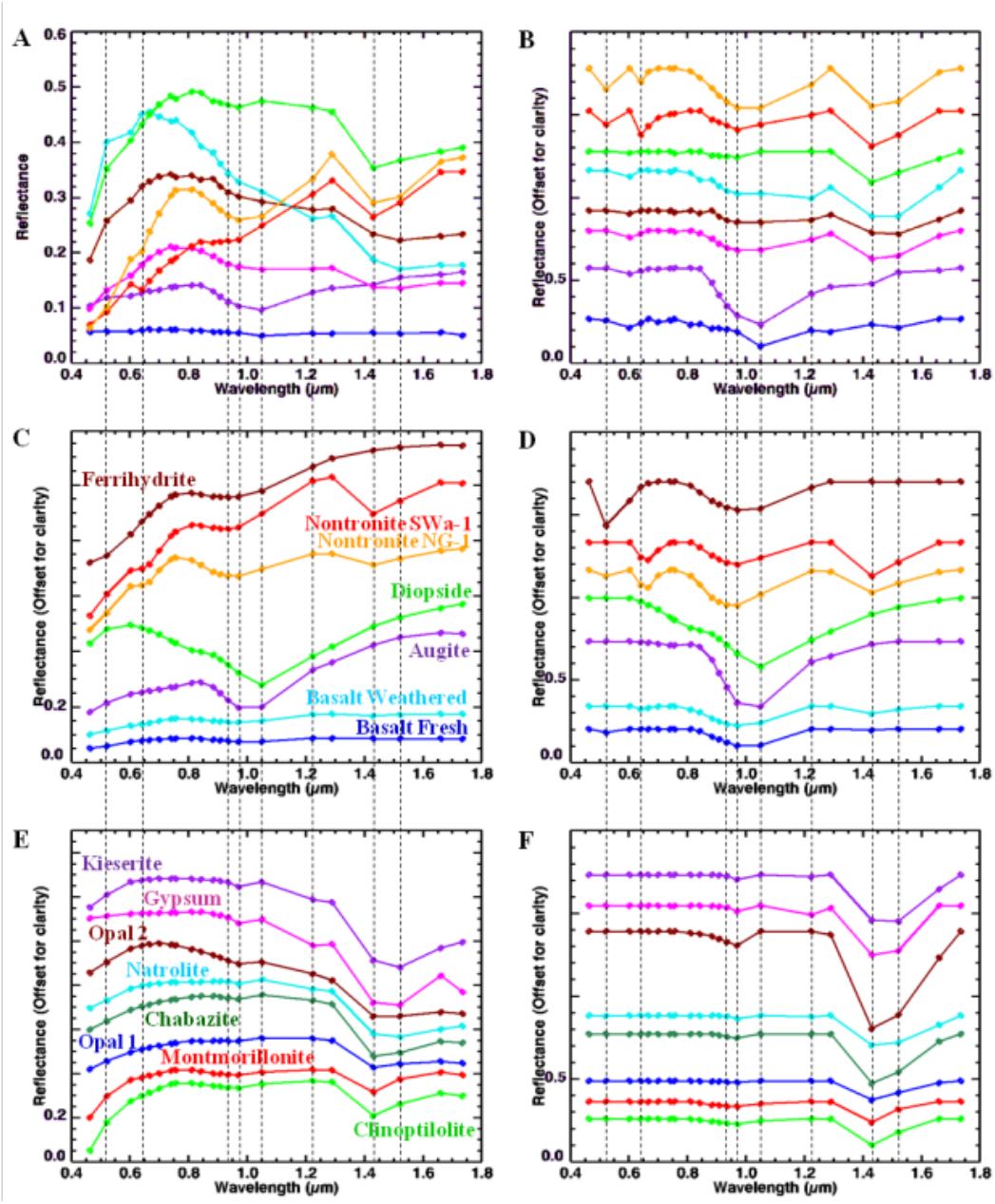

Figure 2.26. MMI-Generated Spectra of End-Members of Sample 10 Compared to Library Spectra. MMI-generated spectra of end-members (A & B) from sample Unknown 10 (Figure 2.25) and representative matching library spectra convolved to MMI bandpasses in table 1 (C – F). Vertical lines correspond to MMI bands 0.522, 0.641, 0.935, 0.97, 1.05, 1.224, 1.43, and 1.521 μm. See text for details on features and discussion. Spectra on the left are normal, while spectra on the right are continuum-removed. Continuum-removed and library spectra are offset for clarity.

The spectral end-member mapped in purple, is associated with the alteration rind of the central clast located in the middle of the image and with small fracture fills within the same clast. The spectrum has a positive slope from 0.463 to 0.842 μm, a peak at 0.842 μm, a broad absorption centered between 0.97 and 1.05 μm (centered at 1.05 μm with 0.97 μm band as a shoulder for continuum-removed), a positive slope from 1.05 to 1.735 μm, and a weak 1.43 μm absorption.

The spectral end-member mapped as magenta is associated with the light-grey cement component in the visible-color image (Figure 2.25A). This end member primarily lines the walls of pores between clasts. The spectrum has a positive slope from 0.463 to 0.741 μm, a broad peak at 0.756 μm, a negative slope towards the infrared from 0.811 to 1.735 μm, an absorption centered between 0.97 and 1.05 μm (centered between 0.97 and 1.05 μm for continuum-removed), and a broad absorption at 1.43 and 1.521 μm (centered at 1.43 and 1.521 μm for continuum-removed).

The spectral end-member mapped as brown is associated with some of the white colored cement in the visible-color image (Figure 2.25A). The spectrum is somewhat similar to the spectrum mapped as magenta (see above), but has a higher reflectance and slightly different features. The spectrum has a positive slope from 0.463 to 0.7 μm, a broad peak centered at 0.756 μm, a negative slope towards the infrared from 0.884 to 1.735 μm, an absorption centered between 0.97 and 1.05 μm (centered between 0.97 and 1.05 μm for continuum-removed), and a

broad absorption at 1.43 and 1.521 μm (centered between 1.43 and 1.521 μm for continuum-removed).

The spectral end-member, mapped in light-blue is also associated with the white colored cement in the visible-color image (Figure 2.25A). The spectrum has a strong positive slope from 0.463 to 0.641 μm, a peak centered at 0.667 μm, a negative slope towards the infrared from 0.756 to 1.735 μm, absorptions centered at 0.97 and 1.224 μm, and a broad absorption feature at 1.43 and 1.521 μm (centered between 1.43 and 1.521 μm for continuum-removed).

The spectral end-member mapped as green is also associated with the white-colored cement in the visible-color image (Figure 2.25A). The spectrum has a strong positive slope from 0.463 to 0.741 μm, a negative slope from 0.811 to 1.735 μm, and absorptions centered at 0.97 and 1.43 μm.

The spectral end-member mapped as red is the associated with the orange-colored cement in the visible-color image (Figure 2.25A). The spectrum has a positive slope towards the infrared from 0.463 to 1.735 μm, an inflection at 0.522 μm, peaks at 0.842 and 1.29 μm, and absorptions centered at 0.641, 0.935, and 1.43 μm (centered at 0.641, 0.97 and 1.43 μm respectively for continuum- removed).

The last spectral end-member, mapped as orange, is also associated with the orange- colored cement. The spectrum has a positive slope from 0.463 to 0.756 μm, an inflection at 0522 μm, a peak from 0.756

to 0.811 μm, a slight positive slope from 0.811 to 1.735 μm, and absorptions centered at 0.641 μm, between the 0.97 and 1.05 μm (centered between 0.97 and 1.05 μm for continuum-removed) and 1.43 and 1.521 μm (centered between 1.43 and 1.521 μm for continuum-removed).

2.5.3.2. Comparison to Library Spectra

To determine best fit minerals, MMI end-member spectra were compared to library spectra from USGS and RELAB spectral libraries convolved to the MMI range and resolution (see Table 2.1; Figure 2.26).

The blue end-member spectrum is most consistent with the library spectrum for basalt. Generally speaking, basalt has a flat spectrum in the visible/near-infrared (VNIR) due to the intimate mixture of the fine-grained minerals and volcanic glass. However, the weak absorption at 1.05 μm may be due to the presence of high-Ca clinopyroxene, or olivine.

The purple end-member spectrum compares best with the library spectrum for clinopyroxene (best matched is with augite). At the MMI range and resolution, augite has a characteristic broad absorption centered between 0.97 and 1.05 μm (centered at 1.05 μm with 0.97 μm band forms a shoulder for continuum-removed) along with a positive slope towards the infrared. The weak 1.43 μm absorption is most likely a contribution from a hydrated mineral phase. Given the context of the purple spectral end-member as a rind, and lack of Fe-oxide absorption feature in the spectrum from weathering of pyroxene, the spectrum is most

like a mixture of pyroxene with hydrated glass. The unique alteration rind seen in this clast and compositional differences, suggests it was derived from a different source material, with a different diagenetic history.

The magenta end-member spectrum is most likely a mixture of different materials. The absorption feature including the 0.97 and 1.05 μm bands (centered between 0.97 and 1.05 μm for continuum-removed) is consistent with the absorption feature observed in the purple spectrum for pyroxene, and is most likely augite. The broad 1.43 and 1.521 μm absorption is consistent with a hydrated mineral like opaline silica, a hydrated sulfate, or perhaps a zeolite, like natrolite. At the MMI wavelength range and resolution, these minerals have a broad absorption feature that encompasses both the 1.43 and 1.521 μm bands from the OH stretching overtone. In contrast, smectite clay minerals like montmorillonite, or nontronite, as well as other clays, like kaolinite, have a narrower OH stretching overtone absorption centered at 1.43 μm.

The brown end-member spectrum has a shape similar to the magenta end-member spectrum, but with minor differences, including a higher reflectance curve and a broad absorption feature centered at 1.43 and a deeper absorption at the 1.521 μm. Like the magenta end-member spectrum, the absorption feature including the 0.97 and 1.05 μm bands (centered between 0.97 and 1.05 μm for continuum-removed) is consistent with the spectrum for pyroxene, most likely augite. The broad 1.43 and 1.521 μm absorption is also most consistent with a hydrated

mineral, like opaline silica, a hydrated sulfate, or zeolite, such as natrolite. The higher reflectance curve of the spectrum and shallower band depth of the broad 0.97 and 1.05 μm absorption feature suggests a lower pyroxene component.

The light-blue end-member spectrum is most consistent with an unspecified hydrated mineral. However, at the MMI wavelength range and resolution, the absorptions at 0.97 and 1.224 μm, along with the broad absorption centered at 1.43 and 1.521 μm, have positive comparisons with library spectra for zeolites like natrolite, or sulfates, like gypsum, or kieserite. Laboratory spectra of zeolites, like chabazite, heulandite, and stilbite, have minor absorption features centered at ~ 0.97 and ~1.15 μm due to the (2v1 + v3) and (v1 + v2 + v3) combination and overtone bands for water, respectively (Herzberg 1945; Hunt and Salisbury 1970; Clark et al. 1990) while laboratory spectra of sulfates like gypsum and kieserite have similar absorption features due to water centered at ~0.98 and ~1.20 μm. When the spectra are convolved to the MMI wavelength bandpasses (see Table 2.1), the 0.97 – 0.98 μm feature in both mineral types is carried over to the 0.97 μm MMI band. In contrast, the ~1.15 μm absorption feature of the zeolites chabazite and heulandite are not carried over, while the ~1.20 μm absorption feature of natrolite and sulfates like gypsum and kieserite is carried over to the 1.224 μm MMI band, convolved to the MMI wavelength resolution. Thus, the 1.224 μm band feature provides additional useful information to narrow choices to either the zeolite

natrolite, or a hydrated sulfate like gypsum, or keiserite. However, it is not possible to distinguish further between these mineral phases.

The green end-member spectrum is most consistent with a hydrated mineral like a clay mineral (e.g. montmorillonite), opaline silica, or a zeolite (e.g. chabazite). The absorption feature centered at 1.43 μm is narrower than the other spectral end-members, which encompass both the 1.43 and 1.521 μm bands. Hydrated sulfate minerals like gypsum, or kieserite, and zeolites, like natrolite, have a broader absorption feature that includes both the 1.43 and 1.521 μm bands. Given the fact that the distinguishing absorption features between phyllosilicates (e.g. montmorillonite), opaline silica, and zeolites (e.g. chabazite) are outside of the MMI range, it is not possible to narrow the possible choices further.

The red end-member spectrum is most consistent with the library spectra for the Fe-smectite, nontronite, along with a minor component of Fe oxide/hydroxide, possibly ferrihydrite. At the MMI wavelength range, nontronite exhibits broad absorptions at ~0.64 and ~0.95 μm due to Fe^{3+} and ~1.43 μm due to OH-stretching overtones associated the 2Fe-OH combination tones (Clark et al. 1990, Bishop et al. 2002c). When convolved to the MMI bandpasses, the 0.64 and 0.95 μm absorption features are carried over to the 0.641 μm band and between the 0.935 and 0.97 μm bands (0.641 and 0.97 μm respectively for continuum-removed), while the 1.43 μm absorption is carried over to the 1.43 μm band (1.43 μm band for continuum-removed). This combination of features

enables the distinction of nontronite from other mineral types. The inflection at 0.522 μm, the slope of the curve, and contribution of the absorption feature at 0.935 μm, are most likely due presence of an Fe-oxide/hydroxide, such as ferrihydrite.

The orange end-member spectrum appears to be a mixture of materials from the red and magenta end-member spectra. The inflection at 0.522 μm and the 0.641 μm absorption are contributed by the red end-member spectrum while the broad absorption features between bands 0.97 and 1.05 μm as well as between 1.43 and 1.521 μm are contributed by a mixture of the two end-member spectra. As a result, the orange end-member spectrum is possibly a mixture of pyroxene (best fit to augite), nontronite, Fe-oxide/hydroxide, and a hydrated mineral, such as natrolite. Compared to spectra in the literature, the orange end-member spectrum is most consistent with palagonitized basalt (e.g., Warner and Farmer 2010). Palagonite is a heterogeneous material derived from aqueous alteration of basalt or basaltic glass. It has been defined in various ways in the literature with differing compositions and textures (Peacock 1926; Moore 1966; Thorseth et al. 1991). Depending on the stage of alteration, its composition varies from hydrated Fe-oxides in early stages of alteration that is often typical of low-temperature weathering (Thorseth et al. 1991; Bishop et al. 2002c; Drief and Schiffman 2004; Pokrovsky et al. 2005) to Fe, Mg-rich clay minerals, zeolites and hydrated silica for more advanced

alteration at elevated temperatures (Griffith and Shock 1995; Bishop et al. 2002c; Warner and Farmer 2010).

2.5.3.3. Interpretation of MMI Results

The MMI images and spectra reveal that sample 10 is a volcanic breccia composed of basaltic clasts that were cemented by Fe-oxides/hydroxides, hydrated silica, zeolites and crystalline clays, probably under low temperature hydrothermal conditions. Rounded to subangular clast shapes indicate moderate transport from the source, consistent with brecciation during eruption and subsequent transport in the subglacial volcanic environment. The uniformity of clast texture and composition (monolithologic) is consistent with derivation from a single volcanic source. However, there is evidence of minor mixing of clasts with a second population with alteration rinds enriched in hydrated silica (a common aqueous alteration product of basalt) and pyroxene. The depositional context (subglacial volcanic setting) and composition of cements in sample 10 are consistent with palagonitization under low hydrothermal temperatures (e.g., Warner and Farmer 2010).

2.5.3.4. Laboratory Observations of Sample 10

2.5.3.4.1. Visible/Near-Infrared Spectroscopy

Visible/near-infrared spectra were collected from three locations (A-C) on the surface of sample 10, to target the major compositional and microtextural components of the sample (Figure 2.27).

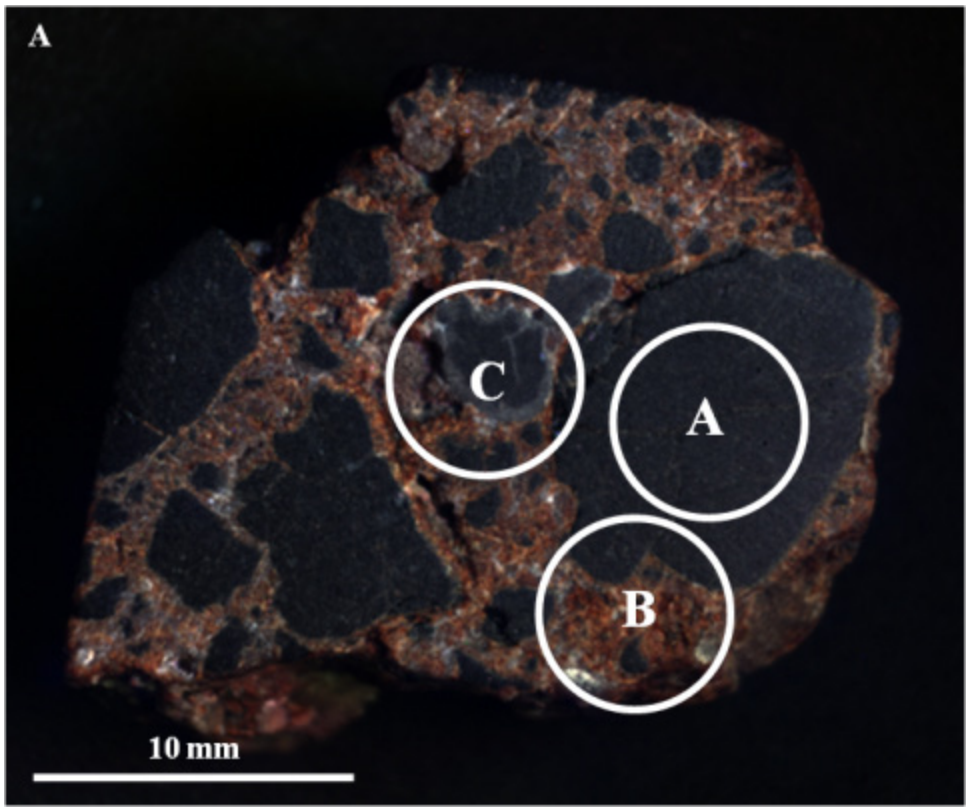

Figure 2.27. Areas on Sample 10 Analyzed with Visible/Near-Infrared Spectrometer. Visible-color, sub-frame image of sample Unknown 10 acquired by the Multispectral Microscopic Imager (MMI) composed of bands RGB = 0.641, 0.522, 0.463 μm respectively to simulate true-color with white circles (A – C) marking areas analyzed by visible/near-infrared laboratory spectrometer (spectra are shown in Figure 2.28A). Image size is 30x25 mm at 62.5 μm/ pixel. Visible/near-infrared laboratory spectrometer spot size diameter is ~6 mm.

Figure 2.28 displays the spectra acquired over the range 0.35 μm to 2.50 μm along with corresponding library spectra. The positions of absorption features are marked with vertical dashed lines. Because the ASD spot size is ~6 mm in diameter, care was taken to ensure that each spot was centered on the major component of interest. However, as with samples 14 and 17, data obtained were composite spectra that included more than one phase, and fabric element.

Spot A on sample 10 (red spectrum in Figure 2.28A & B), was centered of the largest dark- toned clast in the image. The spectrum has relatively flat reflectance with a very weak absorption feature at 1.0 μm. Compared to spectra in the USGS spectral library (Clark et al. 2007), the absorption features at 1.0 μm is most consistent with the library spectrum for augite. Augite is a major component of the dark, fine grained mafic volcanic rock, basalt.

Spot B on sample10 (blue spectrum in Figure 2.28A & B), was centered on the orange- colored cement, but also included some of the smaller dark-toned clasts. The composite spectrum exhibits a broad absorption at 1.00 μm (1.01 μm for continuum-removed), narrower absorptions at 1.42, 1.91 and 2.29 μm, and additional weak absorptions at 1.78 and 2.39 μm. Compared to spectra in the USGS spectral library (Clark et al. 2007), the broad absorption centered at 1.00 μm is attributed to augite. The other absorptions are most consistent with the Fe-smectite clay, nontronite (a common hydrothermal mineral).

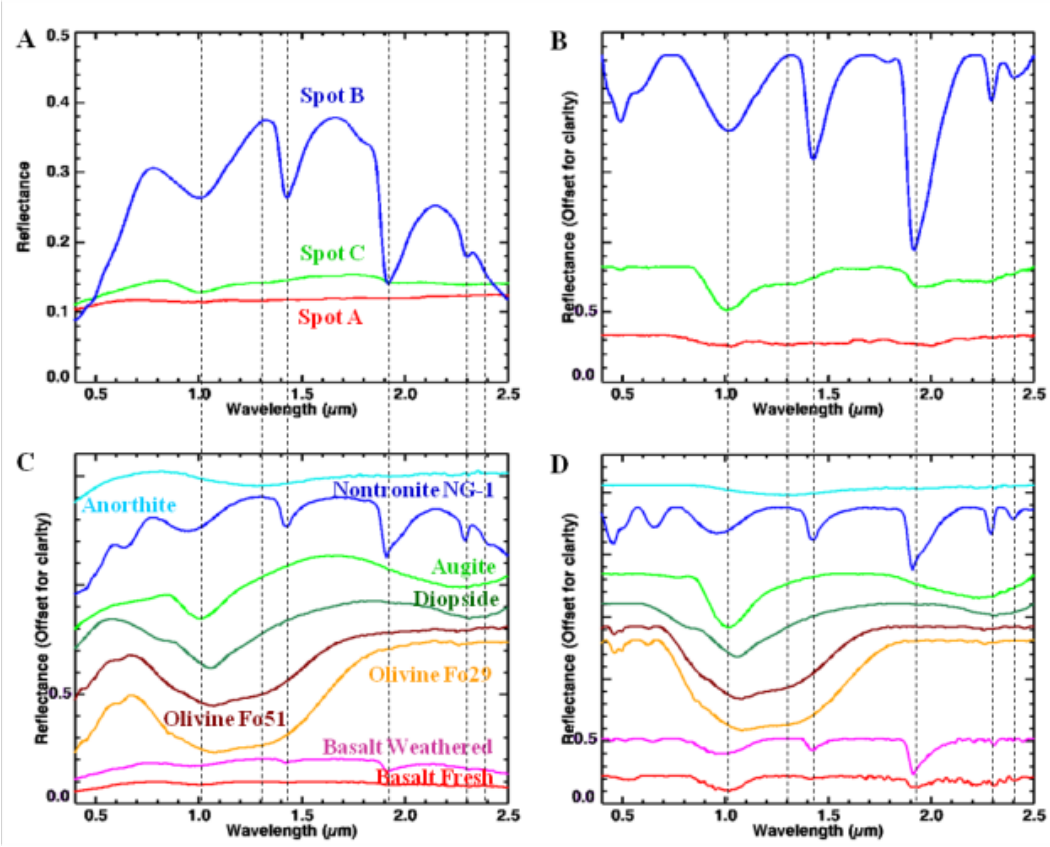

Figure 2.28. Visible/Near-Infrared Spectra of Sample 10 Compared to Library Spectra. Visible/near-infrared spectra (A & B) collected from spots A – C on sample Unknown 10 (Figure 2.27) with laboratory spectrometer and representative matching library spectra (C & D). Vertical lines correspond to features at 1.01, 1.28, 1.42, 1.91, 2.29, and 2.39 μm. See text for details on features and discussion. Spectra on the left are normal, while spectra on the right are continuum-removed. Continuum-removed and library spectra are offset for clarity.

Spot C on sample 10 (green spectrum in Figure 2.28A & B), centers the data collection on the rim of the central clast. The spectrum exhibits a broad absorption centered at 1.0 μm and weaker broad absorption features at 1.28, 1.95, and 2.27 μm. Compared to spectra in the USGS spectral library (Clark et al. 2007) and RELAB (Pieters and Hiroi 2004), the 1.0 μm feature is most consistent with the mineral augite. Similar to sample 17, the broad 1.28 μm absorption for sample 10 is attributed to fine-grained olivine pheonocrysts in the matrix of the volcanic clasts. Plagioclase feldspar, which appears white in visible color, does not exhibit diagnostic absorption features within the visible/near-infrared range. To detect fundamental Si-O absorption features associated with feldspar, or quartz, one needs to search in the mid-infrared (Clark 1999 and references therein). However, Fe^{2+} substituting Ca^{2+} in seven coordinated sites in plagioclase feldspar produces crystal field electronic transitions resulting in broad, shallow bands in the VNIR range at about 1.2–1.3 μm (Burns 1993). This absorption feature in feldspars is pretty weak and would likely be swamped by stronger absorptions in similar positions from Fe-bearing minerals. The position of the 1.28 μm feature is consistent with the position for plagioclase feldspar, however the 1.28 μm absorption has a narrower full width at half maximum, when compared to library spectra for plagioclase feldspar. Therefore, this feature is therefore more consistent with the shoulder seen in olivine. The absorptions at 1.95

and 2.27 μm suggest a hydrated mineral; however, precise mineral identification cannot be made based on the data in hand.

2.5.3.4.2. X-ray Diffraction

X-ray diffraction (XRD) of bulk powdered materials from sample 10 was used to determine the bulk mineralogy and provide a “ground truth” for the MMI and visible/near-infrared results. The powder diffractogram for sample 10 shows maximum 2θ intensity peaks for the Ca-Na zeolite, chabazite at 9.64° and 20.68°, for pyroxene (best fit to high-Ca clinopyroxene) at 29.95°, for olivine at 36.11°, for Ca-rich plagioclase feldspar (best fit to anorthite) at 27.91°, and the Fe-smectite, nontronite, at 6.38° (Figure 2.29). Small minor peaks for illite are also present. There is a significant amount of background intensity attributed to amorphous volcanic glass and nanophase Fe oxides/hydroxides (Moore and Reynolds 1997). Such amorphous Fe materials are common alteration products of basaltic glass and are difficult to analyze via standard XRD methods (Bishop et al. 2002c, Warner and Farmer 2010). The 2θ peaks are consistent with both primary basaltic minerals (e.g. pyroxene, plagioclase feldspar, and olivine), along with secondary alteration minerals and cements (e.g. zeolite and clay minerals).

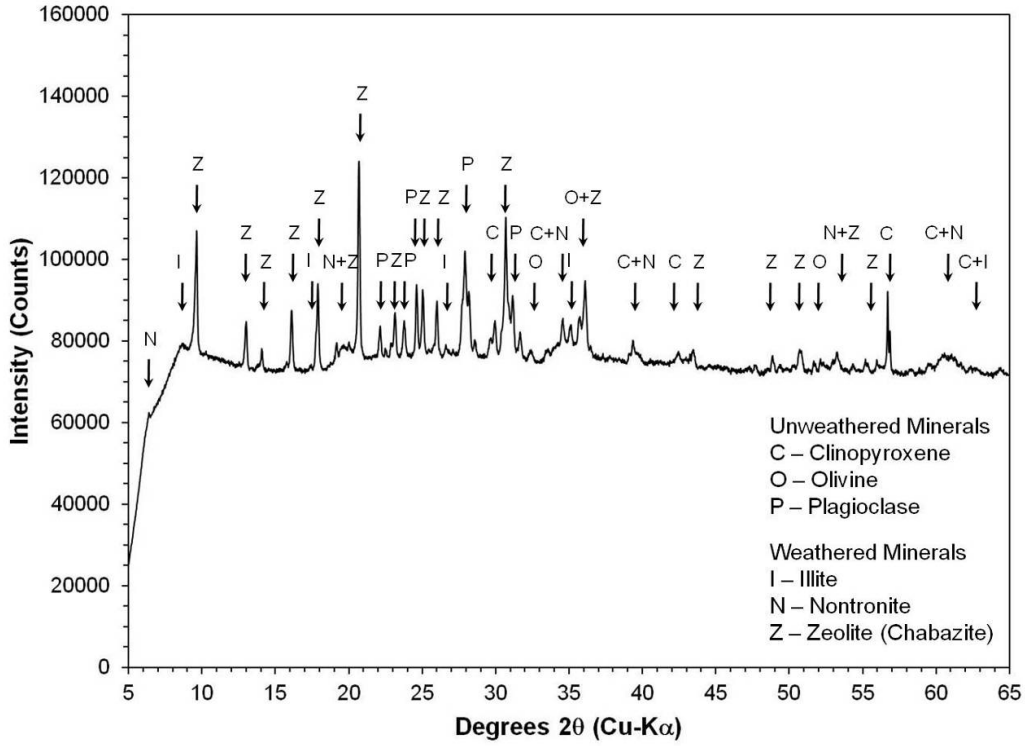

Figure 2.29. X-Ray Diffractogram of Sample 10. X-ray powder diffractogram of bulk powder of sample Unknown 10. Mineral symbols on the peaks are clinopyroxene (C), illite (I), nontronite (N), olivine (O), plagioclase feldspar (P), and zeolite, best match to chabazite (Z). Significant background intensity is related to amorphous and/or nanophase Fe-hydroxides (Moore and Reynolds 1997), which are common alteration products of basaltic glass and are difficult to analyze via standard XRD methods (Bishop et al. 2002c).

2.5.3.4.3. Thin Section Petrography

Petrographic thin sections were obtained of sample 10 and analyzed to constrain the mineralogy and to provide a microtextural context for understanding the XRD and VNIR results. Observations under plain and cross-polarized light revealed sub-angular to rounded basalt clasts, consisting of predominantly small phenocrysts of plagioclase feldspar and pyroxene, in a fine-grained, glassy groundmass containing small microlites of plagioclase and pyroxene (Figures 2.30 and 2.31). In thin section, the clasts show a distinct discoloration at their edges which is visible only in plane light. This appears to be due to the glassy matrix being lighter in color. In the case of small clasts, the discoloration of the matrix encompasses the entire clast (Figure 2.31). While the discoloration boundary may be indicative of an alteration front in the matrix, there is no visible evidence for alteration of plagioclase, or pyroxene phenocrysts (Figure 2.31). This suggests that the alteration is limited to the glassy matrix. Clasts are rimmed by a thin orange-colored film composed of yellow-green colored fibrous crystals of what are inferred to be nontronite and in some locations, by fine-grained, amorphous iron oxide/hydroxide (Figure 2.31). In the areas between clasts and within vugs, zeolites dominate; however, nontronite is also present in the central areas of filled pore spaces surrounded by zeolites. The undercompacted texture of the rock, limited clast alteration, and overlapping paragenesis is consistent

with extremely rapid precipitation and very early cementation of the clasts by saturated, silica- and iron-rich hydrothermal fluids.

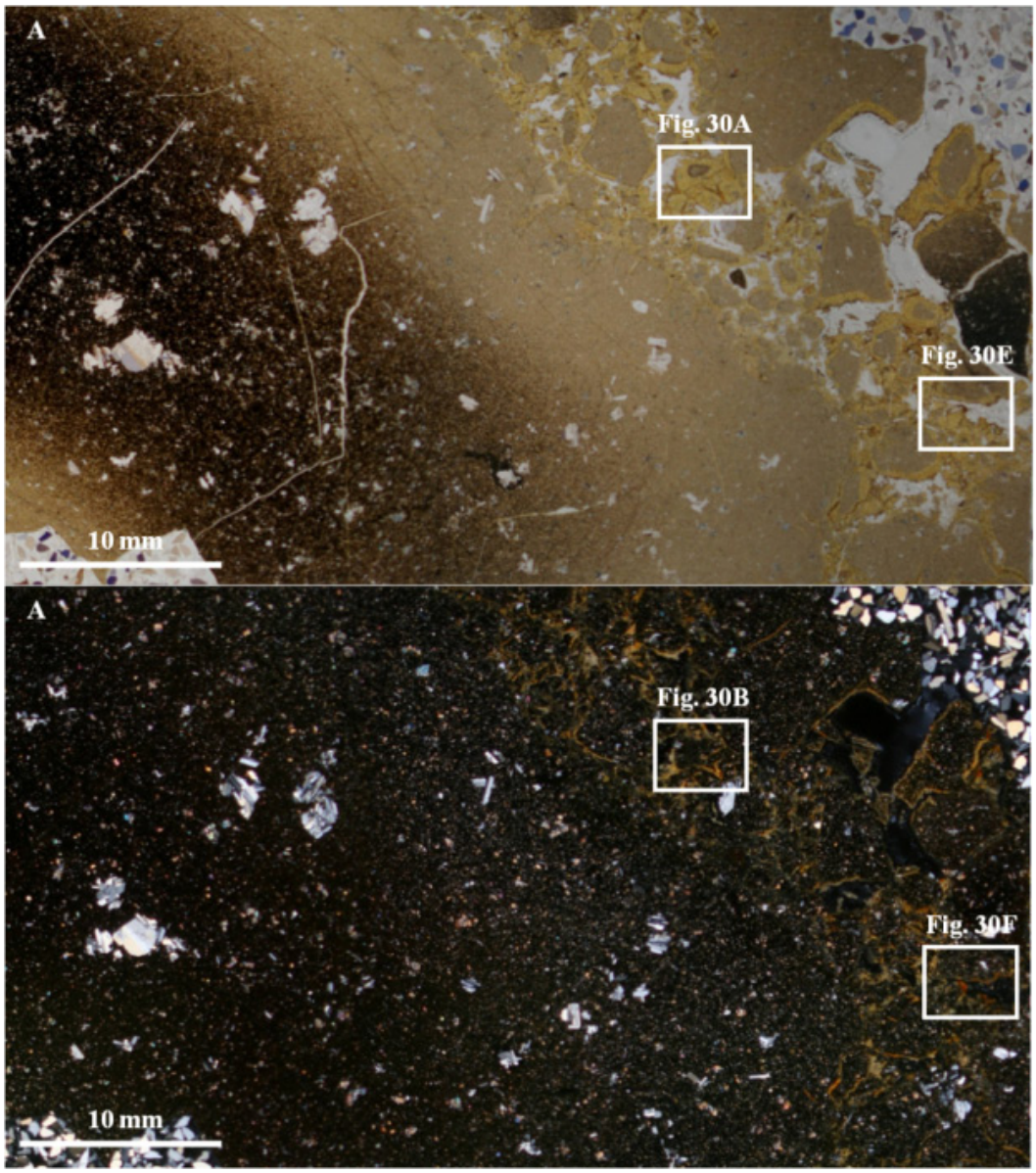

Figure 2.30. Plain- and Crossed-Polarized Light Context Images of Thin Section of Sample 10. Plain-polarized light (A) and crossed-polarized light (B) thin section mosaic images of sample Unknown 10 with outlines of close-up images shown in Figure 2.31 targeting main elements and matrix components of the sample. These include matrix cements and clasts.

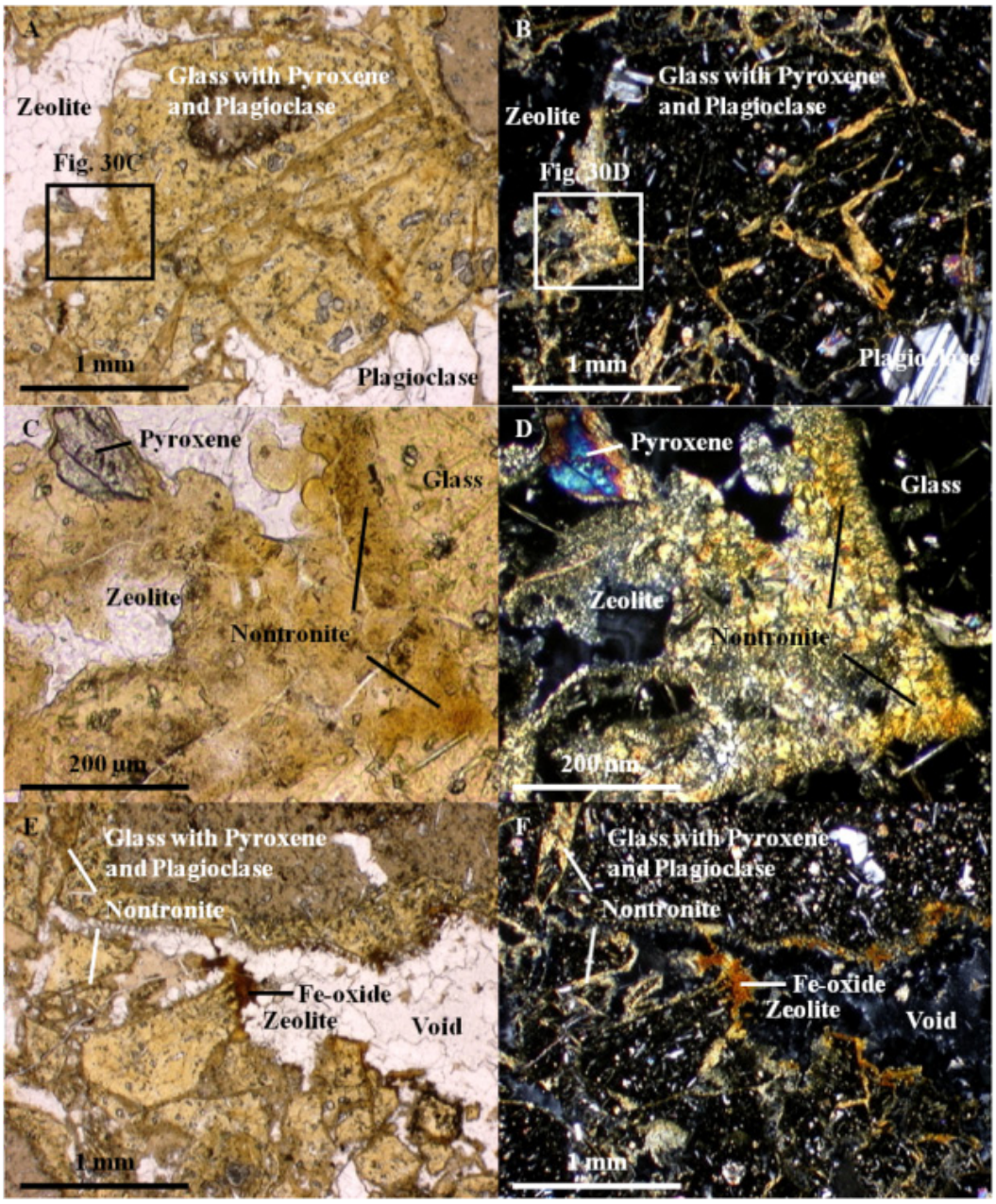

Figure 2.31. Plain- and Crossed-Polarized Light Images of Magnified Areas of Thin Section of Sample 10. Zoomed-in plain light (left) and crossed-polarized light (right) thin section images of Unknown 10 targeting main elements and matrix components labeled. These include matrix cements and clasts. Images C & D are close-ups of A & B to show the cross-cutting relationships of the cements to the clasts. The crossed-polarized images are slightly overexposed to bring out color variations between the first-order colors of zeolites, and clasts' glass matrix.

Table 2.4. Mineral Phases Identified with the MMI and Laboratory Methods

Mineral Phases Identified	MMI	VNIR	XRD	Thin Section
Vesicular Basalt (Sample 17)				
Olivine	X	X	X	X
Plagioclase Feldspar	X	X	X	X
Pyroxene	X	X	X	X
Glass				X
Silicic Volcanic Breccia (Sample 14)				
Plagioclase Feldspar			X	X
Quartz			X	X
Calcite		X	X	X
Goethite	X	X	X	Fe-oxide
Hematite	X	X	X	Fe-oxide
Celadonite	Hydrated Mineral	X		
Kaolinite	Hydrated Mineral	Hydrated Mineral	X	
Opal A	Hydrated Mineral	X		
Zeolite	Hydrated Mineral	X	X	X
Glass				X
Basaltic Volcanic Breccia (Sample 10)				
Olivine		X	X	
Plagioclase Feldspar			X	X
Pyroxene	X	X	X	X
Fe-oxides/oxyhydroxides	X	X		X
Nontronite	X	X	X	
Zeolite	Hydrated Mineral	Hydrated Mineral	X	X
Glass				X

X - Mineral phase detected

Table 2.5. Estimated Modal Abundances for Vesicular Basalt (Sample 17) Based on MMI End-Member Map and Thin Section

Sample Phases	MMI (62.5 µm/pixel)	Thin Section (62.5 µm/pixel)	Thin Section (9.5 µm/pixel)
Olivine	0.53%	0.85%	0.97%
Plagioclase Feldspar	9.29%	13.66%	14.57%
Pyroxene	1.58%	15.16%	17.01%
Matrix	88.65%	70.33%	67.45%

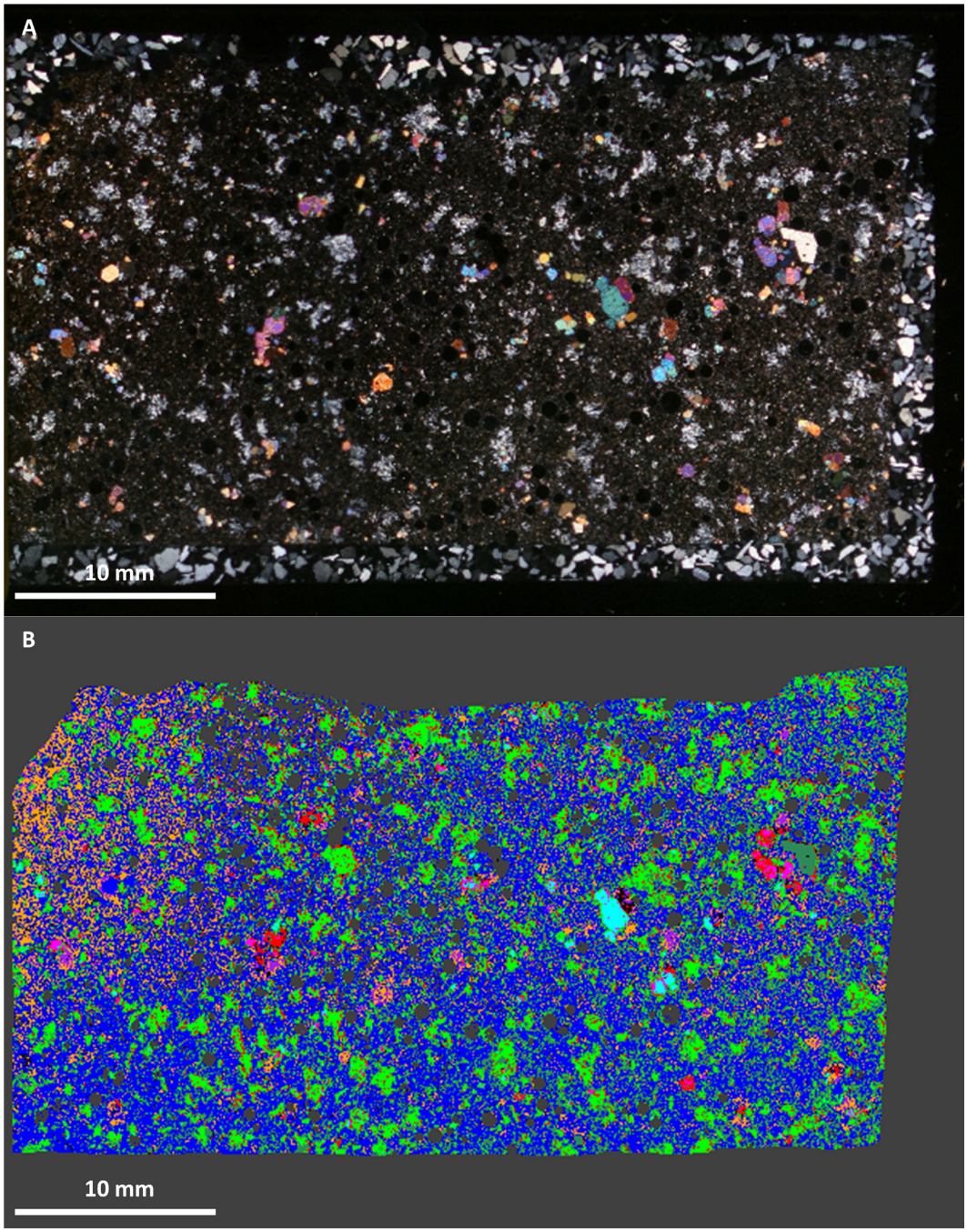

Figure 2.32. Thin Section images of Sample 17 resized to MMI spatial resolution to estimate modal abundances. A: Crossed-polarized light thin section image of sample 17 (same as in Figure 2.15B) resized to MMI spatial resolution of 62.5 µm/pixel. B: Supervised classification of thin section image (A) identifying different phases from which modal abundances in Table 2.5 were estimated: olivine (light blue); plagioclase feldspar (light green); pyroxene (red, magenta, orange, purple); matrix (dark blue, dark green).

2.6. Discussion

2.6.1. Comparison of MMI Results to Laboratory Results

2.6.1.1. Vesicular Basalt (Sample 17)

Sample 17 was a great example to test the performance of the MMI with Mars relevant igneous rocks of mafic composition, and to highlight strengths and weaknesses of the instrument. Overall, the MMI results appear to be consistent with the laboratory results for sample 17. The MMI images faithfully resolved the major microtextural features of the sample (as small as 200 μm, i.e. at least 3 pixels), while the application of spectral end-member mapping revealed all major spectral (i.e. mineral) components (see Table 2.4). MMI spectra were most useful in detecting and distinguishing major and minor phases that exhibit diagnostic absorption features within the MMI wavelength range and resolution, namely features associated with electronic processes from Fe^{2+} in pyroxene and olivine, between 0.9 μm and 1.0 μm and those associated with plagioclase feldspars between 1.2 μm and 1.3 μm (Clark 1990; Burns 1993). These minerals were identified in the laboratory VNIR spectra (Figure 2.13), XRD diffractogram (Figure 2.14) and in thin sections (Figures 2.15 and 2.16), supporting the MMI-based interpretations (see Table 2.4). These minerals were also successfully located and mapped in the sample. Additionally, the MMI was effective in mapping zonation within some of the larger pyroxene and olivine phenocrysts, showing olivine crystals being replaced by pyroxene during crystallization (Figure 2.10)

based on the change in shape of the curve and width in the 1.05 μm feature (Figure 2.11). Interestingly, while the laboratory VNIR observations of the largest zoned phenocryst in the MMI image was consistent with olivine (Figure 2.13), the pyroxene component identified by the MMI observation could not be detected in the laboratory spectrum due to the lower spatial resolution.

The identification of the matrix (i.e. groundmass) in sample 17 proved to be challenging because of the fine grain size (each mineral grain < pixel size of 62.5 μm, thereby resulting in a non-linear composite spectrum for each pixel from an intimate mixture). However, the relatively flat spectrum with a weak absorption feature at 1.05 μm proved to be consistent with the library spectrum for basalt. Determining the composition of the matrix was not possible at the MMI wavelength range and resolution, except for the presence of pyroxene or olivine. This required the higher resolution possible by combining petrography with XRD.

Comparison of modal abundances of major phases identified using the MMI and thin section petrography (Table 2.5, Figure 2.32) also highlight some of the challenges of identifying fine-grained mineral components using the MMI and potential biases it can cause in estimating mineral abundances of a rock. Analysis of the MMI end-member map (Figure 2.10D) and threshold mapping of a digital 3-color (RGB) image of a petrographic thin section (Figure 2.15B, Figure 2.32) of sample 17

resulted in different estimated modal abundances based on the percent area covered by each phase (Table 2.5). The MMI end-member map (Figure 2.10D) resolution is at 62.5 μm/pixel while the thin section image (Figure 2.15B) resolution is at 9.5 μm/pixel. To provide a more direct comparison to the MMI, the thin section image was also resized to the MMI pixel scale (Figure 2.32, Table 2.5). While the MMI modal abundances only differed from the estimated thin section (high resolution – 9.5 μm/pixel) abundances by approximately 0.4% to 5% for olivine and plagioclase feldspar components respectively, they differed significantly more by approximately 15% and 21% for pyroxene and matrix components respectively. The difference in values improve when the MMI abundances are compared to the thin section image resized to the MMI spatial resolution (Figure 2.32, Table 2.5). However, the MMI values for pyroxene and matrix components still differ from the thin section values by approximately 13% and 18% respectively. A portion of the imprecision may be due to natural grain size variation within a sample. However, most of the discrepancy may be due to the coarser spatial resolution of the MMI allowing for only the coarse grains to be considered in the estimation. The discrepancy between the thin section image at the same spatial resolution as the MMI may be accounted by the fact that the fine-grained mineral components in the matrix are better identified in the thin section image compared to the MMI image.

2.6.1.2. Silicic Volcanic Breccia (Sample 14)

Sample Unknown 14 also proved to be a great example to test the performance of the MMI and highlight strengths and weaknesses of the instrument. Overall, MMI results were consistent with laboratory analyses for sample 14 (see Table 2.4). The MMI images faithfully resolved the major microtextural features of the sample (particle grains as small as 200 μm – i.e. fine sand), while the application of spectral end-member mapping revealed most major mineral components (see below for phases not identified). The MMI was most effective in detecting and distinguishing major and minor phases that exhibited diagnostic absorption features associated with electronic processes due to Fe^{3+} at ~0.9 μm (associated with iron oxides and oxyhydroxides, see Clark 1999) and vibrational stretching overtones resulting from OH and combination overtones of H_2O at ~1.4 μm (due to hydrated minerals). As a result, the MMI was most effective in detecting and distinguishing major and minor iron-bearing phases (e.g. hematite vs. goethite) in sample 14, as well as detecting the presence of hydrated minerals. These phases were confirmed in laboratory VNIR spectra (Figures 2.20 and 2.21) and with XRD diffraction analysis (Figure 2.22), supporting the MMI results. These minerals were also successfully mapped in the sample, establishing paragentic relationships with iron oxide cements precipitating first. These relationships established with MMI data were confirmed by petrographic thin section analysis (Figures 2.23 and 2.24).

Where spectra lacked diagnostic absorption features, the microtextural information provided by MMI images, and inferred paragenetic relationships of spectral end members provided useful constraints for estimating the types of minerals that might be present. For example, in sample 14, the blue spectral end-member was clearly a cementing mineral that exhibited a relatively flat undiagnostic spectrum within the MMI wavelength range and resolution. However, the lack of an absorption at 1.43 μm eliminated hydrated minerals, thereby narrowing the list of candidate minerals to non-hydrated cements, like carbonates (e.g., calcite), anhydrous evaporites (e.g. anhydrite), or quartz. In the next analytical steps, laboratory analyses (including VNIR, XRD, and petrography) clearly identified calcite as the cement (also see Table 2.4). Even though the spectral range of the MMI was unable to capture absorptions for calcite in the short-wave infrared, namely the paired features at 2.3 and 2.5 μm (see Figures 2.7F, 2.8F, 2.20 and 2.21), the synergy with other more definitive mineralogical techniques, like XRD and VNIR/SWIR, which are instruments likely to be included with the MMI in future payloads, enabled reasonable connections to be made, even for methods like XRD where the spatial context is lost during sample preparation, or using spectral methods that produce composite spectra due to large analytical spot sizes. Extending the number of MMI bands and spectral range to 2.5 μm could improve these constraints.

Identification of the fine grained minerals and volcanic glass comprising the groundmass of clasts in sample 14 was the most difficult challenge for MMI spectral analysis with this sample. The first challenge was the very fine-grained nature of the groundmass, with crystals being smaller than the MMI pixel size of 62.5 μm. This resulted in a non-linear composite spectrum for each pixel due from intimate mixing. The second challenge was that the minerals in the groundmass, ultimately identified as predominantly quartz and plagioclase feldspar by XRD and petrography, do not exhibit diagnostic absorption features within the VNIR range and more specifically, within MMI wavelength range and resolution (see Figure 2.18; Table 2.4). The absorptions present at 0.884 and 1.43 μm suggested the presence of both hematite and a hydrated mineral. But given the microtextural context, these minerals could have been alteration products. The clast shapes and fine-grained microtexture, as well as the poorly sorted, clast-supported fabric indicated a minimal to no transport environment for the clasts (see Figure 2.17). Comparison of the bulk spectrum for clasts and library spectra suggested a potential match with rhyolite, based on the overall shape of the curve (Figure 2.18). Certainly the lack of absorption features associated with Fe/Mg-bearing mafic silicate minerals, and the light-toned color of the clasts, was consistent with a felsic or intermediate composition. However, this was not a definitive line of evidence due to the lack of diagnostic absorption features. The composition of the clasts was only confirmed later by lab analysis

using XRD and petrography (Table 2.4). The shape and width of the 1.43 μm in the green end-member spectrum of sample 14 was useful for eliminating hydrated sulfates as possible candidate minerals, since sulfates exhibit a broad absorption feature that encompasses both the 1.43 and 1.521 μm bands.

Lessons learned for sample 14 included a focused discussion of the optimal spatial resolution of the MMI. Field geologists who routinely analyzed rocks in the field using a handlens will attest to the fact that fine-grained rocks often pose a major challenge to petrogenetic analysis in the field. Sample 14 along with sample 17 highlighted this limitation for the MMI instrument as well. At the present spatial resolution of 62.5 μm/pixel, aphanitic volcanic rocks (like basalt and rhyolite) and fine grained sedimentary rocks, like siltstone or shale, can pose major challenges for the MMI, both in visualizing microtexture and in obtaining interpretable mineralogical spectra. While the first inclination would be to increase the spatial resolution to the maximum attainable within a realistic depth of field and working distance, there is more to consider. Experience suggests that 30-70 μm/pixel resolution represents an optimum range for resolving a majority of microtextural types and lithologies (i.e. fine sand and above, see for example Herkenhoff et al. 2003). On the other hand, at a scale of 10 μm/pixel or less, it is harder to define microtextural types, which provide a key observational step for inferring petrogenensis. The 30-70 μm/pixel resolution window is considered a “sweet spot” for field-based

microtextural analysis, building on more than a century of published petrogenetic observations as well as almost a decade of rover-based exploration of Mars (e.g, Herkenhoff et al. 2003).

2.6.1.3. Basaltic Volcanic Breccia (Sample 10)

Sample 10 was included to test the performance of the MMI as well as highlight some of the strengths and weaknesses of the instrument since similar lithologies have been previously studied as potential analogs for habitable hydrothermal environments on Mars (Warner and Farmer 2010). Overall, the MMI results obtained for sample 10 were consistent with laboratory results using pre-definitive analytical methods (Table 2.4). The MMI images faithfully resolved the major microtextural features of the sample (mineral grains as small as 200 μm – i.e. fine sand), while the application of spectral end-member mapping successfully captured all of the major mineral components. MMI spectra were most useful for detecting and distinguishing major and minor mineral phases that exhibited diagnostic absorption features within the MMI wavelength range and resolution, namely, those associated with electronic processes from Fe^{2+} at ~1.0 μm, associated with pyroxene, Fe^{3+} between 0.9 μm and 1.0 μm associated with iron oxides and oxyhydroxides, and vibrational stretching overtones of OH and combinational overtones of H_2O at ~1.4 μm, associated with hydrated minerals. In other words, the MMI was most effective for detecting and distinguishing between ferric and ferrous iron minerals present in the sample, as well as detecting hydrated minerals,

including the Fe-smectite mineral nontronite. These same minerals were subsequently identified in the laboratory VNIR spectra (Figure 2.28) and by XRD (Figure 2.29), directly supporting the MMI results (Table 2.4). In addition, MMI spectra pointed to hydrated phases, including phyllosilicates, opaline silica, and/or zeolites (e.g. chabazite and analcime) as secondary cements. The narrower 1.43 μm absorption feature was more consistent with hydrated phyllosilicates, opaline silica, and zeolites, like chabazite and analcime. In contrast, the absorption feature encompassing both the 1.43 and 1.521 μm bands was more consistent with a hydrated sulfate like gypsum or zeolites, like natrolite.

Thin section petrography of sample 10 (Figures 2.30 and 2.31) showed that spectral end member maps prepared from MMI data provided a basis for initial interpretations of paragenesis for major microtextural types and minerals in sample 10. This included the recognition of an alteration rind for a single basaltic clasts (blue end-member, Figure 2.25D) that was enriched in both pyroxene and/or hydrated mineral phases (magenta end-member). The fact that this alteration rind was seen in only one clast suggested a mixing of clasts with slightly different paragenetic histories. Thin section observations confirmed the presence of the alteration rinds and were consistent with an enrichment of the rind in hydrated minerals (possibly as hydrated glass). The secondary, pore-filling cements comprising the orange end-member in the spectral map for sample 10 (Figure 2.25D), were interpreted to be a mixture of pyroxene

with Fe-oxides/hydroxides and hydrated minerals, specifically nontronite, based on spectral shape. Thin section observations revealed that nontronite and fine-grained Fe-oxides/oxyhydroxides (possibly ferrihydrite) were present as early paragenetic pore-lining cements coating pore spaces between clasts, followed in paragenesis by pore-filling zeolites (Figures 2.30 and 2.31). At the spatial scale of the MMI pixel size (62.5 μm/pixel), these relationships between cement phases were not possible to reliably establish and interpretations were based on composite spectral signatures. However, the end- member locality is consistent with thin section observations for the mixed materials. In some instances, the material size is large enough that it can generate a less mixed spectrum as in the case of the red and green end-members (Figure 2.25D). The spatial correlation of these end- members as predominantly space-filling material between clasts is consistent with thin section observations. This example highlights some of the spatial and spectral limitations of the MMI instrument, but also demonstrates the capabilities of the instrument to provide enough mineralogical information (Table 2.4) within a microtextural context to inform back-looking re-interpretations based on higher resolution mineralogical information from XRD, or spot VNIR to place specific phases within a paragenetic framework.

2.6.2. Comparison of MMI to Current Micro-Imagers

The Microscopic Imager (MI) on the Mars Exploration Rovers (MER) demonstrated the value of microtextural imaging for planetary

missions (Herkenhoff et al. 2003, 2004); the capability form microscale imaging is now considered essential for follow-on landed missions (MEPAG ND-SAG 2008). While successful, the MI lacks the ability to provide color information (see Table 2.2). Efforts to include color information with MI images have proven somewhat successful by merging MI images with low-resolution color information from PanCam images of similar targets. This has allowed investigators to extract some color and spectral information from microtextural features at the MI scale (e.g., Herkenhoff et al. 2004; Weitz et al. 2010) but with low spatial resolution, when translating spectral information to the MI imaging scale.

The Robotic Arm Camera (RAC) on the Phoenix mission provided color imaging through use of specific red, green and blue light-emitting diodes (LEDs), with a CCD focal plane array (Keller et al. 2008; see Table 2.2). This presented the first opportunity for imaging of soils and small clasts in color at the microscale on Mars, as well as individual pixel scale analysis.

The Mars Hand Lens Imager (MAHLI) on the Mars Science Laboratory (MSL) will also provide color imaging using a CCD detector; however, with an RGB Bayer Pattern filter arrangement, similar to a digital camera (Edgett et al. 2009; see Table 2.2). White light LEDs provide additional lighting under dark conditions, while long-wave ultraviolet (UV) LEDs will be used to search for fluorescent materials. This arrangement will provide color information at the microscale, but not at the individual

pixel scale as each individual pixel in a Bayer Pattern arrangement has a red, green, or blue color filter.

Color imaging at the microscale, comparable to a geologist's hand lens, provides a wealth of information to enable the trained field geologist to quickly infer mineralogy based on the color and shape of mineral grains, as well as their organization into discrete microtextural domains. As noted previously, this approach is challenged by fine grained rocks below the typical spatial resolution of a 10X to 20X hand lens. The Multispectral Microscopic Imager (MMI) advances the capabilities of current micro-imagers (see Table 2.2) by employing multispectral capabilities employed normally by panoramic cameras (see Table 2.3 for comparison), like the MER Panoramic Cameras (PanCam) (Bell et al. 2003), to: 1) create microscale multispectral images (62.5 μm/pixel) and 2) extend the spectral range from 1.0 to 1.75 μm. By increasing the number of bands and extending the spectral range into the near infrared, the MMI can create multispectral images in the visible/near-infrared, while distinguishing a wide variety of minerals otherwise unresolved in the visible range. The samples discussed in this paper highlight the benefit of extending the spectral range into the near infrared, and using the spectral information of each pixel to 1) natural color images (Figures 2.10A, 2.17A, and 2.25A), and false-color composite images (Figures 2.10B, 2.17B, and 2.25B), to map spectral end members in relationship to microtextural domains in a sample (Figures 2.10D, 2.17D, and 2.25D), and to compare these spectral

end-members with published spectral libraries to begin to interpret mineralogy (Figures 2.11, 2.18, and 2.26). These capabilities are unmatched by other color imagers (see Table 2.2 and 2.3) and would significantly advance the science of future missions by improving field-based petrogenetic interpretations.

2.6.3. Applications to Mars exploration

Over the past decade of Mars exploration, observations by landed and orbital spacecraft have revealed a rich mineralogic record of aqueous deposition and alteration on Mars that complements preexisting geomorphic data, and offering tantalizing clues of many ancient habitable environments (e.g., Christensen et al. 2001, 2005; Squyres et al. 2004; Bibring et al. 2006; Squyres et al. 2008; Murchie et al. 2009). These investigations have now identified several major mineral groups that are the products of water/rock interactions (e.g., phyllosilicates, sulfates, Fe-oxides, carbonates, halides, and hydrated silica, etc.), which form over a broad range of environmental conditions on Earth that support life (e.g., Christensen et al. 2001, 2005; Langevin et al. 2005; Bibring et al. 2006; Bishop et al. 2008; Milliken et al. 2008; Mustard et al. 2008; Osterloo et al. 2008; Poulet et al. 2008; Ehlman et al. 2009; Ruff et al. 2011). Many of these environments appear to be favorable for the capture and long-term preservation of fossil biosignatures (Farmer and Des Marais 1999). With such discoveries, our understanding of the history of the surface of Mars and its composition has grown by leaps and bounds. The reliable

identification of sites where habitable conditions existed in the past is now possible and the latest Planetary Decadal Survey for the decade 2013-2022 has deemed the first step in a Mars Sample Return (MSR) campaign at the end of the decade to be the highest priority Flagship mission (NRC 2011). One concept for an MSR mission suggests a two step scenarios with a caching rover landing first to explore a high priority astrobiological site and conduct detailed in situ scientific investigations employing a suite of arm and rover-body mounted instruments. Over the period of the mission, the rover would collect and cache a suite of carefully selected rock cores and regolith samples for potential return to Earth (MEPAG ND-SAG 2008; MEPAG MRR-SAG 2009; NRC 2011). Critical capabilities identified for the caching rover to successfully achieve the desired mission objectives include arm-mounted instruments, capable of interrogating the abraded surfaces of rocks to create co-registered 2-D maps of microtexture, major element geochemistry, mineralogy, and organic geochemistry (MEPAG ND-SAG 2008; MEPAG MRR- SAG 2009). Such spatially-correlated data sets are considered crucial for identifying the best candidates for caching through in situ petrogenetic interpretations, assessments past habitability and of the potential for preserving biosignatures. The MMI, with its ability to integrate microimaging with multispectral capabilities to create co-registered high resolution 2-D maps of microtexture with mineralogy, as illustrated by the examples discussed in this study, directly addresses some of the important measurement

requirements identified for the proposed sample caching mission to achieve the primary in situ science objectives for MSR (MEPAG ND-SAG 2008; MEPAG MRR-SAG 2009).

2.7. Future Work

Development of the MMI is ongoing. While the MMI is a very capable instrument in its current configuration, there is still room for improvement to make the MMI a more capable *in situ* instrument for future astrobiological missions to Mars. The next improvement is to miniaturize the instrument to achieve a more flight-like size and mass by upgrading to a smaller and more compact camera and illumination system. These improvements will reduce the size and mass of the instrument to be comparable to similar arm-mounted microimagers, such as the MI on MER and MAHLI on MSL. The second improvement will be to increase the spatial resolution of the optical system from 62.5 μm/pixel to 30 μm/pixel, comparable to the MI on MER. This improvement will enable the instrument to resolve individual grains and microtextural features as small as ~100 μm (equivalent to fine sand). At this scale it is still not possible to resolve individual cells, but is sufficient to resolve most biologically-mediated microfabrics (see Farmer 2000). Furthermore, given the fixed size of the MMI FPA, the 30 μm/pixel resolution provides a reasonable compromise between high spatial resolution, field of view, and depth of field. This compromise is necessary to maintain adequate focus when imaging natural rough surfaces, to provide adequate spatial coverage to

recognize discrete microtextural elements in support of petrogenetic interpretations, and to accurately place MMI images within larger context images from a mast-mounted camera. The third improvement involves the addition of ultraviolet (UV) LEDs, which would enable the detection of fluorescent materials, including many minerals and potentially, organic materials. Specifying the spatial location of organics within a rock's microtextural framework would be very useful for astrobiology in identifying which part of a sample should be subsampled for onboard organics analysis, as well as identifying the best samples to cache for sample return. The fourth improvement would be to increase the number of spectral bands to improve spectral resolution, and to extend the spectral range into the infrared region between 1.8 and 2.5 μm. This extension of spectral range would enhance the ability of the MMI to detect important aqueous mineral groups, including sulfates, carbonates, zeolites and clay minerals. An increase in the number of spectral bands would provide a modest increase in science capability with little additional penalty in mass, power and cost. However, while extending the detection range beyond 1.8 μm would provide a significant increase in instrument capability, it would come with a significant penalty in mass, power consumption and cost. For example, replacing the un-cooled InGaAs detector with a HgCdTe detector would extend the spectral detection range from 1.8 to 2.6 μm, but would require a substantial increase in mass and power consumption by requiring active cooling of the detector using a

thermoelectric cooler (TEC). While this may not be an issue with instruments that are housed inside a rover body, it can be limiting for contact instruments that are mounted on a robotic arm, where mass is highly constrained. Work is being done to identify the best compromise for balancing scientific capabilities, against mass, power and cost constraints.

2.8. Conclusions

The Multispectral Microscopic Imager (MMI) is a new microimager that is being developed for future planetary rover missions. The MMI provides multispectral, microscale reflectance images of geological samples, where each image pixel is a visible/short-wave infrared spectrum ranging from 0.463 to 1.735 μm. This spectral range enables the discrimination of a wide variety of rock-forming minerals, especially Fe-bearing phases, and the identification and placement of hydrated minerals within a microtextural framework. The MMI advances beyond the capabilities of current microimagers such as the Mars Exploration Rover (MER) Microscopic Imager (MI) and the Mars Science Laboratory (MSL) Mars Hand Lens Imager (MAHLI), by extending the spectral range into the infrared, and increasing the number of spectral bands. The MMI design employs multispectral light-emitting diodes (LEDs) and an un-cooled Indium-Gallium-Arsenide (InGaAs) focal plane array to achieve the low-mass and high reliability (no moving parts) required for an arm-mounted instrument on a planetary rover. This study reports the results of a multi-year study of MMI capabilities by the analysis of 20 unknown samples,

pre-selected to represent Mars-relevant analog environments, including igneous and sedimentary rocks of interest to astrobiology. MMI data sets were used to obtain information about microtexture and mineralogy, and spectral end members were mapped to reveal the paragenetic relationships between minerals and microtextural elements comprising rock samples. These observations were used as a basis for initial interpretations of petrogenesis. The same sample suite was studied in the laboratory using higher resolution methods (hyperspectral visible/near-infrared spectroscopy, X-ray diffraction and thin section petrography) to establish ground truth for comparison and interpretations based on lab analyses compared to MMI-based interpretations. The comparative study showed that the MMI is capable of resolving the fine-scale microtextural features of samples color in images. In addition, the application of ENVI-based spectral end-member mapping successfully identified the distribution of Fe-bearing minerals (including silicates, oxides and oxyhydroxides), and the presence of hydrated minerals. End-member maps also reliably documented basic aspects of the paragenetic history and provided a robust basis for petrogenetic interpretations. These results demonstrated the value of the MMI for future *in situ*, rover-mediated exploration of Mars and the selection of Martian samples for onboard astrobiological analysis or sample return.

CHAPTER 3

EXPLORING THE MOON AT THE MICROSCALE: OBSERVATIONS OF APOLLO SAMPLES WITH THE MULTISPECTRAL MICROSCOPIC IMAGER

3.1. Introduction

Our understanding of the Moon has evolved significantly in the past 50 years. This understanding is grounded in telescopic, robotic and human exploration of the Moon during the late 1960s and early 1970s. As a result of the six Apollo and three Soviet Luna missions, we have an extensive collection of samples from the Moon. Detailed analyses of these well-documented collections, combined with those of lunar meteorites, have answered many fundamental questions about the origin and evolution of lunar rocks and soils and have provided essential “ground truth” for interpretations of recent remote sensing observations (e.g., see reviews by Wilhelms 1987; Heiken et al. 1991; Jolliff et al. 2006). Although the wealth of data from the Apollo era was substantial and can be used to address remaining questions, the limited spatial sampling significantly constrains our understanding of the distribution of rocks and soils on the Moon, their range of compositional diversity, and soil physical properties.

Since the Apollo-era formulation of lunar evolution, remote sensing missions (Galileo, Clementine, Lunar Prospector, and more recently Smart-1, Chandrayaan-1, and Lunar Reconnaissance Orbiter) and lunar meteorite studies revealed a lunar crust that varies both laterally and

vertically in composition, age, and mode of emplacement. Despite our knowledge of basic lunar minerals, we have an incomplete sampling of the lunar crust (e.g., Wilhelms 1987; Heiken et al. 1991;Robinson and Riner 2005; Jolliff et al. 2006; NRC 2007a), necessitating additional landed missions to sample and return lunar material of unexplored areas of Moon, such as the South Pole-Aitken basin in the far side of the Moon (e.g., NRC 2007a).

To maximize their scientific return, future robotic and human missions to the Moon will need to have *in situ* capabilities to enable the selection of the highest value samples for return to Earth, or for analysis in laboratories on the Moon. To accomplish this task efficiently, samples need to be characterized using a suite of robotic instruments that provide crucial information about elemental composition, mineralogy, and microtexture. Such spatially-correlated data sets, which place mineralogy into a microtextural context, are considered crucial for correct petrogenetic interpretations. Multispectral, visible-to- near-infrared microimages from a microscopic imager could provide valuable context information for evaluating the spatial (and implied temporal) relationships between constituent mineral phases that have been characterized by more definitive mineralogical methods (e.g. X-ray diffraction) which lack context information. Microimaging could also provide highly desirable contextual information for guiding the subsampling of rocks for additional analyses with other *in situ* instruments or caching for potential return to Earth.

The Multispectral Microscopic Imager (MMI) multispectral, microscale reflectance images (See Table 2.1 for a list of band centers) enable the discrimination of a wide variety of rock-forming minerals, especially Fe-bearing phases, within a microtextural framework.

This chapter provides an overview of recent observations and interpretations of lunar samples using the MMI deployed in a nitrogen glovebox in the Lunar Experiment Laboratory at NASA's Johnson Space Center. The goal of this study is to assess the value of the MMI as a tool for lunar exploration. Toward this end, we used the MMI instrument to image 18 lunar rocks and four soils, selected from a reference suite that spanned a diverse range of compositions found in the Apollo collection. To assess the effectiveness of MMI for identifying petrogenesis of lunar rocks and soils, MMI-based petrogenetic interpretations were compared with results published in the literature. The data sets obtained reveal *in situ* capabilities in an environments that simulates actual mission applications to support human exploration of the moon

3.2. Methods

3.2.1. Suite of Samples Used for Test and Setup

A reference suite of 18 lunar rocks and 4 soils, spanning a broad compositional and petrographic range found in the Apollo collection, was selected by The Johnson Space Center Astromaterials Acquisition and Curation Office (JSC Curation) specifically to support MMI instrument development and testing (Allen et al. 2009, 2010). These samples were

characterized in detail as a part of previous curatorial efforts and science investigations. The results of these earlier investigations are summarized in The Lunar Sample Compendium, published on-line at http://www-curator.jsc.nasa.gov/lunar/compendium.cfm. Table 3.1 lists the samples used in the reference suite and analyses done with the MMI.

The MMI observations of the Apollo samples marked a first step in evaluating the utility of the instrument as a tool for quickly assessing and prioritizing lunar samples for *in situ* analysis, or Earth return. We also assessed the first field-portable, tripod-mounted version of the MMI instrument (Sellar et al. 2008; Nuñez et al. 2009, 2010). The MMI was transported to the Lunar Experiment Laboratory at NASA's Johnson Space Center (Allen et al. 2009, 2010; Nuñez et al. 2009, 2010) and deployed inside a room temperature, nitrogen-filled glove box (Figure 3.1). The instrument was then used to image each of 18 lunar rocks and four soils comprising a reference suite that spanned a diverse range of compositions in the Apollo collection (Allen et al. 2009, 2010; Nuñez et al. 2009, 2010).

Table 3.1. Lunar Samples Imaged with the MMI

Samples Imaged by MMI	Parent Sample	Apollo Mission	Station/Landmark[1]	Rock Type[1]	Description[1]
Rocks					
10017,30	10017	11	LM	Basalt	High Ilmenite Basalt
10048,203	10048	11	LM	Breccia	Regolith Breccia
12002,492	12002	12	LM	Basalt	Olivine Basalt
12052,26	12052	12	Head Crater	Basalt	Pigeonite Basalt
14310,220	14310	14	G	Breccia	Impact Melt Rock
14311,23	14311	14	D	Breccia	Crystalline Matrix Breccia
14321,88	14321	14	C1	Breccia	Clast-rich Crystalline Matrix Breccia
15015,226	15015	15	8	Breccia	Regolith Breccia
15459,53	15459	15	7	Breccia	Glass-matrix Regolith Breccia
15555,62	15555	15	9A	Basalt	Olivine-normative Mare Basalt
15556,111	15556	15	9A	Basalt	Vesicular Mare Basalt
15565,131	15565	15	9A	Breccia	Regolith Breccia
60025,174	60025	16	LM	Anorthosite	Ferroan Anorthosite
61016,484	61016	16	1	Breccia/Anorthosite	Impact Melt Rock with Shock/Melted Anorthosite Cap
64435,95	64435	16	4	Breccia	Breccia with Glass Coat
66095,146	66095	16	6	Breccia	Impact Melt Rock with rusted grains
70215,312	70215	17	LM/SEP	Basalt	Mare Basalt
73255,27	73255	17	3	Breccia	Aphanitic Impact-melt Breccia
Soils					
10084,27	10084	11	LM	Soil	Bulk soil sample; Fines < 1 mm; Fe-rich
14163,179	14163	14	LM	Soil	Bulk soil sample; Fines < 1 mm
64501,12	64500	16	4	Soil	Bulk soil sample; Fines < 1 mm; Al-rich
75081,14	75080	17	5	Soil	Bulk soil sampe; Fines < 1 mm; Fe-rich

[1.] Sources: Lunar Sample Catalog and Lunar Science Conpendium

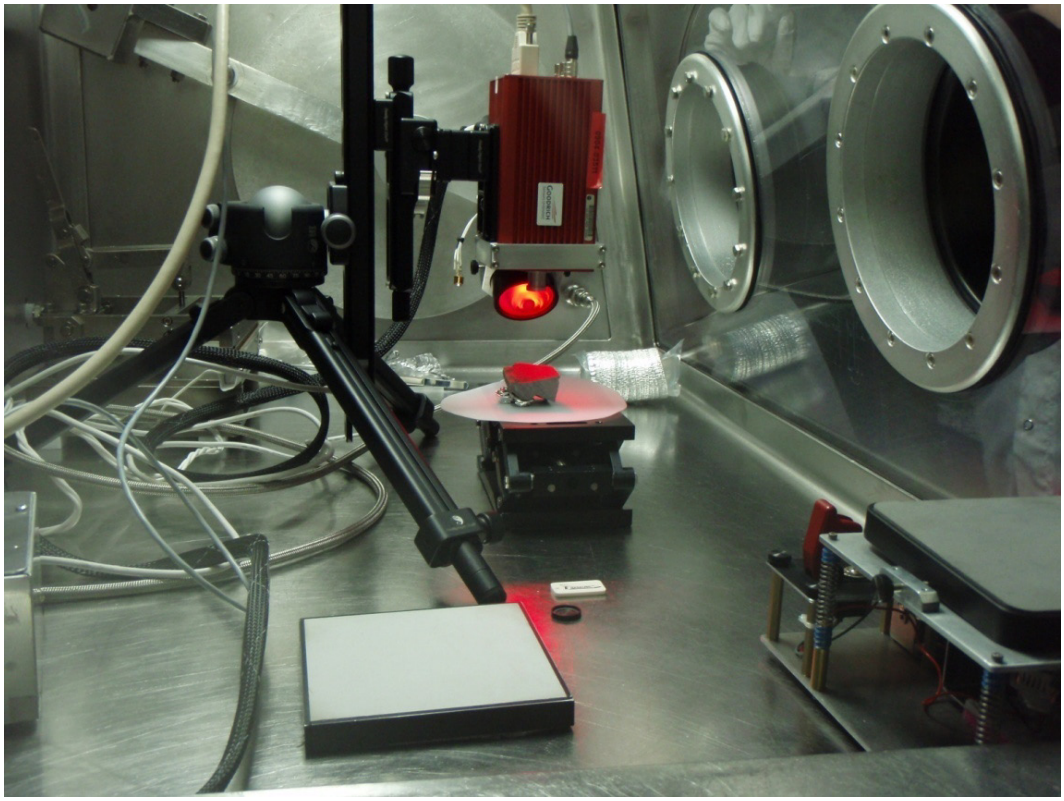

Figure 3.1. Image of the Multispectral Microscopic Imager (MMI) in Glovebox at the Lunar Receiving Laboratory. MMI shown with field-portable, tripod-mounted, un-cooled Indium-Gallium-Arsenide (InGaAs) focal plane array (FPA) camera (red) and illumination device (black), i.e. illuminator, containing 21-band multi-wavelength light-emitting diode (LED) illumination array deployed in a N_2-filled glovebox at the Lunar Receiving Laboratory at NASA's Johnson Space Center.

3.2.2. Instrument Description

A detailed description of the version of the Multispectral Microscopic Imager (MMI) used to acquire the datasets discussed in this report may be found in Núñez et al. (2012; manuscript in review). In brief, the MMI system used consists of a field-portable, tripod-mounted, camera outfitted with an uncooled Indium- Gallium-Arsenide (InGaAs) focal plane array (FPA) and a 21-band multi-wavelength light-emitting diode (LED) illumination array. The LED array illuminates the geological samples in 21 separate wavelengths to generate multispectral, microscale, reflectance images, where each pixel of an image consists of a spectrum ranging from the visible (0.463 μm) to the short-wave infrared (1.735 μm) (Figure 3.1; Table 2.1). The InGaAs FPA consists of 640 x 512 pixels, which along with a slow focal ratio lens (F/10), results in an instantaneous field of view (IFOV) of 62.5 μm/pixel and a 40 mm x 32 mm field of view (FOV), at a distance of 63 mm from the lens to the sample. The resulting IFOV of 62.5 μm/pixel was a tradeoff that balances the desire to maximize depth of field (5 mm) suitable for imaging natural surfaces with significant microtopography (Sellar et al. 2006; Nuñez et al. 2009), while retaining a large enough FOV to accurately place MMI images into larger context images acquired with other instruments. This tradeoff enabled the successful imaging of the majority of the microtextural elements in the lunar samples, with good focus over the entire FOV and with no sample

preparation requirements, or the need for step-integrated image mosaics obtained at different working distances.

3.2.3. Data Acquisition and Calibration

Data acquisition and calibration is described in more detail in Núñez et al. (2012; manuscript in review). In brief, MMI-generated 21-band dark-subtracted images of samples, as well as a 50 % reflectance Lambertian Spectralon standard (produced by Labsphere) under low ambient illumination. Next, automated routines written in the Interactive Data Language (IDL) program (sold by ITT Visual Information Solutions) were utilized to replace bad pixels in each image, and to apply a flat-field correction and calibration for each sample image. Subsequently all co-registered sample images were stacked together along the 3rd axis (wavelength dimension) to form an image data cube. The bad pixels were corrected by replacing each bad pixel with a mean of nearby pixels, weighted by the distance of the nearby pixel from the bad pixel. Each wavelength target image was flat-fielded and converted from raw DN to reflectance using the respective wavelength image of the 50% reflectance Spectralon standard. The calibrated images were co-registered and stacked together along the 3rd axis (wavelength dimension) to form an image data cube with spatial coordinates (X, Y) and wavelength in the third dimension (Z). Accordingly, each pixel contained a spectrum of 21 bands ranging from the visible (0.463 μm) to the short-wave infrared (1.735 μm).

3.2.4. Color Imaging and Spectral Analysis

MMI multispectral images were processed and analyzed using the remote sensing and image analysis software package, ENVI (Environment for Visualizing Images), a commercial software package sold by ITT Visual Information Solutions. Prior to applying band ratios, spectral parameters, or analyzing the spectral data, masks were applied to remove or minimize effects of shadows, specular surfaces, and the background FOV.

3.2.4.1. Color Imaging

Visible color bands 0.641, 0.522, and 0.463 μm were used, respectively, to generate the RGB color composite images to simulate natural color, while other visible/infrared bands (ex. RGB: 1.43, 0.908, and 0.522 μm) were used to generate the visible/near-infrared color composite images. Each image employed a default linear stretch to enhance color differences. The RGB color composite images proved useful for highlighting compositional and textural differences within lunar samples.

3.2.4.2. Application of Spectral Parameters

Spectral parameters have been widely employed in the interpretation of multispectral data from landed, orbital, or telescopic observations of the Moon (e.g., Belton et al. 1992; Pieters et al. 1994, 1997, 2001; Dhingra 2008; and Borst et al. 2011) and Mars (e.g., McSween et al. 1999; Bell et al. 2000; Murchie et al. 2000; Morris et al. 2002; Farrand et al. 2007; and Pelkey et al. 2007). Useful parameters

include band ratios, spectral slopes, and depths of absorptions bands to map compositional variations in lunar surface materials.

For the present study, we employed a series of spectral parameters for highlighting spectral differences between broad lithologoc types, and to map specific mineral assemblages within the lunar samples. Included were two types of parameter sets that were extensively used by previous authors to map compositional variations on the Moon using data from the Solid-State Multispectral Imaging System (SSI) on the Galileo spacecraft and the ultraviolet-visible (UVVIS) camera on the Clementine spacecraft. Additional parameters were also applied to take advantage of the extended detection range provided by the MMI. The parameters used in the present study along with brief description, rationale and source are listed in Table 3.2.

Table 3.2. Spectral Parameters Used in this Study

Parameter	Description	Rationale	Source
Clementine UVVIS-derived Parameters			
756 nm / 463 nm ratio (Red Channel)	R756/R463	Favors spectra with steep continuum slope due to glasses and mature soils	Modified from Belton et al. 1992
756 nm / 970 nm ratio (Green Channel)	R756/R970	Favors minerals with Ferrous iron	Modified from Belton et al. 1992
463 nm / 756 nm ratio (Blue Channel)	R463/R756	Favors spectra with flat continuum slope or presence of opaques	Modified from Belton et al. 1992
Band Curvature (Red Channel)	R756/R908 + R1050/R908	Favors low-Ca pyroxene	Modified from Dhingra 2008
Band Tilt (Green Channel)	R908/R1050	Favors high-Ca pyroxene and/or olivine	Modified from Dhingra 2008
Band Strength (Blue Channel)	R1050/R756	Favors Fe-poor materials like anorthosite or mature soils	Modified from Pieters et al. 2001

The first parameter set consisted of band ratios similar to those employed by Belton et al. (1992) for data from the Solid-State Multispectral Imaging System (SSI) onboard the Galileo spacecraft. The same parameter set was later employed by Pieters et al. (1994) for analyzing data from the ultraviolet-visible (UVVIS) camera on the Clementine spacecraft. These parameters were chosen to bring out important mineralogical features of the lunar surface. Similar parameter sets were created using comparable MMI bands to highlight petrologic characteristics of the Apollo lunar samples imaged with the MMI in the present study and correlate with orbital data.

The “red channel” is the 756/463 nm ratio, which is analogous to the SSI 760/410 nm and the UVVIS 750/415 nm ratios. If the spectrum shows a steep continuum slope (i.e. background with steep slope), the ratio will be relatively high and the image will appear red. A steep continuum slope is characteristic of the spectrum for glass (e.g., Tompkins and Pieters 2010) or for mature soils, the latter showing increasing amounts of nanophase metallic iron ($npFe^0$) and agglutinates with time due to space weathering (McCord and Adams 1973; McKay et al. 1991; Hawke et al. 2001; and Taylor et al. 2001). Space weathering is a term used for a number of processes that affect the physical and optical surface properties of any airless body exposed to the harsh space environment. The optical changes associated with space weathering are largely initiated by two of these processes, micrometeorite bombardment and charged

particle irradiation. Both processes create nanophase metallic iron ($npFe^0$), nanometer-scale particles of metallic iron distributed in amorphous silicate, that has been vapor/sputter deposited on soil particle surfaces and inside agglutinates (McCord and Adams 1973; McKay et al. 1991; Hawke et al. 2001; and Taylor et al. 2001). Additionally, materials rich in plagioclase feldspar, or poor in iron will also be high in the red channel.

In contrast, the blue channel is the inverse of the ratio in the red channel (i.e., 463/756 nm ratio, which is analogous to the SSI 410/760 nm and UVVIS 415/750 nm ratios). Thus it is sensitive to flatter continuum slopes, characteristic of surfaces that have undergone less space weathering and which are characterized by lower abundances of nanophase Fe^0 and agglutinates, as in the case of an immature regolith. A flatter, or shallow, spectral slope also reflects the influence of opaque mineral phases, such as ilmenite (dark and flat spectrum) (Charette et al. 1974). Ilmenite is the dominant opaque mineral found in most lunar basalts (e.g., Papike et al. 1974). Thus, geological materials that appear blue in the image are typically glass-poor, as in immature regolith, or which have an abundance of ilmenite, as in TiO-rich basalts.

The “green channel” corresponds to the 756/970 nm ratio, which is analogous to the SSI 760/990 nm and UVVIS 750/950 nm ratios. The green channel is sensitive to the presence of FeO in silicate minerals and glasses. Absorption in the 1-μm region is caused by the presence of

ferrous iron (Burns 1982) and is stronger for Fe-bearing minerals or mafic surfaces seen in orbital data. The 1-μm absorption feature is weaker where there has been more space weathering (Pieters et al. 1993; Fischer and Pieters 1996). Thus, the green channel is brightest where there is a strong mafic absorption and little evidence of space weathering in the form of immature mafic soils, or Fe-rich minerals.

The MMI band ratio color composite images provide clear distinctions between mafic Fe-rich minerals, the presence of plagioclase and glasses, and the effects of space weathering in soils.

An alternative set of parameters was developed by Pieters et al. (1997, 2001), Tompkins and Pieters (1999) and later modified by Dhingra (2008) to investigate the rock types in and around the South Pole-Aitken Basin. This same parameter set was adapted by Borst et al. (2011) using Clementine UVVIS data. A similar parameter set was also obtained using MMI bands to map different minerals and rock types in Apollo lunar samples.

Three optical parameters have been used to characterize the type of mafic mineral present using Clementine UVVIS data are band strength, band curvature, and band tilt (e.g., Pieters et al. 1997). For the MMI, we utilized three shape-based parameters seen in absorption spectra of mafic rocks, focusing on the shape of the 1-μm absorption, to distinguish between different mafic-bearing rock types, such as anorthosite, norite and basalt/gabbro/troctolite.

The first parameter, band strength (bs), is approximated by the ratio 1000/750 nm and assigned to the blue channel in an RGB composite (Pieters et al. 1997 and 2001). In the case of the MMI bands, we used the 1050/756 nm band ratio. As the MMI does not have a 1000 nm band, the closest available was the 1050 nm band. The use of the 1050 band makes the ratio more sensitive to the presence of olivine. The ratio compares the intensity within the ferrous absorption to that outside the band at shorter wavelengths on the continuum. Band strength values are high for rocks with low ferrous absorption, such as anorthosites (Pieters et al. 1997 and 2001), or mature soils, which weakens the ferrous absorption due to space weathering (Tompkins et al.1997). Thus, Fe-poor materials like anorthosites, or mature soils will appear blue in an RGB composite (see below for other parameters).

The second parameter, band curvature (bc), describes the curvature along the 750–900–1000 nm range. The parameter is assigned to the red channel in an RGB composite (Pieters et al. 1997 and 2001). A high band curvature is characteristic of materials with abundant low-Ca pyroxene (orthopyroxene). In contrast, areas with abundant high-Ca pyroxene have a lower band curvature, while areas that are olivine-rich show little curvature. Pieters and co-workers (1997 and 2001) calculated the band curvature as an angular measurement between the reflectance values of 750 to 900 to 1000 nm (see Pieters et al. 2001 for description). Dhingra (2008) and later Borst et al. (2011) subsequently approximated

band curvature to consist of an additive combination of band ratios, namely: 750/900 nm and 1000/900 nm. The method by Dhingra (2008) has the advantage that it is able to capture the variation in the parameter in a similar way to that developed by Pieters et al. (1997 and 2001), yet it is simpler to calculate. We adopted the approach of Dhingra (2008), using the MMI bands 756, 908, and 1050 nm to calculate the parameter as 756/908 nm + 1050/908 nm. As a result, areas with abundant low-Ca pyroxene (noritic composition) appear red in RGB composite images.

The third parameter, band tilt (bt), is assigned to the green channel in the RGB composite and measures the change from the 900 nm band to the 1000 nm band. Pieters and co-workers (1997 and 2001) measured the change as a difference in reflectance from 900 nm to 1000 nm. Dhingra (2008) and later Borst and co-workers (2011) subsequently modified band tilt to the band ratio, 900/1000 nm. High values of this parameter reflect units that are characteristic of materials containing abundant high-Ca pyroxene and olivine, as these minerals exhibit high values of tilt with little curvature in their spectra. However, this parameter alone does not distinguish between the two minerals. Areas that appear green or yellow are thus interpreted to contain abundant high-Ca pyroxene and/or olivine and represent gabbroic/basaltic or troctolitic compositions. To calculate the band tilt, we used the approach by Dhingra (2008), taking the ratio of MMI bands 908 and 1050 nm.

Using the above approaches, MMI band ratio color composite images typically allow for clear distinctions between mafic Fe-rich minerals and rocks.

3.2.4.3. Identification of ROIs for End-member Extraction and Spectral Analysis

In combination with the spectral parameters listed above, we used the Minimum Noise Fraction transformation (MNF) function (Green et al. 1988) and Pixel Purity Index (PPI) algorithm (Kruse et al. 1993; Rowan et al. 2004) provided with the software ENVI to identify regions of interest (ROIs) from which representative spectra, i.e. “spectral end-members”, were extracted for spectral analysis. These end-member spectra were subsequently used to produce maps showing the distribution of these end-members in sample images using the Spectral Angle Mapper (SAM) supervised classification method also included with ENVI. The spectral end-members, which consisted of averages of 50 to 1000 pixels, were in some cases, single phases, but more often, consisted of mixed phase assemblages (particularly where fine-grained materials too small to resolve at the MMI pixel scale were present). End-members were most often associated with specific microtextural domains in samples and when mapped, helped define the both the microtexture and paragenesis of a rock. A more detailed description of the methods used to extract the end-member spectra, and to map the distribution of the end-members using the Spectral Angle Mapper (SAM) method in ENVI is given in Chapter 2.

Average spectra for each spectral end-member were next compared to library spectra from the USGS spectral library (Clark et al. 2007), as well as the Keck/NASA Reflectance Experiment Laboratory (RELAB) database (Pieters and Hiroi 2004). To identify best–fit minerals (or in some cases rocks) for each spectral end-member library spectra were convolved to the MMI wavelength range and resolution, using the Spectral Analyst tool in ENVI. The Spectral Angle Mapper (SAM) and Spectral Feature Fitting (SFF) methods within the Spectral Analyst tool were also used to rank the match of each end-member spectrum in relation to those included in the spectral libraries. The suggested spectral library matches were ranked in order of best-to-worst matches. Spectra of the suggested spectral library matches and spectral end-members were then visually compared, in order to identify the best-fit spectra based on absorption band center position and band width. Best matches considered not only single mineral(s), but also mineral group(s), mineral assemblages and whole rock spectra. Careful attention was given ensuring that the suggested matches “made sense” in relationship to the inferred rock origin, based on independent criteria, like geologic context, petrogenetic interpretations based on microtexture, and general composition, and considering the limitations of the wavelength range and resolution of the MMI.

3.3. Results

In this section we provide imaging results obtained with the Multispectral Microscopic Imager (MMI) of selected lunar samples from the reference suite of 18 lunar rocks and 4 soils, spanning a broad compositional and petrographic range found in the Apollo collection. MMI results are compared to previous interpretations of microtexture and mineralogy for similar lunar samples published in the literature and summarized in the Lunar Sample Conpendium (http://www-curator.jsc.nasa.gov/lunar/compendium.cfm). This comparison provides a basis for assessing the effectiveness and performance of the MMI in providing quick *in situ* petrogenetic interpretations of lunar samples at the hand lens scale, with little, or no sample preparation required.

3.3.1. MMI Observations of Apollo Sample 14321,88

The Apollo 14 astronauts returned 43 kg of lunar material from the Fra Mauro region, of which some “football-sized” rocks were collected (Swann et al. 1972a). The largest of these rocks was sample 14321, which came to be informally known as “Big Bertha” (Lunar Sample Conpendium). The sample was collected during the second EVA at station C1 near the edge of Cone Crater, which is a 370-m-diameter Copernican Age crater (Swann et al. 1972a) that provided access to the excavated Fra Mauro Formation (Swann et al. 1972a, 1977). The Fra Mauro formation is believed to be ejecta deposited from the Imbrium Basin (Eggleton 1964; Wilhelms 1970; Swann et al. 1972a, 1977). The Fra Mauro formation is

interpreted to have an approximate age of 3.85 Ga (e.g., Stöffler and Ryder 2001). Sample 14321 is a clast-rich, crystalline matrix breccia (Wilshire and Jackson 1972) with about 30% lithic and microbreccia clasts (Duncan et al. 1975a, 1975b; Grieve et al. 1975; Simonds et al. 1977) that is interpreted to be a piece of the Fra Mauro formation (e.g., Wilshire and Jackson 1972, Grieve et al. 1975; Swann et al. 1972a, 1977).

Figure 3.2 shows MMI color composite images, and RGB maps of spectral parameters adapted from Belton et al. (1992) and Dhingra (2008) for Clementine UVVIS data and the corresponding spectral end-member map of sample 14321,88 based on supervised classification with ROIs as input parameters. Included is a visible color RGB composite image composed of MMI bands 0.641, 0.522, and 0.463 μm (respectively), to simulate natural-color and a visible/near-infrared color RGB composite image composed of MMI bands 1.43, 0.908, and 0.641 μm (respectively), designed to bring out subtle color differences in materials resulting from spatial variations in mineral composition (Figures 3.2A & B). Figures 3.2C & D show RGB color maps using MMI bands which mimic the spectral parameters adapted from Pieters et al. (1994) and Dhingra (2008), respectively for Clementine UVVIS data. Figure 2F shows a spectral end-member map generated in ENVI using a supervised classification with ROIs (Figure 3.2E) as input parameters for mapping end-member distributions. The color maps of spectral parameters adapted from Pieters et al. (1994) and Dhingra (2008) for Clementine UVVIS data using MMI

bands were used, along with the Minimum Noise Fraction Transformation (MNF) function (Green et al. 1988) and Pixel Purity Index (PPI) algorithm (Kruse et al. 1993; Rowan et al. 2004) provided in ENVI, to identify ROIs from which spectral end-members could be extracted for spectral analysis and for generating a spectral end-member map. Figure 3.3 shows spectral plots for the corresponding end-member spectra, along with matching library spectra taken from the USGS and RELAB spectral libraries.

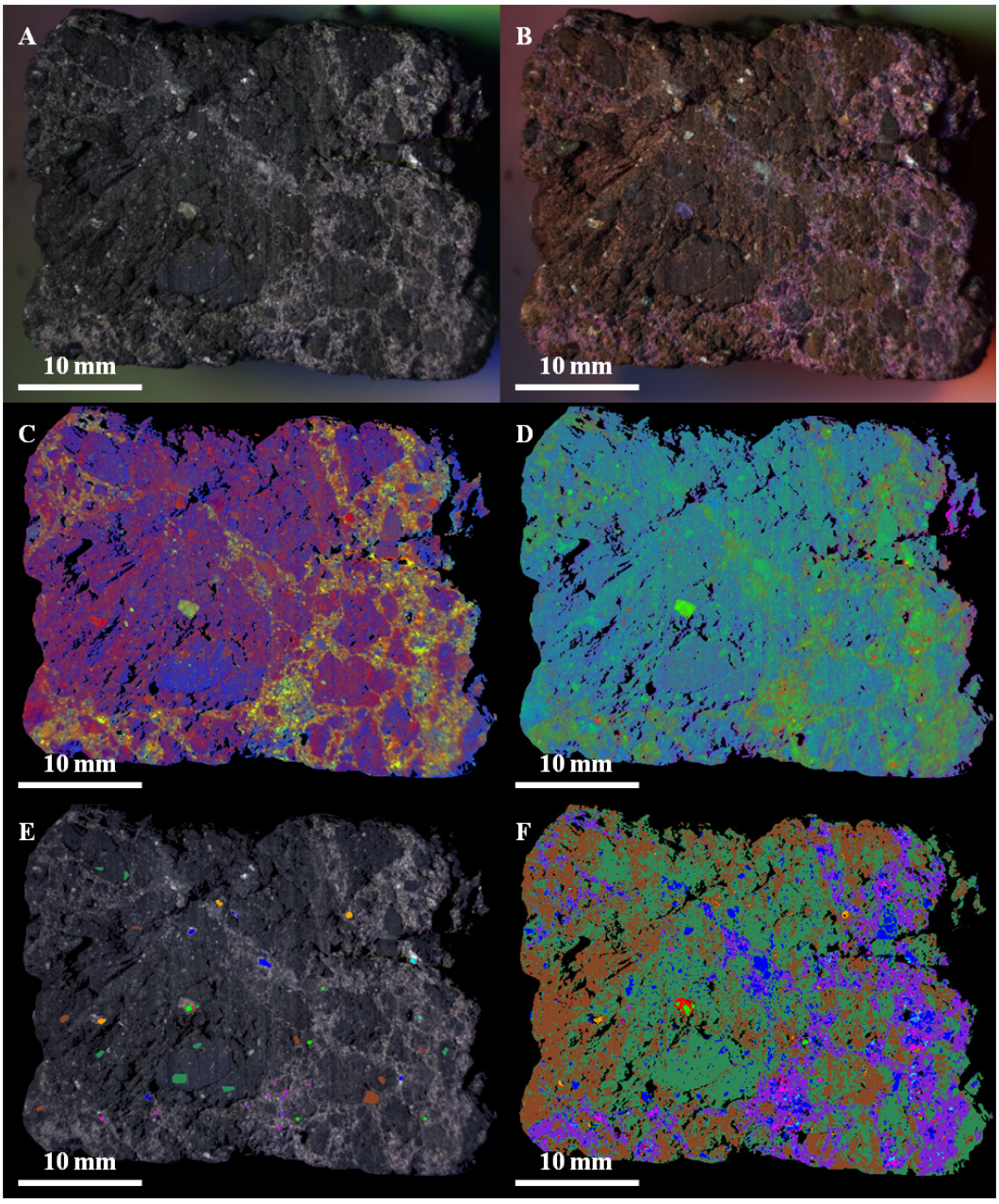

Figure 3.2. MMI-Generated Color Composite Images, Spectral Parameter Maps, and End-Member Map of Sample 14321,88. MMI-generated color composite images (A & B), RGB maps of spectral parameters adapted from Pieters et al. (1994) and Dhingra (2008) for Clementine UVVIS data (C & D) and corresponding spectral end-member map (F) based on supervised classification with ROIs as input parameters (E) of sample 14321,88. MMI Image size is 40x32 mm at 62.5 µm/ pixel. Figures A-B are linear stretched. Figure 3.2A: Visible-color RGB composite image composed of MMI bands 0.641, 0.522, and 0.463 µm respectively to simulate true-color. Figure 3.2B: False-color RGB composite image

composed of MMI bands 1.43, 0.908, and 0.641 μm respectively to bring out subtle color differences in materials due to variations in composition. Figures 3.2C & 3.2D: RGB color maps composed of spectral parameters adapted from Pieters et al. (1994) and Dhingra (2008), respectively for Clementine UVVIS data, using MMI bands. Figure 3.2E: Visible-color RGB composite similar to figure A with regions of interest (ROIs) used to generate end-member map (Figure 3.2F) and spectral end-members (Figures 3.3A & 3.3B). Figure 3.2F: End-member map generated in ENVI using supervised classification with ROIs as input parameter to map end-members distribution.

The MMI images reveal that the sample consists of very poorly sorted mixture of fine grained clasts of different compositions (polymictic) with angular to sub-rounded (roundness ranges from 0.15-0.5 using the visual estimator of Powers 1953) shapes in a crystal-rich matrix-supported fabric. The matrix consists of predominantly light-grey and white-colored components (visible color image, Figure 3.2A) that are at the limit of the resolving power of the MMI (62.5 μm/pixel), along with coarser-grained crystal and lithic grains ranging in size from 0.25 up to 1 mm in diameter. The clasts are predominantly very fine-grained and do not show internal fabrics, such as vesicularity, bedding or other features. Clasts are of different compositions and textures (i.e., polymictic), ranging in size from medium sand (0.25 mm), to medium pebbles (10 mm), with the small, to medium pebble-sized fraction dominating the sample. Clasts contain both crystalline and lithic components and can be subdivided into three different types: 1) dark fine-grained clasts, 2) small breccia clasts containing smaller crystalline and lithic fragments (i.e., microbreccias), and 3) cemented fine-grained crystal-rich fragmental materials (i.e., cemented

regolith). The dark fine-grained clasts are characterized by sub-angular to sub-rounded shapes and have a very fine-grained (i.e., aphanitic) texture with a few small phenocrysts. They are dark in the visible/near-infrared color composite image (Figure 3.2B). The small breccia clasts are characterized by angular and sub-angular shapes, appear light brown to dark brown in the false-color composite image (Figure 3.2B) and appear to contain smaller lithic and crystalline clasts, including some dark- and light-colored clasts, in a fine-grained matrix. The cemented crystal-rich material has a very fine-grained texture and is characterized by a light brown color in the visible/near-infrared color composite image (Figure 3.2B).

Analysis of color maps using MMI bands designed to emulate the spectral parameters adapted of Pieters et al. (1994) and Dhingra (2008) for Clementine UVVIS data (Figures 3.2C & D) reveal that the fine-grained matrix surrounding the clasts consists predominantly of ferrous silicate minerals (yellow color in Figure 3.2C), most likely, pyroxene of varying composition (green and orange-red colors in Figure 3.2D). The orange-red color in Figure 3.2D is consistent with low-Ca pyroxene. Dark clasts have a flat spectral slope with low reflectance and likely contain opaque minerals, such as ilmenite, which is also consistent with the dark blue colors seen in Figure 3.2C. The light blue colors in Figure 3.2D suggest the presence of plagioclase feldspar. The small breccia clasts in Figure 3.2C have a reddish color, and increasing spectral slope towards the infrared suggestive of a glass component, a mature soil, or Fe-poor

mineralogy, such as plagioclase feldspar. The dark blue color of some of the small fragments contained within the breccia clasts in Figure 3.2C is consistent with a low spectral slope, comparable to the dark clasts. These blue fragments also show a light blue color in Figure 3.2D, which suggests the presence of plagioclase feldspar. In the visible color image in Figure 3.2A, there is a 1.5 mm grey-colored clast that was incorporated into one of the larger breccia clasts towards the center of the field of view. The color indicates a predominantly ferrous mineralogy (yellow color in Figure 3.2C), consistent with high-Ca pyroxene, or olivine (e.g. green colors in Figure 3.2D). The fine-grained, crystal-rich material has a reddish color in Figure 3.2C, consistent with an increasing spectral slope towards the infrared that suggests a predominance of glass, or mature (space weathered) soils. This is also the case for white clasts found within the matrix that stand out because of a bright red color in Figure 3.2C.

Spectral analysis of the MMI images reveals the presence of nine spectral end-members associated with sample 14321,88 (as seen in Figures 3.2F and 3.3A). Two of these spectral end-members are associated with the light-grey matrix while the remaining seven are associated with the light and dark clasts.

The first spectral end-member associated with the matrix is mapped as purple and consists of the light grey crystalline material (in visible color, Figure 3.2A). This material appears yellow in Figure 3.2C and light green in Figure 3.2D. The spectrum has a positive slope from

0.463 to 0.741 μm, a peak at 0.741 μm, a broad absorption centered at 0.935 μm (centered at 0.935 μm for continuum-removed), a positive slope from 0.97 to 1.224 μm, and a negative slope from1.229 to 1.735 μm. Compared with library spectra from USGS and RELAB spectral libraries, convolved to the MMI range and resolution, the spectrum is most consistent with low-Ca pyroxene, such as pigeonite.

The second spectral end-member associated with the matrix (mapped as magenta), consists of the dark pink colored (in visible/near-infrared bands, Figure 3.2B) crystal-rich material. This differs from the material in the purple end-member in that the purple end-member appears light pink in the visible/near-infrared bands in Figure 3.2B. This material is colored orange-red in Figure 3.2D. The spectrum is somewhat similar to the purple end-member (see above), but with some notable differences. The spectrum has a positive slope from 0.463 to 0.741 μm, a peak at 0.741 μm, a broad absorption centered at 0.908 μm (centered at 0.908 μm for continuum-removed), a positive slope from 0.935 to 1.224 μm, and a negative slope from1.229 to 1.735 μm. The spectrum is most consistent with the library spectrum for the orthopyroxene mineral, enstatite.

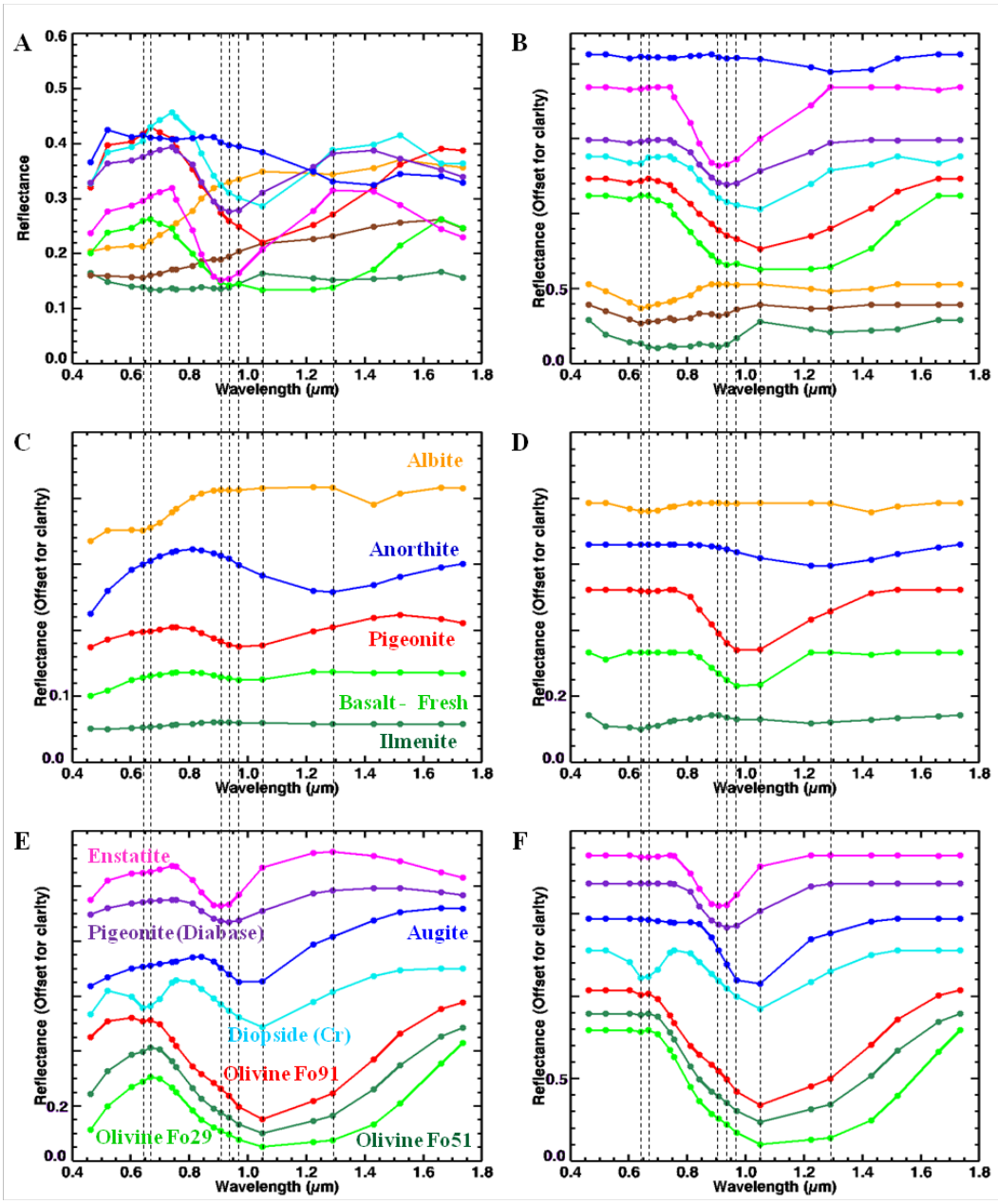

Figure 3.3. MMI-Generated Spectra of End-Members of Sample 14321,88 Compared to Library Spectra. MMI-generated spectra of end-members (A & B) from sample 14321,88 (Figure 3.2) and representative matching library spectra convolved to MMI bandpasses in table 1 (C & F). Vertical lines correspond to MMI bands 0.641, 0.667, 0.908, 0.935, 0.97, 1.05, and 1.29 μm. See text for details on features and discussion. Spectra on the left are normal, while spectra on the right are continuum-removed. Continuum-removed and library spectra are offset for clarity.

The spectral end-member mapped in dark green, is associated with the fine-grained clasts with low reflectance. This material is dark blue in Figure 3.2C and has a low reflectance, relatively flat spectral slope. The spectrum has a negative slope from 0.463 to 0.603 μm, a small absorption centered at 0.908 μm (centered at 0.908 μm for continuum-removed), and a broad, weak absorption centered at 1.29 μm. Compared to library spectra from USGS and RELAB spectral libraries, the spectrum appears to be a composite of more than one mineral phase. The flat spectrum is suggestive of basalt with the small absorption at 0.908 μm consistent with orthopyroxene and the weak broad absorption at 1.29 μm consistent with plagioclase feldspar. The negative slope from 0.463 to 0.603 μm, paired with the flat spectrum, suggests the presence of an opaque mineral, such as ilmenite.

The spectral end-member mapped in brown, is associated with the fine-grained cemented material and brown-colored matrix (in visible/near-infrared bands, Figure 3.2B) of the breccia clasts. This material appears red in Figure 3.2C. The spectrum has low reflectance and a positive slope towards the infrared. Similar to the dark green end-member, the spectrum has a small absorption centered at 0.908 μm (centered at 0.908 μm for continuum-removed), and a weak broad absorption centered at 1.29 μm. The weak absorptions at 0.908 μm and at 1.29 μm are consistent with orthopyroxene and plagioclase feldspar, respectively. The positive slope

of the spectrum towards the infrared is consistent with the presence of glass, or mature soil.

The spectral end-member mapped as orange, is associated with the white clasts found within the matrix and embedded within the cemented crystal-rich materials which stand out with a bright red color in Figure 3.2C. The spectrum has a broad shallow absorption at 1.29 μm and positive slope towards the infrared, similar to the brown end-member, but with a greater steepness. However, unlike the brown end-member, the orange end-member has a distinct inflection at 0.641 μm and no absorption at 0.908 μm. Compared to library spectra from USGS and RELAB spectral libraries, the 1.29 μm absorption suggests the presence of plagioclase feldspar, while the shape of the curve and inflection at 0.641 μm is consistent with library spectrum for the mineral albite. Albite is the Na end-member of the plagioclase feldspar series and is mostly associated with igneous rocks of granitic, or intermediate composition. An alternative interpretation for the spectrum is that the strong positive slope of the spectrum towards the infrared is consistent with the presence of glass, or mature soils, with the inflection at 0.641 μm attributable to an Fe-bearing phase.

The spectral end-member mapped as dark blue is associated with the white-colored clasts (in visible-color and visible/near-infrared images, Figures 3.2A and 3.2B) that are found within the matrix and larger breccia clasts. These appear light red and blue-green in Figures 3.2C and 3.2D,

respectively. The spectrum has a high reflectance relative to the other end-members and is characterized by a broad, sinusoidal shape, with a broad peak centered on the 0.842 μm band, a gradual decreasing slope towards the infrared and a broad, shallow absorption centered around the 1.29 μm band. Compared to library spectra from USGS and RELAB spectral libraries, the shape of the curve and 1.29 μm absorption is consistent with plagioclase feldspar, particularly the calcic variety, anorthite. Like quartz, plagioclase does not exhibit diagnostic absorption features within the visible/near-infrared range. To detect fundamental Si-O absorption features associated with quartz, or plagioclase requires the detection of spectral features in the mid-infrared (Clark 1999 and references therein). However, Fe^{2+} substituting Ca^{2+} in seven coordinated sites in plagioclase produces crystal field electronic transitions that produce broad, shallow bands in the VNIR range between 1.2–1.3 μm (Burns 1993). Given the white color in the visible color composites and the broad, shallow absorption at 1.29 μm, the dark blue spectral end-member is consistent with plagioclase feldspar.

The spectral end-member mapped in light green, is associated with the grey clast (in visible color, Figure 3.2A), which is embedded in a larger breccia clast located toward the middle of the image. Similar grey clasts are also present within some of the smaller clasts. These clasts appear yellow and green in Figures 3.2C and 3.2D, respectively. Their spectrum is characterized by a peak centered at 0.667 μm, a broad, bowl-shaped

absorption feature centered at 1.05 μm, and a strong positive slope towards the infrared between 1.29 and 1.735 μm. Comparing to library spectra, the light green end-member provides a match with library spectra for olivine, with the best match being with Fe-rich olivine, or possibly olivine of intermediate Fe-Mg composition. At the MMI range and resolution, olivine has a characteristic broad, bowl-shaped absorption centered at 1.05 μm. In comparison, clino-pyroxenes, such as diopside, also have an absorption at 1.05 μm, but is distinguished by a narrower V-shaped absorption feature (Figure 3.3F). Since the exact position of the 1.05 μm olivine absorption depends on the Mg/Fe ratio (Burns 1970; King and Ridley 1987; Sunshine and Pieters 1998; Isaacson and Pieters 2010), the shift can be used to further distinguish between Fe-rich and Mg-rich olivine. Fe-rich olivine (fayalite) exhibits a broader-shaped absorption at 1.05 μm, compared to Mg-rich olivine (forsterite). In addition, the position of the associated peak shifts from 0.603 μm for Mg-rich, to 0.667 μm for an intermediate to Fe-rich composition (Figure 3.3F). The peak position at 0.667 μm, along with the broad-shaped absorption at 1.05 μm, is consistent with an olivine of intermediate, to Fe-rich composition.

The spectral end-member mapped as red, is also associated with the grey clast (in visible color, Figure 3.2A), which is embedded in a larger breccia clast towards the middle of the image. Similar to the light green end-member, the spectrum is characterized by a peak centered at 0.667 μm, an absorption centered at 1.05 μm, and a strong positive slope

towards the infrared from 1.29 to 1.735 μm. However, unlike the light green end-member, the red end-member spectrum has a narrower absorption at 1.05 μm. Compared to library spectra, the red end-member matches library spectra for olivine, with the best match being with Mg-rich olivine, or possibly olivine of intermediate Fe-Mg composition.

The spectral end-member mapped as light blue is associated with small grains within the matrix that have a bright yellow color in Figure 3.2C and bright green color in Figure 3.2D. These are not as widespread as the other matrix components. The spectrum is characterized by a positive slope from 0.463 to 0.741 μm, a peak at 0.741 μm, a broad absorption centered at 1.05 μm (centered at 1.05 μm for continuum-removed), with a shoulder at 0.97 μm, a positive slope from 1.05 to 1.521 μm, and a negative slope from1.521 to 1.735 μm. Compared to library spectra from the USGS and RELAB spectral libraries, the spectrum is most consistent with a high-Ca pyroxene, with possible matches to the minerals augite, or diopside.

3.3.2. Interpretation of MMI Results: 14321,88

MMI images and associated spectra of Apollo sample 14321,88 suggest that the sample is a polymict, breccia with a crystal-rich matrix that has experienced a complex history. The matrix consists of fine-grained crystalline material composed of predominantly low-Ca pyroxene (as pigeonite), with smaller amounts of plagioclase feldspar, orthopyroxene (as enstatite), and high-Ca pyroxene (as augite or

diopside), respectively. Three distinct different types of clasts were identified, including: 1) dark, subrounded basaltic clasts with pyroxene, plagioclase feldspar and small amount of ilmenite, 2) cemented fine-grained crystalline material (i.e., cemented regolith) that is glass-rich, or which has experienced significant space weathering, and 3) breccia clasts composed of smaller fragments of basalt, plagioclase- and olivine-rich clasts, and mature regolith. Additional fragments of granitic composition (or alternatively mature soils) were also found as constituents of larger breccia clasts. The diversity of the clast types and compositions and range of textures, suggests a complex paragenetic history in which basalt, plagioclase- and olivine-rich clasts, and granitic fragments, were incorporated into a space weathered regolith, possibly during an early impact event, and subsequently lithified to form a complex lunar breccia. A subsequent impact event lithified the brecciated material with additional basaltic fragments and the crystalline matrix to form the parent sample 14321.

3.3.3. Observations of Apollo Sample 15555,62

The Apollo 15 mission carried out geological exploration and sampling of the mare surface of Palus Putredinis near Hadley Rille and the frontal scarp of the Apennine Mountain range, along the eastern edge of the Imbrium Basin (Swann et al. 1972b). The Apennine Mountains were thought to be fault blocks that have been uplifted and segmented by the Imbrian impact (Swann et al. 1972b). Apollo 15 returned approximately 78

kg of lunar material from the Apennine Front on the Moon, which included sample 15555. Sample 15555 came to be informally known as “Great Scott”, after its collector Dave Scott (Lunar Sample Conpendium). The sample was collected at station 9A near the edge of Hadley Rille (Swann et al. 1972b), that provided access to exposed mare basalts (Swann et al. 1972b). Sample 15555 is interpreted as a coarse-grained, porphyritic basalt, with pyroxene and olivine phenocrysts, with the latter having a normative composition (Rhodes and Hubbard 1973, Ryder and Shuraytz 2001).

MMI-generated color composite images, RGB maps of spectral parameters adapted from Belton et al. (1992) and Dhingra (2008) for Clementine UVVIS data were used to produce a corresponding spectral end-member map of sample 15555,62. The map was based on a supervised classification using ROIs as input parameters (ROI’s are shown in Figure 3.4). Included is a visible-color RGB composite image composed of MMI bands 0.641, 0.522, and 0.463 μm (respectively), which simulates natural-color and a false-color RGB composite images composed of MMI bands 1.43, 0.908, and 0.641 μm (respectively). As noted earlier, the false color image was used to bring out subtle color differences in materials due to spatial variations in mineral composition (Figures 3.4A & B). Figures 3.4C & D show RGB color maps composed of spectral parameters adapted from Belton et al. (1992) and Dhingra (2008), respectively for Clementine UVVIS data, using MMI bands. Figure 3.4F

shows a spectral end-member map generated in ENVI using a supervised classification of ROIs (Figure 3.4E) as input parameters for mapping the spatial distribution of spectral end-members. The color maps of spectral parameters adapted from Belton et al. (1994) and Dhingra (2008) for Clementine UVVIS data using MMI bands were used, along with ENVI's the Minimum Noise Fraction Transformation (MNF) function (Green et al. 1988) and Pixel Purity Index (PPI) algorithm (Kruse et al. 1993; Rowan et al. 2004), to identify ROIs from which spectral end-members could be extracted for spectral analysis. These spectral end-members were used to generate the spectral end-member maps. Figure 3.5 shows plots of the corresponding end-member spectra, along with matching library spectra from the USGS and RELAB spectral libraries.

The MMI images reveal that the sample to be a porphyritic, crystalline rock with rounded to sub-rounded, dark-grey phenocrysts, in a light-grey to white matrix (visible color image, Figure 3.4A). In the false-color composite image obtained using visible and near-infrared bands (Figure 3.4B), the dark-grey phenocrysts separate into magenta-colored and purple colored phenocrysts that range in size from 0.3 to 1.5 mm and 0.9 to 1.3 mm, respectively. A few "zap pits" (e.g. micrometorite impact pits) are also visible on the surface that range in size from 1.0 to 1.5 mm.

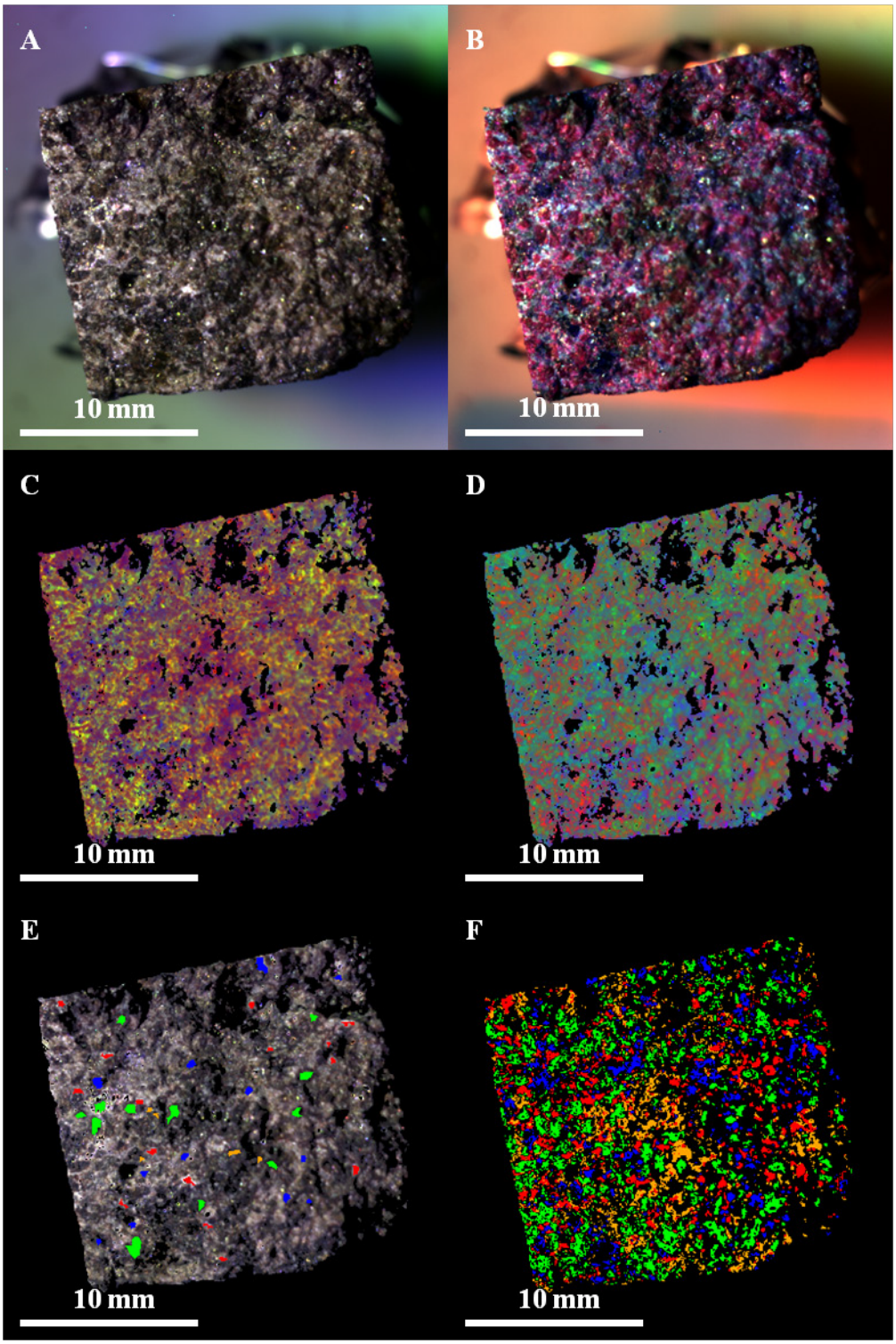
A
10 mm
B
10 mm
C
10 mm
D
10 mm
E
10 mm
F
10 mm

Figure 3.4. MMI-Generated Color Composite Images, Spectral Parameter Maps, and End-Member Map of Sample 15555,62. MMI-generated color composite images (A & B), RGB maps of spectral parameters adapted from Pieters et al. (1994) and Dhingra (2008) for Clementine UVVIS data (C & D) and corresponding spectral end-member map (F) based on supervised classification with ROIs as input parameters (E) of sample 15555,62. MMI Image sub-frame size is 25x25 mm at 62.5 μm/ pixel. Figures A-B are linear stretched. Figure 3.4A: Visible-color RGB composite image composed of MMI bands 0.641, 0.522, and 0.463 μm respectively to simulate true-color. Figure 3.4B: False-color RGB composite image composed of MMI bands 1.43, 0.908, and 0.641 μm respectively to bring out subtle color differences in materials due to variations in composition. Figures 3.4C & 3.4D: RGB color maps composed of spectral parameters adapted from Pieters et al. (1994) and Dhingra (2008), respectively for Clementine UVVIS data, using MMI bands. Figure 3.4E: Visible-color RGB composite similar to figure A with regions of interest (ROIs) used to generate end-member map (Figure 3.4F) and spectral end-members (Figures 3.5A & 3.5B). Figure 3.4F: End-member map generated in ENVI using supervised classification with ROIs as input parameter to map end-members distribution.

Analysis of color maps generated using the spectral parameters adapted from Belton et al. (1992) and Dhingra (2008) for Clementine UVVIS data (Figures 3.4C & D) reveal that the phenocrysts consist predominantly of a ferrous mineral (yellow color in Figure 3.4C), with the magenta- and purple-colored phenocrysts matching low-Ca and high-Ca pyroxene/ olivine compositions, respectively (orange-red and green colors respectively in Figure 3.4D). The light-grey, to white matrix material (Figure 3.4A) appears light-red and light-blue in Figures 3.4C and 3.4D, respectively suggesting a plagioclase-rich composition. Alternatively, these colors are also consistent with an increasing spectral slope towards the infrared consistent with the presence of glass, or mature soil. However, a plagioclase-rich interpretation would perhaps be more consistent with the porphyritic texture of the rock.

Spectral analysis of the MMI images reveals the presence of four spectral end-members associated with sample 15555,62 (as seen in Figures 3.4F and 3.5A). Two of these spectral end-members are associated with the light-grey matrix, while the other two are associated with the dark-grey phenocrysts.

The spectral end-member mapped as blue, is associated with the purple-colored phenocrysts (in visible/near-infrared color bands, Figure 4B). The phenocrysts appear yellow and green in Figures 3.2C and 3.2D, respectively. The spectrum is characterized by a peak centered at 0.667 μm, a broad, bowl-shaped absorption centered at 1.05 μm, and a strong

positive slope towards the infrared from 1.29 to 1.735 μm. Compared to library spectra, the blue end-member matches library spectra for olivine, with best match to Fe-rich olivine, or possibly olivine of intermediate Fe-Mg composition. At MMI range and resolution, olivine has a characteristic broad, bowl-shaped absorption centered at 1.05 μm. In comparison, clinopyroxenes, such as diopside, also have an absorption at 1.05 μm, but are distinguished by a narrower V-shaped absorption feature (Figure 3.3F). Fe-rich olivine (fayalite) exhibits a broader absorption centered at 1.05 μm, compared to Mg-rich olivine (forsterite), which includes a shoulder at 1.224 μm. This shoulder can be further used to distinguish between Fe-rich and Mg-rich olivine compositions. The peak position at 0.667 μm, along with the broad-shaped absorption at 1.05 μm and shoulder at 1.224 μm, are all consistent with an olivine of intermediate, to Fe-rich composition.

The spectral end-member mapped as green is associated with the magenta-colored phenocrysts (in visible/near-infrared color bands, Figure 3.2B), which appear yellow and orange-red in Figures 3.2C and 3.2D, respectively. The spectrum has a positive slope from 0.463 to 0.741 μm, a peak at 0.741 μm, a broad absorption centered at 0.908 and 0.935 μm (centered at 0.908 and 0.935 μm for continuum-removed), with a shoulder at 1.05 μm, a positive slope from 1.05 to 1.43 μm, and a negative slope from1.43 to 1.735 μm. The spectrum is most consistent with the library spectrum (convolved to the MMI range and resolution) for low-Ca

pyroxene, such as pigeonite, with a high-Ca pyroxene component (such as augite).

The first spectral end-member associated with the light-grey and white-colored matrix (in visible color, Figure 3.4A) is mapped in red. The material appears light-red and light-blue in Figures 3.4C and 3.4D, respectively. The spectrum is characterized by a broad, sinusoidal shape, with a peak centered at 0.7 μm, a decreasing slope from 0.741 to 1.224 μm, a broad absorption centered at 1.224 μm, and a positive slope from 1.224 to 1.735 μm, towards the infrared. Compared to library spectra from USGS and RELAB spectral libraries, the shape of the curve and absorption at 1.224 μm is consistent with plagioclase feldspar, particularly the calcic-rich variety, anorthite. Like quartz, plagioclase does not exhibit diagnostic absorption features within the visible/near-infrared range. To detect fundamental Si-O absorption features associated with quartz or plagioclase, requires spectral features in the mid-infrared (Clark 1999 and references therein). However, Fe^{2+} substituting Ca^{2+} in seven coordinated sites in plagioclase produces crystal field electronic transitions resulting in broad, shallow bands in the VNIR range at about 1.2–1.3 μm (Burns 1993). Given the light-grey, to white color (seen in the visible color composites Figure 4A) and the broad, shallow absorption at 1.2 μm, the red spectral end-member is consistent with plagioclase feldspar.

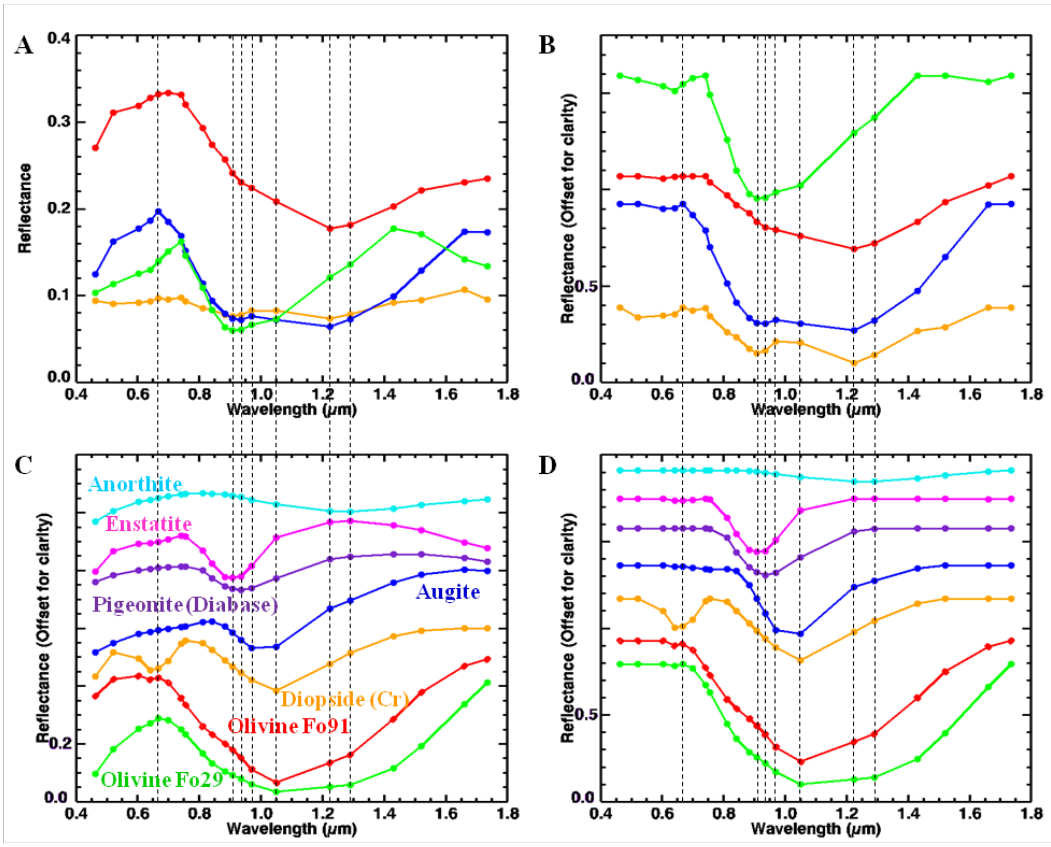

Figure 3.5. MMI-Generated Spectra of End-Members of Sample 15555,62 Compared to Library Spectra. MMI-generated spectra of end-members (A & B) from sample 15555,62 (Figure 3.4) and representative matching library spectra convolved to MMI bandpasses in Table 2.1 (C & D). Vertical lines correspond to MMI bands 0.667, 0.908, 0.935, 0.97, 1.05, 1.224 and 1.29 μm. See text for details on features and discussion. Spectra on the left are normal, while spectra on the right are continuum-removed. Continuum-removed and library spectra are offset for clarity.

The second spectral end-member associated with the light-grey and white-colored matrix (in visible color, Figure 3.4A) is mapped as orange, and also appears light-red and light-blue in Figures 3.4C and 3.4D, respectively. The spectrum has a lower reflectance than the other end-members and is characterized by a relatively flat shape, with weak absorptions similar to the green and red end-members, centered at 0.908 and 0.935 μm (centered at 0.908 and 0.935 μm for continuum-removed), as well as 1.224 μm (centered at 1.224 μm for continuum-removed). These absorptions are consistent with the presence of low-Ca pyroxene and plagioclase feldspar, while the low reflectance, relatively flat spectrum is suggestive of a glassy component.

3.3.4. Interpretation of MMI Results: 15555,62

MMI images and associated spectra of sample 15555,62 suggest that the sample is a porphyritic basalt, with pyroxene and olivine phenocrysts in a glassy, plagioclase-rich matrix. The pyroxene phenocrysts are of low-Ca composition (as pigeonite), with an additional component of high-Ca pyroxene (as augite), while the olivine phenocrysts have an Fe-rich to intermediate composition. The porphyritic texture of the basalt suggests that some cooling of the parent magma occurred prior to extrusion, compared to fine grained, glassy basalts. The intermediate, to Fe-rich composition of the olivine suggests that the magma originated from a more evolved mantle source (BVSP 1981). Small zap pits

associated with micrometeorite bombardment on the imaged surface suggests that the sample was exposed on the lunar surface for some time.

3.4. Discussion

3.4.1. Comparison of MMI Observations of Apollo Samples to Existing Literature

3.4.1.1. Apollo Sample 14321,88

Sample 14321 is a clast-rich, crystalline matrix breccia (Wilshire and Jackson 1972), with about 30% lithic and microbreccia clasts (Duncan et al. 1975a, 1975b; Grieve et al. 1975; Simonds et al. 1977), and interpreted to be a piece of the Fra Mauro formation (e.g., Wilshire and Jackson 1972, Grieve et al. 1975; Swann et al. 1972a, 1977). This sample proved to be a very useful example to test the performance of the MMI and for highlighting strengths and weaknesses of the instrument. Overall, the MMI results appear to be consistent with observations of the texture and mineralogy published in the literature. Studies by Grieve et al. (1975), Duncan et al. (1975a, 1975b) and Morgan et al. (1975) showed that 14321 is a polymict breccia containing a variety of lithic and microbreccia clasts. These breccia clasts contain larger basalt clasts, as well as microbreccia clasts from a mare-type basalt, anorthosite and olivine microbreccias, rhyolitic glass and microgranite (Duncan et al. 1975; Grieve et al. 1975).

The MMI images faithfully resolved the major microtextural features of the sample (as small as 180 μm, i.e. at least 3 pixels), while the application of spectral end-member mapping revealed all major spectral

(i.e. mineral) components. MMI spectra were most useful for detecting and distinguishing major and minor phases that exhibit diagnostic absorption features within the MMI wavelength range and resolution, namely features associated with electronic processes from Fe^{2+} in pyroxene and olivine, between 0.9 μm and 1.0 μm and those associated with plagioclase feldspars between 1.2 μm and 1.3 μm (Clark 1990; Burns 1993). The identification of the basalt clasts in sample 14321,88 proved to be challenging because of the fine grain size (each mineral grain < pixel size of 62.5 μm, thereby resulting in a non-linear composite spectrum for each pixel from an intimate mixture). However, the relatively flat spectrum with weak absorptions at 0.908 and 1.29 μm proved to be consistent with library spectra for basalt. Determining the composition of the matrix was not possible at the MMI wavelength range and resolution, except for the presence of pyroxene and plagioclase feldspar.

The MMI was also able to identify the presence of mature soils incorporated into the sample by the steep slope in the spectrum towards the infrared, as well as the presence of ilmenite in some of the basalt clasts. Studies of the basalt clasts in parent sample 14321 showed that it contains low-Ti, aluminous mare basalts, with pyroxene and olivine compositions ranging from low-Ca, to high-Ca pyroxene and olivines of intermediate composition (Fo45-75; Chao et al. 1972, Taylor et al. 1972, Wänke et al. 1972, Duncan et al. 1975a,b, Grieve et al. 1975, Ware and Green 1977, Takeda et al. 1980, Shervais et al. 1984, Shervais et al.,

1985, Dickinson et al. 1985, Neal et al. 1988, 1989). However, studies of basalt clasts found in sample 14321,88 by Ware and Green (1977) indicated that clasts to contain up to 5 wt% opaques, primarily as ilmenite. The identification of the presence of opaques by the MMI spectra in the basalt clasts is consistent with the observations by Ware and Green (1977).

Mafic mineral components found in the matrix consist predominantly of orthopyroxene and low-Ca pyroxene, with smaller amounts of high-Ca pyroxene (Simonds et al. 1977, Stoffler and Knoll 1977). MMI observations of the matrix components are also in agreement with previous petrologic observations. One notable observation with the MMI, is the observation of granitic material within sample 14321,88. While granitic material is not common on the lunar surface, it was reported for sample 14321 by Duncan et al. (1975), Grieve et al. (1975) and Warren et al. (1983), also occurring in other samples collected by the Apollo missions as well (see review by Jolliff et al. 2006). Thus, the identification of granitic material by the MMI highlights the power of the MMI to identify and map a variety of mineral compositions, over a range of textures and compositions, and at the pixel scale consistent with thin section based petrologic observations previously published in the literature.MMI capabilities would be highly advantageous for future landed missions to the Moon, for rapid screening of lunar materials for analysis in a lunar lab, or for sample return.

3.4.1.2. Apollo Sample 15555,62

Sample 15555,62 also proved to be a very useful sample for testing the performance of the MMI in characterizing basaltic samples and for highlighting the strengths and limitations of the instrument. Overall, the MMI results are consistent with observations of the texture and mineralogy published in the previous literature. Sample 15555 is a coarse-grained, porphyritic basalt, with olivine and pyroxene phenocrysts, and with olivine phenocrysts of normative composition (i.e. Fe-rich to intermediate compositions, Fo67-16; Brown et al. 1972; Rhodes and Hubbard 1973; Ryder and Shuraytz 2001).

MMI images faithfully resolved the major microtextural features of this sample (features as small as 200 μm, i.e. at least 3 pixels), namely the porphyritic texture and zap pits, while the application of spectral end-member mapping revealed all major spectral (and mineral) components. MMI spectra were most useful in detecting and distinguishing major and minor phases that exhibit diagnostic absorption features within the MMI wavelength range and resolution, namely features between 0.9 μm and 1.0 μm associated with electronic processes from Fe^{2+} in pyroxene and olivine, and those associated with plagioclase feldspars between 1.2 μm and 1.3 μm (Clark 1990; Burns 1993). In particular, the pyroxene and olivine phenocrysts were easily distinguished in false-color composite images using the visible/near-infrared bands and color maps based on spectral parameters, which helped define ROIs for constructing spectral

end-member maps. The identification of low-Ca pyroxene (as pigeonite) with a high-Ca pyroxene (as augite) component in the MMI spectra is consistent with results published by Brown et al. (1972), Bence and Papike (1972) and Walker et al. (1977), who reported that the pyroxene grains are zoned, and contain both pigeonite and augite components. While the 62.5 μm/pixel resolution of the MMI was unable to spatially resolve or localize the zonation in pyroxene, it was still able to identify the presence of the two pyroxene components from the composite spectrum.

MMI observations of olivine and plagioclase compositions are also consistent with studies by Longhi et al. (1972, 1976) and Walker et al. (1977); however, similar to pyroxene observations, mineral zonation was not observed, due to the coarser MMI spatial resolution. Additionally, other mineral phases, such as spinel and silica (as cristobalite) previously identified as being present in the matrix (e.g., Longhi et al. 1972), were not identified by the MMI. This is mostly due to the fact that these minerals do not exhibit characteristic absorptions within the MMI detection range, as compared to Fe-bearing minerals. In conclusion, Apollo sample 15555,62 served to highlight some of the strengths and limitations of the MMI through the identification of different, independently confirmed Fe-bearing silicates, while missing other phases that lack definitive absorption features within the MMI spectral range.

3.4.2. Applications of the MMI to Future Lunar Robotic and Human Exploration

Since the Apollo-era formulation of lunar origins and evolutionary history have showed the lunar crust to be variable both laterally and vertically, in its composition, age, and mode of formation, remote sensing missions (Galileo, Clementine, Lunar Prospector, and more recently Smart-1, Chandrayaan-1, and Lunar Reconnaissance Orbiter), along with lunar meteorite studies, have revealed we have an incomplete sampling of the lunar crust (e.g., Robinson and Riner 2005; Jolliff et al. 2006; NRC 2007a). Thus additional landed missions are needed to sample and return lunar material of unexplored areas of Moon, such as the South Pole-Aitken basin on the far side of the Moon (e.g., NRC 2007a). To maximize the scientific return, future robotic and human missions to the Moon will need to have *in-situ* capabilities that provide information about mineralogy and microtexture of lunar materials to enable the identification of rock types and thereby, enable the selection of the highest value samples for further analysis in a lunar lab, or for return to Earth.

Lessons from lander and rover-based exploration of Mars (e.g., Herkenhoff et al. 2004; Keller et al. 2008) have successfully demonstrated the utility of microscopic imaging at the hand lens scale. In fact, this capability has proven so vital to the success of surface missions that a microimager is one of the instruments now recognized as essential for all future Mars surface missions (e.g., NRC 2007b; MEPAG ND-SAG 2008;

MEPAG MRR-SAG 2009). The microtexture of rocks and soils may be defined as the microspatial interrelationships between constituent mineral grains, pore spaces, and secondary (authigenic) phases (e.g., cements) of minerals. Microtextural observations provide essential data for identifying the petrogenetic processes responsible for the formation of rocks, and for understanding their diagenetic (post-formational) history.

Critical capabilities needed for future sample caching and sample return from Mars are similar to those required to support a lunar sample return mission: arm-mounted instruments, capable of interrogating the surfaces of rocks to create co-registered 2-D maps of microtexture, major element geochemistry, mineralogy, and organic geochemistry (MEPAG ND-SAG 2008; MEPAG MRR-SAG 2009). Such spatially-correlated data sets are considered crucial for identifying the best samples for caching based on rapid *in situ* petrogenetic interpretations. The MMI, with its ability to integrate microimaging with multispectral capabilities to create co-registered high resolution 2-D maps of microtexture with mineralogy, directly addresses some of the most important measurement requirements identified for future lunar sample return missions (NRC 2007a).

3.5. Conclusions

In this study, we used the MMI to characterize 18 lunar rocks and four soils, selected from a reference suite that spanned a broad range of compositions found in the Apollo sample collection. To accomplish this task, a field portable, tripod mounted version of the MMI was deployed to

a nitrogen-filled glove box housed in the Lunar Experiment Laboratory at NASA's Johnson Space Center. Analysis of MMI spectral data cubes revealed that MMI composite images faithfully resolved the microtextural features of samples, while the application of ENVI-based spectral end-member mapping performed well in mapping the distribution of Fe-bearing mineral phases (olivine and pyroxene), as well as plagioclase feldspars in rock samples, over a broad range of lithologies and grain sizes. The MMI composite images also revealed the presence of secondary mineral phases, glasses, as well as detecting the subtle effects of space weathering in samples. MMI-based petrogenetic interpretations compared favorably with previously published descriptions of the same samples, revealing the valuable observations the MMI instrument can contribute to future lunar exploration.

CHAPTER 4

FIELD ANALOG STUDIES WITH THE MULTISPECTRAL MICROSCOPIC IMAGER: APPLICATIONS FOR MOON/MARS EXPLORATION

4.1. Introduction

Terrestrial analog environments are places on Earth with geological and environmental characteristics that resemble those that exist on an extraterrestrial body, like the Moon, or Mars. During the 1960s, a variety of terrestrial analog environments were used as training grounds for the Apollo astronauts in preparation for the Apollo lunar missions (e.g., NASA 1963; Goddard et al. 1965; Shoemaker et al. 1965). Such terrestrial training grounds have played a vital role in: 1) learning about basic planetary systems and processes; 2) testing methodologies, protocols, strategies, and technologies; and 3) training highly-qualified personnel, as well as science and operation teams (e.g., Shoemaker et al. 1965; Léveillé 2009).

To assess the value of the Multispectral Microscopic Imager (MMI) as a tool for future field-based applications, a ruggedized, field-portable, tripod-mounted version of the MMI was deployed in the field as part of two distinctly different field analog tests, namely the 2010 International Lunar Surface Operations *In-Situ* Resource Utilization (ILSO-ISRU) Field Test on the slopes of Mauna Kea, Hawaii (Sanders and Larson 2011; Núñez et al. 2012; ten Kate et al. in press) and inside the GeoLab in the Deep Space

Habitat (DSH) as part of the 2011 Desert Research and Technology Studies (D-RATS) field test at the Black Point Lava Flow in northern Arizona (Evans et al. 2012; in press; Farmer et al. 2011) (Figures 4.1 and 4.2).

4.1.1. The 2010 International Lunar Surface Operations In-Situ Resource Utilization (ILSO-ISRU) Field Test

The 2010 International Lunar Surface Operation - In-Situ Resource Utilization Analog Test (ILSO-ISRU, Sanders and Larson 2011; ten Kate et al. in press), held on the Mauna Kea volcano in Hawaii, was coordinated by the Northern Centre for Advanced Technology (NORCAT) in collaboration with the Canadian Space Agency (CSA), the German Aerospace Center (DLR), and the National Aeronautics and Space Administration (NASA), operating through the PISCES program. The test built upon the success of the first ISRU and lunar surface operations analog test held in Hawaii in 2008 (Sanders and Larson 2011), which performed the first end-to-end test of excavation, oxygen production, and product storage in an integrated system configuration and scale relevant for future human lunar missions. The test demonstrated hardware and operations associated with mobile resource prospecting, to demonstrate the feasibility for a future lunar polar mission. The 2010 ILSO-ISRU field test primarily focused on hardware testing of technologies and systems related to resource identification, extraction, storage and utilization, with a small but growing role designated for *in situ* science measurements.

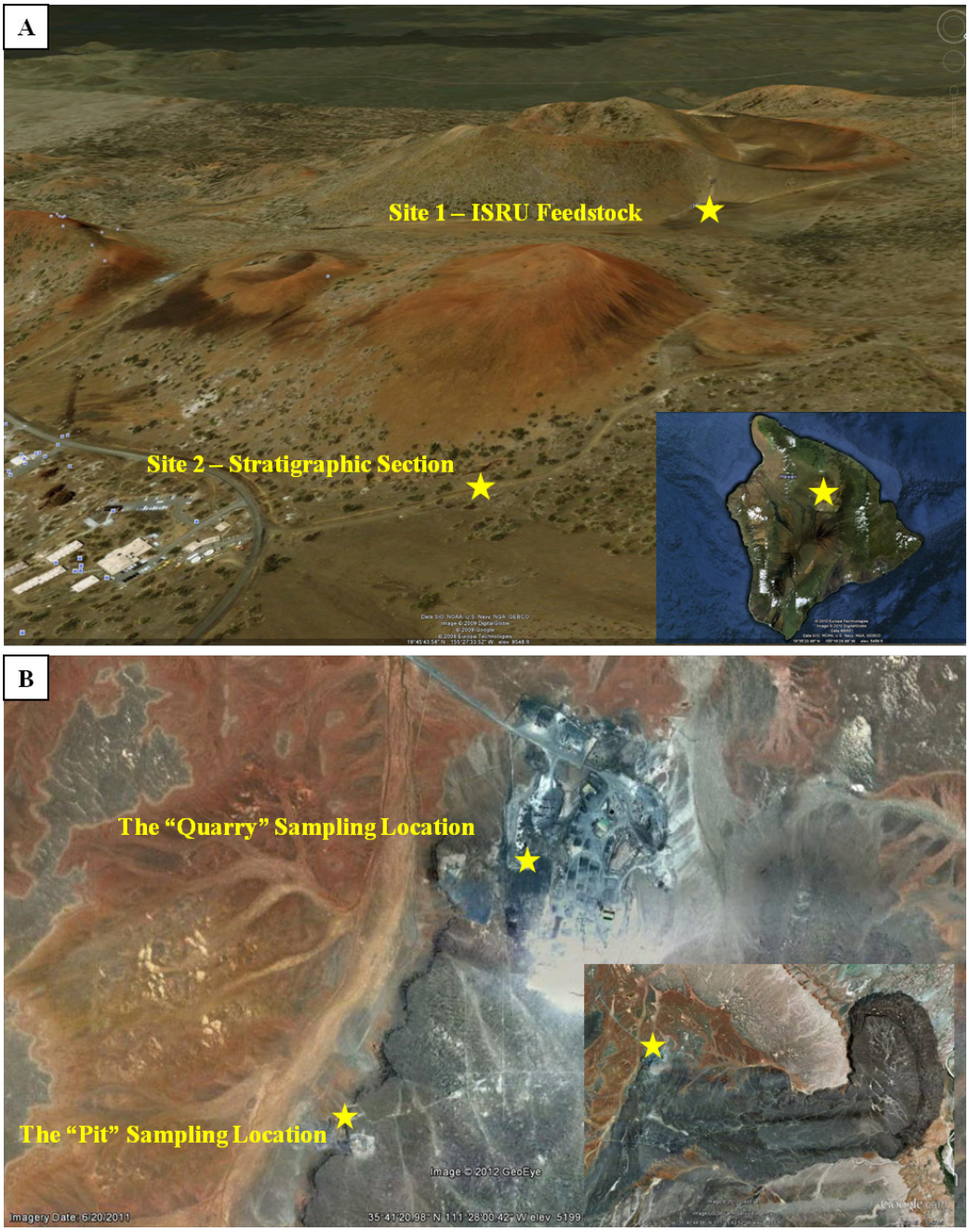

Figure 4.1. Locations and Sampling of the 2010 ILSO-ISRU and 2011 Desert RATS Field Tests. Location of the 2010 ILSO-ISRU field test on the slopes of Mauna Kea, Hawaii (A; View looking SW) and the 2011 Desert RATS field test at the Black Point Lava Flow northeast of Flagstaff, Arizona (B). Stars mark locations of surface material and rock samples from which MMI data collected is presented in this paper.

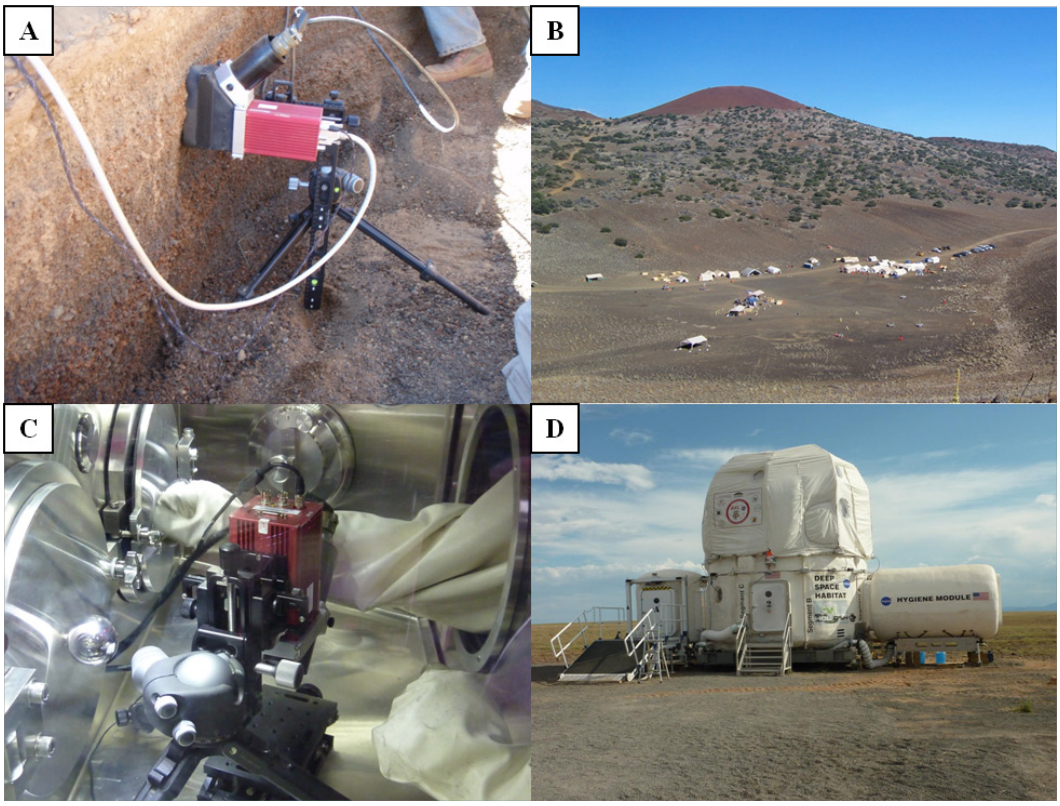

Figure 4.2. Field Deployments of the MMI in the 2010 ILSO-ISRU and 2011 Desert RATS Field Tests. The MMI was deployed in the 2010 ILSO-ISRU field test on the slopes of Mauna Kea, Hawaii (A-B) and inside the GeoLab in the Deep Space Habitat (DSH) as part of the 2011 Desert RATS field test at the Black Point Lava Flow northeast of Flagstaff, Arizona (C-D). Figure 4.2A: Deployment of the MMI with sunshade along 50 cm high vertical section discussed in the paper and shown in Figures 5-6. Figure 4.2B: Base camp of 2010 ILSO-ISRU Field Test on the slopes of Mauna Kea, Hawaii. This is also the location of Site 1 labeled in Figure 4.1A. View is looking NE towards cinder cone near Site 2 labeled in Figure 4.1A. Figure 4.2C: Deployment of the MMI with the sunshade inside the GeoLab, in the Deep Space Habitat (DSH; 4.2D). The DSH was located in the base camp near the “Quarry” sampling location, labeled in Figure 4.1B.

The primary goals of the campaign were to: 1) advance ISRU hardware and systems demonstrated over first analog field test; 2) expand ISRU system/capability integration with other transportation and surface elements (such as power and propulsion) and science activities; and 3) provide field characterization of feedstock materials using field portable scientific instruments.

The MMI was one of several science instruments used in the field test, which was funded through NASA's Moon, Mars Analog Mission Activity (MMAMA) and Field Science Analog Test (FSAT) programs as well as through the Canadian Space Agency. The application of the MMI was to provide complementary data to help locate, identify and characterize the surface and subsurface regolith at the test site (Site 1 in Figure 4.1A), which provided feedstock materials for ISRU experiments (Sanders et al. 2011; ten Kate et al. in press). Although the feedstock for the ISRU oxygen production plant was pre-selected for the field tests, operations simulated *in situ* scientific “prospecting” and field characterization of feedstock for the ISRU oxygen production units. Geologic materials with a high total iron and ilmenite ($FeTiO_3$) contents make good feedstock for oxygen production using the hydrogen reduction process (e.g., Allen et al. 1993, 1994, 1996).

The 2010 ILSO-ISRU field test provided the first opportunity to deploy the MMI in the field. The main objectives for the MMI were to image rocks and soil materials from both the surface regolith and from

subsurface cores acquired with a drill. The characterization was accomplished in the field using a tripod mounted version of the MMI, with little to no sample preparation. This simulated the rapid *in situ* characterization of geological materials to document the basic mineralogy and microtexture of the materials and provided a basis for follow-up analysis in the lab, using other instruments, while supporting real-time planning of science activities. Because the 2010 ILSO-ISRU field test was first field deployment of the MMI, it provided a unique opportunity to assess the performance of the MMI and its ability to successfully operate in a Moon/Mars analog site under daylight illumination to image rocks and soils with unprepared, irregular surfaces.

4.1.2. The 2011 Desert Research and Technology Studies (D-RATS) Field Test

NASA's Desert Research and Technology Studies (Desert RATS) is a multi-year series of tests carried out annually in the high desert of northern Arizona to test prototype surface hardware and representative mission operation scenarios for future human and rover-based exploration of planetary surfaces (Ross et al. in press). The 2011 Desert RATS analog mission conducted over a period of nine days in August-September 2011, simulated several different exploration and operations strategies over a series of single-day mission scenarios (e.g., operations with one Space Exploration Vehicle (SEV) vs. two SEVs) that might be used for a manned near-Earth asteroid (NEA) mission (Janoiko and Johnson 2012). The

single-day tests involved different combinations of rovers, crew members, and mechanisms for crew mobility, as well as a communications time delay equal to 50 seconds of one-way travel time and remote mission operation and science support associated with a NEA mission. Mission operations were staged at two locations near Black Point Lava Flow north of Flagstaff, Arizona (Figure 4.1B), while mission operation and science support personnel participated remotely from Johnson Space Center's (JSC) Mission Control Center (MCC) in Houston, Texas (Janoiko and Johnson 2012).

In parallel with rover and crewed field operations, sample processing, curation and analysis strategies within mission operations constraints of a NEA mission were tested inside the GeoLab in the Deep Space Habitat (Figure 4.2). The GeoLab is a prototype glovebox workstation designed for the preliminary examination and characterization of geologic samples collected by astronaut crews during EVAs (Evans et al. 2010; Evans et al. 2012; Evans et al. in press). The objective is to provide information about surface materials to help guide future traverses and sampling as well as to "high grade" samples for potential return to Earth (Evans et al. 2010; Evans et al. 2012; Evans et al. in press). Primary objectives for the 2011 D-RATS test consisted of testing mission science operations, sample handling protocols and preliminary sample analysis protocols, and the integration of new instruments (including the MMI) into the sample processing workflow, all within the constraints of a simulated

mission to an asteroid. The activity included single crew-member operations, using a remotely-located science team, operations under time constraints, which limited the number of samples processed during a single operations cycle by the crew member, and 50 second one-way communications and data transfer delays to simulate actual mission conditions (Evans et al. 2012). The MMI was deployed inside the GeoLab and integrated within the sample processing workflow (Figure 4.3) to support the preliminary examination and characterization of geologic samples collected by astronaut crews during EVAs. The main objectives for the MMI were to image the field samples with little or no sample preparation and provide rapid characterization of mineralogy and microtexture: 1) for further analysis using other instruments in the GeoLab, and 2) to support real-time planning of science activities (both rover operations and astronaut EVAs) during Desert RATS. The 2011 Desert RATS field test provided a unique opportunity assess the performance of the MMI to operate under the simulated mission constraints, including communications and data transfer delays, and training of astronaut crews in Geolab operations, and under different operational time constraints.

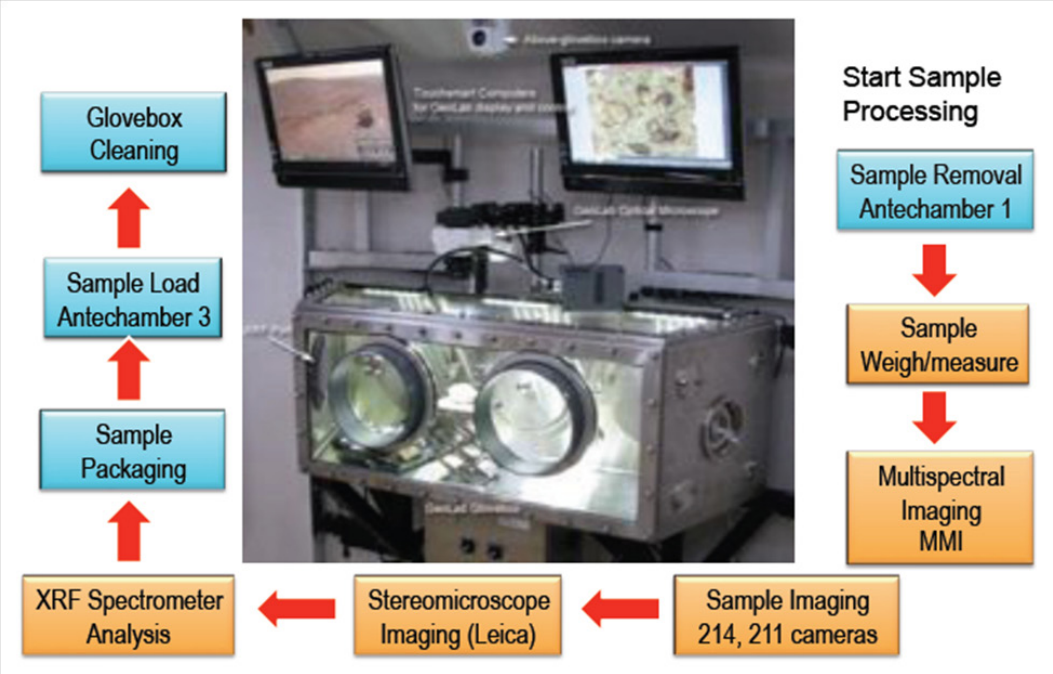

Figure 4.3. Processing Flow of Samples in the GeoLab. Processing flow of samples in the GeoLab, which includes analysis with the MMI. Orange boxes correspond to measurement and data collection steps.

4.2. Methods

4.2.2. Instrument Description

A detailed description of the version of the Multispectral Microscopic Imager (MMI) used to acquire the datasets presented here can be found in Núñez et al. (manuscript in review 2012). In brief, the current system consists of a field-portable, tripod-mounted, un-cooled Indium-Gallium-Arsenide (InGaAs) focal plane array (FPA) and a 21-band multi-wavelength light-emitting diode (LED) illumination array, which generates multispectral, microscale, reflectance images of geological samples, where each pixel of an image consists of a spectrum ranging from the visible (0.463 μm) to the short-wave infrared (1.735 μm) (Table 2.1). The InGaAs FPA consists of 640 x 512 pixels which along with a slow focal ratio lens (F/10) results in an instantaneous field of view (IFOV) of 62.5 μm/pixel and field of view (FOV) of 40 mm x 32 mm, at a working distance of 63 mm from the lens to the working plane. The resulting instantaneous field of view (IFOV) of 62.5 μm/pixel was a trade-off, reflecting the desire to optimize both resolution and the depth of field (5 mm) suitable for imaging natural surfaces (Sellar et al. 2006; Nuñez et al. 2009), while retaining a large enough FOV to be able to accurately place MMI images into larger context images obtained with other instruments. This enabled the in focus imaging of a majority of rocks and soils in the FOV, with no sample preparation, or need for z-stacking of images The MMI was deployed with a custom-built dark, solid sun shade (see Figure

4.2), to enable the imaging of surfaces under full daylight illumination while in the field. The sun shade was designed and built at the Jet Propulsion Laboratory (JPL). Design considerations required the sun shade to be light-weight, durable, opaque to daylight covering the entire detection range of the MMI camera, and easily mounted to the existing instrument.

4.2.3. Data Acquisition and Calibration

Data acquisition and calibration is described in more detail in Núñez et al. (manuscript in review, 2012). In brief, MMI-generated 21-band dark-subtracted images were obtained under low ambient illumination of both a sample target, and a 50 % reflectance Lambertian Spectralon target (produced by Labsphere). Automated routines written in IDL were then applied to data sets to replace the bad pixels in each image, to apply a flat field correction and to calibrate each image. Next all co-registered sample images were stacked together on the 3rd axis (wavelength dimension) to form an image datacube. The bad pixels were corrected by replacing each bad pixel with the mean value obtained by averaging adjacent pixels, weighted by the distances of the averaged pixels from the bad pixel. Each wavelength comprising the target image was flat-fielded and converted from raw DN, to reflectance, using the respective wavelength image of the 50 % reflectance Spectralon standard. Calibrated images were co-registered and stacked together along the 3rd axis (wavelength dimension) to form an image datacube with spatial coordinates (X, Y spatial dimensions) and wavelength in the 3rd dimension

(Z). As a result, data for each pixel contains a spectrum of 21 bands, ranging from the visible (0.463 μm), to the short-wave infrared (1.735 μm).

4.2.4. Color Imaging and Spectral Analysis

Applying remote sensing techniques developed for analysis of multispectral imagery, MMI multispectral images were processed and analyzed using the remote sensing and image analysis software package ENVI (Environment for Visualizing Images) - a commercial software package sold by ITT Visual Information Solutions.

4.2.4.1. Color Imaging

Simple three-band RGB color composites simulating natural color and visible/near-infrared images were prepared for each sample, or surface image. Visible color bands 0.641, 0.522, and 0.463 μm were used, respectively, to create RGB color composite images, to simulate natural color, while other visible/infrared bands (ex. 1.43, 0.908, and 0.522 μm) were used to generate the visible/near-infrared color composite images. Each image employed a default linear stretch to enhance color differences. The RGB color composite images were useful for highlighting compositional differences within different lithologies of samples.

4.2.4.2. Identification of ROIs for End-Member Extraction and Spectral Analysis

Regions of Interest (ROIs) were identified in sample images based on microtextural and potential compositional differences. Representative spectra, i.e. “spectral end-members”, were extracted from each ROI and

subsequently used to generate spectral end- member maps showing their spatial distribution in the sample. End-member spectra were identified using the Minimum Noise Fraction Transformation (MNF) function and Pixel Purity Index (PPI) algorithm (Kruse et al. 1993; Rowan et al. 2004) in ENVI, and maps were generated using the Spectral Angle Mapper (SAM) supervised classification method (Green et al. 1988). The spectral end members, which were defined by averaging from 50 to 1000 pixels, were in some cases, single phases, but more often were mixed phase assemblages (particularly where sample were dominated by fine-grained materials too small to be resolved at the MMI). Spectral end-members were strongly related to microtextural domains and when mapped to the sample or surface material, helped define the paragenesis of the rocks and soils. A more detailed description of the methods used to extract the end-member spectra as well as map the distribution of the end-members using the SAM method in ENVI is provided in Núñez et al. (manuscript in review, 2012).

To identify minerals present in samples, each end-member spectrum was compared to library spectra from the USGS spectral library (Clark et al. 2007), convolved to the MMI wavelength range and resolution. For this step in the analysis, we used the Spectral Analyst tool in ENVI to identify best– fit minerals (or in some cases, whole rocks). The Spectral Angle Mapper (SAM) and Spectral Feature Fitting (SFF) methods within the Spectral Analyst tool were used to rank the match of each end-

member spectrum, in comparison with those in the spectral library. The suggested spectral library matches were ranked in order of best-to-worst match. Spectra of the suggested spectral library matches and spectral end-members were visually compared to identify the best-fit mineral identifications, based on absorption band center position and band width, whether mineral(s), mineral group(s), assemblages or whole rock. Careful consideration was taken to make sure that the suggested matches “made sense” in relationship to the inferred rock origin, based on the geologic context, microtexture, and general composition, within the limitations of the wavelength range and resolution of the MMI.

4.3. Results

In this section we provide results obtained with the Multispectral Microscopic Imager (MMI) for selected rocks samples and outcrops studied during the 2010 ILSO-ISRU and 2011 Desert RATS field tests. The results are analyzed to assess the effectiveness and performance of the MMI in providing petrogenetic information of rocks and soils at the hand lens scale under field conditions, with little or no sample preparation and under bright daylight illumination and simulated mission constraints.

4.3.1. MMI Results from 2010 ILSO-ISRU Field Test

During the 2010 ILSO-ISRU field test on the slopes of Mauna Kea volcano, Hawaii, the MMI participated in daily simulations of mission activities, in coordination with other instruments (e.g., ten Kate et al. in press). Objectives were to locate, identify and characterize the near

surface regolith at the primary field test site (labeled Site 1 in Figure 4.1), which provided feedstock materials for the ISRU experiments used during the test (Sanders et al. 2011). Although the feedstock for the ISRU oxygen production plant was pre-selected before the field test, the operations simulated *in-situ* scientific exploration and characterization and "prospecting" for feedstock materials for the ISRU oxygen production units. Geologic materials with a high total iron and ilmenite ($FeTiO_3$) contents make good feedstock for oxygen production by the hydrogen reduction process (e.g., Allen et al. 1993, 1994, 1996). Presented below are results from *in-situ* investigations with the MMI of the surface regolith at the test site (labeled Site 1 in Figure 4.1), as well as from an exposed 50 cm meter section of basaltic pyroclastic deposits at the foot of a cinder cone, north east of the test site (labeled Site 2 in Figure 4.1). Because the MMI operates by illuminating a surface using LEDs, artificial ambient light, or daylight illumination is significantly stronger and poses a challenge for collecting data with sufficient SNR, unless ambient light intensity is reduced using a sunshade (see Figure 4.2). While a rigid sunshade helps reduce ambient light, such design usually fail due to light leakage resulting from an inability to form a perfect seal with irregular substrates encountered with natural soils or rock surfaces. Assessing field performance of the MMI under full daylight illumination, and in imaging unprepared, irregular surfaces was, therefore, a major focus of this field test.

4.3.1.1. Site 1 – ISRU Feedstock Material

The surface regolith material was imaged with the MMI *in-situ* at the Test Site 1 (Figure 4.1). This provided an opportunity to image surface feedstock materials under full daylight illumination and significant surface roughness.

MMI-generated color composite images and a corresponding spectral end-member map of surface regolith are shown in Figure 4.4. Included is a visible color (RGB composite) image (Figure 4.4A), consisting of MMI bands 0.641, 0.522, and 0.463 μm, to simulate natural-color. Also presented is a visible/near-infrared RGB composite image (Figure 4.4B) consisting of MMI bands 1.43, 0.908, and 0.525 μm. This band combination emphasizes subtle color differences arising from spatial variations in mineral composition. Figure 4.4D shows a spectral end-member map generated in ENVI using a supervised classification with the ROIs shown in Figure 4.4C. Figure 4.5 shows plots of each end-member spectra, along with matching library spectra from the USGS spectral library.

The MMI images reveal the surface sediments at the test site consist of a poorly-sorted volcaniclastic conglomerate (Figure 4.4A). The coarser size fraction consists of subrounded clasts of coarse sand to small pebbles with light-toned, to rust-colored alteration rinds (in visible color RGB image, Figure 4.4A). The matrix of this sediment consists of angular to sub-rounded sand grains that generally lack alteration rinds. In the

visible/near-infrared color composite image (Figure 4B), grains making up the matrix appear dark blue in color. The finest fraction of the matrix appears to be a mixture of: 1) dark (possibly unaltered) sand grains similar in color to the larger, dark clast in the image; 2) lighter-toned grains showing rust-colored alteration coatings, or altered grain interiors, and 3) a poorly characterized reddish matrix material of silt to clay-sized particles that is too fine to resolve with the MMI. The dark pebbles of this sample are finely porphyritic and contain microlites of light-toned plagioclase feldspar in a black aphanitic, to glassy matrix. The surface materials at this site also contain fine-grained dark, opaque grains (possibly magnetite and/or ilmenite) which, along with the pebbles, appear to form a surface lag that has been concentrated by wind erosion.

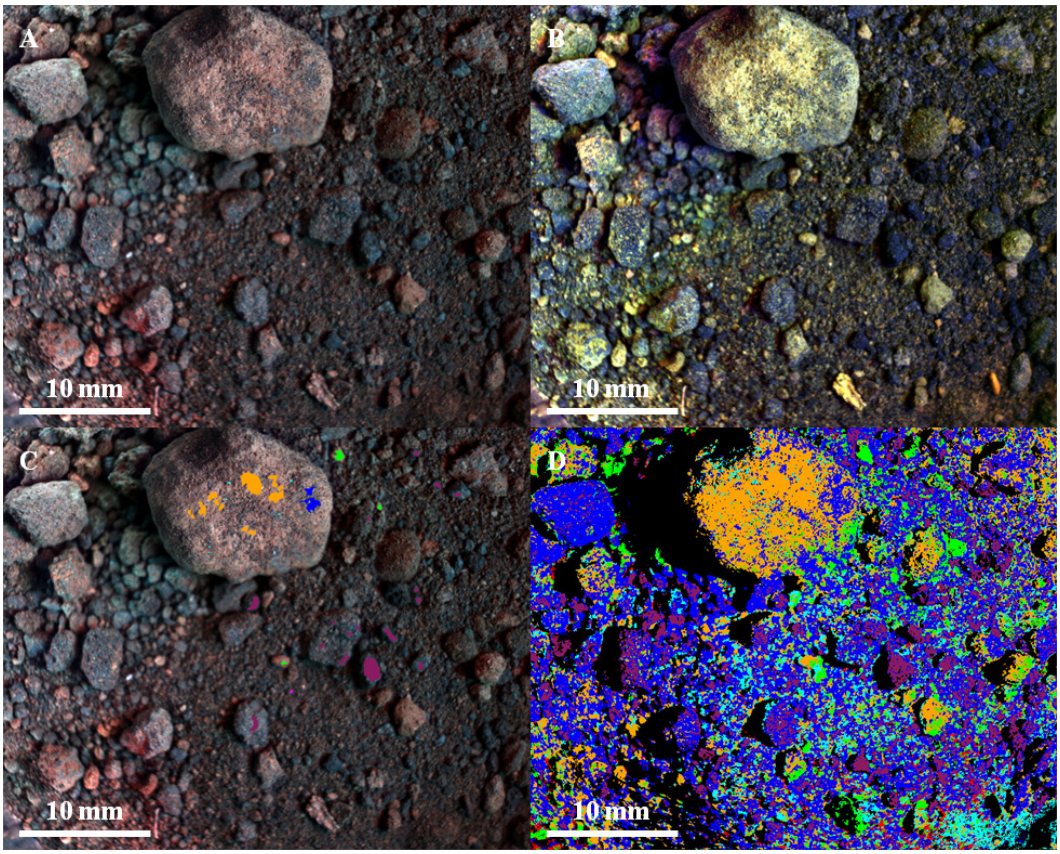

Figure 4.4. MMI-Generated Color Composite Images and End-Member Map of Site 1. MMI-generated color composite images (A & B) and corresponding spectral end-member map (D) based on supervised classification with ROIs as input parameters (C) of surface regolith (Site 1) that served as ISRU feedstock material. MMI Image size is 40x32 mm at 62.5 µm/ pixel. Figures A-B are linear stretched. Figure 4.4A: Visible-color RGB composite image composed of MMI bands 0.641, 0.522, and 0.463 µm respectively to simulate true-color. Figure 4.4B: False-color RGB composite image composed of MMI bands 1.43, 0.908, and 0.522 µm respectively to bring out subtle color differences in materials due to variations in composition. Figure 4.4C: Visible-color RGB composite similar to figure A with regions of interest (ROIs) used to generate end-member map (Figure 4.4D) and spectral end-members (Figures 4.5A). Figure 4.4D: End-member map generated in ENVI using supervised classification with ROIs as input parameter to map end-members distribution.

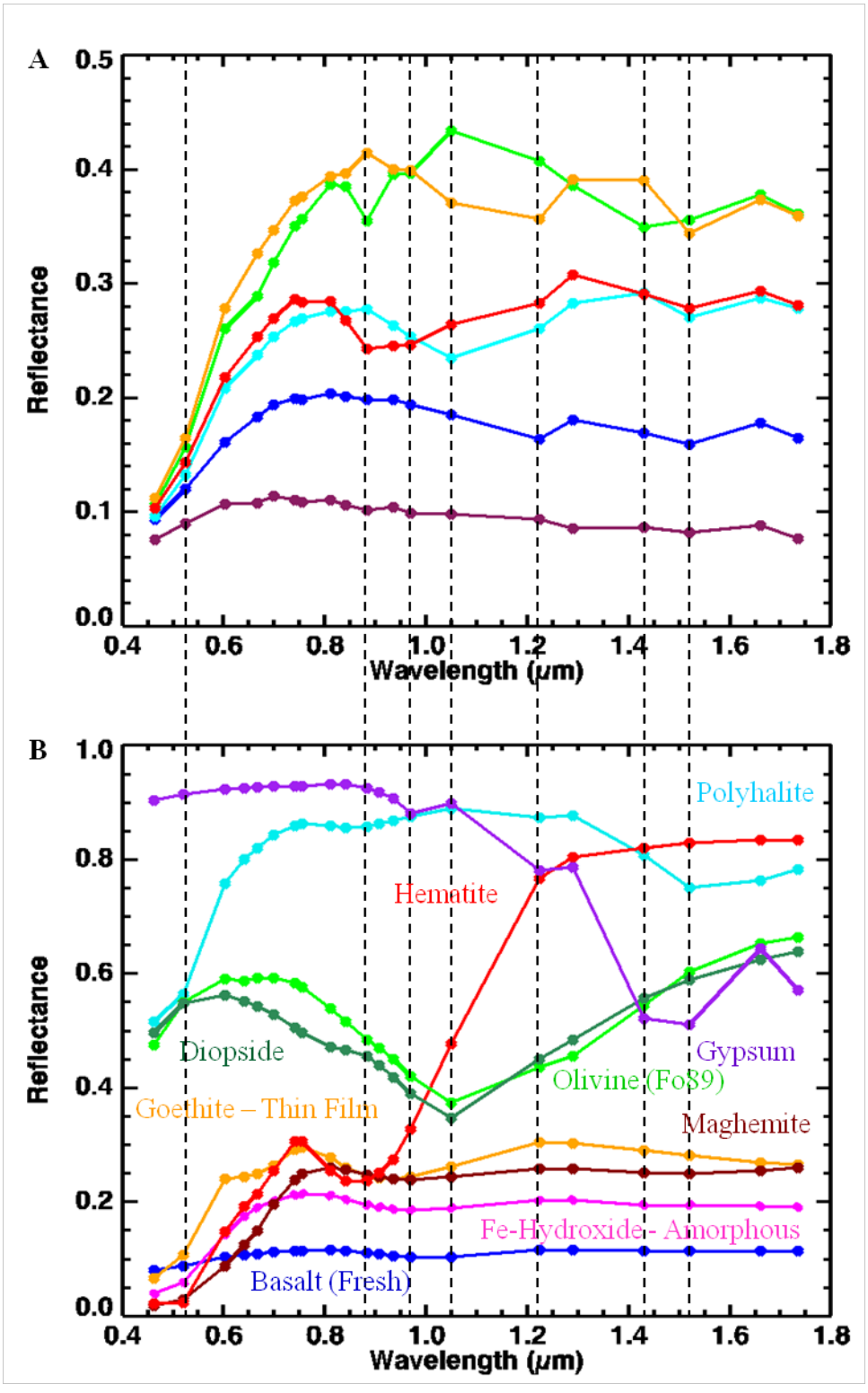
A
Reflectance
Wavelength (μm)
B
Reflectance
Wavelength (μm)
Polyhalite
Hematite
Diopside
Gypsum
Olivine (Fo89)
Goethite – Thin Film
Maghemite
Fe-Hydroxide - Amorphous
Basalt (Fresh)

Figure 4.5. MMI-Generated Spectra of End-Members of Site 1 Compared to Library Spectra. MMI-generated spectra of end-members (A) of surface regolith (Site 1) that served as ISRU feedstock material (Figure 4.4) and representative matching library spectra convolved to MMI bandpasses in table 1 (B). Vertical lines correspond to MMI bands 0.522, 0.884, 0.97, 1.05, 1.224, 1.43, and 1.521 μm. See text for details on features and discussion.

Spectral analysis reveals the presence of six end-members, two associated with the dark-colored materials and four with the light-toned surface coatings and reddish matrix material (Figures 4.4D and 4.5A).

The end-member associated with the darker clasts is mapped in the spectral end member map as maroon. This end-member shows a flat, low reflectance spectrum with no apparent absorption features (Figure 4.5A), consistent with glassy basalt.

The dark blue spectral end-member is associated with lighter-toned clasts in Figure 4.4B. Similar to the maroon end-member, the spectrum has a relatively flat shape that is also consistent with glassy basalt. However, unlike the maroon end-member, these clasts have a higher reflectance, with absorptions at 1.224 and 1.521 μm. These absorptions are consistent with a hydrated surface coating, including the sulfate, gypsum.

The orange end-member is associated with clasts having light-toned to rust-colored alteration rinds (Figure 4.4A). It is characterized by a high reflectance and absorptions at 1.05, 1.224 and 1.521 μm. These spectral features are consistent with halide, or sulfate salts that have

precipitated on grain surfaces by the evaporation of pore water within the upper capillary fringe zone of the regolith. Halite is not a hydrated phase. However, if it shows a hydration feature as the example from the spectral library shows (Figure 4.5), it must be from fluid inclusions present. A minor absorption edge at 0.522 μm is also present, which is due to the presence of nanophase Fe-oxides (e.g., Morris et al. 1993) and is consistent with the rust color in the visible color image (Figure 4.4A). The 1.05 μm absorption may be contributed by a primary mafic mineral, such as high-Ca pyroxene, or olivine, which is present in the unweathered host rock. An alternative interpretation suggests that the 1.05 μm absorption is contributed by amorphous Fe-oxides, which would also be consistent with the rust color in the visible color image (Figure 4.4A).

The green end-member is associated with light-toned matrix materials. It has a high reflectance similar to the orange end-member, but with absorptions at 0.884, 0.97, and 1.43 μm. These absorptions are consistent with Fe-oxide (e.g. hematite), plus oxyhydroxide and another hydrated mineral, possibly a clay mineral, or a hydrated silicate (e.g. opaline silica).

The red end-member is associated with some of the rust-colored grains (Figure 4.4A). It shows absorptions at 0.884, 0.97, 1.224 and 1.521 μm, which are consistent with an Fe-oxide (as hematite) and oxyhydroxide, as well as a hydrated salt, possibly as a halide or sulfate.

The light blue end-member is associated with some of the lighter clasts and matrix materials. It is characterized by a high reflectance and a strong absorption at 1.05 μm, along with weaker absorptions at 1.224 and 1.521 μm. Similar to the orange and red end-members, the high reflectance, with absorptions at 1.224 and 1.521 μm, is consistent with a hydrated salt, possibly a halide, or sulfate. However, the strong 1.05 μm suggests a mafic mineral, such as high-Ca pyroxene, or olivine.

4.3.1.2. Interpretation of MMI Results

The surface regolith at the main mining site for the Hawaii ISRU test consists of poorly-sorted volcaniclastic materials ranging in grain size from pebbles to sand. The lighter-toned subrounded clasts in this surface assemblage have coatings of halide and/or sulfate salts, as well as Fe-oxides and oxyhydroxides. Salts may have precipitated on grain surfaces by the evaporation of pore water within the upper capillary fringe zone of the soil. In contrast, the Fe-oxide and oxyhydroxide coatings are a result of hydration and oxidation reactions from water-mediated weathering processes. The fine sand matrix component appears to be a mixture of: 1) dark (unaltered), glassy basalt grains, 2) basalt grains with coatings of hydrated sulfate salts and Fe-oxides/oxyhydroxides, and 3) a poorly characterized reddish matrix material of silt to clay-sized particles composed of Fe-oxides/oxyhydroxides and clay minerals.

4.3.1.3. Site 2 – Stratigraphic Section

The MMI investigation at Site 2 (Figure 4.1) provided an opportunity to use the MMI in its field-deployed configuration to create an image mosaic of a 50 cm high outcrop exposure of bedded volcaniclastic rocks. This stratigraphic section exposed a range of textures and compositions exposed in a small gully that has cut into the basal units of a cinder cone. This site provided a unique opportunity to evaluate the capabilities of the MMI to image a rough, vertical surface under daytime illumination (Figure 4.2) and to create a large image mosaic using the mechanical positioning of the camera to produce overlapping microscale images covering the entire 50 cm stratigraphic section (Figure 4.6). The mosaic was stitched together from 17 overlapping MMI images obtained from the vertical section. The left images consists of visible color bands (RGB = 0.63, 0.525, 0.465 μm), to simulate natural color, while the right column shows images created using visible and near-infrared bands (RGB = 1.43, 0.908, 0.525 μm). The red boxes highlight units with distinctive microtextural and compositional features for three major regions of the mosaic: 1) Upper section, 0-4 cm from top of section, 2) Middle section, 12-16 cm from top and 3) Bottom Section: 45-49 cm from top (Figure 4.6). The boxed areas are shown at higher resolution in individual MMI images in Figure 4.7.

MMI-generated color composite images and a corresponding spectral end-member map of the top (0-4 cm from top), middle (12-16 cm from top), and bottom (45-49 cm from top) sections of the outcrop are

shown in Figure 4.7. The map is based on a supervised classification using ROIs as input parameters. Included are visible-color RGB composite images composed of MMI bands 0.63, 0.525, and 0.465 μm, to simulate natural-color and visible/near-infrared RGB color composite images composed of MMI bands 1.43, 0.908, and 0.525 μm, to bring out subtle color differences in materials arising from spatial variations in mineral composition within each section (Figure 4.7: A-B, D-E, G-H). Figures 4.7C, 4.7F, and 4.7I (as well as Figures 4.8A, 4.8C, and 4.8E) show spectral end- member maps generated in ENVI using a supervised classification with ROIs (not shown) as input parameters for mapping end-member distributions. Figure 4.8 shows the end-member maps for each domain (same as Figures 4.7C, 4.7F, and 4.7I), along with spectral plots for the corresponding end-member spectra (Figures 4.8B, 4.8D, and 4.8F). Matching library spectra from the USGS spectral library are not shown for this example due to space limitations; however, they are discussed in the text below.

4.3.1.3.1. MMI Observations of Upper Section (0-4 cm from Top) of Outcrop

The MMI images for the Upper Section (Figures 4.7A-B) show rounded lapilli-sized clasts in a beige, fine-grained matrix. The matrix component consists of fine-sand to clay sized grains and is light-red in the stretched visible color composite image (Figure 4.7A). The sediment is poorly sorted and shows a matrix-supported fabric. The clasts show fine-

grained coatings that are similar in color to the matrix, limiting observation of underlying materials. Where exposed, fresh rock surfaces are dark gray in color in the visible color composite image (Figure 4.7A) and have a fined-grained, ”aphanitic” microtexture. These clasts appear dark blue in the visible/near-infrared color composite image (Figure 4.7B). Small roots from surface vegetation can be seen in the upper left portion of the image (Figures 4.7A and 4.7B). No fine-scale internal layering is visible.

Spectral analysis reveals the presence of eight spectral end-members associated with the upper part of the section (Figure 4.8, A-B). The green and orange end-members correspond to half of the surface imaged with the MMI, including the beige matrix and surface coatings of the rounded lapilli-sized clasts. With minor exceptions, the spectra show similar reflectance and spectral shapes. Both have an absorption edge at 0.525, a peak at 0.811, and absorptions at 0.884, 0.97, and 1.43 μm. The green end-member has a broader absorption at 1.43 μm, encompassing the 1.29 μm band. These features are consistent with library spectra for Fe-oxides/oxydroxides such as hematite and ferrihydrite, and another hydrated mineral, possibly a clay mineral. The absorption edge at 0.525 μm may also be attributed to the presence of nanophase Fe-oxides (e.g., Morris et al. 1993).

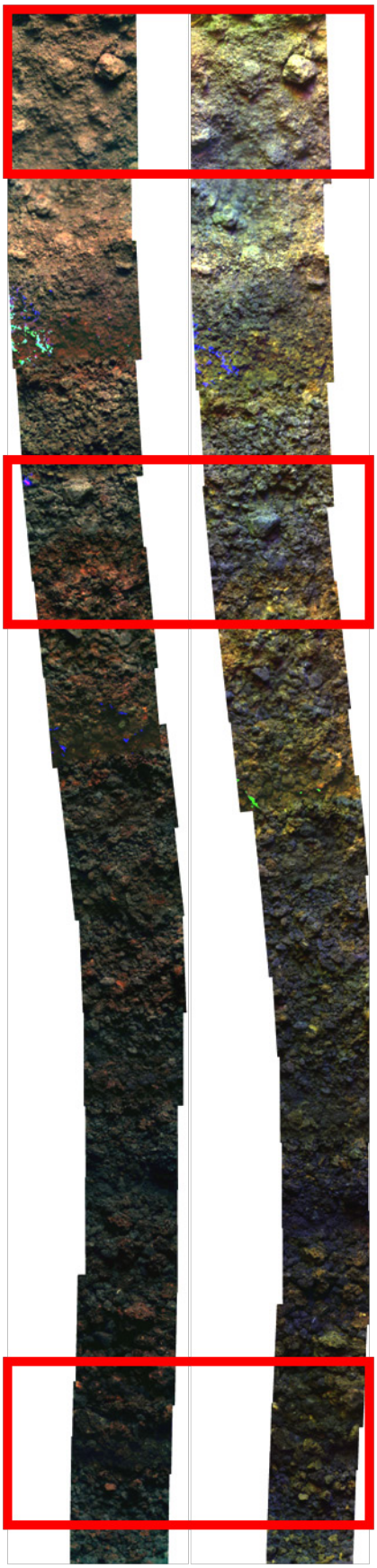

Figure 4.6. Mosaic of MMI Images of 50 cm Vertical Section in Site 2. Mosaic of microscale multispectral reflectance images obtained with the MMI deployed on a 50 cm high outcrop of layered pyroclastic deposits on the flanks of a volcano (Site 2, Figure 4.1A). The mosaic was stitched together from 17 overlapping MMI images obtained along the entire stratigraphic section. The left images consist of visible color bands (RGB = 0.63, 0.525, 0.465 μm), to simulate natural color, while the right column shows images in visible and near-infrared bands (RGB = 1.43, 0.908, 0.525 μm) bring out subtle color differences in materials due to spatial variations in mineral composition. The red boxes highlight distinct textural and mineralogical domains along the top (0-4 cm from top), middle (upper middle, 12-16 cm from top) and bottom (45-49 cm from top) sections of the outcrop that are visible in the mosaic and which are expanded and shown in more detail at higher magnification as individual MMI images in Figure 4.7. Warped view of the section is due to offset positioning of the instrument along the vertical face.

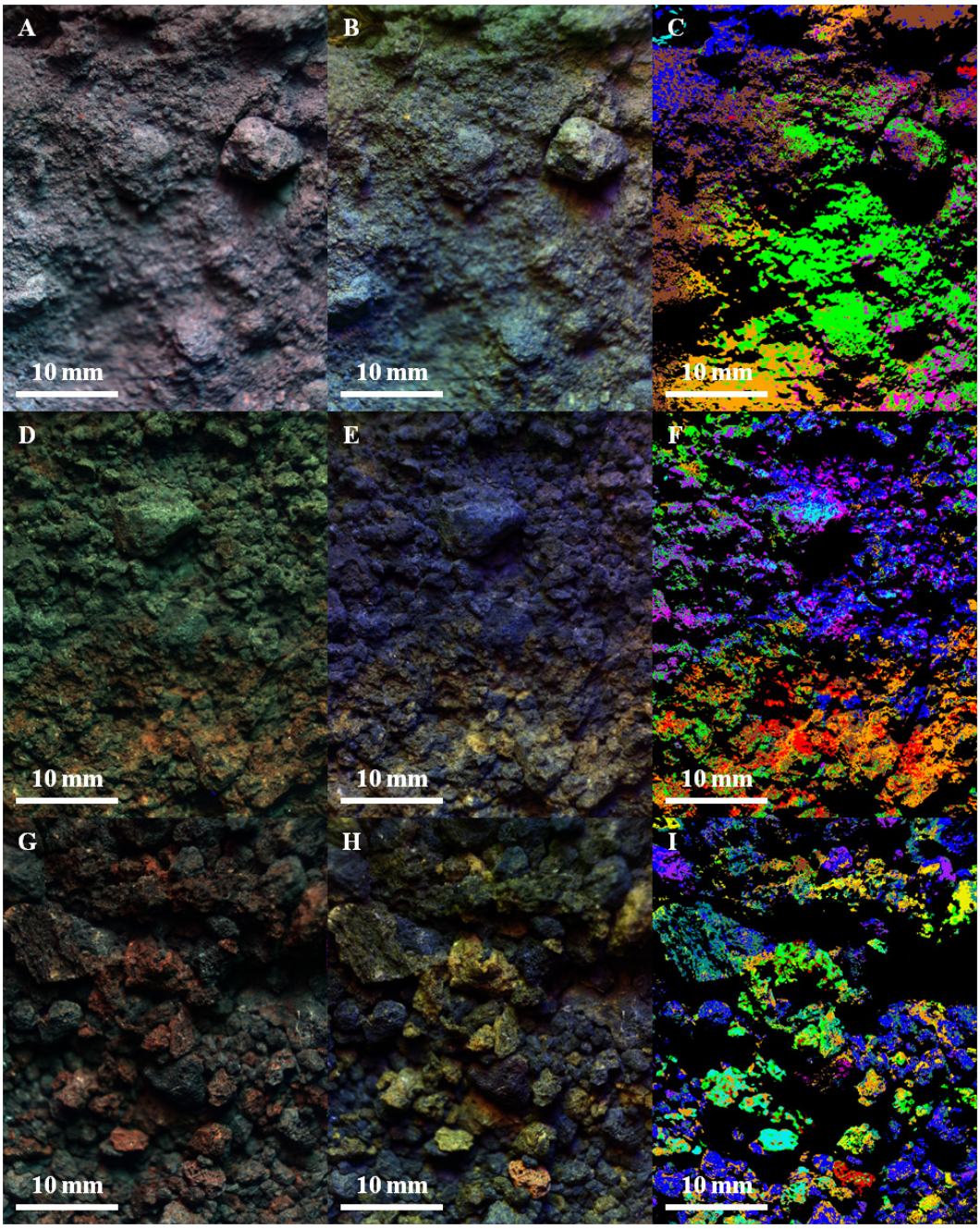
A
10 mm
B
10 mm
C
10 mm
D
10 mm
E
10 mm
F
10 mm
G
10 mm
H
10 mm
I
10 mm

Figure 4.7. MMI-Generated Color Composite Images and End-Member Map of Top, Middle, and Bottom Sections of Vertical Section in Site 2. MMI-generated color composite images (A-B, 6D-E, 6G-H) and corresponding spectral end-member maps (C, F, G) of the top (A-C; 0-4 cm from top), middle (D-F; upper middle, 12-16 cm from top), and bottom (G-I; 45-49 cm from top) sections of the outcrop (marked by red boxes in Figure 6) based on supervised classification with ROIs as input parameters (not shown) of 50 cm tall section of pyroclastic deposits. MMI Image size is 40x32 mm at 62.5 µm/ pixel. Figures A-B, D-E, and G-H are linear stretched. Included are visible-color RGB composite images composed of MMI bands 0.63, 0.525, and 0.465 µm (respectively), to simulate natural-color (Figures A, D, G) and false-color RGB composite images composed of MMI bands 1.43, 0.908, and 0.525 µm (respectively), to bring out subtle color differences in materials due to spatial variations in mineral composition (Figures B, E, H). Figures C, F, and I show spectral end- member maps generated in ENVI using a supervised classification with ROIs (not shown) as input parameters for mapping end-member distributions. Plots of end-members are shown in Figure 4.8.

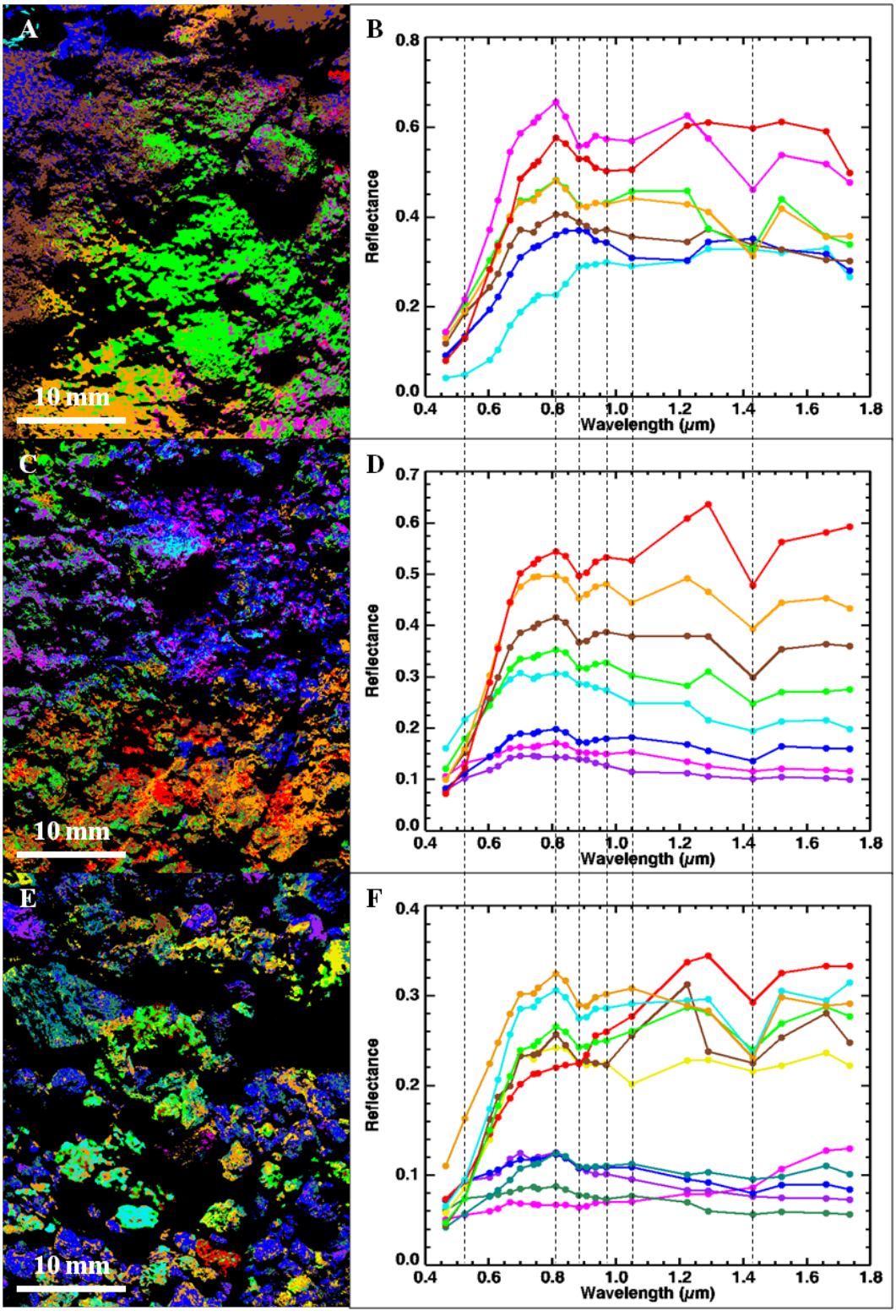
A
10 mm
B
Reflectance
Wavelength (μm)
C
10 mm
D
Reflectance
Wavelength (μm)
E
10 mm
F
Reflectance
Wavelength (μm)

Figure 4.8. MMI-Generated End-Member Maps and Spectra of Top, Middle, and Bottom Sections of Vertical Section in Site 2. MMI-generated end-member maps (A, C, E) and corresponding spectra (B, D, F) of end-members of top (A; 0-4 cm from top), middle (C; upper middle, 12-16 cm from top), and bottom (E; 45-49 cm from top) sections of the outcrop (marked by red boxes in Figure 4.6). Representative matching library spectra convolved to MMI bandpasses are not shown due to space limitations. Vertical lines correspond to MMI bands 0.522, 0.811, 0.884, 0.97, 1.05, and 1.43 μm. See text for details on features and discussion.

The red end-member corresponds to small domains of bright-red material (in the visible color image, Figure 4.6A). The spectrum is characterized by an absorption edge at 0.525, a peak at 0.811, a broad absorption at 0.97 and 1.05 μm, and a weak absorption at 1.43 μm. The spectrum is consistent with ferrihydrite. The absorption edge at 0.525 μm also suggests the presence of nanophase Fe-oxides (e.g., Morris et al. 1993).

The magenta end-member corresponds to fine grained, light-red materials in the matrix (see visible color image, Figure 4.7A). The spectrum is characterized by an absorption edge at 0.525, a peak at 0.811, a broad absorption at 0.97 and 1.05 μm, and absorptions at 0.884 and 1.43 μm. The spectrum is consistent with the presence of hematite, ferrihydrite and a hydrated mineral, possibly a clay mineral. The absorption edge at 0.525 μm is attributed to the presence of nanophase Fe-oxides (e.g., Morris et al. 1993).

The dark blue and brown end-members correspond to the material in the upper part of the image. Both spectra have an absorption edge at 0.525 and broad absorptions at 1.05 and 1.224 μm. Spectra are consistent with the presence of nanophase Fe-oxides/oxyhydroxides (e.g., Morris et al. 1993), and pyroxene or olivine.

The light-blue end-member corresponds to the plant root in the upper left part of the image and is consistent with library spectra for vegetation (library spectrum not shown due to space limitations).

4.3.1.3.2. MMI Observations of Middle Section (12-16 cm from Top) of Outcrop

The MMI images for the Middle Section (Figures 4.7D-E) reveal two distinct layers, a dark, to light-grey layer and a reddish layer (see visible color composite, Figure 4.7D) towards the top and in the bottom half of the images. The dark, to light-grey layer is clast-supported lapillistone, containing angular to subrounded, dark, to light-grey colored lapilli-sized pyroclasts, surrounded by a moderately well-sorted, ash matrix. Some pyroclasts are coated by a thin layer of white, fine-grained material, which imparts a light-toned color to the clasts. Where freshly exposed, rock surfaces are dark gray in color (see visible color composite, Figure 4.7D), showing an aphanitic texture. Clasts appear dark blue in the visible/near-infrared color composite image (Figure 4.7E).

The reddish layer is also a clast-supported lapillistone with angular to subrounded, dark to light-grey lapilli-sized clasts, in moderately sorted, fine grained ash matrix. However, many of the clasts are coated with fine-grained reddish material. The fine-grained coating also fills the space between pyroclasts. The reddish material appears yellow in the visible/near-infrared color composite image (see Figure 4.7E).

Spectral analysis of the middle section reveals the presence of eight spectral end-members, with four corresponding to the upper dark- to light-grey layer and four, to the lower reddish layer (Figure 4.8, C-D).

The blue, purple and magenta end-members map to the dark clasts. All have a relatively flat spectrum, with low reflectance. The purple spectrum has an absorption at 1.05 μm, while the magenta and blue spectra have absorptions at 0.884 and 1.43 μm (stronger for the blue end-member). The spectra are consistent with both fresh and weathered basalt. The 0.884 and 1.43 μm absorptions are consistent with hematite and a hydrated mineral, respectively, while the 1.05 μm absorption is consistent with high-Ca pyroxene, or olivine.

The light-blue end-member corresponds to the thin fine-grained, white-colored material coating some of the dark clasts. The spectrum has a negative slope towards the infrared, with absorptions at 1.05 and 1.43 μm, consistent with pyroxene or olivine, plus a hydrated mineral (possibly as opaline silica).

The brown, orange and red end-members are associated with the reddish matrix and clast-coating materials. They all have similar spectral shapes and absorptions, with a few notable differences. All of these spectra have a higher reflectance curve, compared to spectra of the dark clasts, as well as an absorption edge at 0.525, a peak at 0.811 and absorptions at 0.884 and 1.43 μm. However, the orange and red spectra also show an absorption at 1.05 μm, while the brown spectrum does not. The absorptions at 0.884 and 1.43 μm are consistent with hematite and a hydrated mineral, respectively, while the 1.05 μm absorption is consistent

with pyroxene, or olivine. The absorption edge at 0.525 μm suggests the presence of nanophase Fe-oxides/oxyhydroxides (e.g., Morris et al. 1993).

The green end-member has a spectrum that is similar to the brown end-member, with a peak at 0.881 and absorptions at 0.884 and 1.43 μm. However, it has a negative slope towards the infrared with an additional absorption centered at 1.224 μm. The absorptions at 0.884 and 1.43 μm are consistent with hematite and a hydrated mineral, respectively. The 1.224 μm absorption could be due to plagioclase feldspar, or if combined with the 1.43 μm absorption, a hydrated mineral different from the one in the brown, orange and red end-members.

4.3.1.3.3. MMI Observations of Lower Section (45-49 cm from Top) of Outcrop

The MMI images for the Lower Section (Figures 4.7G-H) reveal dark-grey, and dark-red colored, lapilli-sized pyroclasts within a clast-supported fabric (see visible color composite, Figure 4.7G). Layers show moderate- to well-sorted angular pyroclasts, with vesicular textures. Some clasts are coated by a thin layer of white, fine-grained material that imparts a light-grey color to the clasts. Freshly exposed rock surfaces are dark gray in color (see visible color composite, Figure 4.7G) with an aphanitic texture. The dark gray pyroclasts appear dark blue in the visible/near-infrared color composite image (Figure 4.7H). In contrast, the dark-red clasts appear yellow in the visible/near-infrared color composite image

(Figure 4.7H). Unlike the upper and middle sections, there is little fine-grained material filling the spaces between clasts in the lower section.

Spectral analysis reveals the presence of eleven spectral end-members associated with the lower section, of which five correspond to the dark clasts and six to the reddish clasts (Figure 4.8, E-F).

The blue, dark green, purple and turquoise colored end-members have similar-looking, low reflectance spectra. The blue, purple and turquoise spectra have absorptions at 0.884 and 1.43 μm (stronger for the blue end-member). The spectrum for the blue end-member is similar in shape to the blue end-member seen in the middle section. The dark green end-member has weaker absorptions at 0.97 and 1.43 μm, compared to the blue end-member. The spectra are consistent with both fresh and weathered basalt. The 0.884 and 1.43 μm absorptions are consistent with hematite and a hydrated mineral, respectively, while the 0.97 μm absorption along with the lack of an absorption edge at 0.525 μm is consistent with a ferrous silicate mineral, best matched with pyroxene.

The orange, light blue, light green, and brown end-members are associated with the reddish clasts. Their spectra have relatively similar shapes and absorptions, with a few notable differences. All have a higher reflectance than the spectra associated with the dark clasts, as well as an absorption edge at 0.525, a peak at 0.811 and absorptions at 0.884 and 1.43 μm. The brown end-member is also characterized by an absorption at 0.97 μm and a broader absorption at 1.43 μm. The absorptions at 0.884

and 1.43 μm are consistent with hematite and a hydrated mineral, respectively, while the 0.811 μm peak and 0.97 μm absorption are consistent with ferrihydrite. The absorption edge at 0.525 μm may also be explained by the presence of nanophase Fe-oxides/oxyhydroxides (e.g., Morris et al. 1993).

The red end-member is associated with the light-red clast towards the bottom of the visible/near-infrared color composite image (Figure 4.7H). Unlike the orange, light blue and light green end-members, the red end-member spectrum is characterized by a strong spectral slope towards the infrared, along with an absorption edge at 0.525 μm and absorptions at 0.884, 0.97 and 1.43 μm. The absorptions at 0.884 and 1.43 μm are consistent with hematite and a hydrated mineral respectively, while the absorption at 0.97 μm, along with the shape of the spectrum, is consistent with ferrihydrite. The absorption edge at 0.525 μm may be explained by the presence of nanophase Fe-oxides/oxyhydroxides (e.g., Morris et al. 1993).

The yellow end-member is associated with the reddish material towards the top-right part in the natural color image (Figure 4.7G). The spectrum has a high reflectance, along with an absorption edge at 0.525, a peak at 0.811 and absorptions at 0.884, 1.05 and 1.43 μm. The absorptions at 0.884 and 1.43 μm are consistent with hematite and a hydrated mineral, respectively, while the absorption at 1.05 μm is consistent with pyroxene, or olivine. The absorption edge at 0.525 μm may

be explained by the presence of nanophase Fe-oxides/oxyhydroxides (e.g., Morris et al. 1993).

4.3.1.4. Interpretation of MMI Results

The general results for the stratigraphic section described above indicate that it consists of layered pyroclastic deposits, dominated by poorly sorted, angular to subangular, lapilli-sized, basalt pyroclasts with vesicular textures. Alternating layers of angular pyroclastic material in the lower 2/3 of the section and clast-supported fabrics, are consistent with an origin from a series of volatile-rich, explosive volcanic eruptions and deposition as an airfall tuff. The location of the outcrop within a water-carved channel on the flank of a cinder cone provides a strong supporting context for this interpretation. However, the upper 1/3 of the section is different, being dominated by matrix-supported fabrics, better sorting and clast shapes that are more rounded. A thin light toned bed which caps the whole sequence is a well-sorted fine sandstone that shows small scale cross bedding. These features are more consistent with water transport and deposition by a combination of channelized flow and slope wash. In addition, the abundance of Fe-oxides coating clasts and including a significant hydrated mineral (possibly clay mineral) component indicates a greater degree of water-mediated, *in situ* weathering (by hydration/oxidation reactions) during diagenesis.

To test these depositional hypotheses will require broader stratigraphic sampling to build up an inventory of local and regional

observations to further constrain events in local geologic history. However, this example serves to demonstrate how the MMI can contribute to such efforts, which lie at the heart of planetary exploration.

4.3.2. MMI Results from the 2011 Desert RATS Field Test

During the 2011 Desert RATS field test, samples were collected by astronaut crew members at sites on the Black Point Lava Flow, in northern Arizona (Figure 4.1). These samples were subsequently examined by the "back room" science team who prioritized them for further analysis. The prioritized sample suite was evaluated the following day by the same astronaut crew using instruments (including the MMI) housed inside the GeoLab in the Deep Space Habitat (DSH, Figure 4.2). Primary objectives for the GeoLab were to test science operations, including evaluating sample handling and characterization protocols, for a simulated mission to an asteroid. Additionally, the integration of new science instruments, including the MMI, into the sample processing workflow was also evaluated. Science operations with the GeoLab included single crew-member operations using a remotely-located science team, restricted operations time by the crew member limiting the number of samples processed in a day, and data transfer delay to remote science team (Evans et al. 2012). The 50 second one-way communications delay was not implemented during GeoLab operations. The MMI imaged rocks and soils, collected by the astronaut crews during EVAs, in support of science operations. The performance of the MMI to operate under the simulated

mission constraints and support science operations were evaluated. Analysis of MMI data collected from some examples is listed below.

4.3.2.1. MMI Observations of Basalt Sampled Inside the “Quarry”

On Test Day 1, sample 0002 was collected by an astronaut crew member from a basalt flow exposed in the north wall of the “Quarry” site in Figure 4.1. The sample was imaged the following day inside the GeoLab in the DSH, using the MMI (Figure 4.2).

Figure 9 shows MMI imaging data for sample 0002. Included is a visible color RGB composite image, composed of MMI bands 0.641, 0.522, and 0.463 μm, to simulate natural color and a visible/near-infrared color RGB composite image composed of MMI bands 1.521, 1.05, and 0.741 μm, to bring out subtle color differences in materials due to spatial variations in mineral composition (Figures 4.9A & 4.9B). Figure 4.9D shows a spectral end- member map generated in ENVI using a supervised classification from ROIs (Figure 4.9C). Figure 4.10 is a plot that shows the end-member spectra mapped in Figure 4.9D, along with matching library spectra from the USGS spectral library.

The MMI images reveal that the sample is a fine-grained (aphanitic), vesicular crystalline rock, most likely of basaltic composition (based on visible color, Figure 4.9A). Fresh rock surfaces are dark greenish gray in color (using visible color bands, Figure 4.9A). Vesicles range in size from ~1.5 mm to 8 mm in diameter, are nearly spherical in shape, with a vesicle density averaging 0.2 vesicles per cm^2. Vesicles

appear to be coated with a fine-grained yellowish–orange colored mineral. The matrix surrounding vesicles is finely crystalline (aphanitic) with abundant white-colored phenocrysts (avg. 1.5 mm). Additionally, smaller dark phenocrysts (not distinguishable from the surrounding matrix in the visible color RGB image, Figure 4.9A) appear purple in the visible/near-infrared color RGB image (Figure 4.9B).

Spectra were obtained for two major microtextural domains (matrix and vesicles) by averaging approximately 200-1200 pixels from Regions of Interest (ROIs) (Figure 4.9C). A spectral end-member map was generated in ENVI to show the spatial distribution of the different spectral types, using a supervised classification based on average spectra from the ROIs (Figure 4.9D). Finally, end member spectra were compared to spectra from the USGS Spectral Library, convolved to MMI spectral bandpasses.

Spectral analysis using the above methods showed that the matrix of the rock consists of two spectral end-members. The two components are visible as dark and light grey regions in the visible/near-infrared color composite image (Figure 4.9B), but are invisible in the visible color composite image (Figure 4.9A).

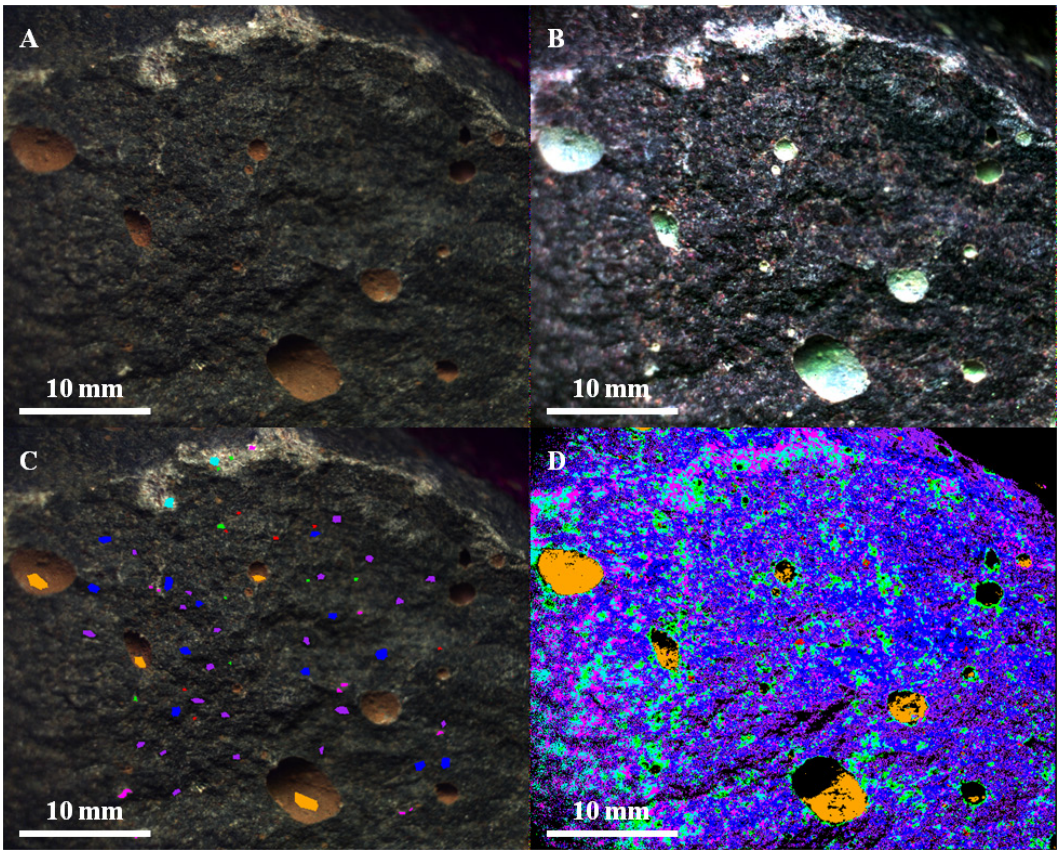

Figure 4.9. MMI-Generated Color Composite Images and End-Member Map of Basalt (Sample 0002). MMI-generated color composite images (A & B) and corresponding spectral end-member map (D) based on supervised classification with ROIs as input parameters (C) of basalt (sample 0002) sampled in the “Quarry” (location labeled in Figure 4.1B). MMI Image size is 40x32 mm at 62.5 µm/ pixel. Figures A-B are linear stretched. Figure 4.9A: Visible-color RGB composite image composed of MMI bands 0.641, 0.522, and 0.463 µm respectively to simulate true-color. Figure 9B: False-color RGB composite image composed of MMI bands 1.521, 1.05, and 0.741 µm respectively to bring out subtle color differences in materials due to variations in composition. Figure 4.9C: Visible-color RGB composite similar to figure A with regions of interest (ROIs) used to generate end-member map (Figure 4.9D) and spectral end-members (Figures 4.10A). Figure 4.9D: End-member map generated in ENVI using supervised classification with ROIs as input parameter to map end-members distribution.

The dark-grey matrix component is mapped as purple (=dark grey regions in natural color images), while the light-grey matrix component in natural color images is mapped as dark blue in the end member map. Together these spectral types account for most of the matrix component of the rock.

The spectrum of the dark component of the matrix (mapped as purple) shows a flat, low reflectance spectrum, with no apparent absorption features (Figure 4.10, top panel; Note: we interpret the feature at 1.66 μm to be a spectral artifact.). This flat spectrum is most likely due to volcanic glass. In contrast, the light-grey component in the matrix (mapped as blue in Figure 4.9D) also has a relatively flat, low reflectance spectrum (similar to purple spectrum), but with a small absorption at 1.05 μm. The absorption at 1.05 μm is consistent with the library spectrum for Fe^{2+} present as clinopyroxene, or olivine.

Similarly, the light-blue end-member also shows prominent absorption feature at 1.05 μm, consistent with library spectrum for clinopyroxene (best match, diopside). The spectrum of the light-green end-member is similar to the spectrum of the light blue end-member, but with a lower reflectance. As with the dark and light blue end members discussed above, there is a prominent absorption at 1.05 μm, consistent with library spectrum for clinopyroxene (possibly diopside).

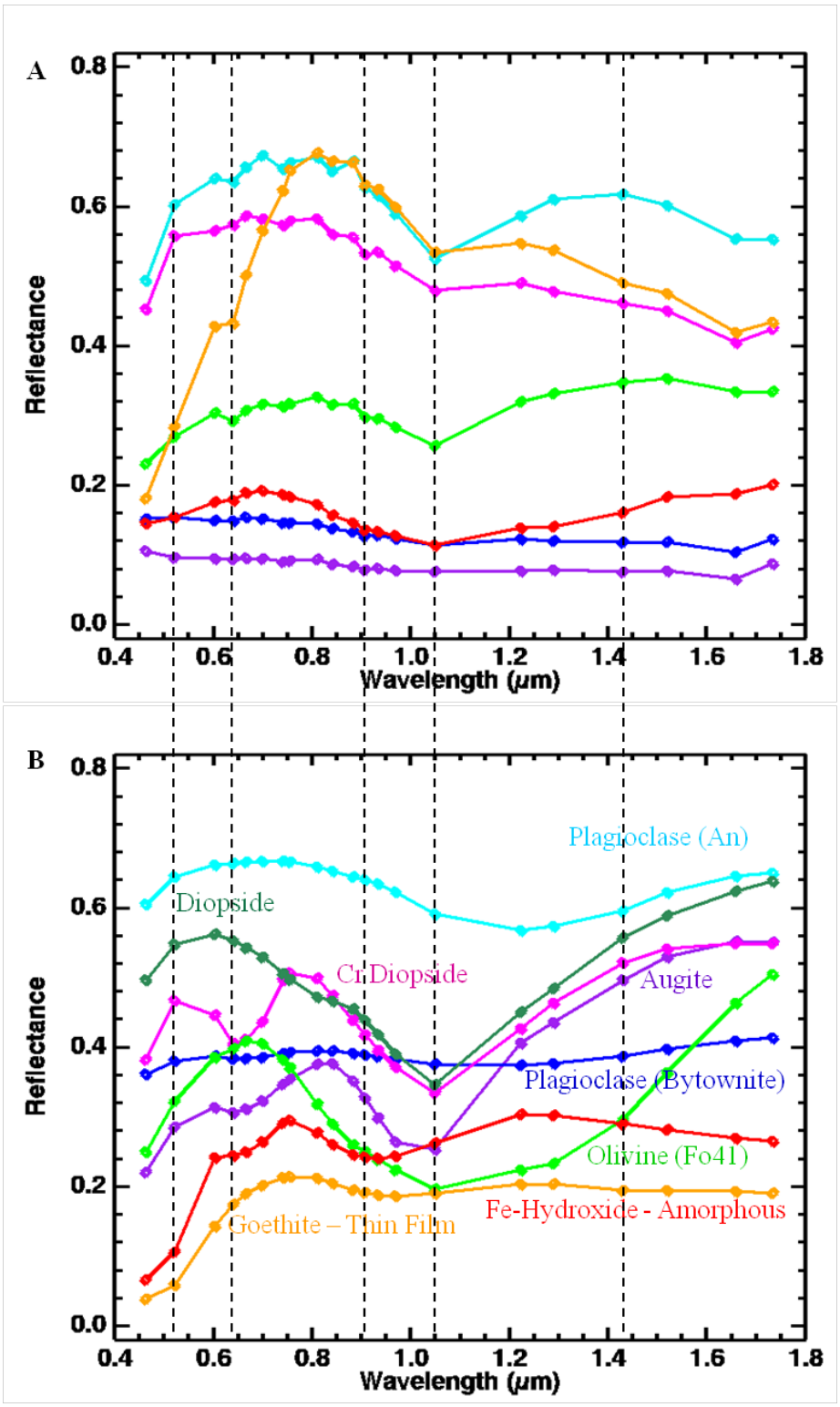
A
Reflectance
Wavelength (μm)
B
Reflectance
Wavelength (μm)
Plagioclase (An)
Diopside
Cr-Diopside
Augite
Plagioclase (Bytownite)
Olivine (Fo41)
Fe-Hydroxide - Amorphous
Goethite – Thin Film

Figure 4.10. MMI-Generated Spectra of End-Members of Basalt (Sample 0002) Compared to Library Spectra. MMI-generated spectra of end-members (A) of basalt (sample 0002; shown in Figure 4.9) sampled in the “Quarry” (location labeled in Figure 4.1B) and representative matching library spectra convolved to MMI bandpasses in Table 2.1 (B). Vertical lines correspond to MMI bands 0.522, 0.641, 0.908, 1.05, and 1.43 μm. See text for details on features and discussion.

The red end-member has a very broad absorption centered at 1.05 μm (broader than light blue and light green ROIs) with local maximum at 0.7 μm and positive slope towards the infrared. The spectrum is best matched with the library spectrum for olivine.

The magenta end-member is representative of the white-colored phenocrysts in the sample matrix (Figure 4.9A). The spectrum has a high reflectance curve with negative slope towards the infrared, and an absorption at 1.05 μm. The absorption at 1.05 μm is consistent with pyroxene or olivine (most likely contributed from surrounding dark minerals). The white color in the visible image and high reflectance spectrum suggest a match with plagioclase feldspar. However it is not possible to confirm due to the lack of diagnostic absorptions in the MMI range.

The orange end-member corresponds to the fine-grained, orange-colored material lining the walls of the vesicles. The spectrum has a steep positive slope from 0.463 to 0.811 μm and negative slope towards the infrared. The sample has a strong absorption at 1.05 μm and weak feature at 1.43 μm as well as a shoulder at 0.603 μm. The spectrum is most consistent with an Fe-hydroxide, either as poorly ordered ferrihydrite, or the crystalline phase, goethite. The feature at 1.05 μm is difficult to interpret, but could be contributed from pyroxene in the underlying groundmass, or nanophase Fe-oxides/oxyhydroxides (Morris et al. 1993).

4.3.2.2. Interpretation of MMI Results

The microtexture and composition of Desert RATS sample 0002, based on MMI results, is consistent with rapid cooling and crystallization of olivine-rich basaltic lava that had a moderate volatile content. The fine-grained yellowish-orange material lining the walls of the vesicles, is interpreted to have formed by the precipitation of Fe-oxydydroxides formed by the oxidative, aqueous weathering of the basaltic host rock.

4.3.2.3. MMI Observations of Sandstone Sampled near the “Pit”

Desert RATS sample 0035, was collected by an astronaut crew at station P20A. The rock unit is a cross-bedded, reddish-colored sandstone that underlies the capping basalt flow, north of the “Pit”, a small quarry southwest of the base camp (“Quarry” site in Figure 4.1). The sample was investigated with the MMI inside the GeoLab in the Deep Space Habitat (DSH) on Test Day 2 (Figure 4.2).

MMI data for Desert RATS sample 0035 are shown in Figure 4.11. Included is a visible color RGB composite image composed of MMI bands 0.641, 0.522, and 0.463 μm, to simulate natural-color and a visible/near-infrared color RGB composite image composed of MMI bands 1.521, 1.05, and 0.741 μm, to bring out subtle color differences in materials due to spatial variations in mineral composition (Figures 4.11A & 4.11B). Figure 4.11D shows a spectral end- member map generated in ENVI using a supervised classification of ROIs (Figure 4.11C). Figure 4.12 shows plots

for the corresponding end-member spectra, along with matching library spectra from the USGS spectral library.

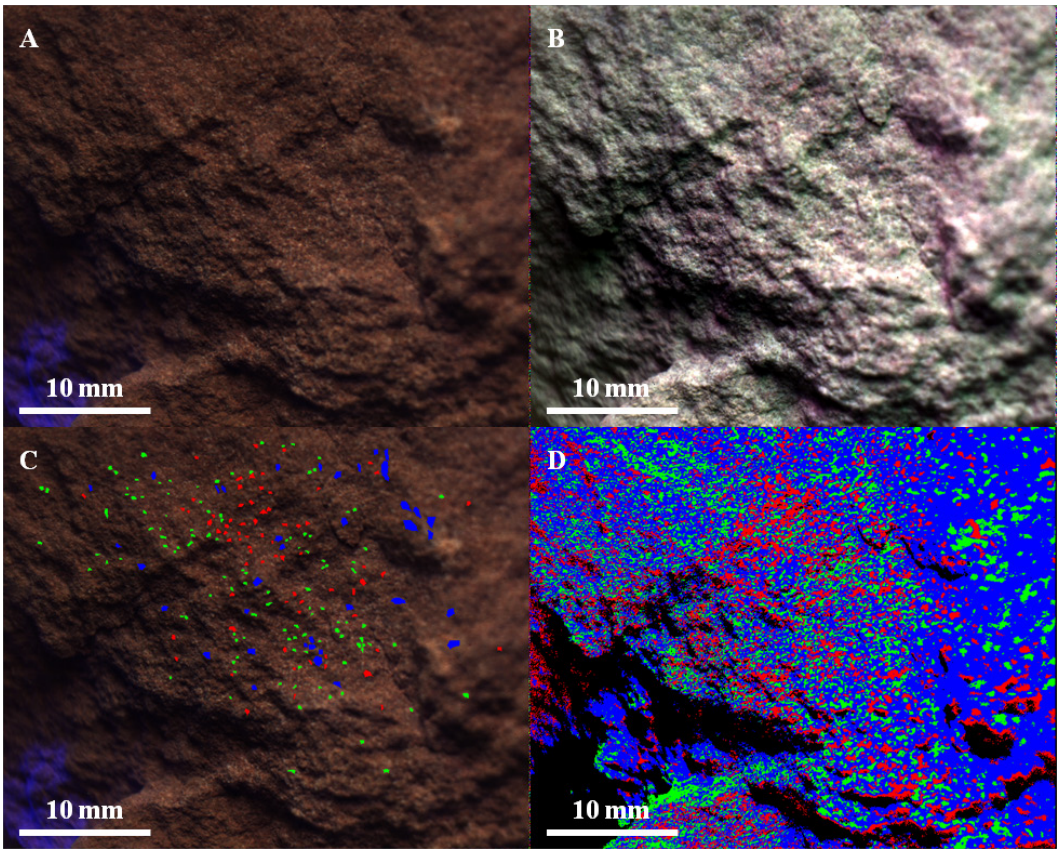

Figure 4.11. MMI-Generated Color Composite Images and End-Member Map of Sandstone (Sample 0035). MMI-generated color composite images (A & B) and corresponding spectral end-member map (D) based on supervised classification with ROIs as input parameters (C) of sandstone (sample 0035) sampled near the “Pit” (location labeled in Figure 4.1B). MMI Image size is 40x32 mm at 62.5 µm/ pixel. Figures A-B are linear stretched. Figure 4.11A: Visible-color RGB composite image composed of MMI bands 0.641, 0.522, and 0.463 µm respectively to simulate true-color. Figure 4.11B: False-color RGB composite image composed of MMI bands 1.521, 1.05, and 0.741 µm respectively to bring out subtle color differences in materials due to variations in composition. Figure 4.11C: Visible-color RGB composite similar to figure A with regions of interest (ROIs) used to generate end-member map (Figure 4.11D) and spectral end-members (Figures 4.12A). Figure 4.11D: End-member map generated in ENVI using supervised classification with ROIs as input parameter to map end-members distribution.

The MMI images reveal the sample to be a well-sorted, fine-grained sandstone, cemented by iron-oxide(s) (orange-brown color in Figure 4.11A). Characterization of this rock proved to be challenging due to its fine-grained, well-sorted nature. However, discrete light-toned angular grains, within the size range of fine sand, are clearly visible in the RGB image (Figure 4.11A). Scattered uniformly through the rock is a light-toned phase, possibly a clay mineral replacement of original feldspar(s) and a highly reflective crystalline phase. It is uncertain whether these are framework grains (e.g. mica, or feldspar), or a secondary cement phase, like carbonate. While this rock has a high textural maturity (very well-sorted), the compositional maturity is less clear at this scale. Small-scale sedimentary structures (including microscale cross laminations and lenticular bedding) are present in the outcrop, however they are not visible in the MMI image of the sample.

Spectra were obtained for two major microtextural domains (grains and intergranular cement) by averaging approximately 1200-1300 pixels from Regions of Interest (ROIs) (Figure 4.11C). A spectral end-member map was generated in ENVI to show the spatial distribution of the different spectral types using a supervised classification based on average spectra from ROIs (Figure 4.11D). Finally, end member spectra were compared to spectra from the USGS Spectral Library, convolved to MMI spectral bandpasses (shown in Figure 4.12).

Spectral analysis using the above methods showed that the orange-brown, fine-grained matrix of the rock consists of two spectral end-members, while the angular fine sand grains make up a third end-member. The two matrix components are visible as dark and light regions in the visible/near-infrared color composite image (Figure 4.11B), but are indistinguishable in the visible color composite image (Figure 4.11A).

The blue end-member corresponds to the lighter component of the fine-grained, orange-brown matrix, concentrated between the light-toned, angular sand grains. The spectrum has an absorption edge at 0.522 μm, a shoulder at 0.603 μm, a local maximum at 0.756 μm, and a broad absorption centered at 1.05 μm. An additional smaller absorption is present at 0.842 μm. The absorption edge at 0.522 μm and shoulder at 0.603 μm are characteristic of Fe^{3+}, while the absorption at 1.05 μm is characteristic of Fe^{2+}. The 1.05 μm feature is consistent with the library spectrum for clinopyroxene (possibly diopside). However, this mineral is inconsistent with the overall composition of the rock and for this reason the origin of the 1.05 μm absorption remains unclear. An alternative interpretation of the 1.05 μm absorption is a nanophase Fe-oxide/oxyhydroxide, which absorption is shifted towards 1 μm in the infrared (Morris et al. 1993).

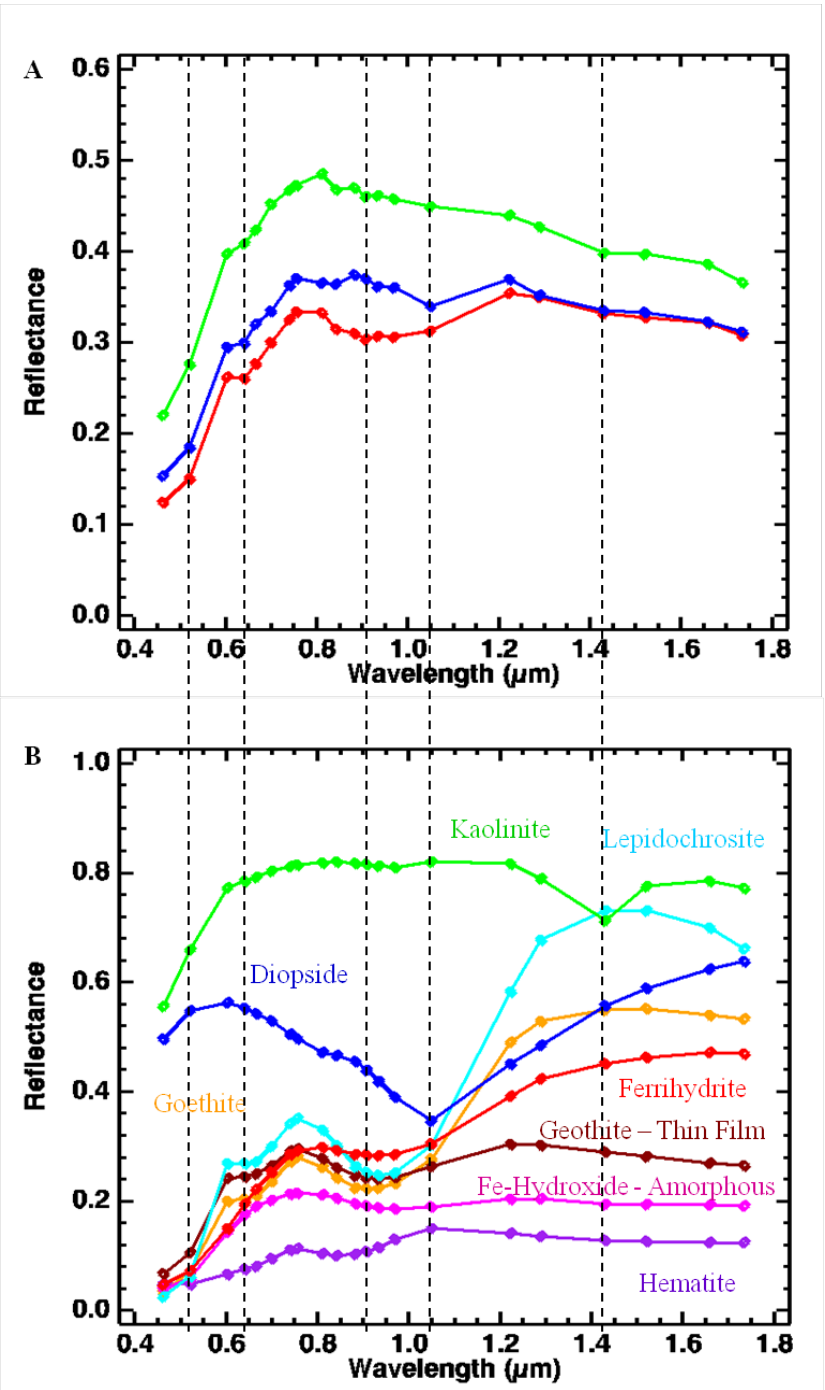

Figure 4.12. MMI-Generated Spectra of End-Members of Sandstone (Sample 0035) Compared to Library Spectra. MMI-generated spectra of end-members (A) of sandstone (sample 0035; shown in Figure 4.11) sampled near the “Pit” (location labeled in Figure 4.1B) and representative matching library spectra convolved to MMI bandpasses in Table 2.1 (B). Vertical lines correspond to MMI bands 0.522, 0.641, 0.908, 1.05, and 1.43 μm. See text for details on features and discussion.

The red end-member corresponds to the darker component of the fine-grained, orange-brown matrix between the light-toned, angular sand grains. The spectrum has an absorption edge at 0.522 μm, a shoulder at 0.603 μm, a local maximum at 0.756 and 0.811 μm, and a very broad absorption centered at 0.908 μm. A small absorption is also present at 1.43 μm. The absorption edge at 0.522 μm, shoulder at 0.603 μm, and broad 0.908 μm absorption are characteristic of Fe3+, while the 1.43 μm absorption is characteristic of the presence OH/H_2O. The spectrum is consistent with the library spectra for Fe-oxyhydroxide, with a best match to fine-grained goethite. The OH/H_2O feature is possibly due to adsorbed water, or the presence of a hydrated mineral, possibly a clay mineral. The clay mineral may be derived from the *in situ* weathering of feldspars.

The green end-member is representative of the light-toned, angular sand grains. The spectrum has a higher reflectance curve, compared to the matrix components, with an absorption edge at 0.522 μm, a shoulder at 0.603 μm, a local maximum at 0.811 μm, a negative slope towards the infrared and an absorption centered at 1.43 μm. The absorption edge at 0.522 μm and shoulder at 0.603 μm are characteristic of Fe^{3+}, while the 1.43 μm absorption is characteristic of OH/H_2O. The Fe^{3+} features are most likely contributed by the fine-grained Fe-oxyhydroxide cement, while OH/H_2O absorption may be due to adsorbed water, or the presence of a hydrated mineral (e.g. a clay mineral).

4.3.2.4. Interpretation of MMI Results

Texturally, the rock is a fine-grained sandstone. The diagenetic history of this sandstone included pervasive post-burial cementation by crystalline and nanophase Fe-oxides/oxyhydroxides. The angular sand grains with a spectrum matching a hydrated mineral, perhaps a clay mineral, suggest they are a product of *in situ* weathering perhaps formed by the hydration of original feldspars. This is consistent with the parent rock being a fine-grained, (texturally mature) arkosic (feldspar-containing) sandstone. Small-scale sedimentary structures (microscale cross laminations and lenticular bedding) in the parent rock suggests deposition by tractive bottom currents (e.g., water or wind).

4.4. Discussion

4.4.1. Evaluation of Performance of MMI during 2010 ILSO-ISRU Field Test

The biggest question leading up to the field deployment of the MMI for 2010 ILSO-ISRU field test, was whether the MMI would be capable to operating under daylight illumination. Prior to the field test, the MMI had demonstrated its ability to successfully image a wide variety of rocks and soils samples, including lunar samples collected during the Apollo missions, under a variety of controlled laboratory conditions, including a glovebox at the Lunar Receiving Laboratory at NASA's Johnson Space Center (Núñez et al. manuscript in review, 2012). Lab applications included imaging of samples under reduced ambient illumination.

However, because the MMI operates by illuminating a sample surface using low power LEDs, artificial ambient light or daylight illumination is significantly stronger and thus overwhelm the LED illumination, unless data collection was done after sunset or daylight illumination was reduced such as with a sunshade (see Figure 4.2). While limiting operations to night-time acquisition was the simplest solution and required little hardware modification, it severely restricted the amount of time needed for data collection and prevented coordinated operations with other instruments, which operated during the day. To address these challenges, a sunshade was attached to the MMI to reduce, or eliminate ambient light pollution. While the instrument with the sunshade performed well in tests prior to the 2010 ILSO-ISRU field test, it remained uncertain how the instrument would perform under actual field conditions (including full daylight illumination) and for imaging rough surfaces.

As shown by the two examples presented in this paper for the 2010 ILSO-ISRU field test, the MMI successfully imaged a variety of rock and soil materials under daytime illumination conditions, providing microtextural and compositional information of feedstock materials to support of ISRU activities. The MMI composite images faithfully resolved the microtextural features of rocks and soils in surface materials and outcrops over a broad range of lithologies and grain sizes. The application of spectral end-member mapping (using ENVI) revealed the distribution of Fe-bearing mineral phases within samples, including silicates (e.g., olivine

and pyroxene), oxides/hydroxides (e.g., hematite, goethite, and ferrihydrite) and plagioclase feldspar. The MMI composite images and spectra also revealed the presence of hydrated minerals in samples. These observations provided useful context information for interpreting data from other instruments (e.g., VaPor) used in the 2010 ILSO-ISRU field test (ten Kate et al. in press).

The mosaic imaging of the face of a vertical stream cut provided a unique opportunity to test the performance of the MMI for imaging a rough, vertical surface under daytime illumination (Figure 4.1), and to demonstrate mechanical positioning of the camera necessary to produce a mosaic of overlapping microscale images over a entire stratigraphic section that was 50 cm high (Figure 4.2A). Such capabilities are highly desirable for rover-deployed field instrument that can provide microtextural and mineralogical information of outcrop surfaces at a level of detail not yet demonstrated in surface missions.

4.4.2. Evaluation of Performance of MMI during 2011 Desert RATS Field Test

Following the successful demonstration of the MMI during the 2010 ILSO-ISRU field test, the MMI was used to characterize rocks and soils collected during astronaut EVAs, in the GeoLab during the 2011 Desert RATS field test. DRATS provided a unique opportunity to test whether the MMI could also be used effectively by astronauts exploring other planetary surfaces. In particular, the test provided the opportunity to assess whether

the MMI could be: 1) successfully integrated into GeoLab operations, specifically, everyday sample processing workflow; 2) operated by crew members with little instrument familiarity and limited support from mission control; 3) used to provide a rapid characterization of mineralogy and microtexture of samples for further analysis with other GeoLab instruments, for prioritizing samples for sample return and in support of real-time planning of science activities (e.g. astronuat EVAs); and 4) operated under the simulated mission constraints, including data transfer delays to the remote science team and limited time constraints for sample analysis.

The MMI was successfully deployed inside the GeoLab, and following initial tests, operations were successfully integrated into the overall workflow for sample processing. Furthermore, because the instrument user interface is simple and data acquisition automated (once sample was in focus, the crew members simply hit the acquire button), the crew members quickly mastered instrument use. This enabled the rapid processing of samples (up to four samples in an afternoon session). While the data transfer delays did provide some challenges for the analysis of data collected, this did not hinder GeoLab operations and sample processing. As shown with the two examples presented in the results section, the MMI-generated datasets (e.g. Figures 4.9 and 4.11), including color composite images, end-member maps and spectra, successfully provided the mineralogical and microtextural information needed for

correct petrogenetic interpretations of samples collected by astronaut crew members. Because the field test was structured as single-day missions to test different field operations scenarios (e.g., one SEV vs. two SEV operations), information gained about samples in the GeoLab using the MMI and other instruments could not be fed back to the astronaut teams to inform and support future planning of science activities. This was an artifact of the test that would not be there in an actual mission. Clearly such information would be invaluable for informing both astronaut crews and the ground-based science team about sampling priorities for future EVAs and for sustaining hypothesis-driven science activities during a mission. To demonstrate this will require two- to three-day mission scenarios to close this feedback loop between GeoLab analyses and mission science planning.

4.4.3. Lessons Learned and Improvements to the MMI

Field deployments of the MMI during the 2010 ILSO-ISRU and 2011 Desert RATS field tests provided unique opportunities to test the performance of the MMI over a broad range of field and laboratory applications, and operational constraints, including human mission simulations. These field deployments have lead to important lessons learned that will guide improvements in the MMI design and operations. The goal is to increase the effectiveness and value of the MMI for future rover-based and astronaut-based exploration of planetary surfaces. While some improvements are not as important for rover-based exploration, they

are quite significant for human exploration. One such improvement is a reduction in the time required to acquire an image. Under field conditions, this required between 5 and 10 minutes per sample. While 5-10 minutes is not a long acquisition time for a rover mission, such as the Mars Exploration Rovers, which operate on a 24 hr cycle, it can be a significant amount of time in a human mission where astronaut crew members are severely time limited. Such time constraints were clearly experienced by astronauts operating the MMI in the GeoLab, which resulted in a backlog of samples. One way to reduce the amount of time required for a data acquisition cycle is to increase the intensity of the LEDs. Doing so would reduce the exposure time required per image to achieve adequate SNR, which in turn would cumulatively reduce the total time over all the bands. An added benefit of increasing the LED intensity and reducing the exposure time per image would be an increased SNR where there is ambient light pollution. Another improvement that would also help reduce the cycling time between samples would be the addition of an automated focusing mechanism, similar to those used by commercial digital cameras. During Desert RATS, crew members spent between three to five minutes setting up the samples and getting them into focus. Over the course of an hour, or four samples, that amount of time added up to almost 20 minutes spent setting up and focusing the samples. Reducing the sample setup and focusing times to about a minute would enable an additional sample to be analyzed within the same time frame. Combined, these two

improvements would significantly reduce the amount spent with the samples and help reduce the sample backlog.

In addition to instrument miniaturization that is expected with the development of a rover-mounted MMI instrument, these two improvements would add a significant improvement to the MMI and increase the value of the MMI as a geological tool for supporting real-time exploration of planetary surfaces by human explorers.

4.5. Conclusions

The utility of the MMI for characterizing the microtexture and mineralogy of rocks and soils has been successfully demonstrated over a broad range of field and laboratory applications, as well as mission simulations, including field deployments during the 2010 ILSO-ISRU and 2011 Desert RATS field tests. Ruggedization and packaging of the MMI for remote field and lab deployments has significantly advanced the Technology Readiness of the MMI for future mission opportunities and increased the value of the MMI for rover-based and astronaut exploration of planetary surfaces.

CHAPTER 5

CONCLUDING THOUGHTS

The research presented in this dissertation is a marriage of science and engineering with the primary goal of developing and advancing the Technology Readiness level and science capabilities of the MMI to maximize the scientific return from future rover and human-based exploration of planetary surfaces. The breadth of the work presented encompasses both the development of the MMI and applications of the instrument over a broad range of laboratory and field applications, including field deployments and simulated mission scenarios, to characterize the microtexture and mineralogy of rocks and soils of different planetary surfaces. Such spatially-correlated information is considered crucial for correct petrogenetic interpretations. For the astrobiological exploration of Mars, these petrological observations are key for creating scale-integrated paleoenvironmental interpretations to assess the nature and persistence of past habitable zones and their potential for supporting life. This data will also enable the selection of the highest value samples for further analysis using analytical instruments onboard the rover body or inside the space habitat, for caching and high-grading for future return to Earth.

Analyses of geological samples comprising a wide range of Mars-relevant analog environments with the MMI with comparisons to laboratory methods (including VNIR, XRD, Thin section petrography) have

demonstrated the capabilities of the MMI to resolve the fine-scale microtextural features of samples, and provide important mineralogical information to help constrain composition. In particular, the MMI has the ability to map the distribution of Fe-bearing minerals (including silicates and oxides) with high fidelity, along with the presence of hydrated minerals. The ability to map hydrated minerals in a microtextural context *in situ* is crucial for future astrobiological missions to Mars to identify mineral assemblages that provide information about past habitable environments and also have the potential of preserving biosignatures. Multispectral, visible-to- near-infrared microimages generated by the MMI could also provide context information for evaluating the spatial (and implied temporal) relationships between constituent mineral phases characterized by other mineralogical methods that provide high spectral resolution to identify specific mineral assemblages, but lack context information such as spot VNIR and XRD. Integrating the capabilities of the MMI to provide critical contextual and coarse mineralogical information *in situ* via deployment on a rover arm with the high resolution mineralogical information provided by VNIR or XRD would present a powerful combination for the exploration of Mars that would enable proper assessment of the origins rocks and soils, and create scale-integrated paleoenvironmental interpretations to assess the nature and persistence of past habitable zones and their potential for supporting life. Furthermore, this data will also enable the selection of the highest value samples for

further analysis using other analytical instruments onboard the rover body (such as for geochemical analysis) or for caching for future return to Earth.

Similar to the Mars analog samples, analysis of lunar rocks and soils representing a broad range of compositions found in the Apollo collection, revealed that MMI composite images faithfully resolved the microtextural features of samples, while the application of ENVI-based spectral end-member mapping performed well in mapping the distribution of Fe-bearing mineral phases (olivine and pyroxene), as well as plagioclase feldspars in rock samples, over a broad range of lithologies and grain sizes. The MMI composite images also revealed the presence of opaques, glasses, as well as detecting the subtle effects of space weathering in samples. MMI-based petrogenetic interpretations compared favorably with previously published descriptions of the same samples, revealing the valuable observations the MMI instrument can contribute to future lunar exploration. The ability to map a variety of minerals *in situ* via deployment on a rover arm for robotic exploration of the Moon or via deployment inside a glovebox for a human mission would provide valuable information about the composition of lunar rock and soils that would enable the selection of the highest value samples for further analysis with other instruments (such as XRD or X-ray fluorescence, XRF, detector) or potential return to Earth.

Given that we have an incomplete sampling of the lunar crust as revealed by analysis of returned lunar samples and remote sensing

missions (e.g., Wilhelms 1987; Heiken et al. 1991; Robinson and Riner 2005; Jolliff et al. 2006; NRC 2007a), additional landed missions are needed to sample and return lunar material of unexplored areas of Moon, such as the South Pole-Aitken basin on the far side of the Moon (e.g., NRC 2007a) to improve our understanding of the lunar surface but also help constrain early solar system history such as the late heavy bombardment (NRC 2007a). The MMI would contribute greatly to help answer such questions by enabling the identification of different rock and soil types as well as help target specific samples of interest for further analysis, or for return to Earth.

Field deployments of the MMI in the 2010 ILSO-ISRU and 2011 Desert RATS field tests revealed the ability of the MMI to successfully operate under field conditions (including daylight illumination) and mission constraints to support future human exploration of planetary surfaces. The successful deployment of the MMI in the field in Hawaii as part of the 2010 ILSO-ISRU field test not only revealed the ability of the MMI to operate under field conditions vital for deployments on a robotic rover or by astronauts during EVAs, but also support ISRU activities by helping prospect for and provide field characterization of geologic materials with a high total iron content, which make good feedstock for oxygen production using the hydrogen reduction process, for extracting oxygen and water. Future human missions to the Moon or Mars will need to be able to “live off the land” and thus be able to utilize ISRU instruments to extract oxygen

and water from the local regolith. Deployed on a prospecting rover with other instruments, the MMI would be a valuable tool for prospecting for ISRU feedstock material by characterizing the surrounding geologic materials and identifying minerals with a high iron content. In the case of Mars, the MMI would also be useful for identifying hydrated minerals, from which water could readily be extracted. Additionally, the MMI would provide a microtextural context for other instruments that can identify specific mineral assemblages, but lack context information such as a Mössbauer spectrometer or an XRD. With this information, astronauts could thus identify the best sites for mining for ISRU feedstock material to maximize the extraction of oxygen and water from the local regolith.

Deployment of the MMI inside the GeoLab as part of the 2011 Desert RATS field test demonstrated the ability of the MMI to operate under mission operations constraints associated with a manned mission and provided the mineralogical and microtextural information needed for rapid correct petrogenetic interpretations of samples collected by astronaut crew members, thus revealing the value of the MMI to support future manned missions to planetary surfaces. Because the field test was structured as single-day missions to test different field operations scenarios (e.g., one SEV vs. two SEV operations), information gained about samples in the GeoLab using the MMI and other instruments could not be fed back to the astronaut teams to inform and support future planning of science activities. However, this would not be the case for an

actual mission. Clearly rapid sample characterization as provided by the MMI would be invaluable for informing both astronaut crews and the ground-based science team about sampling priorities for future EVAs and for sustaining hypothesis-driven science activities during a mission.

Combined, these investigations have demonstrated the capabilities of the MMI to provide crucial spatially-correlated mineralogy and microtexture of a wide variety of rocks and soils in outcrops and samples over a broad range of lithologies, grain sizes and surface roughness in a variety of field and mission-related applications. Lessons from this research will lead to further improvements to the MMI that will result in a more effective tool to support future rover and human exploration of planetary surfaces.

REFERENCES

Adams, J. B. 1974. Visible and near-infrared diffuse reflectance spectra of pyroxenes as applied to remote sensing of solid objects in the solar system. *Journal of Geophysical Research* 79: 4829– 4836.

Allen, C. C., R. V. Morris, H. V. Lauer Jr., and D. S. McKay. 1993. Microscopic iron metal on glass and minerals - A tool for studying regolith maturity. *Icarus* 104: 291-300.

Allen, C. C., R. V. Morris, and D. S. McKay. 1994. Experimental reduction of lunar mare soil and volcanic glass. *Journal of Geophysical Research* 99: 23,173-23,185.

Allen, C. C., R. V. Morris, and D. S. McKay. 1996. Oxygen extraction from lunar soils and pyroclastic glass. *Journal of Geophysical Research* 101: 26,085-26,095.

Allen, C., G. Sellar, J. Nunez, A. Mosie, C. Schwartz, T. Parker, D. Winterhalter, and J. Farmer. 2009. High-Grading Lunar Samples. *2nd Lunar Science Forum*, Moffett Field, CA.

Allen, C., G. Sellar, J. I. Nuñez, D. Winterhalter, and J. Farmer. 2010. Lunar Reference Suite to Support Instrument Development and Testing. *41st Lunar and Planetary Science Conference*, The Woodlands, TX, Abstract 1457.

Allton, J. H. 1989. Catalog of Apollo Lunar Surface Geological Sampling Tools and Containers. NASA Johnson Space Center Document JSC-23454. Available at <http://www.hq.nasa.gov/alsj/tools/Welcome.html>

Baldridge, A. M., S.J. Hook, C.I. Grove and G. Rivera. 2009. The ASTER Spectral Library Version 2.0. *Remote Sensing of Environment* 113: 711-715.

Basaltic Volcanism Study Project. 1981. *Basaltic Volcanism on the Terrestrial Planets*. New York: Pergamon Press, Inc.

Bence, A. E. and J. J. Papike. 1972. Pyroxenes as recorders of lunar basalt petrogenesis: Chemical trends due to crystal liquid interaction. *Proceedings of the 3rd Lunar Science Conference, Geochimica et Cosmochima Acta* 1 (Suppl. 3): 431-469.

Bell, J. F., III, T. B. McCord, and P. D. Owensby. 1990. Observational evidence of crystalline iron oxides on Mars. *Journal of Geophysical Research* 95: 14,447–14,461.

Bell, J. F., III, H. Y. McSween Jr., J. A. Crisp, R. V. Morris, S. L. Murchie, N T . Bridges, J. R. Johnson, D. T. Britt, M. P. Golombek, H. J. Moore, A. Ghosh, J. L. Bishop, R. C. Anderson, J. Brückner, T. Economou, J. P. Greenwood, H. P. Gunnlaugsson, R. M. Hargraves, M. S . Hviid, J. M. Knudsen, M. B. Madsen, R. Reid, R. Rieder, and L. Soderblom. 2000. Mineralogic and compositional properties of Martian soil and dust: Results from Mars Pathfinder. *Journal of Geophysical Research* 105: 1721– 1755.

Bell, J. F., III, S. W. Squyres, K. E. Herkenhoff, J. N. Maki, H. M. Arneson, D. Brown, S. A. Collins, A. Dingizian, S. T. Elliot, E. C. Hagerott, A. G. Hayes, M. J. Johnson, J. R. Johnson, J. Joseph, K. Kinch, M. T. Lemmon, R. V. Morris, L. Scherr, M. Schwochert, M. K. Shepard, G. H. Smith, J. N. Sohl-Dickstein, R. J. Sullivan, W. T. Sullivan, and M. Wadsworth. 2003. Mars Exploration Rover Athena Panoramic Camera (Pancam) investigation. *Journal of Geophysical Research* 108(E12): 8063. doi:10.1029/2003JE002070.

Bell, J. F., III, M. C. Malin, M. A. Caplinger, M. A. Ravine, A. S. Godber, M. C. Jungers, M. S. Rice, and R. B. Anderson. 2012. Mastcam Multispectral Imaging on the Mars Science Laboratory Rover: Wavelength Coverage and Imaging Strategies at the Gale Crater Field Site. *43rd Lunar and Planetary Science Conference*, The Woodlands, TX, Abstract 2541.

Belton, M. J. S., J. W. Head, C. M. Pieters, R. Greeley, A. S. McEwen, G. Neukum, K. P. Klaasen, C. D. Anger, M. H. Carr, C. R. Chapman, M. E. Davies, F. P. Fanale, P. J. Gierasch, R. Greenberg, A. P. Ingersoll, T. Johnson, B. Packzkowski, C. B. Pilcher, J. Veverka. 1992. Lunar impact basins and crustal heterogeneity: New western limb and farside data from Galileo. *Science* 255: 570-576.

Bibring, J.P., Y. Langevin, J. F. Mustard, F. Poulet, R. Arvidson, A. Gendrin, B. Gondet, N. Mangold, P. Pinet, F. Forget, and the OMEGA Team. 2006. Global mineralogical and aqueous Mars history derived from OMEGA/Mars Express data. *Science* 312:400–404.

Bishop, J. L., C. M. Pieters, and J. O. Edwards. 1994. Infrared spectroscopic analyses on the nature of water in montmorillonite. *Clays and Clay Minerals* 42: 701-715.

Bishop, J., J. Madejova, P. Komadel, and H. Froschl. 2002a. The influence of structural Fe, Al, and Mg on the infrared OH bands in spectra of dioctahedral smectites. *Clay Minerals* 37: 607–616. doi:10.1180/0009855023740063.

Bishop, J. L., E. Murad, and M. D. Dyar. 2002b. The influence of octahedral and tetrahedral cation substitution on the structure of smectites and serpentines as observed through infrared spectroscopy. *Clay Minerals* 37: 617–628. doi:10.1180/0009855023740064.

Bishop, J. L., P. Schiffman, and R. Southard. 2002c. Geochemical and mineralogical analyses of palagonitic tuffs and altered rinds of pillow basalts in Iceland and applications to Mars. In *Volcano-Ice Interaction on Earth and Mars*, Geological Society of London Special Publication 202, pp 371–392.

Bishop, J. L., M. D. Lane, M. D. Dyar, and A. J. Brown. 2008. Reflectance and emission spectroscopy study of four groups of phyllosilicates: smectites, kaolinite-serpentines, chlorites and micas. *Clay Minerals* 43: 35-54. doi:10.1180/claymin.2008.043.1.03.

Borst, A.M., B. H. Foing, G. R. Davies, and W. van Westrenen. 2011. Surface mineralogy and stratigraphy of the lunar South Pole-Aitken basin determined from Clementine UV/VIS and NIR data. *Planetary and Space Science* doi:10.1016/j.pss.2011.07.020.

Bowen, L.H., E. De Grave, D. A. Reid, R. C. Graham, and S. B. Edinger. 1989. Mössbauer study of a California desert celadonite and its

pedogenically-related smectite. *Physics and Chemistry of Minerals* 16: 697-703.

Brown, G. M., C. H. Emeleus, G. J. Holland, A. Peckett and R. Phillips. 1972. Mineral-chemical variations in Apollo 14 and Apollo 15 basalts and granitic fractions. *Proceedings of the 3rd Lunar Science Conference, Geochimica et Cosmochima Acta* 1 (Suppl. 3): 141-157.

Burns, R.G. 1970. Crystal field spectra and evidence of cation ordering in olivine minerals. *American Mineralogist* 55: 1608–1632.

Burns, R. G., K. M. Parkin, B. M. Loeffler, I. S. Leung, and R. M. Abu-Eid. 1976. Further characterization of spectral features attributable to titanium on the moon. *Proceedings of the 7th Lunar Science Conference* 3: 2561-2578.

Burns, R. G. 1982. *Mineralogical Applications of Crystal Field Theory*. 2nd Ed. New York: Cambridge Univ. Press.

Burns, R. G. 1993. *Mineralogical Applications of Crystal Field Theory*. 2nd Ed. New York: Cambridge Univ. Press.

Chao, E.C.T., J. A. Minkin, and J. B. Best. 1972. Apollo 14 breccias: General characteristics and classification. *Proceedings of the 3rd Lunar Science Conference, Geochimica et Cosmochima Acta* 1 (Suppl. 3): 645-659.

Charette, M. P., T. B. McCord, and C. Pieters. 1974. Application of remote spectral reflectance measurements to lunar geology classification and determination of titanium content of lunar soils. *Journal of Geophysical Research* 79: 1605–1613. doi:10.1029/JB079i011p01605.

Christensen, P. R., J. L. Bandfield, M. D. Smith, V. E. Hamilton, and R. N. Clark. 2000. Identification of a basaltic component on the Martian surface from Thermal Emission Spectrometer data. *Journal of Geophysical Research* 105: 9609–9621.

Christensen, P.R., J. L. Bandfield, V. E. Hamilton, S. W. Ruff, H. H. Kieffer, T. N. Titus, M. C. Malin, R. V. Morris, M. D. Lane, R. L. Clark, B. M. Jakosky, M. T. Mellon, J. C. Pearl, B. J. Conrath, M. D. Smith, R. T. Clancy, R. O. Kuzmin, T. Roush, G. L. Mehall, N. Gorelick, K. Bender, K. Murray, S. Dason, E. Greene, S. Silverman, and M. Greenfield. 2001. Mars Global Surveyor Thermal Emission Spectrometer experiment: investigation description and surface science results. *Journal of Geophysical Research* 106: 23823–23871.

Christensen, P.R., S. W. Ruff, R. Fergason, N. Gorelick, B. M. Jakosky, M. D. Lane, A. S. McEwen, H. Y. McSween, G. L. Mehall, K. Milam, J. E. Moersch, S. M. Pelkey, A. D. Rogers, and M. B. Wyatt. 2005. Mars Exploration Rover candidate landing sites as viewed by THEMIS. *Icarus* 176: 12–43.

Clark, R. N., and T. L. Roush. 1984. Reflectance spectroscopy: Quantitative analysis techniques for remote sensing applications: *Journal of Geophysical Research* 89: 6329-6340.

Clark, R. N., T. V. V. King, M. Klejwa, and G. A. Swayze. 1990. High spectral resolution reflectance spectroscopy of minerals. *Journal of Geophysical Research* 95: 12653-12680.

Clark, R.N. 1999. Chapter 1: Spectroscopy of Rocks and Minerals and Principles of Spectroscopy, In *Manual of Remote Sensing*. A. N. Rencz (Ed.). pp. 3-58. New York: John Wiley and Sons.

Clark, R. N., G. A. Swayze, K. E. Livo, R. F. Kokaly, S. J. Sutley, J. B. Dalton, R. R. McDougal, and C. A. Gent. 2003. Imaging spectroscopy: Earth and planetary remote sensing with the USGS Tetracorder and expert systems. *Journal of Geophysical Research* 108(E12): 5131. doi:10.1029/2002JE001847.

Clark, R. N., G. A. Swayze, R. Wise, E. Livo, T. Hoefen, R. Kokaly, and S. J. Sutley. 2007. *USGS Digital Spectral Library splib06a*. U.S. Geological Survey, Digital Data Series 231.

Cloutis, E. A., M. J. Gaffey, T. L. Jackowski, and K. L. Reed. 1986. Calibrations of phase abundance, composition, and particle size

distribution for olivine-orthopyroxene mixtures from reflectance spectra. *Journal of Geophysical Research* 91: 11,641–11,653.

Cloutis, E. A., K. A. McCormack, J. F. Bell III, A. R. Hendrix, D. T. Bailey, M. A. Craig, S. A. Mertzman, M. S. Robinson, M. A. Riner. 2008. Ultraviolet spectral reflectance properties of common planetary minerals. *Icarus* 197: 321-347.

Cornell, R. M., and U. Schwertmann. 1996. *The Iron Oxides*. Hoboken, N.J.: John Wiley.

Des Marais, D. J., J. A. Nuth III, L. J. Allanmandola, A. P. Boss, J. D. Farmer, T. M. Hoehler, B. M. Jakosky, V. S. Meadows, A. Pohorille, B. Runnegar, and A. M. Spormann. 2008. The NASA Astrobiology Roadmap. *Astrobiology* 8: 715-730. doi: 10.1089/ast.2008.0819.

Dhingra, D. 2008. Exploring links between crater floor mineralogy and layered lunar crust. *Advances in the Space Research* 42: 275–280.

Dickinson, T., G. J. Taylor, K. Keil, R. A. Schmitt, S. S. Hughes, and M. R. Smith. 1985. Apollo 14 aluminous mare basalts and their possible relationship to KREEP. *Proceedings of the 15th Lunar and Planetary Science Conference, Journal of Geophysical Research* 90: C365-C374.

Drief, A. and P. Schiffman. 2004. Very low-temperature alteration of sideromelane in hyaloclastites and hyalotuffs from Kilauea and Mauna Kea volcanoes: implications for the mechanism of palagonite formation. *Clays and Clay Minerals* 52: 622–634.

Duncan, A. R., S. M. McKay, J. W. Stoeser, M. M. Lindstrom, D. J. Lindstrom, J. S. Fruchter, and G. G. Goles. 1975a. Lunar polymict brecia 14321: a compositional study of its principal components. *Geochimia et Cosmochimica Acta* 39: 247-260.

Duncan, A. R., R. A. F. Grieve, and D. F. Weill. 1975b. The life and times of Big Bertha: lunar breccia 14321. *Geochimia et Cosmochimica Acta* 39: 265-273.

Edgett, K. S., M. A. Ravine, M. A. Caplinger, F. T. Ghaemi, J. A. Schaffner, M. C. Malin, J. M. Baker, D. R. DiBiase, J. Laramee, J. N. Maki, R. G. Willson, J. F. Bell III, J. F. Cameron, W. E. Dietrich, L. J. Edwards, B. Hallet, K. E. Herkenhoff, E. Heydari, L. C. Kah, M. T. Lemmon, M. E. Minitti, T. S. Olson, T. J. Parker, S. K. Rowland, J. Schieber, R. J. Sullivan, D. Y. Sumner, P. C. Thomas, and R. A. Yingst. 2009. The Mars Science Laboratory (MSL) Mars Hand Lens Imager (MAHLI) Flight Instrument. *40th Lunar and Planetary Science Conference*, League City, TX, Abstract 1197.

Eggleton, R E. 1964. Preliminary geology of the Riphaeus quadrangle of the Moon and definition of the Fra Mauro Formation. In *Astrogeological Studies Annual Progress Report*, August 25, 1962 to July 1, 1963, pt. A: U.S. Geological Survey open-file report, p. 46-63.

Ehlmann, B. L., J. F. Mustard, G. A. Swayze, R. N. Clark, J. L. Bishop, F. Poulet, D. J. Des Marais, L. H. Roach, R. E. Milliken, J. J. Wray, O. Barnouin-Jha, and S. L. Murchie. 2009. Identification of hydrated silicate minerals on Mars using MRO-CRISM: Geologic context near Nili Fossae and implications for aqueous alteration. *Journal of Geophysical Research* 114: E00D08. doi:10.1029/2009JE003339.

Evans, C. A., M. J. Calaway and M. S. Bell. 2010. GeoLab in NASA's first generation pressurized excursion module: operational Concepts. *41st Lunar and Planetary Science Conference*, The Woodlands, TX, Abstract 1480.

Evans, C. A., M. J. Calaway and M. S. Bell. 2012. GeoLab 2011: New Instruments and Operations Tested at Desert RATS. *41st Lunar and Planetary Science Conference*, The Woodlands, TX, Abstract 1186.

Evans, C. A., M. J. Calaway, M. S. Bell, K. E. Young. In Press. GeoLab—A habitat-based laboratory for preliminary examination of geological samples. *Acta Astronautica*. doi:10.1016/j.actaastro.2011.12.008.

Farmer, J. D., and D. J. Des Marais. 1999. Exploring for a record of ancient Martian life. *Journal of Geophysical Research* 104(E11): 26,977–26,995. doi:10.1029/1998JE000540.

Farmer, J. D., J. I. Núñez , R. G. Sellar, and P. B. Gardner. 2011. Multispectral Microscopic Imager (MMI): Spectral Imaging of Geological Materials at a Handlens Scale. *EOS Transactions AGU Fall Meeting*, San Frasisco, CA, Abstract P33B-1767.

Farrand, W. H., J. F. Bell III, J. R. Johnson, S. W. Squyres, J. Soderblom, and D. W. Ming. 2006. Spectral variability among rocks in visible and near-infrared multispectral Pancam data collected at Gusev crater: Examinations using spectral mixture analysis and related techniques. *Journal of Geophysical Research* 111: E02S15. doi:10.1029/2005JE002495.

Farrand, W. H., J. F. Bell III, J. R. Johnson, B. L. Jolliff, A. H. Knoll, S. M. McLennan, S. W. Squyres, W. M. Calvin, J. P. Grotzinger, R. V. Morris, J. Soderblom, S. D. Thompson, W. A. Watters, and A. S. Yen. 2007. Visible and near-infrared multispectral analysis of rocks at Meridiani Planum, Mars, by the Mars Exploration Rover Opportunity. *Journal of Geophysical Research* 112: E06S02. doi:10.1029/2006JE002773.

Fischer, E. M., and C. M. Pieters. 1996. Composition and exposure age of the Apollo 16 Cayley and Descartes regions from Clementine data: Normalizing the optical effects of space weathering. *Journal of Geophysical Research* 101: 2225-2234.

Gaffey, S. J. 1987. Spectral reflectance of carbonate minerals in the visible and near infrared (0.35 – 2.55 um): Anhydrous carbonate minerals. *Journal of Geophysical Research* 92: 1429–1440. doi:10.1029/JB092iB02p01429.

Gillespie, A. R., A. B. Kahle, and R. E. Walker. 1986. Color enhancement of highly correlated images. Part I. Decorrelation and HSI contrast stretches. *Remote Sensing of Environment* 20: 209– 235. doi:10.1016/0034-4257(86)90044-1.

Goddard, E. N., E. J. Mackin, E. M. Shoemaker, and A. Waters. 1965. Objectives of Apollo Geological Field Investigations & Proposal for Development of an Apollo Field Exploration Program. Project

Apollo Field Geology Planning Team. 61p. <http://www.lpi.usra.edu/lunar/documents/>

Gorevan, S. P., T. Myrick, K. Davis, J. J. Chau, P. Bartlett, S. Mukherjee, R. Anderson, S. W. Squyres, R. E. Arvidson, M. B. Madsen, P. Bertelsen, W. Goetz, C. S. Binau, and L. Richter. 2003. Rock Abrasion Tool: Mars Exploration Rover mission. *Journal of Geophysical Research* 108(E12): 8068. doi:10.1029/2003JE002061.

Green, A. A., M. Berman, P. Switzer, and M. D. Craig. 1988. A transformation for ordering multispectral data in terms of image quality with implications for noise removal. *IEEE Transactions Geoscience and Remote Sensing* 26: 65– 74.

Grieve, R. A., G. A. McKay, H. D. Smith, and D. F. Weill. 1975. Lunar polymict breccia 14321: a petrographic study. *Geochimia et Cosmochimica Acta* 39: 229-245.

Griffith, L.L. and E. L. Shock. 1995. A geochemical model for the formation of hydrothermal carbonates on Mars. *Nature* 377: 406–408.

Hamilton, V. E., and P. R. Christensen. 2005. Evidence for extensive, olivine-rich bedrock on Mars. *Geology* 33: 433– 436.

Haskin, L. A., A. Wang, B. L. Jolliff, H. Y. McSween, B. C. Clark, D. J. Des Marais, S. M. McLennan, N. J. Tosca, J. A. Hurowitz, J. D. Farmer, A. Yen, S. W. Squyres, R. E. Arvidson, G. Klingelhöfer, C. Schröder, P. A. de Souza Jr, D. W. Ming, R. Gellert, J. Zipfel, J. Brückner, J. F. Bell III, K. Herkenhoff, P. R. Christensen, S. Ruff, D. Blaney, S. Gorevan, N. A. Cabrol, L. Crumpler, J. Grant, and L. Soderblom. 2005. Water alteration of rocks and soils on Mars at the Spirit rover site in Gusev crater. *Nature* 436: 66-69. doi:10.1038/nature03640.

Hapke, B. 1993. *Introduction to the Theory of Reflectance and Emittance Spectroscopy*. New York: Cambridge University Press.

Hapke, B. 2001. Space weathering from Mercury to the asteroid belt. *Journal of Geophysical Research* 106(E5): 10,039-10,073.

Hawke, B. R., P. G. Lucey, G. A. Smith, G. J. Taylor, D. J. Lawrence, and P. D. Spudis. 2001. Remote sensing studies of selected spectral anomalies on the Moon. *32nd Lunar and Planetary Science Conference*, Houston, TX, Abstract 1241.

Hecht, M. H., J. Marshall, W. T. Pike, U. Staufer, D. Blaney, D. Braendlin, S. Gautsch, W. Goetz, H.-R. Hidber, H. U. Keller, W. J. Markiewicz, A. Mazer, T. P. Meloy, J. M. Morookian, C. Mogensen, D. Parrat, P. Smith, H. Sykulska, R. J. Tanner, R. O. Reynolds, A. Tonin, S. Vijendran, M.Weilert, and P. M.Woida. 2008. Microscopy capabilities of the Microscopy, Electrochemistry, and Conductivity Analyzer. *Journal of Geophysical Research* 113: E00A22. doi:10.1029/2008JE003077.

Heiken, G. H., D. T. Vaniman, and B. M. French. 1991. *Lunar Sourcebook: A User's Guide to the Moon*. pp. 736. New York: Cambridge University Press.

Herkenhoff, K. E., S. W. Squyres, J. F. Bell III, J. N. Maki, H. M. Arneson, P. Bertelsen, D. I. Brown, S. A. Collins, A. Dingizian, S. T. Elliott, W. Goetz, E. C. Hagerott, A. G. Hayes, M. J. Johnson, R. L. Kirk, S. McLennan, R. V. Morris, L. M. Scherr, M. A. Schwochert, L. R. Shiraishi, G. H. Smith, L. A. Soderblom, J. N. Sohl-Dickstein, and M. V. Wadsworth. 2003. Athena Microscopic Imager investigation. *Journal of Geophysical Research* 108(E12): 8065. doi:10.1029/2003JE002076.

Herkenhoff, K.E., S.W. Squyres, R. Arvidson, D.S. Bass, J.F. Bell, III, P. Bertelsen, B.L. Ehlmann, W. Farrand, L. Gaddis, R. Greeley, J. Grotzinger, A.G. Hayes, S.F. Hviid, J.R. Johnson, B. Jolliff, K.M. Kinch, A.H. Knoll, M.B. Madsen, J.N. Maki, S.M. McLennan, H.Y. McSween, D.W. Ming, J.W. Rice, Jr., L. Richter, M. Sims, P.H. Smith, L.A. Soderblom, N. Spanovich, R. Sullivan, S. Thompson, T. Wdowiak, C. Weitz, and P. Whelley. 2004. Evidence from Opportunity's Microscopic Imager for water on Meridiani Planum. *Science* 306: 1727-1730. doi:10.1126/science.1105286.

Herkenhoff, K.E., S.W. Squyres, R. Anderson, B.A. Archinal, R.E. Arvidson, J.M. Barrett, K.J. Becker, J.F. Bell III, C. Budney, N.A.

Cabrol, M.G. Chapman, D. Cook, B.L. Ehlmann, J. Farmer, B. Franklin, L.R. Gaddis, D.M. Galuszka, P.A. Garcia, T.M. Hare, E. Howington-Kraus, J.R. Johnson, S. Johnson, K. Kinch, R.L. Kirk, E.M. Lee, C. Leff, M. Lemmon, M.B. Madsen, J.N. Maki, K.F. Mullins, B.L. Redding, L. Richter, M.R. Rosiek, M.H. Sims, L.A. Soderblom, N. Spanovich, R. Springer, R.M. Sucharski, T. Sucharski, R. Sullivan, J.M. Torson, and A. Yen. 2006. Overview of the Microscopic Imager investigation during Spirit's first 450 sols in Gusev crater. *Journal of Geophysical Research* 111: E02S04. doi:10.1029/2005JE002574.

Herkenhoff, K.E., J. Grotzinger, A.H. Knoll, S.M. McLennan, C. Weitz, A. Yingst, R. Anderson, B.A. Archinal, R.E. Arvidson, J.M. Barrett, K.J. Becker, J.F. Bell III, C. Budney, M.G. Chapman, D. Cook, B. Ehlmann, B. Franklin, L.R. Gaddis, D.M. Galuszka, P.A. Garcia, P. Geissler, T.M. Hare, E. Howington-Kraus, J.R. Johnson, L. Keszthelyi, R.L. Kirk, P. Lanagan, E.M. Lee, C. Leff, J.N. Maki, K.F. Mullins, T.J. Parker, B.L. Redding, M.R. Rosiek, M.H. Sims, L.A. Soderblom, N. Spanovich, R. Springer, S.W. Squyres, D. Stolper, R.M. Sucharski, T. Sucharski, and R. Sullivan. 2008. The surface processes recorded by rocks and soils on Meridiani Planum, Mars: Microscopic Imager observations during Opportunity's first three extended missions. *Journal of Geophysical Research* 113: E12S32. doi:10.1029/2008JE003100.

Herzberg, G. 1945. *Infrared and Raman Spectroscopy*. New York: Von Nostrand Reinhold Company, Inc.

Hunt, G. R., and J. W. Salisbury. 1970. Visible and near infrared spectra of minerals and rocks, I, Silicate minerals. *Modern Geology* 1: 283-300.

Hunt, G. R., and J. W. Salisbury. 1971. Visible and near-infrared spectra of minerals and rocks: II. Carbonates. *Modern Geology* 2: 23–30.

Isaacson, P. J., and C. M. Pieters. 2010. Deconvolution of lunar olivine reflectance spectra: Implications for remote compositional assessment. *Icarus* 210: 8–13. doi:10.1016/j.icarus.2010.06.004

Isaacson, P. J., A. B. Sarbadhikari, C. M. Pieters, R. L. Klima, T. Hiroi, Y. Liu, and L. A. Taylor. 2011. The lunar rock and mineral characterization consortium: Deconstruction and integrated mineralogical, petrologic, and spectroscopic analyses of mare basalts. *Meteoritics and Planetary Science* 46: 228-251. 10.1111/j.1945-5100.2010.01148.x.

Janoiko, B. A., and J. E. Johnson. 2012. Desert Research and Technology Studies (D-RATS) 2011 Mission Overview. *43rd Lunar and Planetary Science Conference*, The Woodlands, TX, Abstract 1604.

Jolliff, B. L., M. A. Wieczorek, C. K. Shearer, and C. R. Neal (Eds.). 2006. New Views of the Moon. *Reviews in Mineralogy and Geochemistry* 60: pp. 772.

Keller, H. U., W. Goetz, H. Hartwig, S. F. Hviid, R. Kramm, W. J. Markiewicz, R. Reynolds, C. Shinohara, P. Smith, R. Tanner, P. Woida, R. Woida, B. J. Bos, and M. T. Lemmon. 2008. Phoenix Robotic Arm Camera. *Journal of Geophysical Research* 113: E00A17. doi:10.1029/2007JE003044.

King, T. V. V., and W. I. Ridley. 1987. Relation of the spectroscopic reflectance of olivine to mineral chemistry and some remote sensing implications. *Journal of Geophysical Research* 92: 11457–11469.

Klima, R.L., C. M. Pieters, J. W. Boardman, R. O. Green, J. W. Head III, P. J. Isaacson, J. F. Mustard, J. W. Nettles, N. E. Petro, M. I. Staid, J. M. Sunshine, L. A. Taylor, S. Tompkins. 2011. New insights into lunar petrology: distribution and composition of prominent low-Ca pyroxene exposures as observed by the Moon Mineralogy Mapper (M3). *Journal of Geophysical Research* 116: E00G06. doi:10.1029/2010JE003719.

Kruse, F.A., A. B. Lefkoff, J. B. Boardman, K. B. Heidebreicht, A. T. Shapiro, P. J. Barloon, and A. F. H. Goetz. 1993. The spectral image processing system (SIPS)—interactive visualization and analysis of imaging spectrometer data. *Remote Sensing of Environment* 44:145–163.

Lane, M. D., and P. R. Christensen. 1997. Thermal emission spectroscopy of anhydrous carbonates. *Journal of Geophysical Research* 102: 25,581 – 25,592. doi:10.1029/97JE02046.

Langevin, Y., F. Poulet, J. Bibring, and B. Gondet. 2005. Sulfates in the north polar region of Mars detected by OMEGA/Mars Express. *Science* 307: 1584–1586.

Léveillé, R. 2009. Validation of astrobiology technologies and instrument operations in terrestrial analogue environments. *Comptes Rendus Palevol* 8: 637-648.

Loeffler, B.M., R. G. Burns, K. H. Johnson, J. A. Tossell and D. J. Vaughn. 1974. Charge transfer in lunar materials - Interpretation of ultraviolet-visible spectral properties of the moon. *Proceedings of the 5th Lunar Science Conference, Geochimica et Cosmochimica Acta* 1 (Suppl. 5): 3007-3016.

Loeffler, B.M, R. G. Burns, and J. A. Tossell. 1975. Metal-to-metal charge transfer transitions - Interpretation of visible-region spectra of the moon and lunar materials. *Proceedings of the 6th Lunar Science Conference* 3: 2663-2676.

Longhi, J., D. Walker, E. N. Stolper, T. L. Grove, and J. F. Hays. 1972. Petrology of mare/rille basalts 15555 and 15065. In *The Apollo 15 Lunar Samples*. p. 131-134.

Longhi, J., D. Walker, and J. F. Hays. 1976. Fe and Mg in plagioclase. *Proceedings of the 7th Lunar Science Conference.* 1281-1300.

Malin, M. C., M. A. Caplinger, K. S. Edgett, F. T. Ghaemi, M. A. Ravine, J. A. Schaffner, J. M. Baker, J. D. Bardis, D. R. DiBiase, J. N. Maki, R. G. Willson, J. F. Bell III, W. E. Dietrich, L. J. Edwards, B. Hallet, K. E. Herkenhoff, E. Heydari, L. C. Kah, M. T. Lemmon, M. E. Minitti, T. S. Olson, T. J. Parker, S. K. Rowland, J. Schieber, R. J. Sullivan, D. Y. Sumner, P. C. Thomas, and R. A. Yingst. 2009. The Mars Science Laboratory (MSL) Mast-Mounted Cameras (Mastcams) Flight Instruments. *41st Lunar and Planetary Science Conference*, The Woodlands, TX, Abstract 1123.

McCord, T. B., and J. B. Adams. 1973. Progress in remote optical analysis of lunar surface composition. *The Moon* 7: 453–474. doi:10.1007/BF00564646.

McKay, D. S., G. H. Heiken, A. Basu, G. Blanford, S. Simon, R. Reedy, B. M. French, and J. Papike. 1991. The lunar regolith. In *The Lunar Sourcebook: A User's Guide to the Moon*. Heiken, G. H., D. T. Vaniman, and B. M. French (Eds.). pp. 285–356. New York: Cambridge University Press.

McSween, H. Y., Jr., S. L. Murchie J. A. Crisp, N. T. Bridges, R. C. Anderson, J. F. Bell III, D. T. Britt, J. Brückner, G. Dreibus, T. Economou, A. Ghosh, M. P. Golombek, J. P. Greenwoo1d, J. .R. Johnson, H. J. Moore, R. V. Morris, T. J. Parker, R. Rieder, R. Singer, and H. Winke. 1999. Chemical, multispectral and textural constraints on the composition and origin of rocks at the Mars Pathfinder landing site. *Journal of Geophysical Research* 104: 8679– 8716.

McSween, H. Y., Jr., T. L. Grove, and M. B. Wyatt. 2003. Constraints on the composition and petrogenesis of the Martian crust. *Journal of Geophysical Research* 108(E12): 5135. doi:10.1029/2003JE002175.

McSween, H. Y., S. W. Ruff, R. V. Morris, J. F. Bell III, K. Herkenhoff, R. Gellert, K. R. Stockstill, L. L. Tornabene, S. W. Squyres, J. A. Crisp, P. R. Christensen, T. J. McCoy, D. W. Mittlefehldt, and M. Schmidt. 2006a. Alkaline volcanic rocks from the Columbia Hills, Gusev crater, Mars. *Journal of Geophysical Research* 111: E09S91. doi:10.1029/2006JE002698.

McSween, H. Y., M. B Wyatt, R. Gellert, J. F. Bell III, R. V. Morris, K. E. Herkenhoff, L. S. Crumpler, K. A. Milam, K. R. Stockstill, L. L. Tornabene, R. E. Arvidson, P. Bartlett, D. Blaney, N. A. Cabrol, P. R. Christensen, B. C. Clark, J. A. Crisp, D. J. Des Marais, T. Economou, J. D. Farmer, W. Farrand, A. Ghosh, M. Golombek, S. Gorevan. 2006b. Characterization and petrologic interpretation of olivine-rich basalts at Gusev Crater, Mars. *Journal of Geophysical Research* 111: E02S10. doi:10.1029/2005JE002477.

MEPAG. 2010. *Mars Scientific Goals, Objectives, Investigations, and Priorities*. J.R. Johnson, Ed., 49 p. white paper posted September, 2010 by the Mars Exploration Program Analysis Group (MEPAG) at http://mepag.jpl.nasa.gov/reports/index.html.

MEPAG MRR-SAG. 2009. *Mars Astrobiology Explorer-Cacher: A potential rover mission for 2018*. Final report from the Mid-Range Rover Science Analysis Group (MRR-SAG). 94 pp. posted November 10, 2009, by the Mars Exploration Program Analysis Group (MEPAG) at http://mepag.jpl.nasa.gov/reports/.

MEPAG ND-SAG. 2008. *Science Priorities for Mars Sample Return*. Unpublished white paper, 73 p, posted March 2008 by the Mars Exploration Program Analysis Group (MEPAG) at http://mepag.jpl.nasa.gov/reports/ndsag.html.

Milliken, R. E., G. A. Swayze, R. E. Arvidson, J. L. Bishop, R. N. Clark, B. L. Ehlmann, R. O. Green, J. P. Grotzinger, R. V. Morris, S. L. Murchie, J. F. Mustard, C. Weitz. 2008. Opaline silica in young deposits on Mars. *Geology* 36(11): 847-850. doi:10.1130/G24967A.1.

Moore, J.G. 1966. Rate of palagonitization of submarine basalt adjacent to Hawaii. *U.S. Geological Survey Professional Paper* 550-D: 163–171.

Moore, D.M. and R. C. Reynolds, Jr. 1997. Identification of clay minerals and associated minerals. In *X-ray Diffraction and the Identification and Analysis of Clay Minerals*. pp. 203-240. New York: Oxford University Press.

Morris, R. V., H. V. Lauer Jr., C. A. Lawson, E. K. Gibson Jr., G. A. Nace, and C. Stewart. 1985. Spectral and other physiochemical properties of submicron powders of hematite (α-Fe_2O_3), maghemite (γ-Fe_2O_3), magnetite (Fe_3O_4), goethite (α-FeOOH), and lepidocroicite (γ-FeOOH). *Journal of Geophysical Research* 90: 3126–3144.

Morris, R. V., D. C. Golden, J. F. Bell III, H. V. Lauer Jr., and J. B. Adams. 1993. Pigmenting agents in Martian soils: Inferences from spectral,

Mossbauer, and magnetic properties of nanophase and other iron oxides in Hawaiian palagonitic soil PN-9. *Geochimica et Cosmochimica Acta* 57: 4597–4609.

Morris, R. V., D. C. Golden, J. F. Bell III, T. D. Shelfer, A. C. Scheinost, N. W. Hinman, G. Furniss, S. A. Mertzman, J. L. Bishop, D. W. Ming, C. C. Allen, and D. T. Britt. 2000. Mineralogy, composition, and alteration of Mars Pathfinder rocks and soils: Evidence from multispectral, elemental, and magnetic data on terrestrial analogue, SNC meteorite, and Pathfinder samples. *Journal of Geophysical Research* 105: 1757–1817.

Morris, R. V., J. F. Bell III, W. H. Farrand, and M. J. Wolff. 2002. Constraints on Martian global surface mineralogical composition, albedo and thermal inertia from Hubble Space Telescope extended-visible multispectral data. 33rd Lunar and Planetary Science Conference, Houston, TX, Abstract 1913.

Mottola, S., G. Arnold, H. G. Grothues, R. Jaumann, H. Michaelis, G. Neukum, and J. P. Bibring. 2007. The ROLIS Experiment on the Rosetta lander. *Space Science Reviews* 128: 241–255. doi:10.1007/s11214-006-9004-2

Murchie, S., L. Kirkland, S. Erard, J. Mustard, and M. Robinson. 2000. Near-infrared spectral variations of Martian surface materials from ISM imaging spectrometer data. *Icarus* 147: 444–471.

Murchie, S. L., J. F. Mustard, B. L. Ehlmann, R. E. Milliken, J. L. Bishop, N. K. McKeown, E. Z. Noe Dobrea, F. P. Seelos, D. L. Buczkowski, S. M. Wiseman, R. E. Arvidson, J. J. Wray, G. Swayze, R. N. Clark, D. J. Des Marais, A. S. McEwen, and J. P. Bibring. 2009. A synthesis of Martian aqueous mineralogy after one Mars year of observations from the Mars Reconnaissance Orbiter. *Journal of Geophysical Research* 114: E00D06. doi:10.1029/2009JE003342.

Mustard, J. F., S. L. Murchie, S. M. Pelkey, B. L. Ehlmann, R. E. Milliken, J. A. Grant, J.-P. Bibring, F. Poulet, J. Bishop, E. Noe Dobrea, L. Roach, F. Seelos, R. E. Arvidson, S. Wiseman, R. Green, C. Hash, D. Humm, E. Malaret, J. A. McGovern, K. Seelos, T. Clancy, R. Clark, D. Des Marais, N. Izenberg, A. Knudson, Y. Langevin, T.

Martin, P. McGuire, R. Morris, M. Robinson, T. Roush, M. Smith, G. Swayze, H. Taylor, T. Titus and M. Wolff. 2008. Hydrated silicate minerals on Mars observed by the CRISM instrument on MRO. *Nature* 454: 305– 309. doi:10.1038/nature07097.

National Aeronautics and Space Administration. 1963. *Report of the Ad Hoc Working Group on Apollo Experiments and Training on the Scientific Aspects of the Apollo Program.* The Sonett Report (final edition). 101p. <http://www.lpi.usra.edu/lunar/documents>.

National Research Council. 2007a. *The Scientific Context for Exploration of the Moon: Final Report*. Washington, D.C.: National Academies Press.

National Research Council. 2007b. *An Astrobiology Strategy for the Exploration of Mars*. Washington, D.C.: The National Academies Press.

National Research Council. 2011. *Vision and Voyages for Planetary Science in the Decade 2013-2022*. Washington, D.C.: The National Academies Press.

Neal, C. R., L. A. Taylor, and M. M. Lindstrom. 1988. Apollo 14 mare basalt petrogenesis: assimilation of KREEP-like components by a fractionating magma. *Proceedings of the 18th Lunar and Planetary Science Conference*. 139-153.

Neal, C. R., L. A. Taylor, R. A. Schmitt, S. S. Hughes, and M. M. Lindstrom. 1989. High alumina (HA) and very high potassium (VHK) basalt clasts from Apollo 14 breccia, Part 1: Mineralogy and petrology: Evidence of crystallization from evolving magmas. *Proceedings of the 19th Lunar Planetary Science Conference*. 137-145.

Nuñez, J. I., J. D. Farmer, R. G. Sellar, and P. B. Gardner. 2009a. Multispectral Microscopic Imager (MMI) with Improved Spectral Range and Resolution. *40th Lunar and Planetary Science Conference*, The Woodlands, TX, Abstract 1830.

Nuñez, J. I., J. D. Farmer, R. G. Sellar, C. C. Allen, and C. Meyer. 2009. A Multispectral Micro-Imager for Lunar Field Geology. *2nd Lunar Science Forum*, Moffett Field, CA.

Nuñez, J. I., J. D. Farmer, R. G. Sellar, C. Sarture, and P. B. Gardner. 2009b. Multispectral Microscopic Imager (MMI): Combining Microtexture and Mineralogy in the Robotic Exploration of the Moon and Mars. *2009 Geological Society of America Annual Meeting*, Portland, OR, Paper #95-11.

Núñez, J. I., J. D. Farmer, and R. G. Sellar. 2012. Exploration at the Hand Lens Scale: Results from the 2010 ILSO-ISRU Field Test Using the Multispectral Microscopic Imager. *43rd Lunar and Planetary Science Conference*, The Woodlands, TX, Abstract #2290.

Núñez, J. I., J. D. Farmer, R. G. Sellar, G. A. Swayze, and D. Blainey. In Review. Development and Science Applications of a Multispectral Microscopic Imager (MMI) for the Astrobiological Exploration of Mars.

Núñez, J. I., J. D. Farmer, R. G. Sellar, and C. C. Allen. In preparation. Exploring the Moon at the Microscale: Analysis of Apollo Samples Using the Multispectral Microscopic Imager.

Osterloo, M.M., V. E. Hamilton, J. L. Bandfield, T. D. Glotch, A. M. Baldridge, P. R. Christensen, L. L. Tornabene, and F. S. Anderson. 2008. Chloride-bearing materials in the southern highlands of Mars. *Science* 319: 1651–654.

Peacock, M.A. 1926. The petrology of Iceland. Part I, The basic tuffs. *Transactions of the Royal Society of Edinburgh* 55: 51–76.

Papike, J. J., A. E. Bence, and D. H. Lindsley. 1974. Mare basalts from the Taurus-Littrow region of the Moon. *Proceedings of the 5th Lunar Science Conference, Geochimica et Cosmochimica Acta*, 1(Suppl. 5): 471–504.

Pelkey, S. M., J. F. Mustard, S. Murchie, R. T. Clancy, M. Wolff, M. Smith, R. Milliken, J.-P. Bibring, A. Gendrin, F. Poulet, Y. Langevin, and B. Gondet. 2007. CRISM multispectral summary products:

Parameterizing mineral diversity on Mars from reflectance. *Journal of Geophysical Research* 112: E08S14. doi:10.1029/2006JE002831.

Pieters, C. M. 1993. Compositional diversity and stratigraphy of the lunar crust derived from reflectance spectroscopy. In *Remote Geochemical Analysis: Elemental and Mineralogical Composition*. C. M. Pieters and P. A. J. Englert (Eds.). pp. 309–339. New York: Cambridge University Press.

Pieters, C. M., E. M. Fischer, O. Rode, and A. Basu. 1993. Optical effects of space weathering: The role of the finest fraction. *Journal of Geophysical Research* 98: 20,817–20,824. doi:10.1029/93JE02467.

Pieters, C M, M. I. Staid, E. M. Fischer, S. Tompkins, and G. He. 1994. A sharper view of impact craters from Clementine data. *Science* 266(5192): 1844–1848.

Pieters, C. M., G. He, S. Tompkins, M. I. Staid, and E. M. Fischer. 1995. The low-Ti basalts of Tsiolkovsky as seen by Clementine. *26th Lunar and Planetary Science Conference*, 1121– 1122.

Pieters, C M, S. Tompkins, J. W. Head, and P. C. Hess. 1997. Mineralogy of the mafic anomaly in the South Pole–Aitken basin: Implications for excavation of the lunar mantle. *Geophysical Research Letters* 24(15): 1903–1906.

Pieters, C. M., J. W. Head, L. Gaddis, B. Jolliff, and M. Duke. 2001. Rock types of South Pole–Aitken basin and extent of basaltic volcanism. *Journal of Geophysical Research* 106(E11): 28,001–28,022.

Pieters, C. M., and T. Hiroi. 2004. RELAB (reflectance experiment laboratory): A NASA multiuser spectroscopy facility. *35th Lunar Planetary Science Conference*, Houston, TX, Abstract 1720.

Pokrovsky, O.S., J. Schott, D. I. Kudryavtzev, and B. Dupre. 2005. Basalt weathering in Central Siberia under permafrost conditions. *Geochimica et Cosmochimica Acta* 69: 5659–5680.

Poulet, F., N. Mangold, D. Loizeau, J. P. Bibring, Y. Langevin, J. Michalski, and B. Gondet. 2008. Abundance of minerals in the phyllosilicate-rich units on Mars. *Astronomy and Astrophysics* 487: L41–L44.

Powers, M. 1953. A new roundness scale for sedimentary particles. *Journal of Sedimentary Petrology* 25: 117–119.

Rieder, M., G. Cavazzini, Y. S. D´Yakonov, V. A. Frank-Kamenetskii, G. Gottardi, S. Guggenheim, P. V. Koval, G. Müller, A. M. R. Neiva, E. W. Radoslovich, J. Robert, F. P. Sassi, H. Takeda, Z. Weiss, and D. R. Wones. 1998. Nomenclature of the micas. *The Canadian Mineralogist* 36: 905–912.

Rhodes, J. M., and N. J. Hubbard. 1973. Chemistry, classification, and petrogenesis of Apollo 15 mare basalts. *Proceedings of the 4th Lunar Science Conference, Geochimica et Cosmochimica Acta* 2(Suppl. 4): 1127-1148.

Riner, M. A., P. G. Lucey, S. J. Desch, and F. M. McCubbin. 2009. Nature of opaque components on Mercury: Insights into a Mercurian magma ocean. *Geophysical Research Letters* 36: L02201. doi:10.1029/2008GL036128.

Robinson, M. S., and M. Riner. 2005. Advances in lunar science from the Clementine mission: A decadal perspective. *Journal of Earth System Science* 114: 669-686,

Ross, A. J., J. J. Kosmo, B. A. Janoiko. In Press. Historical synopses of Desert RATS 1997–2010 and a preview of Desert RATS 2011. *Acta Astronautica*, doi:10.1016/j.actaastro.2012.02.003.

Rowan, L.C., C. J. Simpson, and J. C. Mars. 2004. Hyperspectral analysis of the ultramafic complex and adjacent lithologies at Mordor, NT, Australia. *Remote Sensing of Environment* 91:419–431.

Ruff, S. W., J. D. Farmer, W. M. Calvin, K. E. Herkenhoff, J. R. Johnson, R. V. Morris, M. S. Rice, R. E. Arvidson, J. F. Bell III, P. R. Christensen, and S. W. Squyres. 2011. Characteristics, distribution, origin, and significance of opaline silica observed by the Spirit rover

in Gusev crater, Mars. *Journal of Geophysical Research* 116: E00F23. doi:10.1029/2010JE003767.

Ryder, G., and B. C. Schuraytz. 2001. Chemical variations of the large Apollo 15 olivine-normative mare basalt rock samples. *Journal of Geophysical Research* 106(E1): 1435-1451.

Sanders, G. B., and W. E. Larson. 2011. Integration of In-Situ Resource Utilization into lunar/Mars exploration through field analogs. *Advances in Space Research* 47: 20–29.

Sellar, R. G., J. D. Farmer, A. Kieta, J. Huang. 2006. Multispectral Microimager for Astrobiology. *Proceedings of SPIE* 6309: 63090E. doi: 10.1117/12.682272.

Sellar, R. G., J. D. Farmer, M. S. Robinson, and J. I. Nuñez. 2008. Multispectral Hand Lens and Field Microscope. *Joint Annual Meeting of LEAG-ICEUM-SRR*, Cape Canaveral, FL, Abstract 4075.

Sherman, D. M., R. G. Burns, and V. M. Burns. 1982. Spectral characteristics of the iron oxides with application to the Martian bright region mineralogy. *Journal of Geophysical Research* 87: 10,169– 10,180.

Shervais, J. W., S. Knapp, and L. A. Taylor. 1984. *Breccia Guidebook No.7 14321*. JSC 19492.

Shervais, J. W., L. A. Taylor, and M. M. Lindstrom. 1985. Apollo 14 mare basalts: petrology and geochemistry of clasts from consortium breccia 14321. *Proceedings of the 15th Lunar and Planetary Science Conference, Journal of Geophysical Research* 89: C375-C395.

Shoemaker, E. M., E. N. Goddard, E. J. Mackin, H. H. Schmitt, A. C. Waters. 1965. *Geological Field Investigation in Early Apollo Manned Lunar Landing Missions*. 60p. <http://www.lpi.usra.edu/lunar/documents/>.

Smith, P. H., M. G. Tomasko, D. Britt, D. G. Crowe, R. Reid, H. U. Keller, N. Thomas, F. Gliem, P. Rueffer, R. Sullivan, R. Greeley, J. M. Knudsen, M . B. Madsen, H. P. Gunnlaugsson, S. F. Hviid, W. Goetz, L. A. Soderblom, L. Gaddis, and R. Kirk. 1997. The imager for Mars Pathfinder experiment. *Journal of Geophysical Research* 102: 4003–4025. doi:10.1029/96JE03568.

Smith, P. H., R. Reynolds, J. Weinberg, T. Friedman, M. T. Lemmon, R. Tanner, R. J. Reid, R. L. Marcialis, B. J. Bos, C. Oquest, H. U. Keller, W. J. Markiewicz, R. Kramm, F. Gliem, and P. Rueffer. 2001. The MVACS Surface Stereo Imager on Mars Polar Lander. *Journal of Geophysical Research* 106: 17,589–17,607. doi:10.1029/1999JE001116.

Smith, P. H., L. Tamppari, R. E. Arvidson, D. Bass, D. Blaney, W. Boynton, A. Carswell, D. Catling, B. Clark, T. Duck, E. DeJong, D. Fisher, W. Goetz, P. Gunnlaugsson, M. Hecht, V. Hipkin, J. Hoffman, S. Hviid, H. Keller, S. Kounaves, C. F. Lange, M. Lemmon, M. Madsen, M. Malin, W. Markiewicz, J. Marshall, C. McKay, M. Mellon, D. Michelangeli, D. Ming, R. Morris, N. Renno, W. T. Pike, U. Staufer, C. Stoker, P. Taylor, J. Whiteway, S. Young, and A. Zent. 2008. Introduction to special section on the Phoenix Mission: Landing Site Characterization Experiments, Mission Overviews, and Expected Science. *Journal of Geophysical Research* 113: E00A18. doi:10.1029/2008JE003083.

Singer, R. B. 1982. Spectral evidence for the mineralogy of high-albedo soils and dust on Mars. *Journal of Geophysical Research* 87: 10,159–10,168.

Stöffler, D., and H. D. Knoll. 1977. Composition and origin of plagioclase, pyroxene and olivine clasts of lunar breccias 14006, 14063, 14066, 14311, 14320 and 14321. *Proceedings of the 8th Lunar Science Conference*. 1849-1867.

Stöffler, D., and G. Ryder. 2001. Stratigraphy and isotopic ages of lunar geologic units: Chronological standard for the inner solar system. *Space Science Reviews* 96: 9-54.

Strens, R. G. J., and B. J. Wood. 1979. Diffuse Reflectance Spectra and Optical Properties of Some Iron and Titanium Oxides and Oxyhydroxides. *Mineralogical Magazine* 43: 347-354.

Squyres, S.W., R. E. Arvidson, S Ruff, R. Gellert, R. V. Morris, D. W. Ming, L. Crumpler, J. D. Farmer, D. J. Des Marais, A. Yen, S. M. McLennan, W. Calvin, J. F. Bell, B. C. Clark, A. Wang, T. J. McCoy, M. E. Schmidt, and P. A. de Souza. 2008. Detection of silica-rich deposits on Mars. *Science* 320: 1063–1067.

Sunshine, J.M., and C. M. Pieters. 1998. Determining the composition of olivine from reflectance spectroscopy. *Journal of Geophysical Research* 103: 13675–13688.

Swann, G. A., N. G. Bailey, R. M. Batson, R. E. Eggleton, M. H. Hait, H. E. Holt, K. B. Larson, M. C. McEwen, E. D. Mitchell, G. G. Schaber, J. P. Schafer, A. B. Shepard, R. L. Sutton, N. J. Trask, G. E. Ulrich, H. G. Wilshire, and E. W. Wolfe. 1972a. Chapter 3. Preliminary Geologic Investigation of the Apollo 14 landing site. In *Apollo 14 Preliminary Science Report*. NASA SP-272. pp. 39-85.

Swann, G. A., N. G. Bailey. R. M. Batson, V. L. Freeman, M. H. Hair, J. W. Head, H. E. Holt, K. A. Howard. J. B. Irwin, K. B. Larson, W. R. Muehlberger, V. S. Reed, J. J. Rennilson, G. G. Schaber, D. R. Scott, L. T. Silver, R. L. Sutton, G. E. Ulrich, H. G. Wilshire, and E. W. Wolfe. 1972b. Chapter 5. Preliminary Geologic Investigation of the Apollo 15 landing site. In *Apollo 15 Preliminary Science Report*. NASA SP-289. pp. 5-1 – 5-112.

Swann, G. A., N. G. Bailey, R. M. Batson, R. E. Eggleton, M. H. Hait, H. E. Holt, K. B. Larson, V. S. Reed, G. G. Schaber, R. L. Sutton, N. J. Trask, G. E. Ulrich, and H. G. Wilshire. 1977. *Geology of the Apollo 14 landing site in the Fra Mauro Highlands*. U.S. Geological Survey Professional Paper 880.

Swayze, G. A., R. N. Clark, A. F. H. Goetz, T. G. Chrien, and N. S. Gorelick. 2003. Effects of spectrometer band pass, sampling, and signal-to-noise ratio on spectral identification using the Tetracorder algorithm. *Journal of Geophysical Research* 108(E9): 5105. doi:10.1029/2002JE001975.

Takeda, H., M. Miyamoto, and T. Ishii. 1980. Composition of basaltic clasts in lunar and eucrite polymict breccias. *Proceedings of the 11th Lunar and Planetary Science Conference*. 135-147.

Taylor S.R., M. Kaye, P. Muir, W. Nance, R. Rudowski and N. Ware. 1972. Composition of the lunar uplands: Chemistry of Apollo 14 samples from Fra Mauro. *Proceedings of the 3rd Lunar Science Conference, Geochimica et Cosmochimica Acta* 2(Suppl. 3): 1231-1249.

Taylor, L. A., C. M. Pieters, L. P. Keller, R. V. Morris, and D. S. McKay. 2001. Lunar mare soils: Space weathering and the major effects of surface-correlated nanophase Fe. *Journal of Geophysical Research* 106(E11): 27,985–27,999. doi:10.1029/2000JE001402.

ten Kate, I. L., R. Armstrong, B. Bernhardt, M. Blumers, J. Craft, D. Boucher, E. Caillibot, J. Captain, G. Deleuterio, J. D. Farmer, D. P. Glavin, T. Graff, J. C. Hamilton, G. Klingelhöfer, R. V. Morris, J. I. Nuñez, J. W. Quinn, G. B. Sanders, R. G. Sellar, L. Sigurdson, R. Taylor, K. Zacny. In Press. Mauna Kea, Hawai'i as an analogue site for future planetary resource exploration: Results from the 2010 ILSO-ISRU field-testing campaign. *Journal of Aerospace Engineering.*

Thorseth, I. H., H. Furnes, and O. Tumyr. 1991. A textural and chemical study of Icelandic palagonite of varied composition and its bearing on the mechanism of the glass-palagonite transformation. *Geochimica et Cosmochimica Acta* 55: 731–749.

Tompkins, S., J. F. Mustard, C. M. Pieters, D. W. Forsyth. 1997. Optimization of endmembers for spectral mixture analysis. *Remote Sensing of Environment* 59: 472–489.

Tompkins, S., and C. M. Pieters. 1999. Mineralogy of the lunar crust: results from Clementine. *Meteoritics and Planetary Science* 34: 25–41.

Tompkins, S., and C. M. Pieters. 2010. Spectral characteristics of lunar impact melts and inferred mineralogy. *Meteoritics and Planetary Science* 45: 1152–1169. doi:10.1111/j.1945-5100.2010.01074.x.

Walker, D., J. Longhi, A. C. Lasaga, E. M. Stolper, T. L. Grove, and J. F. Hays. 1977. Slowly cooled microgabbros 15555 and 15056. *Proceedings of the 8th Lunar Science Conference.* 1521-1547.

Wanke, H., H. Baddenhausen, A. Balacescu, F. Teschke, B. Spettel, G. Dreibus, H. Palme, M. Quijano-Rico, H. Kruse, F. Wlotzka and F. Begemann. 1973. Multielement analysis of lunar samples and some implications of the results. *Proceedings of the 3rd Lunar Science Conference, Geochimica et Cosmochimica Acta* 2(Suppl. 3): 1251-1268.

Warner, N.H., and J. D. Farmer. 2010. Subglacial Hydrothermal Alteration Minerals in Jökulhlaup Deposits of Southern Iceland, with Implications for Detecting Past or Present Habitable Environments on Mars. *Astrobiology* 10: 523-547.

Warren, P. H., G. J. Taylor, K. Keil, D. N. Shirley, and J. T. Wasson. 1983. Petrology and chemistry of two large granite clasts from the Moon. *Earth and Planetary Science Letters* 64: 175-185.

Weitz, C. M., W. H. Farrand, J. R. Johnson, I. Fleischer, C. Schröder, A. Yingst, B. Jolliff, R. Gellert, J. Bell, K. E. Herkenhoff, G. Klingelhöfer, B. Cohen, W. Calvin, M. Rutherford, and J. Ashley. 2010. Visible and near-infrared multispectral analysis of geochemically measured rock fragments at the Opportunity landing site in Meridiani Planum. *Journal of Geophysical Research* 115: E00F10. doi:10.1029/2010JE003660.

Wilhelms, D. E. 1970. Summary of lunar stratigraphy – Telescopic observations. *U.S. Geological Survey Professional Paper 599-F*. p. F1-F47.

Wilhelms, D. E. 1987. The Geologic History of the Moon. *U.S. Geological Survey Professional Paper 1348*. pp. 302.

Wilshire, H. G., and E. D. Jackson. 1972. Petrology and stratigraphy of the Fra Mauro Formation at the Apollo 14 site. *U.S. Geological Survey Professional Paper 785*.

BIOGRAPHICAL SKETCH

Jorge Iván Núñez Sánchez is originally from Manizales, Colombia. Núñez attended the University of Alabama at Birmingham (UAB) where he received a bachelor of sciences in physics and a bachelor of sciences in mechanical engineering. At UAB he also received minors in biology, chemistry, and mathematics. He continued his education in the School of Earth and Space Exploration (formerly the Department of Geological Sciences) at Arizona State University pursuing a doctorate in Geological Sciences. His research is a marriage of science and engineering that focused on the development and science applications of a novel Multispectral Microscopic Imager (MMI) for future robotic and human exploration of planetary surfaces.

This document was generated using the Graduate College Format Advising tool. Please turn a copy of this page in when you submit your document to Graduate College format advising. You may discard this page once you have printed your final document. DO NOT TURN THIS PAGE IN WITH YOUR FINAL DOCUMENT!
Font Type: Arial
Font size: 12

269

269

269